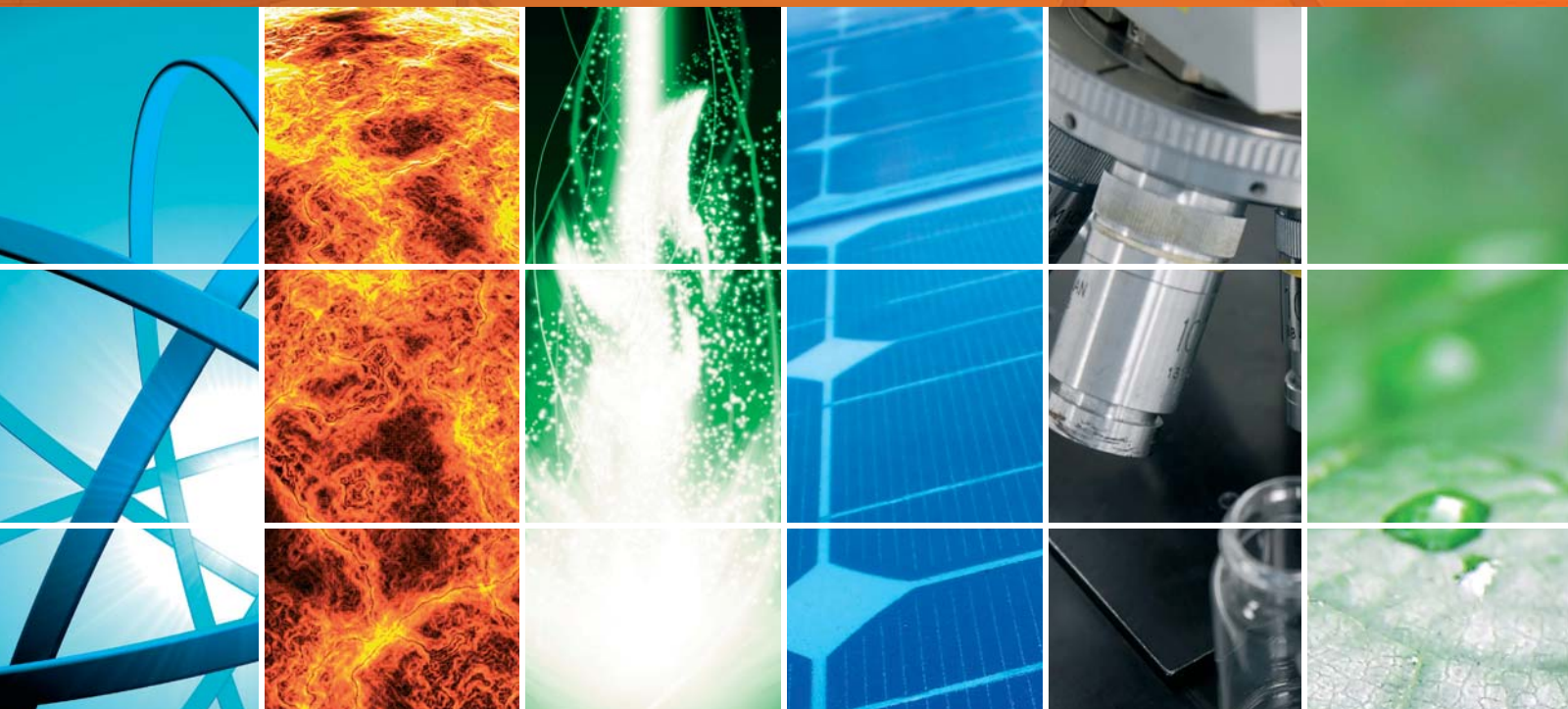


Thin-Film Photovoltaics 2011

Guest Editors: Leonardo Palmisano, Vincenzo Augugliaro,
Gaetano Di Marco, and Mario Pagliaro





Thin-Film Photovoltaics 2011

International Journal of Photoenergy

Thin-Film Photovoltaics 2011

Guest Editors: Leonardo Palmisano, Vincenzo Augugliaro,
Gaetano Di Marco, and Mario Pagliaro



Copyright © 2012 Hindawi Publishing Corporation. All rights reserved.

This is a special issue published in "International Journal of Photoenergy." All articles are open access articles distributed under the Creative Commons Attribution License, which permits unrestricted use, distribution, and reproduction in any medium, provided the original work is properly cited.

Editorial Board

M. S. A. Abdel-Mottaleb, Egypt
Muhammad Abdul Rauf, UAE
Nihal Ahmad, USA
Nicolas Alonso-Vante, France
Wayne A. Anderson, USA
Vincenzo Augugliaro, Italy
Detlef W. Bahnemann, Germany
Ignazio Renato Bellobono, Italy
Raghu N. Bhattacharya, USA
Gion Calzaferri, Switzerland
Vikram L. Dalal, USA
D. Demetriou Dionysiou, USA
Abderrazek Douhal, Spain
Samy El-Shall, USA
Beverley Glass, Australia
Shahed Khan, USA

Cooper H. Langford, Canada
Yuexiang Li, China
Gianluca Li Puma, UK
Panagiotis Lianos, Greece
Stefan Lis, Poland
Gilles Mailhot, France
Ugo Mazzucato, Italy
Jacek Miller, Poland
Franca Morazzoni, Italy
Leonardo Palmisano, Italy
David Lee Phillips, Hong Kong
Xie Quan, China
Tijana Rajh, USA
Saffa Riffat, UK
Peter Robertson, UK
Jean-Louis Scartezzini, Switzerland

Pathiyamattom Joseph Sebastian, Mexico
Panagiotis Smirniotis, USA
Sam-Shajing Sun, USA
Masanori Tachiya, Japan
Gopal N. Tiwari, India
Veronica Vaida, USA
Roel van De Krol, The Netherlands
Mark van Der Auweraer, Belgium
Johannes Vos, Ireland
David Worrall, UK
F. Yakuphanoglu, Turkey
Jimmy C. Yu, Hong Kong
Klaas Zachariasse, Germany
Jincai Zhao, China

Contents

Thin-Film Photovoltaics 2011, Leonardo Palmisano and Gaetano Di Marco
Volume 2012, Article ID 419715, 2 pages

Tailoring the Composition and Properties of Sprayed CuSbS₂ Thin Films by Using Polymeric Additives, Ionut Popovici and Anca Duta
Volume 2012, Article ID 962649, 6 pages

Characterization of Nanocrystalline SiGe Thin Film Solar Cell with Double Graded-Dead Absorption Layer, Chao-Chun Wang, Dong-Sing Wu, Shui-Yang Lien, Yang-Shih Lin, Chueh-Yang Liu, Chia-Hsum Hsu, and Chia-Fu Chen
Volume 2012, Article ID 890284, 6 pages

Polarity Switchable Photovoltages in Miscut La_{0.67}Ca_{0.33}MnO₃ Films, J. Wang, H. Ni, K. Zhao, Y.-C. Kong, H. K. Wong, and S. X. Zhong
Volume 2012, Article ID 547591, 5 pages

Effect of p-Layer and i-Layer Properties on the Electrical Behaviour of Advanced a-Si:H/a-SiGe:H Thin Film Solar Cell from Numerical Modeling Prospect, Peyman Jelodarian and Abdolnabi Kosarian
Volume 2012, Article ID 946024, 7 pages

Performance of Dye-Sensitized Solar Cells with (PVDF-HFP)-KI-EC-PC Electrolyte and Different Dye Materials, M. M. Noor, M. H. Buraidah, S. N. F. Yusuf, M. A. Careem, S. R. Majid, and A. K. Arof
Volume 2011, Article ID 960487, 5 pages

A Convenient Method for Manufacturing TiO₂ Electrodes on Titanium Substrates, Wei Qin, Songtao Lu, Xiaohong Wu, and Song Wang
Volume 2011, Article ID 373210, 4 pages

Optimization of Recombination Layer in the Tunnel Junction of Amorphous Silicon Thin-Film Tandem Solar Cells, Yang-Shin Lin, Shui-Yang Lien, Chao-Chun Wang, Chia-Hsun Hsu, Chih-Hsiang Yang, Asheesh Nautiyal, Dong-Sing Wu, Pi-Chuen Tsai, and Shuo-Jen Lee
Volume 2011, Article ID 264709, 5 pages

Three-Terminal Amorphous Silicon Solar Cells, Cheng-Hung Tai, Chu-Hsuan Lin, Chih-Ming Wang, and Chun-Chieh Lin
Volume 2011, Article ID 813093, 5 pages

Charge-Carrier Transport in Thin Film Solar Cells: New Formulation, Jesús E. Velazquez-Perez and Yuri G. Gurevich
Volume 2011, Article ID 976063, 5 pages

Preparation and Characterization of Coevaporated Cd_{1-x}Zn_xS Alloy Thin Films, Wei Li, Jiayi Yang, Zhen Sun, Lianghuan Feng, Jingquan Zhang, and Lili Wu
Volume 2011, Article ID 969214, 5 pages

Efficiency Considerations and Application Limits of Single-Phase Active Power Filter with Converters for Photoenergy Applications, Saša Sladić, Srđan Skok, and David Nedeljković
Volume 2011, Article ID 643912, 8 pages

TiO₂/Chitosan-NH₄I(+I₂)-BMII-Based Dye-Sensitized Solar Cells with Anthocyanin Dyes Extracted from Black Rice and Red Cabbage, M. H. Buraidah, L. P. Teo, S. N. F. Yusuf, M. M. Noor, M. Z. Kufian, M. A. Careem, S. R. Majid, R. M. Taha, and A. K. Arof
Volume 2011, Article ID 273683, 11 pages

Indium-Doped Zinc Oxide Thin Films as Effective Anodes of Organic Photovoltaic Devices, Ziyang Hu, Baochen Jiao, Jianjun Zhang, Xiaodan Zhang, and Ying Zhao
Volume 2011, Article ID 158065, 5 pages

Load-Resistance- and Voltage-Tunable Photovoltaic Effect in Tilting Manganite Films, X. L. Han, H. Ni, K. Zhao, Y.-C. Kong, H. K. Wong, and S. Q. Zhao
Volume 2011, Article ID 314085, 4 pages

Achievements and Challenges of CdS/CdTe Solar Cells, Zhou Fang, Xiao Chen Wang, Hong Cai Wu, and Ce Zhou Zhao
Volume 2011, Article ID 297350, 8 pages

Theoretical Insight into the Spectral Characteristics of Fe(II)-Based Complexes for Dye-Sensitized Solar Cells Part I: Polypyridyl Ancillary Ligands, Xiaoqing Lu, Shuxian Wei, Chi-Man Lawrence Wu, Ning Ding, Shaoren Li, Lianming Zhao, and Wenyue Guo
Volume 2011, Article ID 316952, 11 pages

Progress in Thin Film Solar Cells Based on Cu₂ZnSnS₄, Hongxia Wang
Volume 2011, Article ID 801292, 10 pages

Influence of Parameters of Cold Isostatic Pressing on TiO₂ Films for Flexible Dye-Sensitized Solar Cells, Yong Peng, Jefferson Zhe Liu, Kun Wang, and Yi-Bing Cheng
Volume 2011, Article ID 410352, 7 pages

Editorial

Thin-Film Photovoltaics 2011

Leonardo Palmisano¹ and Gaetano Di Marco²

¹ University of Palermo, Viale delle Scienze, 90128 Palermo, Italy

² IPCF-CNR, Consiglio Nazionale delle Ricerche, Viale Ferdinando Stagno d'Alcontres 37, 98158 Messina, Italy

Correspondence should be addressed to Leonardo Palmisano, leonardo.palmisano@unipa.it

Received 30 November 2011; Accepted 30 November 2011

Copyright © 2012 L. Palmisano and G. Di Marco. This is an open access article distributed under the Creative Commons Attribution License, which permits unrestricted use, distribution, and reproduction in any medium, provided the original work is properly cited.

The first special issue, concerning thin-film photovoltaic (PV), was published in 2010. It covered progresses in first-, second-, and third-generation PV devices, respectively, including crystalline Si, CdTe, and CuInGaSe₂ (GIGS), organic, and dye-sensitized solar cells that mimic natural photosynthesis. Even today, many researchers are involved to find efficient methods and materials to generate electricity in clean, renewable, sustainable, and economic way. Many of them are convinced that solar energy is able to provide valuable assistance to the world energy needs. In addition, due to apparent global economic crisis, many governments have tried to promote significant public and private investments in order to create new and more numerous jobs. In this special issue are presented scientific papers which also cover theoretical and technical aspects to encourage growth in the PV field. We wish to express our thanks to all the authors who have made this publication possible, and a brief summary of all the eighteen accepted papers is below.

In “TiO₂/chitosan-NH₄I(+I₂)-BMII-based dye-sensitized solar cells with anthocyanin dyes extracted from black rice and red cabbage,” dye -sensitized solar cells (DSSCs) using anthocyanin dye and polymer electrolyte with ammonium iodide (NH₄I) salt are presented. A study, taking into account different dyes, electrolytes, PH, and other parameters, is carried out. Photovoltaic performances are shown and discussed.

In “Performance of dye-sensitized solar cells with (PVDF-HFP)-KI-EC-PC electrolyte and different dye materials,” a polymer electrolyte with poly(vinylidene fluoride hexafluoropropylene) matrix (PVDF-HFP) is used in DSSCs. The cells' performance with different dyes such as N₃, anthocyanin, and chlorophyll are compared. The multidye natural mixture shows interesting conversion efficiency.

In “A convenient method for manufacturing TiO₂ electrodes on titanium substrates,” the possibility of developing microplasma oxidation (MPO) method to prepare TiO₂ thin films, useful to achieve photoanodes for DSSCs devices, is presented. Photoelectricity properties and morphology of the films are investigated.

In “Influence of parameters of cold isostatic pressing on TiO₂ films for flexible dye-sensitized solar cells,” cold isostatic pressing (CIP) is used to make TiO₂ working electrodes for flexible DSSCs. A study varying pressures and holding time, supported by electrochemical impedance spectroscopy (EIS) analysis, is performed on the working electrodes.

In “Indium-doped zinc oxide thin films as effective anodes of organic photovoltaic devices,” indium-doped zinc oxide (IZO) thin films are prepared by low-cost ultrasonic spray pyrolysis (USP). The IZO films are investigated as anodes in bulk-heterojunction organic photovoltaic (OPV) devices, and photoelectrochemical parameters are shown.

In “Theoretical insight into the spectral characteristics of Fe(II)-based complexes for dye-sensitized solar cells—part I: polypyridyl ancillary ligands,” a theoretical investigation on a series of polypyridyl Fe(II)-based complexes, as sustainable dyes for DSSCs, by density functional theory (DFT) and time-dependent DFT (TD-DFT) is performed. Compared with Ru(II) sensitizers, Fe(II)-based complexes show interesting characteristics.

In “Optimization of recombination layer in the tunnel junction of amorphous silicon thin-film tandem solar cells,” amorphous silicon/amorphous silicon (a-Si/a-Si) tandem solar cells are fabricated by high-frequency plasma-enhanced chemical vapor deposition (HF-PECVD). Recombination and the intrinsic layer thickness effects, on the device performance, are investigated.

In “Three-terminal amorphous silicon solar cells,” new three-terminal a-Si p-i-n/n-i-p solar cell, with low recombination rate of photogenerated carriers, is conceived. A comparison between the two-terminal a-Si p-i-n solar cell (control cell) and the former is done.

In “Characterization of nano-crystalline SiGe thin film solar cell with double graded-dead absorption layer,” nanocrystalline silicon-germanium (nc-SiGe) thin films, obtained by plasma-enhanced chemical vapour deposition (HF-PECVD), are used in a silicon-based solar cell. Spectroscopic, microscopic analysis and *I-V* characterization of the cells are shown.

In “Effect of p-layer and i-layer properties on the electrical behaviour of advanced a-Si:H/a-SiGe:H thin film solar cell from numerical modeling prospect,” a two-dimensional computer simulation in amorphous silicon band-gap for the optimization of the single-and double-junction hydrogenated amorphous silicon-germanium solar cells is presented. The electrical, photogeneration, and recombination rate behaviours are investigated.

In “Progress in thin film solar cells based on $\text{Cu}_2\text{ZnSnS}_4$,” the paper reviews the wide range of techniques that have been used to deposit $\text{Cu}_2\text{ZnSnS}_4$ (CZTS) semiconductor thin films. The performance of the thin film solar cells using the CZTS material is discussed.

In “Tailoring the composition and properties of sprayed CuSbS_2 thin films by using polymeric additives,” spray pyrolysis and polymeric additives, to prepare CuSbS_2 thin films, are used. These are characterized by morphological and spectroscopic points of view. The polymeric additives represent a powerful tool for developing efficient n-p junctions in solid-state solar cells.

In “Preparation and characterization of coevaporated $\text{Cd}_{1-x}\text{Zn}_x\text{S}$ alloy thin films,” homogenous $\text{Cd}_{1-x}\text{Zn}_x\text{S}$ thin films are prepared by the vacuum coevaporation of CdS and ZnS. Structural, composition, and optical properties are investigated. A novel $\text{Cd}_{0.4}\text{Zn}_{0.6}\text{S}$ layer is introduced in the CuInS_2 -based solar cells.

In “Achievements and challenges of CdS/CdTe solar cells,” the paper summarizes the latest research and techniques to solve the efficiency problem in CdS/CdTe photovoltaics. It is believed that these devices are good candidates for future low-cost solar cells, so new ideas are offered for further development.

In “Polarity switchable photovoltages in miscut $\text{La}_{0.67}\text{Ca}_{0.33}\text{MnO}_3$ films,” a potential application of the manganite film as photodetector is provided. This idea emerges from the photovoltaic effects observed in the $\text{La}_{0.67}\text{Ca}_{0.33}\text{MnO}_3$ (LCMO) film and LaSrAlO_4 (LSAO) substrate under pulse laser irradiation.

In “Load resistance- and voltage-tunable photovoltaic effect in tilting manganite films,” the photovoltaic properties of miscut $\text{La}_{2/3}\text{Ca}_{1/3}\text{MnO}_3$ films are investigated. The photoreponse depends on bias voltage (V_b) and load resistance (RS). The obtained results suggest potential optoelectronic applications.

In “Efficiency considerations and application limits of single-phase active power filter with converters for photoenergy applications,” a new way of connecting PV sources to adaptive

voltage active power filter (AVAPF) is compared with classic approach including active power filter (APF). Experimental results confirm expectations of increased energy transfer from additional DC source to network.

In “Charge-carrier transport in thin film solar cells: new formulation,” is reported that conventional solar cells plays a major limiting role in the cell efficiency. Moreover a new formulation of the basic equations describing charge-carrier transport in the cell along with a set of boundary conditions is presented.

Leonardo Palmisano
Gaetano Di Marco

Research Article

Tailoring the Composition and Properties of Sprayed CuSbS_2 Thin Films by Using Polymeric Additives

Ionut Popovici and Anca Duta

Department of Renewable Energy Systems and Recycling, Transilvania University of Brasov, Eroilor 29, 500036 Brasov, Romania

Correspondence should be addressed to Anca Duta, a.duta@unitbv.ro

Received 21 June 2011; Accepted 1 November 2011

Academic Editor: Vincenzo Augugliaro

Copyright © 2012 I. Popovici and A. Duta. This is an open access article distributed under the Creative Commons Attribution License, which permits unrestricted use, distribution, and reproduction in any medium, provided the original work is properly cited.

CuSbS_2 thin films were obtained by spray pyrolysis deposition, using polymeric additives for controlling the surface properties and film's composition. Ternary crystalline chalcostibite compounds have been obtained without any postdeposition treatments. XRD spectra and IR spectroscopy were used to characterize films composition and interactions between components. Films morphology and surface energy were investigated using AFM microscopy and contact angle measurements. Hydrophobic and hydrophilic polymers strongly influence the composition and film morphology.

1. Introduction

In heterojunction devices (solar cells), copper-based absorbers have been intensively studied mainly for their p-type conductivity due to copper deficiency [1]. More recently, ternary CIS/CIGS compounds with $\text{Cu}(\text{In}/\text{Ga}/\text{Sb}/\text{Bi})(\text{S}/\text{Se})$ structures were investigated as candidates in non-silicon solar cell application. The In^{3+} or Ga^{3+} ions in the lattice reduce the Cu^+ ions mobility thus increasing the stability comparing to the copper sulfides (Cu_{2-x}S). Most of the studies are focused on $\text{Cu}(\text{In}, \text{Ga})(\text{S}/\text{Se})_2$ while antimony-based compounds are less reported. In this paper CuSbS_2 (chalcostibite) thin films are investigated as an alternative absorber, because of the similar properties required for photovoltaic materials, with the advantage that antimony has a lower purchase price than indium. Also, copper-gold structures that reduce the CIS/CIGS efficiency were not reported for the antimony compound.

The first report on chalcostibite occurrence came from Rhar-el-Anz in Morocco/Tunisia in 1942 as a mineral of dark gray color with metallic luster, [2], with an orthorhombic [JCPDS 44-1417] crystal structure. In terms of structural properties, CuSbS_2 is often formed as a mixture of different phases also including Sb_2S_3 [3], or Cu_3SbS_3 , and Cu_3SbS_4 [1, 4].

Literature reports on its synthesis using different techniques, both in crystalline and amorphous state. Amorphous CuSbS_2 was obtained from vacuum postgrowth treatments of single-source thermal evaporation films, with optical transition in the range 1.8–2 eV [3]. Crystalline CuSbS_2 was obtained by hydrothermal synthesis at 200°C [5] with similar structure as the natural mineral (JCPDS 35-413) and congruent crystallization at 552°C [1]. There are other various deposition techniques reported for obtaining crystalline CuSbS_2 thin films, with variable properties in terms of crystallinity, phase composition, and morphologies: chemical bath deposition, [6], single-source thermal evaporation method [3, 7], solvothermal growth [8], and sputtering [9]. Thin films of CuSbS_2 with different morphologies, varying from brick-like to plank-like, fibbers [10], and spherical morphology are reported to be obtained using spray pyrolysis deposition [8, 10, 11].

Crystalline CuSbS_2 thin films (direct band-gap 1.52 eV and p-type conductivity) have been used in solid state solar cells with the structure: $\text{FTO}/\text{CdS}/\text{Sb}_2\text{S}_3/\text{CuSbS}_2$ [12], $\text{FTO}/\text{TiO}_2/\text{CuSbS}_2/\text{C}$ [11], and $\text{TCO}/\text{CdS}/\text{Sb}_2\text{S}_3/\text{Sb}_2\text{S}_3\text{-CuS}(\text{CuSbS}_2)/\text{Ag}$ [6]. One of the main limitations in the cells efficiency is imposed by the contact at the interface between the n-type and p-type semiconductors. Therefore, there is a strong need for tailoring the thin films morphology,

TABLE 1: Precursor solution composition.

Sample	$\text{CuCl}_2 \cdot 2\text{H}_2\text{O}$ mmol	$(\text{CH}_3\text{COO})_3\text{Sb}$ mmol	H_2NCSNH_2 mmol	Cu : Sb : S molar ratio
A	0.81	1.2	10.5	1 : 1.48 : 13
B	0.81	1.6	10.5	1 : 1.97 : 13
C	0.81	2	10.5	1 : 2.48 : 13
D	0.81	2.81	10.5	1 : 3.47 : 13
E	0.81	3.81	10.5	1 : 4.4 : 13
F	0.87	1.6	10.5	1 : 1.84 : 13
G*	0.87	1.6	10.5	1 : 1.84 : 13
H**	0.87	1.6	10.5	1 : 1.84 : 13

* Polymer additive: HFL-100 ppm.

** Polymer additive: HFB-100 ppm.

supporting a good reciprocal infiltration, and avoiding shunts.

The morphology of the thin layers depends on the deposition conditions, with influence on the ratio between the nucleation and growth rates (e.g., high nucleation/growth ratio results in small grains, dense films). These rates are correlated with the reaction affinity of the precursors' species which, in turn, depends on their stability. The control of the reactants stability in the precursors' solution can be reached using additives able to form physical or chemical bonds with the precursor ions. The usually mentioned additives are low-molecular organic compounds (with OH and C=O groups). Their use, although efficient, can rise toxicity and cause problems. The use of polymers, with variable hydrophobic degree, represents a novel alternative investigated in this paper.

Considering the multilayered structure of a solid state solar cell, another important aspect governing the reciprocal infiltration is a good adherence of the precursor on the host layer, developed as a high energy surface. Therefore, the influence of polymeric additives on the surface properties of the CuSbS_2 films is also reported.

2. Experimental

2.1. Deposition Part. CuSbS_2 thin films were deposited by spray pyrolysis deposition on an automatic installation, on FTO (fluorine-doped thin oxide, TEC 8/3 mm Pilkington) conductive glass. The glass was washed in an ultrasonic bath, in several immersions in alcohol and then dried with compressed air. The glass was heated at the deposition temperature on a thermostatic heating plate. As precursors, aqueous solutions of copper(II)-chloride dehydrate, (Scharlau, $\text{CuCl}_2 \cdot 2\text{H}_2\text{O}$, min 99%), concentration between 16.2–17.4 mM, antimony(III) acetate, (Alfa Aesar, $(\text{CH}_3\text{COO})_3\text{Sb}$, 99.99%), concentration between 24–76.2 mM, and thiourea, concentration 210 mM, (Scharlau, H_2NCSNH_2 , 99%) were prepared, with a small addition of HCl for insuring the solubility of the antimony acetate. Two polymeric additives, sodium maleate-methyl metacrylate (hydrophilic polymer, HFL) and sodium maleate-vinyl acetate (hydrophobic polymer, HFB) were used, completing the complexation effect of thiourea.

Thin films, with different composition and morphology were obtained by varying the precursors' concentrations and molar ratio between components, as presented in Table 1.

For samples G and H polymeric additives were used in 100 ppm concentration.

Previously optimized deposition parameters [11] were used for all the samples: temperature of 240°C, carrier gas (air) pressure of 1.5 bar, spraying height 25 cm, with 60 seconds pause between two spraying sequences.

2.2. Film Characterization. The CuSbS_2 films deposited on FTO were analyzed using X-ray diffraction (XRD, Bruker-AXS-D8, $\text{Cu}_{K\alpha 1}$ radiation) and atomic force microscopy (AFM/STM, NT-MDT model NTEGRA Probe Nanolaboratory), in semicontact mode, with an Si-tip (CSG10, force constant 0.15 N/m, tip radius 10 nm); surface energy and wetting properties were analyzed using the Sessile drop technique for contact angle measurements with a OCA-20 Contact Angle-meter (DataPhysics Instruments). The IR reflectance spectra were recorded with a Spectrum BX FT-IR System (Perkin Elmer).

3. Results and Discussions

At the selected deposition parameters, all films presented a smooth homogenous aspect.

The diffraction analysis of the films show the formation of crystalline CuSbS_2 (PDF 00-009-0143) in orthorhombic polymorph, along with famatinite Cu_3SbS_4 (PDF 00-035-0581), proving that spray pyrolysis can be used as deposition method for crystalline ternary Cu-Sb-S thin films. The Cu_3SbS_4 pattern in the XRD spectra of chalcostibite films was also obtained and explained by Rodríguez-Lazcano et al. as the result of copper sulfide excess which leads to the formation of copper-rich Cu-Sb-S compounds [1]. Literature [1] mentions that antimony in excess can further form binary sulphides either crystalline or amorphous. Still, the results show that, in our experimental conditions, even in Sb-excess precursors only ternary stable compounds are formed and not mixtures of secondary sulphides.

The deposition temperature assures enough thermal energy for the two main processes that take place on the substrate surface: first, the evaporation of solvents and breaking

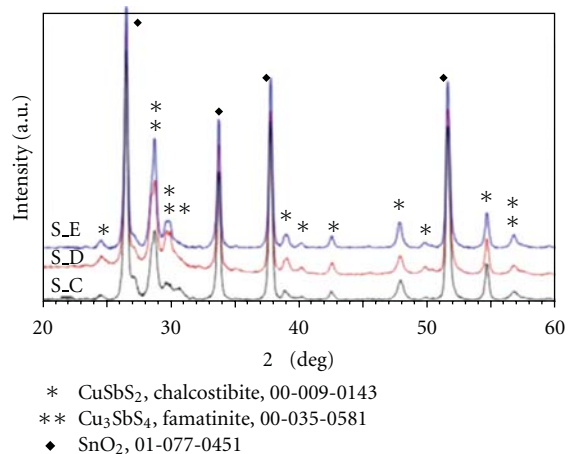


FIGURE 1: XRD spectra recorded for samples C, D, E.

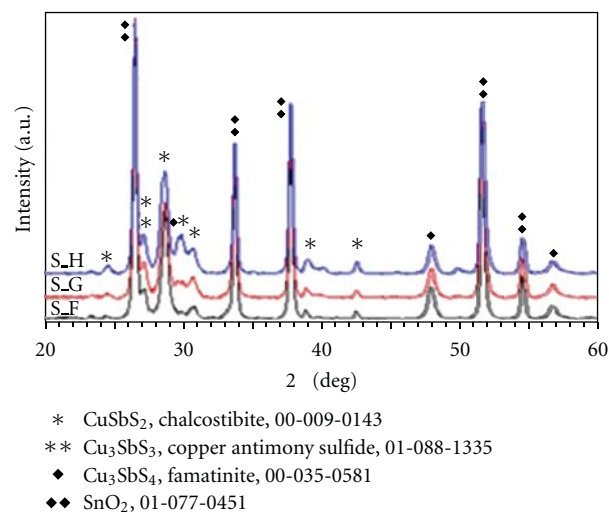


FIGURE 2: XRD spectra recorded for samples F, G, H.

of the chemical bounds in the precursors, followed by nucleation and crystal growth.

Because evaporation of solvents takes place/very/close to the substrate surface, regions with lower temperatures are temporarily created. Thus, an important factor is the pause between the spraying sequences that must be long enough to allow the substrate reheating and the formation of nucleation centers.

The XRD spectra of the C, D, and E samples are presented in Figure 1. Since the films are very thin, the XRD spectrum of tin dioxide SnO_2 (PDF 01-077-0451) from the FTO substrate is also visible.

Figure 2 presents the XRD pattern for F, G, and H samples, having the same precursor solution composition in which polymeric additives were used. At this precursor molar ratio in the solution, a new phase is detected in the XRD pattern, copper antimony sulphide, Cu_3SbS_3 (PDF 01-088-1335). The XRD spectra of these films do not indicate carbon in crystalline form as a residue from the polymers, while amorphous carbon based compounds are in small amounts, as shown in the FTIR spectra. This indicates that the deposition temperature is high enough for the almost total degradation of the organic polymers, forming volatile compounds.

Using the Scherrer's formula, the crystallite dimensions were estimated and are presented for the Cu-Sb-S phases identified in the A–H samples in Table 2.

3.1. Samples without Polymeric Additives. For samples A, B, and E, where the Cu : Sb precursor ratio is under 1 : 2, the Sb content influences both the nucleation and growth rate, this can be deduced from the large differences in the crystallite size and their proportion in the two phases. For sample, F it was registered also a new phase Cu_3SbS_3 . For samples C, D, and E, where the Cu : Sb precursor ratio is between 1 : 2.48–1 : 4.4, the Sb content variation influences only the nucleation rate. The data shows that the crystallite size of the two phases is almost equal for each sample. The nucleation speed for

sample D is the largest of the samples presented, resulting in a large number of crystals with the smaller dimensions.

3.2. Samples with Polymeric Additives. The crystallite size of the Cu_3SbS_3 phase varies in a large range as result of the polymer complexation effect on the film formation rate, (films F, G, and H). This influence is registered only for the Cu_3SbS_3 phase, the CuSbS_2 and Cu_3SbS_4 crystallite sizes remaining almost constant for the three samples. This could be the result of a more sensitive synthesis reaction of Cu_3SbS_3 , when the influence of the polymer-precursor interactions becomes significant. The crystallite sizes of this compound are much larger than the corresponding values for CuSbS_2 , and Cu_3SbS_4 , therefore, we can conclude that there is a lower nucleation rate (more stable polymer-precursors intermediates) and/or a fast growth rate for Cu_3SbS_3 . The samples with polymers contain a smaller amount of CuSbS_2 and a larger amount of Cu_3SbS_4 than the sample with the same composition and no additive, indicating that competitive reactions are running and the reaction affinity is influenced by the polymers.

Infra-red reflectance spectra were recorded for samples F, G, H, Figure 3, looking for residual carbon (crystalline or amorphous) from the polymer that can be additionally found in the films.

The spectra give few clues to the reaction mechanism and the processes that take place in the solutions. The functional groups from the urea compounds, NH_2 , C–N, C–N–H, N–H can be found at 1400, 1500, 1620, 2068, 3350, and 3800 nm [13]. Peaks observed at 702 and 1200 nm are attributed to C=S groups from the thiourea. The vibration at 2350 nm, attributed to O=C=O, can be found only for samples G and H, being related to the polymers composition as trapped or adsorbed compound. The peaks present at 1711 and 1768 nm are assigned to the COO^- and C=O groups from the maleic anhydride. At 2880 a peak can be attributed to an S– CH_3 group.

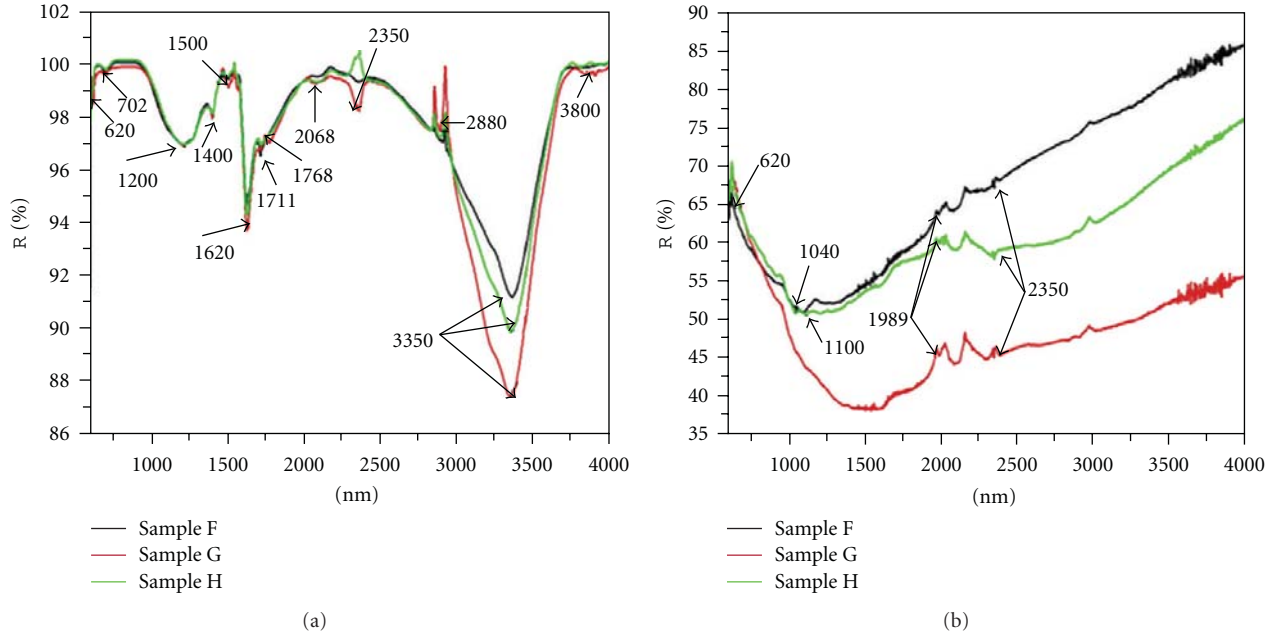


FIGURE 3: FTIR reflectance spectra for samples F, G, H: (a) for films, (b) for precursor solution.

TABLE 2: Crystallite size and phase composition for samples A–H.

Sample	Phase composition (%)			Crystallite size (Å)		
	Cu ₃ SbS ₄	CuSbS ₂	Cu ₃ SbS ₃	Cu ₃ SbS ₄	CuSbS ₂	Cu ₃ SbS ₃
A	34.2	65.8	—	236.1	143.1	—
B	78	22	—	236.1	161.5	—
C	30	70	—	181.9	180.1	—
D	27	73	—	146.3	164.7	—
E	34	66	—	217.3	216.2	—
F	67	28	5	196.3	171.5	352
G	82	11	7	172.4	173.8	577.7
H	82	11	7	159.4	160.7	268.8

The peak at 620 nm, was assigned to Cu₂O [13], in the solution spectra and is found both in the precursors and in the thin films. In the film, the copper oxide however is believed to be in amorphous form because it does not appear in the XRD spectra of the samples.

In the films, the IR peaks positioned at 1989 nm were attributed to C–C groups, and the vibrations found at 1040 and 1110 nm are associated with copper thiourea complexes [14].

The carbon traces revealed in the films by the FTIR analysis, as CO₂ and other C–C groups were not detected by the XRD analysis, confirming the amorphous structures.

Thus, the films contain very low amount of amorphous inorganic phases (Cu₂O) and traces of organic compounds resulted in the thermal decomposition of the polymeric additives.

The morphology of the deposited samples was investigated and the AFM images (Figures 4(a)–4(e)) of the films show the effect of the precursor solution composition and of the polymeric additives.

In Figures 4(a) and 4(b), the AFM images recorded for samples B and D are presented. Sample B presents a multigrain structure with open, micropores, that can have a positive effect on the reciprocal infiltration of the n and p-type semiconductors in the solid state solar cells. The increase in the antimony content leads to the extension of the grains into fiber-like aggregates.

The AFM images recorded for samples F, G, and H are presented in Figures 4(c)–4(e). The use of polymeric additives increases the density of the films. The worm-like structures obtained for sample F tend to bind together and form denser structures in the films were polymeric additives were used. Also a decrease in grain size is observed in these samples. Correlating these results with the XRD data we can assume that the larger crystallites, with regular geometry, are able to (slowly) grow in dense structures, this effect being more evident when the hydrophilic polymer is used.

Contact angle measurements were used to calculate the surface energy of the samples. Because solid state solar cells are constructed by the infiltration of the n and p-type

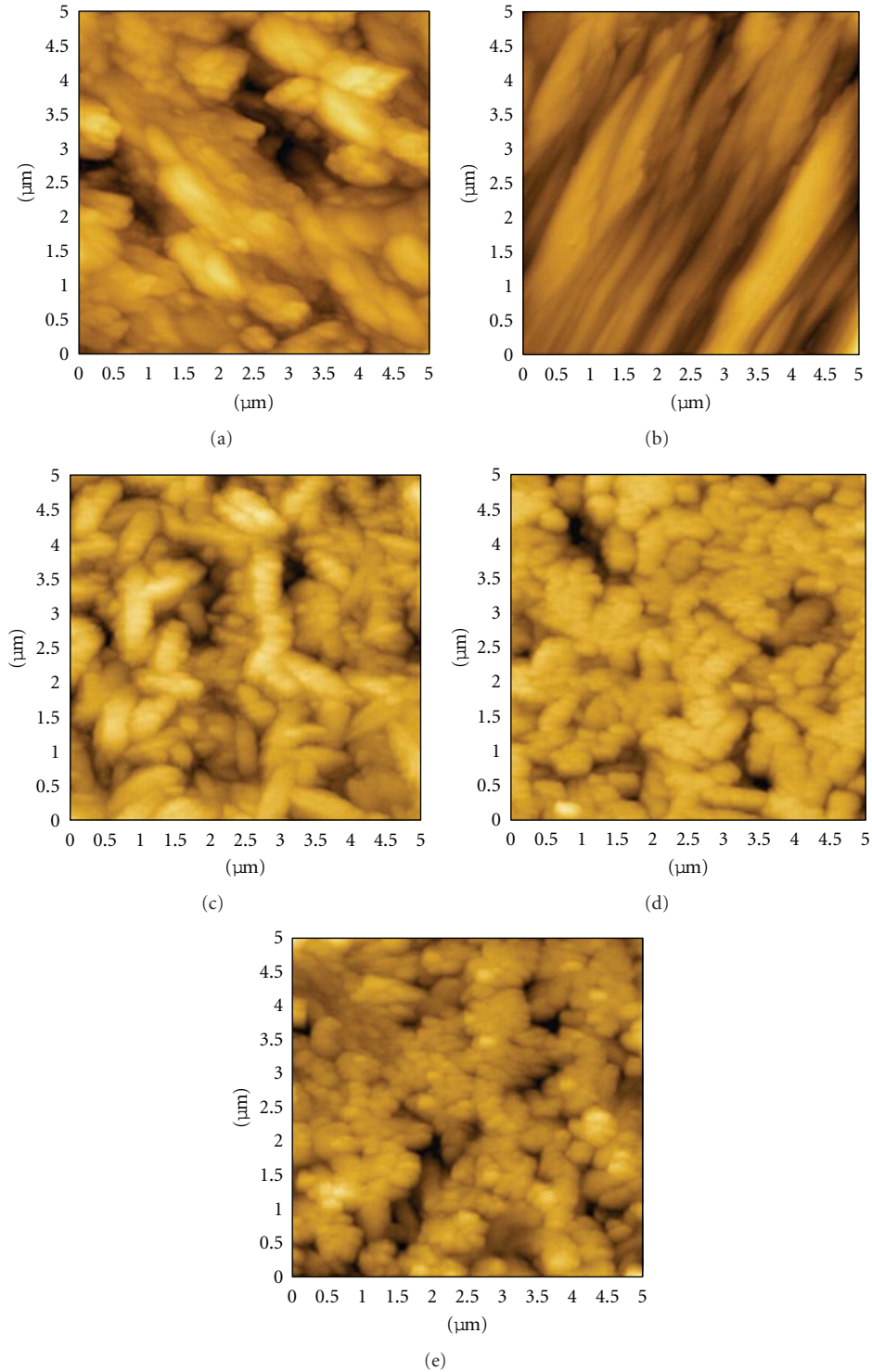


FIGURE 4: AFM image of sample B (a), E (b), F (c), G (d), and H (e) at $5 \times 5 \mu\text{m}$ resolution.

semiconductors, a good contact between the semiconductors is essential. During SPD, deposition takes place from liquid, aqueous solutions; this is why substrates with high surface energy and good wetting capabilities are required. The contact angle measurements were carried out using two liquids: water and glycerol. With the value of the initial

contact angles, energy surface was calculated using Owens, Wendt and Kaelble method [15]. The data are presented in Table 3.

When using glycerol, with low polarity, all the substrates show large and similar contact angle values, corresponding to polar, partially charged, substrates.

TABLE 3: Contact angles and surface energies measured for samples F, G, and H.

Sample	Additive, 100 ppm	Θ water (degree)	Θ glycerol (degree)	Surface energy (mN/m)	Dispersive component (mN/m)	Polar component (mN/m)	Roughness, measured on $20 \times 20 \mu\text{m}$ (nm)
F	—	111	107.5	7.81	3.88	3.93	193
G	HFL	93.5	103.3	23.33	0	23.33	138
H	HFB	78	104.3	74.46	8.13	64.33	152

The contact angles measured for water (with much higher polarity) allow us to sense the differences among the ionic degree of the samples. By using polymeric additives (samples G and H), a decrease in the initial contact angle is observed, in comparison with sample F. This gets the conclusion that polymers also have influence on the surface charge distribution, as result of changing the nucleation and growth ratios. With a contact angle value below 90° , sample H has the best wetting capacity and the largest surface energy from the three samples. The surface roughness can also influence the contact angle (being lower for rough surfaces). It is interesting also to notice the very low dispersive component of the surface energy in sample G (registered as “0”) proving that the hydrophilic polymer supports the formation of rather dense, ionic layers.

4. Conclusions

Thin films of crystalline Cu-Sb-S ternary compounds were obtained on FTO substrate using spray pyrolysis deposition technique, without any postdeposition treatments. Films containing CuSbS_2 , Cu_3SbS_4 , and Cu_3SbS_3 phases were prepared by varying the precursors' composition. Evidences of traces of amorphous carbon-based compounds were recorded in the FTIR spectra, for the samples using polymer additives.

The samples morphology can be varied from multigrain, open pores up to long fiber-like aggregates, and to smaller worm-like morphologies. The use of polymeric additives results in a densification of the films and a decrease in the grain size, containing large crystallites of Cu_3SbS_3 .

The polymeric additives represent a powerful tool also in tuning the surface energy, thus increasing the wetting behavior, as a prerequisite for developing efficient n-p junctions in solid state solar cells.

Acknowledgment

This work was supported by CNCISIS_UEFISCDI Project no. PNII-IDEI 840/2008, Romania.

References

- [1] Y. Rodríguez-Lazcano, M. T. S. Nair, and P. K. Nair, “ CuSbS_2 thin film formed through annealing chemically deposited Sb_2S_3 -CuS thin films,” *Journal of Crystal Growth*, vol. 223, no. 3, pp. 399–406, 2001.
- [2] G. A. Harcourt, “Tables for identification of ore minerals by X-ray powder patterns,” *American Mineralogist*, vol. 27, p. 63, 1942.
- [3] A. Rabhi, M. Kanzari, and B. Rezig, “Growth and vacuum post-annealing effect on the properties of the new absorber CuSbS_2 thin films,” *Materials Letters*, vol. 62, no. 20, pp. 3576–3578, 2008.
- [4] Y. Rodríguez-Lazcano, L. Guerrero, O. Gomez Daza, M. T. S. Fair, and P. K. Nair, “Antimony chalcogenide thin films: chemical bath deposition and formation of new materials by post deposition thermal processing,” *Superficies y Vacío*, vol. 9, pp. 100–103, 1999.
- [5] I. L. Lind and E. Makovicky, “Phase relations in the system Cu-Sb-S at 200°C , 10^8 Pa by hydrothermal synthesis. Microprobe analyses of tetrahedrite—a warning,” *Neues Jahrbuch für Mineralogie, Abhandlungen*, vol. 145, pp. 134–156, 1982, as cited in JCPDS 35-0413.
- [6] S. Messina, M. T. S. Nair, and P. K. Nair, “Antimony sulfide thin films in chemically deposited thin film photovoltaic cells,” *Thin Solid Films*, vol. 515, no. 15, pp. 5777–5782, 2007.
- [7] A. Rabhi, M. Kanzari, and B. Rezig, “Optical and structural properties of CuSbS_2 thin films grown by thermal evaporation method,” *Thin Solid Films*, vol. 517, no. 7, pp. 2477–2480, 2009.
- [8] J. Zhou, G.-Q. Bian, Q.-Y. Zhu, Y. Zhang, C.-Y. Li, and J. Dai, “Solvothetical crystal growth of CuSbQ_2 ($\text{Q}=\text{S}, \text{Se}$) and the correlation between macroscopic morphology and microscopic structure,” *Journal of Solid State Chemistry*, vol. 182, no. 2, pp. 259–264, 2009.
- [9] M. Y. Versavel and J. A. Haber, “Structural and optical properties of amorphous and crystalline antimony sulfide thin-films,” *Thin Solid Films*, vol. 515, no. 18, pp. 7171–7176, 2007.
- [10] S. Manolache, A. Duta, L. Isac, M. Nanu, A. Goossens, and J. Schoonman, “The influence of the precursor concentration on CuSbS_2 thin films deposited from aqueous solutions,” *Thin Solid Films*, vol. 515, no. 15, pp. 5957–5960, 2007.
- [11] S. A. Manolache and A. Duta, “The influence of the spray deposition parameters in the photovoltaic response of the three-dimensional (3D) solar cell: TCO/dense TiO_2 / CuSbS_2 /graphite,” *Journal of Optoelectronics and Advanced Materials*, vol. 9, no. 10, pp. 3219–3222, 2007.
- [12] Y. Rodríguez-Lazcano, M. T. S. Nair, and P. K. Nair, “Photovoltaic p-i-n structure of Sb_2S_3 and CuSbS_2 absorber films obtained via chemical bath deposition,” *Journal of the Electrochemical Society*, vol. 152, no. 8, pp. G635–G638, 2005.
- [13] K. Das, S. K. Panda, S. Gorai, P. Mishra, and S. Chaudhuri, “Effect of Cu/In molar ratio on the microstructural and optical properties of microcrystalline CuInS_2 prepared by solvothermal route,” *Materials Research Bulletin*, vol. 43, no. 10, pp. 2742–2750, 2008.
- [14] P. Bombicz, I. Mutikainen, M. Krunk, T. Leskelä, J. Madarász, and L. Niinistö, “Synthesis, vibrational spectra and X-ray structures of copper(I) thiourea complexes,” *Inorganica Chimica Acta*, vol. 357, no. 2, pp. 513–525, 2004.
- [15] D. K. Owens and R. C. Wendt, “Estimation of the surface free energy of polymers,” *Journal of Applied Polymer Science*, vol. 13, no. 8, pp. 1741–1747, 1969.

Research Article

Characterization of Nanocrystalline SiGe Thin Film Solar Cell with Double Graded-Dead Absorption Layer

Chao-Chun Wang,¹ Dong-Sing Wu,¹ Shui-Yang Lien,² Yang-Shih Lin,¹ Chueh-Yang Liu,² Chia-Hsum Hsu,³ and Chia-Fu Chen²

¹Department of Materials Science and Engineering, National Chung Hsing University, 250 Kuo Kuang Road, Taichung 402, Taiwan

²Department of Materials Science and Engineering, MingDao University, ChungHua 52345, Taiwan

³Graduate Institute of Precision Engineering, National Chung Hsing University, Taichung 402, Taiwan

Correspondence should be addressed to Dong-Sing Wu, dsw@dragon.nchu.edu.tw

Received 1 June 2011; Accepted 17 October 2011

Academic Editor: Leonardo Palmisano

Copyright © 2012 Chao-Chun Wang et al. This is an open access article distributed under the Creative Commons Attribution License, which permits unrestricted use, distribution, and reproduction in any medium, provided the original work is properly cited.

The nanocrystalline silicon-germanium (nc-SiGe) thin films were deposited by high-frequency (27.12 MHz) plasma-enhanced chemical vapor deposition (HF-PECVD). The films were used in a silicon-based thin film solar cell with graded-dead absorption layer. The characterization of the nc-SiGe films are analyzed by scanning electron microscopy, UV-visible spectroscopy, and Fourier transform infrared absorption spectroscopy. The band gap of SiGe alloy can be adjusted between 0.8 and 1.7 eV by varying the gas ratio. For thin film solar cell application, using double graded-dead i-SiGe layers mainly leads to an increase in short-circuit current and therefore cell conversion efficiency. An initial conversion efficiency of 5.06% and the stabilized efficiency of 4.63% for an nc-SiGe solar cell were achieved.

1. Introduction

The band gap of amorphous silicon-germanium (a-SiGe) alloy can be adjusted between 1.4 and 1.7 eV by varying the Ge fraction. This characteristic renders a-SiGe a suitable light absorber material in multijunction amorphous-silicon- (a-Si-) based thin film solar cells, in which the a-SiGe acts as intrinsic layer in middle cells to enhance green-to-red absorption [1, 2]. Though the electronic properties deteriorate with Ge alloying, some earlier studies have shown that these properties can be improved when alloys are deposited at high pressure and high hydrogen dilution [3, 4]. In recent years, significant improvements in solar cell performance were achieved by a band gap graded intrinsic i-layer [5]. However, the solar cells with those a-SiGe films show a significant light degradation [6].

In this work, nanocrystalline SiGe (nc-SiGe) films have been introduced to the single junction p-i-n solar cell, because of the enhanced response in longer wavelength (>650 nm) of solar spectrum and higher light-induced stability. The main structural and optical properties of nc-SiGe

samples deposited at different gas ratios were first described. Then, the double graded nc-SiGe films are used as absorption layer of a solar cell and its photovoltaic performance is also discussed.

2. Experimental

The SiGe films were deposited on glass using high-frequency (27.12 MHz) plasma-enhanced chemical vapor deposition (HF-PECVD) in an ultrahigh-vacuum, single-camber, load-locked deposition system. Table 1 listed the deposition conditions of SiGe films. The gas ratio x , which was defined as $[\text{GeH}_4]/([\text{SiH}_4] + [\text{GeH}_4])$, was changed from 0% to 100% to prepare SiGe films. The thickness for all samples was 700 nm. The samples were characterized by the scanning electron microscopy (SEM) to observe the surface morphology of the films. The spectra of optical absorption were measured by UV-visible spectroscopy for determination of the Tauc optical band gap (E_g) through [7]

$$(\alpha h\nu)^{1/2} = B(h\nu - E_g), \quad (1)$$

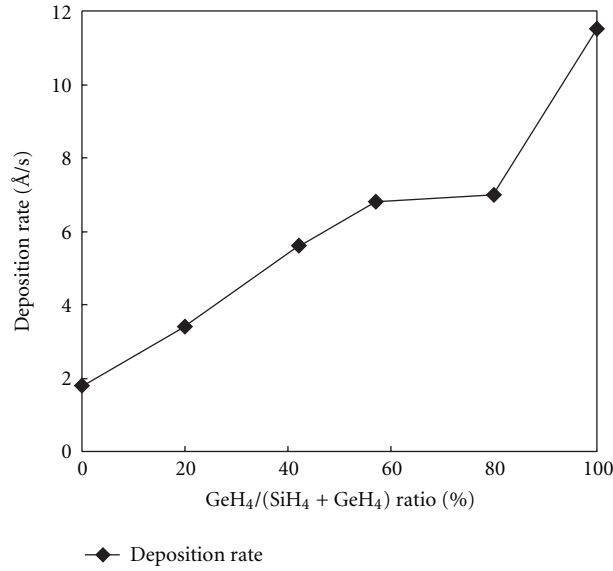


FIGURE 1: Variation of deposition rate as a function of the gas ratio.

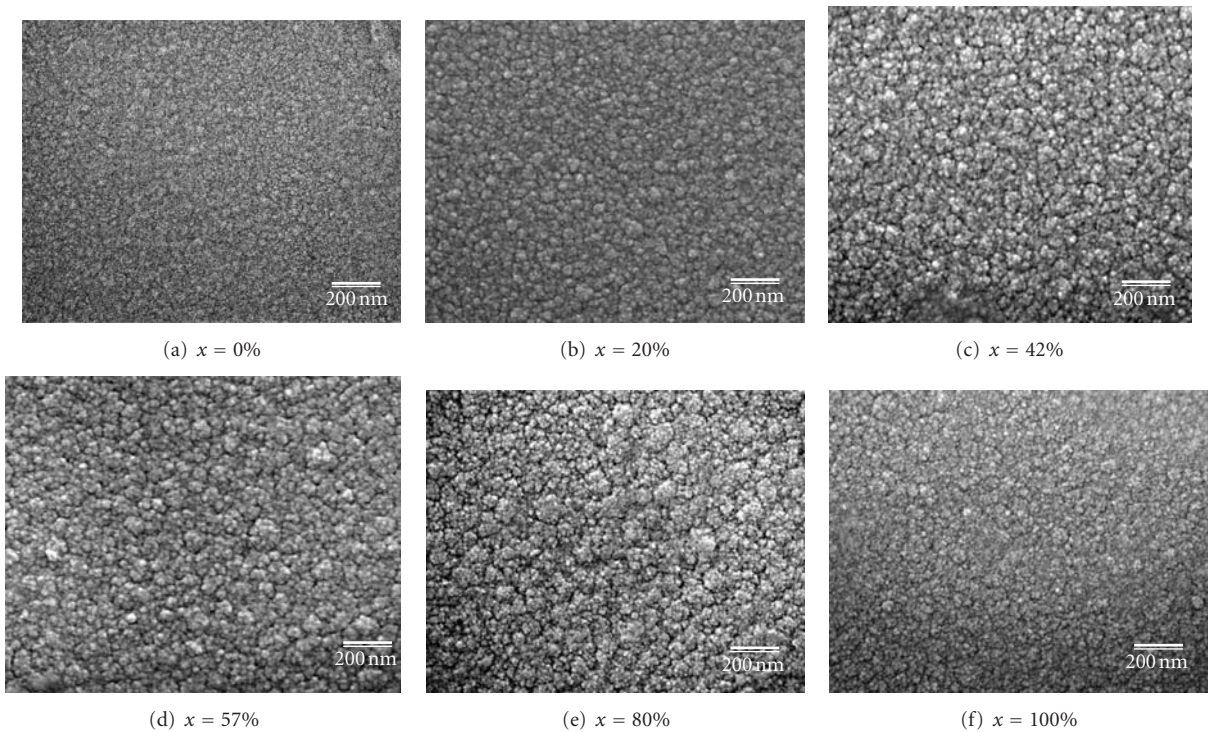


FIGURE 2: The SEM images of the SiGe films deposited at different gas ratios of (a) 0%, (b) 20%, (c) 42%, (d) 57%, (e) 80%, and (f) 100%.

where α , $h\nu$ and B are optical absorption coefficient, photon energy and Tauc slope, respectively. In addition, it is known that the absorption coefficient near the band edge shows an exponential dependence on photon energy [8]:

$$\alpha(\lambda) = \alpha_0 \exp\left(\frac{h\nu}{E_0}\right), \quad (2)$$

where E_0 is the Urbach energy which corresponds to the width of the band tail and can be evaluated as the width of the localized states and α_0 is a constant. Thus, an Urbach plot

of $\ln[\alpha(\lambda)]$ versus photon energy should be linear and optical absorption edge can be obtained from the slope.

Fourier transform infrared (FTIR) absorption measurements were taken for samples on c-Si substrates to obtain information of the concentrations of Ge–H and Si–H bonds. For solar cell application, single-junction p-i-n solar cells using these SiGe films as absorption layer were deposited on ASAHI (type-U) glass substrates. The current-voltage characteristics of the solar cell were measured at 100 mW/cm² by using an AM 1.5 G solar simulator. Light

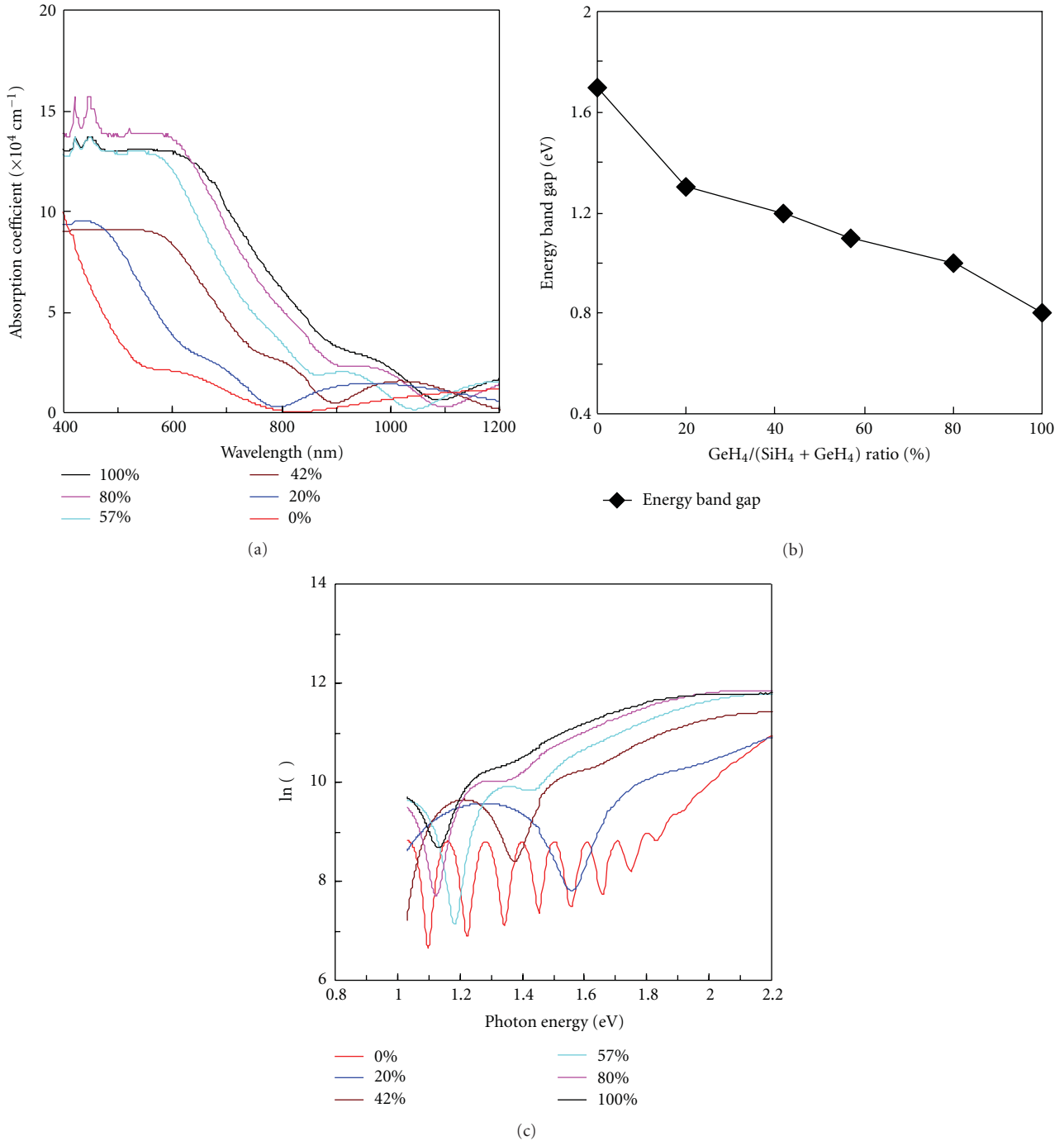


FIGURE 3: (a) The spectral dependence of the absorption coefficient for the SiGe films with different gas ratios. (b) The Tauc energy band gap as a function of the gas ratio. (c) The Urbach plots of the SiGe films with different gas ratios.

soaking was performed under one-sun light intensity using a metal halide lamp at 50°C for 500 h. The intensity was maintained at a level so that a reference Si solar cell generated the same current under a Xe-lamp simulator.

3. Results and Discussion

Figure 1 shows the variation in deposition rate as a function of gas ratio (x). It can be seen that the deposition rate ra-

pidly increases from 1.8 to 11.5 Å/sec with increasing x value from 0% to 100%. A reasonable explanation for this effect is that the addition of the GeH_4 flow rate favors the SiH_4 as well as GeH_4 dissociation, resulting in an increase of concentration of the precursors in the plasma during the deposition process, which causes a higher Si-Ge bond formation and therefore enhances the deposition rate [9]. The similar result was reported by other research groups [10, 11].

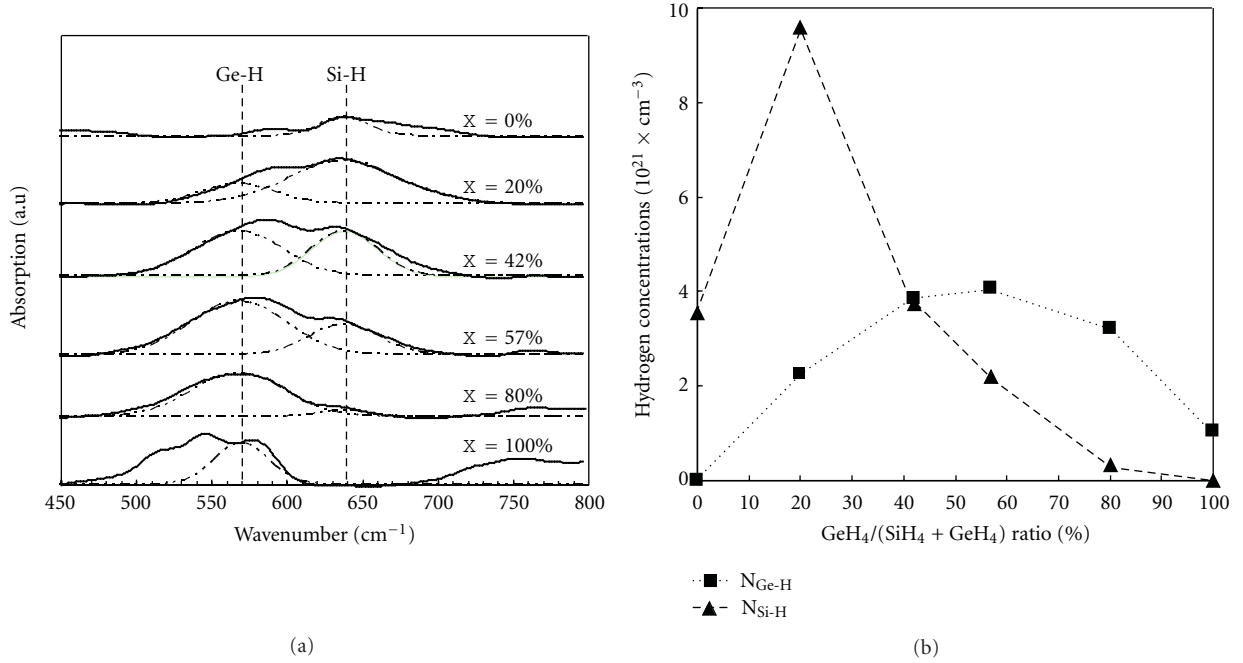


FIGURE 4: (a) Infrared coefficient absorption spectrums of the wagging mode of the a-SiGe:H films deposited at different germanium concentrations. (b) Variation of bonded hydrogen concentration in different configurations as function of the gas ratio.

TABLE 1: The deposition conditions of SiGe films.

Parameter	Value
Power (W)	15
Pressure (Pa)	40
Electrode distance (mm)	14
Substrate temperature (°C)	200
SiH ₄ flow rate (sccm)	40; 40; 40; 30; 10; 0
GeH ₄ flow rate (sccm)	0; 10; 30; 40; 40; 40
Gas ratio (%)	0–100

Figure 2 shows the surface morphologies of the SiGe films deposited at different x values of (a) 0%, (b) 20%, (c) 42%, (d) 57%, (e) 80%, and (f) 100% as observed by SEM. These images indicate that the germane-doped films have similar surface structure with grains in nanoscale (<100 nm). Thus, an increase of amount of germane incorporation to the alloys might promote the formation of nanocrystals.

Figure 3(a) shows the spectral dependence of the absorption coefficient for the SiGe films with different x values. It can be seen that the absorption coefficient obviously increases from about 9×10^4 to 13×10^4 cm⁻¹ when the x value increases to above 80%. In addition, the absorption edge of the SiGe film is shifted to long wavelength mainly due to a decrease in Tauc energy band gap, which is shown as a function of x values in Figure 3(b). The reduction in band gap can be relative to the crystalline phase in the films supported by the SEM results. The Urbach plots for different alloys are shown in Figure 3(c). It can be seen that the optical absorption edge shifts to lower energies when the x value increases. This result shows the similar trend to the Tauc band gap result.

The infrared absorption spectra of SiGe films with different x values are shown in Figure 4(a). The absorption bands of SiGe are assigned to the Si–H and Ge–H wagging vibration located at around 570 and 640 cm⁻¹, respectively [12]. The effect of germane on the alloys is seen in the shift of the peak from 640 cm⁻¹ for $x = 0\%$ to 570 cm⁻¹ for $x = 100\%$. For further investigation, the hydrogen bond concentrations $N(\text{Ge–H})$ and $N(\text{Si–H})$ of these SiGe films are determined by the following equation [13]:

$$N = A \int \frac{\alpha}{\omega} d\omega, \quad (3)$$

where α is the absorption coefficient and ω is the frequency. For the constant A , we use the value given in [12, 14]. The calculated results are shown in Figure 4(b), clearly showing that the Si–H bonds dominate the structure as the x value is below 20%. But when the x value increases above 20%, there is a preferential attachment of H atoms to Ge rather than Si.

Figure 5 shows a comparison of I - V characteristics between the solar cell constructed with single i-SiGe layer ($x = 42\%$, 1 μm thick) and the solar cell with double graded i-SiGe layer of i_1 ($x = 20\%$, 300 nm)/ i_2 ($x = 42\%$, 1 μm). These two cells have the same p-, n-layer, and back electrode (Ag) thickness of 20, 30, and 300 nm, respectively. The V_{oc} values are around 0.58 V showing no significant change, whereas the J_{sc} is higher in double graded-dead i-layer cell than that in single i-layer cell, implying that the carrier collection probability and/or carrier mobility are improved by the reduction of band gap discontinuity. Furthermore, the I - V curve after light soaking of our graded double i-layer is also plotted for the purpose of comparison, and the detailed external parameters are listed in Table 2. The cell conversion efficiency (η) decreases from 5.06% for initial to 4.63% for

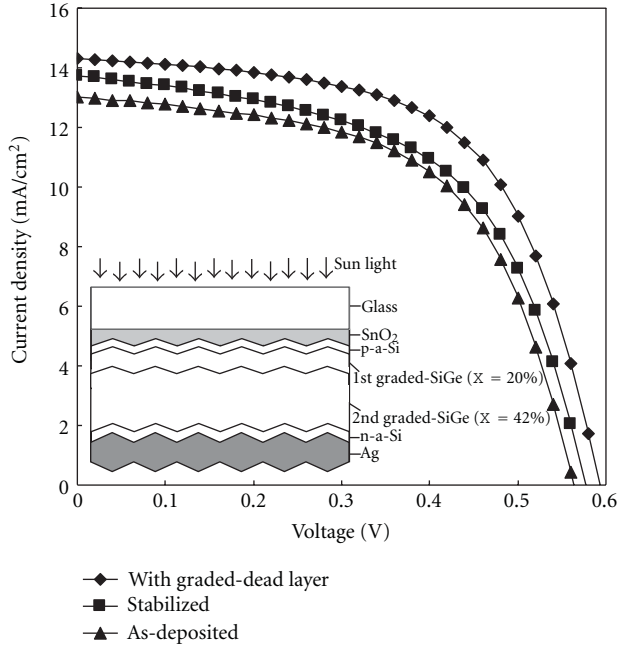


FIGURE 5: Schematic structure of the p-i-n solar cell with double graded-dead nc-SiGe i-layers and I - V characteristics of the solar cells without (as-deposited), with double graded-dead absorption layer, and after light-soaking test for 500 h.

TABLE 2: The external parameters of nc-SiGe thin film solar cells without (as-deposited), with double graded-dead i-layers, and after light-soaking test.

	V_{oc} (V)	J_{sc} (mA/cm ²)	FF (%)	η (%)
As-deposited	0.56	13.01	57.50	4.21
With graded-dead layer	0.59	14.30	59.70	5.06
Stabilized	0.58	13.74	58.12	4.63

stabilized (8.4% degradation), showing that the cell is stable against light soaking. From this result, we speculate that our SiGe solar cell with a reduced sensitivity to the optical degradation (the Staebler-Wronski effect [15, 16]) is mainly due to the crystalline structure of the i-layer.

4. Conclusions

The effects of GeH_4 gas ratio on growth mechanisms and properties of SiGe films are investigated in this paper. By controlling the gas ratio, nc-SiGe films with certain optical band gap can be obtained to be used as absorption layer for solar cell applications. Using double graded-dead i-SiGe layers can increase the J_{sc} and therefore cell conversion efficiency. Furthermore, an initial conversion efficiency of 5.06% and the stabilized efficiency of 4.63% for an nc-SiGe solar cell were achieved.

Acknowledgments

This work is sponsored by Chung-Shan Institute of Science and Technology and the National Science Council of China

under contract nos. 99-2221-E-451-013, 99-2622-E-451-005-CC3, 99-2622-E-451-007-CC2, 99-2221-E-451-011, and 100-3113-E-451-001-CC2.

References

- [1] R. L. Stolk, H. Li, R. H. Franken et al., "Improvement of the efficiency of triple junction n-i-p solar cells with hot-wire CVD proto- and microcrystalline silicon absorber layers," *Thin Solid Films*, vol. 516, no. 5, pp. 736–739, 2008.
- [2] R. E. I. Schropp, H. Li, R. H. J. Franken et al., "Nanostructured thin films for multibandgap silicon triple junction solar cells," *Solar Energy Materials and Solar Cells*, vol. 93, no. 6-7, pp. 1129–1133, 2009.
- [3] H. Kawauchi, M. Isomura, T. Matsui, and M. Kondo, "Microcrystalline silicon-germanium thin films prepared by the chemical transport process using hydrogen radicals," *Journal of Non-Crystalline Solids*, vol. 354, no. 19-25, pp. 2109–2112, 2008.
- [4] Z. Tang, W. Wang, D. Wang, D. Liu, Q. Liu, and D. He, "The influence of H_2/Ar ratio on Ge content of the $\mu\text{C-SiGe:H}$ films deposited by PECVD," *Journal of Alloys and Compounds*, vol. 504, no. 2, pp. 403–406, 2010.
- [5] Q. H. Fan, C. Chen, X. Liao et al., "High efficiency silicon-germanium thin film solar cells using graded absorber layer," *Solar Energy Materials and Solar Cells*, vol. 94, no. 7, pp. 1300–1302, 2010.
- [6] X. Liao, H. Povolny, P. Agarwal, and X. Deng, "Raman and IR study of narrow bandgap A-SiGe and $\mu\text{C-SiGe}$ films deposited using different hydrogen dilution," in *Proceedings of the 29th IEEE Photovoltaic Specialists Conference*, pp. 1150–1153, May 2002.
- [7] J. Tauc and A. Menth, "States in the gap (of chalcogenide glasses)," *Journal of Non-Crystalline Solids*, vol. 8–10, pp. 569–585, 1972.
- [8] F. Urbach, "The long-wavelength edge of photographic sensitivity and of the electronic absorption of solids," *Physical Review*, vol. 92, no. 5, p. 1324, 1953.
- [9] Y. H. Wang, J. Lin, and C. H. A. Huan, "Structural and optical properties of a-Si:H/nc-Si:H thin film," *Materials Science and Engineering B*, vol. 104, no. 1-2, pp. 80–87, 2003.
- [10] S. R. Jadar, J. V. Sali, S. T. Kshirsagar, and M. G. Takwale, "Narrow band gap, high photosensitivity a-SiGe:H films prepared by hot wire chemical vapor deposition (HW-CVD) method," *Materials Letters*, vol. 52, no. 6, pp. 399–403, 2002.
- [11] W. Paul, J. H. Chen, E. Z. Liu, A. E. Wetsel, and P. Wickboldt, "Structural and electronic properties of amorphous SiGe:H alloys," *Journal of Non-Crystalline Solids*, vol. 164–166, no. 1, pp. 1–10, 1993.
- [12] A. A. Langford, M. L. Fleet, B. P. Nelson, W. A. Lanford, and N. Maley, "Infrared absorption strength and hydrogen content of hydrogenated amorphous silicon," *Physical Review B*, vol. 45, no. 23, pp. 13367–13377, 1992.
- [13] M. H. Brodsky, M. Cardona, and J. J. Cuomo, "Infrared and Raman spectra of the silicon-hydrogen bonds in amorphous silicon prepared by glow discharge and sputtering," *Physical Review B*, vol. 16, no. 8, pp. 3556–3571, 1977.
- [14] B. P. Nelson, Y. Xu, D. L. Williamson et al., "Hydrogenated amorphous silicon germanium alloys grown by the hot-wire chemical vapor deposition technique," *Materials Research Society Symposium Proceedings*, vol. 507, pp. 447–452, 1998.
- [15] R. E. I. Schropp, M. B. von der Linden, J. Daey Ouwens, and H. de Gooijer, "Apparent "gettering" of the Staebler-Wronski

effect in amorphous silicon solar cells," *Solar Energy Materials and Solar Cells*, vol. 34, no. 1–4, pp. 455–463, 1994.

- [16] V. Nádaždy, R. Durný, I. Thurzo, and E. Pinčík, "New experimental facts on the Staebler-Wronski effect," *Journal of Non-Crystalline Solids*, vol. 227–230, no. 1, pp. 316–319, 1998.

Research Article

Polarity Switchable Photovoltages in Miscut $\text{La}_{0.67}\text{Ca}_{0.33}\text{MnO}_3$ Films

J. Wang,^{1,2} H. Ni,^{2,3} K. Zhao,^{1,2,3,4} Y.-C. Kong,³ H. K. Wong,³ and S. X. Zhong²

¹ State Key Laboratory of Heavy Oil Processing, China University of Petroleum, Beijing 102249, China

² College of Science, China University of Petroleum, Beijing 102249, China

³ Department of Physics, Chinese University of Hong Kong, Hong Kong

⁴ International Center for Materials Physics, Chinese Academy of Sciences, Shenyang 110016, China

Correspondence should be addressed to K. Zhao, zhk@cup.edu.cn

Received 26 May 2011; Accepted 19 October 2011

Academic Editor: Vincenzo Augugliaro

Copyright © 2012 J. Wang et al. This is an open access article distributed under the Creative Commons Attribution License, which permits unrestricted use, distribution, and reproduction in any medium, provided the original work is properly cited.

We report the transient laser-induced anomalous photovoltaic effect in the $\text{La}_{0.67}\text{Ca}_{0.33}\text{MnO}_3$ film grown on miscut LaSrAlO_4 (001) substrate under 248 nm pulsed laser irradiation at ambient temperature without any applied bias. A photovoltaic pulse signal was observed when the $\text{La}_{0.67}\text{Ca}_{0.33}\text{MnO}_3$ film was irradiated directly, and the signal polarity was reversed when the sample was irradiated through the LaSrAlO_4 substrate, while the signal recorded between the two electrodes on the surface of LaSrAlO_4 was not reversed when the sample was irradiated through $\text{La}_{0.67}\text{Ca}_{0.33}\text{MnO}_3$ film rather than at the surface of LaSrAlO_4 . The switchable signal polarity provides a potential application of miscut manganite films as optical components. A possible mechanism is introduced to explain the experiment results.

1. Introduction

Up to now, investigations of manganites have been focused on their interesting properties, including ferroelectric, ferromagnetic, giant magnetoresistance, and superconducting and electrooptic properties [1–6]. Several researches about photovoltaic effect and thermoelectric response were carried out for exploring their potential applications in detector [7–10]. Anomalous photovoltaic effect has been observed in $\text{La}_{0.8}\text{Sr}_{0.2}\text{MnO}_3$ films grown on SrTiO_3 (001) substrates. The research results provided the anisotropy of the thermoelectric power [11].

It is known that heating the surface of a thin film grown on miscut substrate by the absorption of radiation establishes a temperature gradient ∇T perpendicular to the film surface. Due to the Seebeck effect, a thermoelectric field, $E = S \nabla T$, is generated with the Seebeck tensor S [12]. The lateral voltage can be written as

$$U_l = \frac{l(S_{ab} - S_c) \sin(2\theta) \Delta T}{2d}, \quad (1)$$

where l is the irradiated length by the laser beam between two electrodes, S_{ab} and S_c are the Seebeck coefficients of the

crystalline ab plane and along the c axis, respectively, θ is the tilting angle between the c axis and the direction of laser irradiation, ΔT is the temperature difference between film surface and film bottom, and d is the film thickness.

In this paper, we focus on the polarity-switchable signal which arose in the $\text{La}_{0.67}\text{Ca}_{0.33}\text{MnO}_3$ film (LCMO) grown on miscut LaSrAlO_4 (LSAO) (001) substrate under 248 nm pulsed laser irradiation at ambient temperature without any applied bias. We not only observed a photovoltaic signal produced in LCMO film that was reversed when the sample was irradiated through the substrate rather than at LCMO film, but also found a tiny signal generated in LSAO substrate, which was not reversed when the incident light irradiated the substrate in the opposite direction. The possible mechanism introduced to explain the experiment results provides a potential application of manganite films in optical components.

2. Experimental

Epitaxial LCMO film with a thickness d_1 of about 120 nm was deposited on the LSAO substrate with a thickness d_2 of 0.5 mm and an intentional 10° vicinal cut toward the [010] direction by facing-target sputtering technique. The

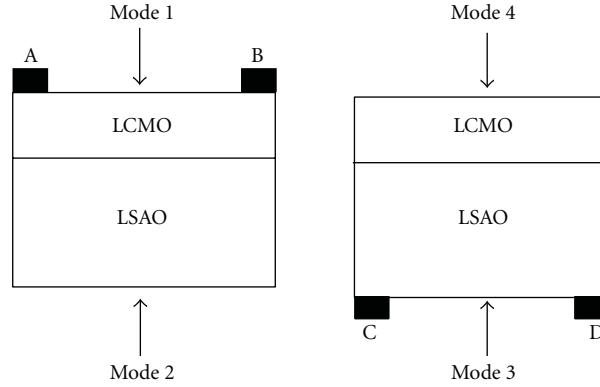


FIGURE 1: Schematic illustration of photoelectrical experiment on LCMO/LSAO sample.

substrate was kept at 680°C with the oxygen pressure of 30 mTorr during deposition. After the deposition, the vacuum chamber was immediately back-filled with 1 atm oxygen gas. The LCMO film was then cooled to room temperature with the substrate heater power cut-off. The structure of the sample was characterized by X-ray diffraction (XRD).

Figure 1 shows the schematic illustrations of photovoltaic response measurement. LCMO/LSAO sample of $5 \times 2.5 \text{ mm}^2$ geometry was used with two in-plane colloidal silver electrodes separated by 3 mm being individually placed on the surface of the LCMO film and LSAO substrate as displayed in Figure 1. Modes 1 and 4 (Modes 2 and 3) stand for irradiating the sample through LCMO film (LSAO substrate) with electrodes on LCMO film and LSAO substrate, respectively. The anode was connected with A (and C), and the cathode was connected with B (and D). The electrodes were always kept in the dark to prevent the generation of any electrical contact photovoltaic effect. The 248 nm KrF excimer laser (pulse duration of 20 ns, repetition rate of 1 Hz) was used as the light source at ambient temperature in air with a pulse energy of 2.88 mJ. The waveform was recorded by a sampling oscilloscope terminated into 1 M Ω .

3. Results and Discussion

The XRD θ - 2θ scan curve of the LCMO/LSAO is presented in Figure 2, where the [001] axis was aligned carefully. Except for the diffraction peaks of LSAO (00 l) and LCMO ($h0h$), there are no diffraction peaks from impurity phases or randomly oriented grains, indicating that the LCMO film is a single phase and [202] oriented.

Figure 3 displays the photovoltaic responses of LCMO/LSAO under the 248 nm pulsed laser irradiation without any applied bias. Two significant characteristics of the photovoltaic signals were observed: (i) the polarity of the signal gotten from LCMO film switched when the sample was irradiated through the substrate rather than at the film surface (Figure 3(a)). While no reversed signal polarity arose for modes 3 and 4 (Figure 3(b)). (ii) The order of the peak photovoltage (U_p) according to intensity is $U_1 > U_2 > U_3 >$

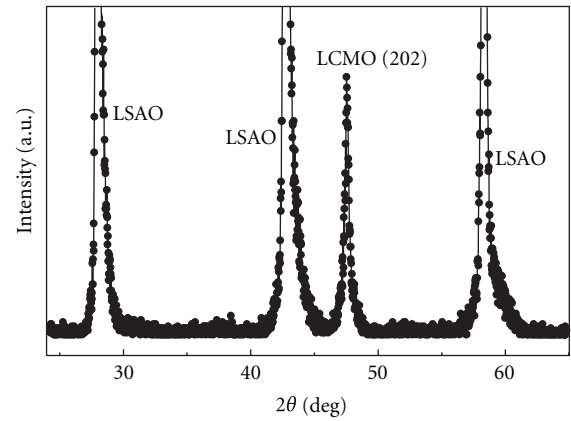


FIGURE 2: XRD pattern of LCMO/LSAO sample.

U_4 , where U_1 , U_2 , U_3 , and U_4 correspond to the peak photovoltage for modes 1, 2, 3, and 4. The maximum U_p of 0.476 V was observed with a rising time of 140 μs and a full width at half maximum (FWHM) of 29 μs in mode 1. While the smallest U_p of 0.013 V was observed in mode 4, almost 40 times lower than that of mode 1.

To investigate the anomalous photovoltaic effect, we measured the absorption spectra of LCMO/LSAO and LSAO single crystal as presented in Figure 4. The absorption edge of LSAO crystal is located at 253 nm in agreement with its band gap of 5.3 eV, indicating that nonequilibrium charge carriers in LSAO crystal can be created under 248 nm ultraviolet irradiation. However, the substrate thickness (0.5 mm) is much longer than the diffusion length of the charge carriers in the LSAO side. In addition, due to the strong absorption in LSAO substrate, few photons can inject into the LCMO layer. As a result, a smaller photovoltage presents for mode 2 compared with that for mode 1.

Concerning to illustrate the generation of polarity switchable photovoltages, several researches focused on changing film thickness and regulating the incident angle were carried out [13–16]. These researches involve both tilted films and single crystals where the Seebeck effect is widely used. The reversal signal generated in LCMO film under working

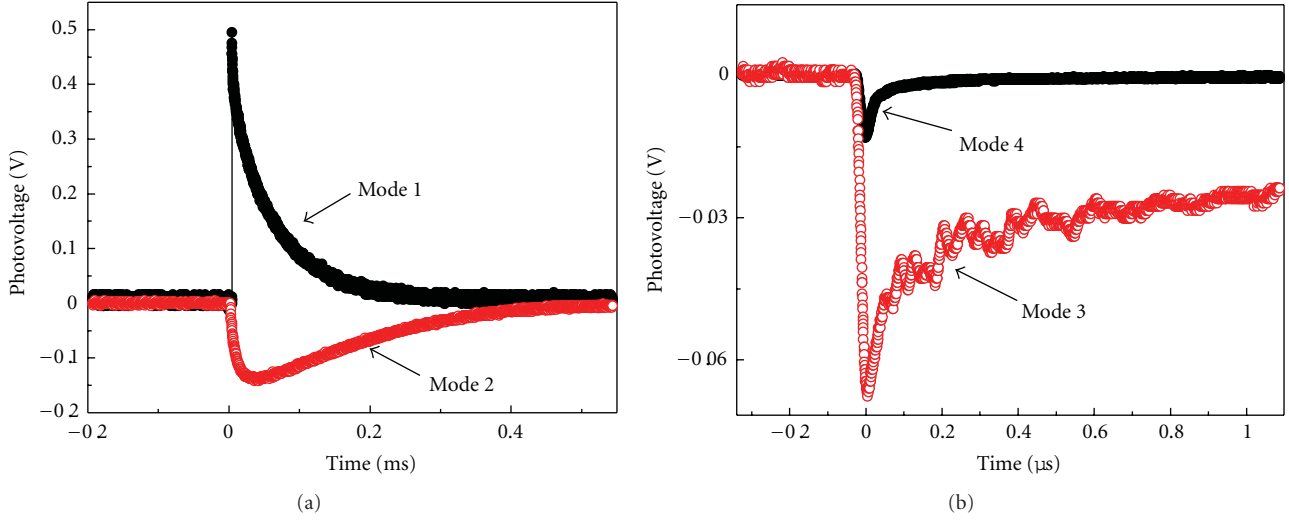


FIGURE 3: Typical photovoltaic pulses as functions of time for LCMO/LSAO sample.

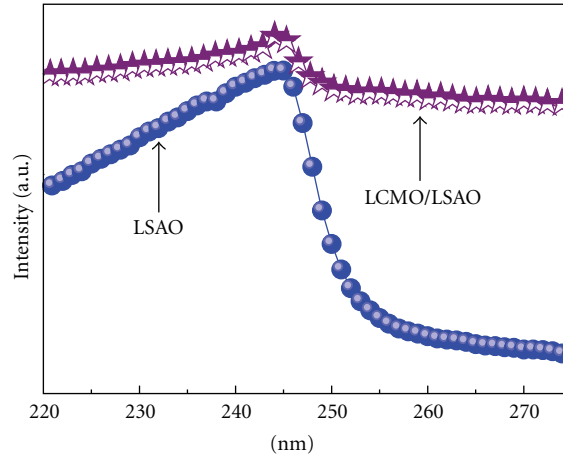


FIGURE 4: The absorption spectra of the LCMO/LSAO sample and LSAO single crystal.

mode 2 is in accordance with our previous study [11], which was attributed mainly to the ∇T reversal between the front and back end of LCMO film. In order to explain the experiment results shown in Figure 3, the schematic model of the procedure of induced charge and Seebeck processes is built in Figure 5. Due to the Seebeck effect, a positive potential difference U_{+AB}^1 along the LCMO film arises when the laser irradiates the sample in the air/LCMO-direction (mode 1). The photo-induced charge carries distribution in LCMO film induces a reversed charge carries distribution along the back-face of LSAO owing to the capacity effect of dielectric, which leads to a negative potential difference U_{-CD}^4 (mode 4).

Irradiating the LSAO substrate directly leads to a negative U_{-CD}^3 along their surface (mode 3), which induced reversed charge distribution on the LCMO/LSAO interface due to the capacity effect and resulted into a positive U_{+AB} in LSMO film. However, a negative lateral voltage U_{-AB} along the LCMO is generated due to reversal of the ∇T in the thickness direction for mode 3. Thus there exist two opposite photovoltages in LCMO. U_{+AB} is much smaller than U_{-AB}

because the induced charge on the interface produced by LSAO dielectrics is an extremely small amount compared to that from the reversed ∇T in LCMO. In sum, a negative U_{-AB}^2 , equal to $U_{-AB} + U_{+AB}$, is generated along the surface of LCMO film (mode 2).

Generally speaking, the polarity of signal generated in LCMO film (modes 1 and 2) is reversed mainly owing to the ∇T reversal between the front and back end of LCMO film according to Seebeck effect. And two different physical mechanisms, capacity effect of dielectric and Seebeck effect, determine the conformity of photovoltaic polarity under working modes 3 and 4. In addition, the polarity of photovoltage generated under working mode 3 is reversed, comparing with that under mode 1, due to the supplementary tilting angle θ and connection pattern of electrodes.

It is easy to understand that the absolute value of U_{+AB}^1 is larger than U_{-AB}^2 because U_{+AB} did much to offset U_{-AB}^2 . Since the thermoelectric field leading to U_{-CD}^3 is much larger than the electric field generated by induced charge of LSAO dielectrics, U_{-CD}^3 is larger than U_{-CD}^4 . The potential

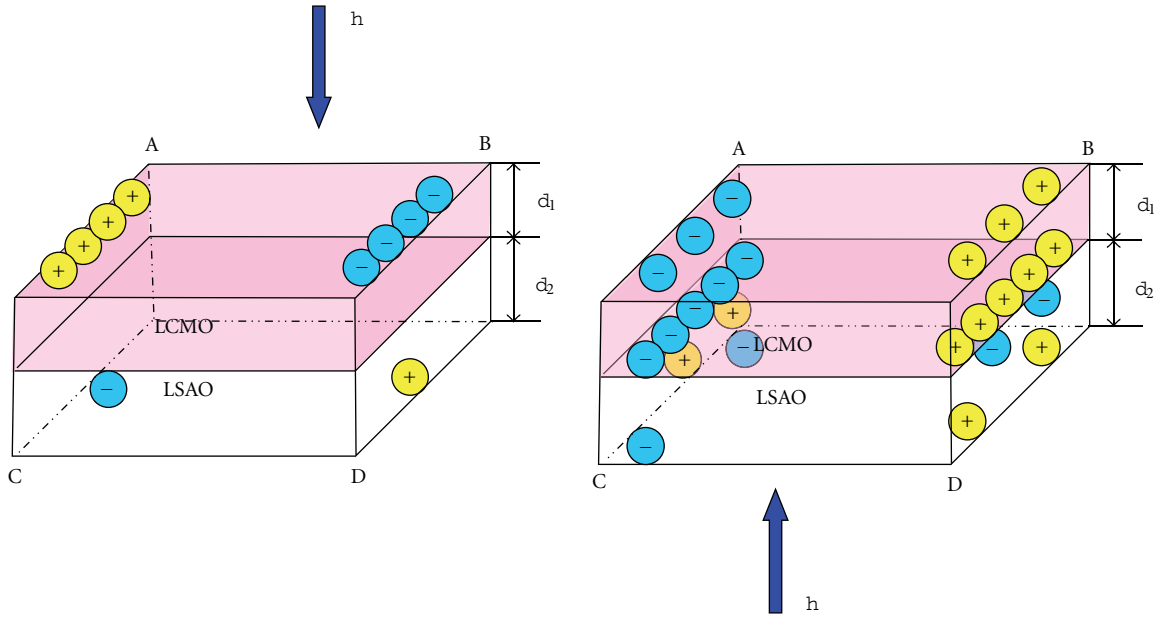


FIGURE 5: The schematic drawing explaining carriers distribution under opposite irradiation directions.

difference produced between A and B on LCMO surface is much larger than that between C and D on LSAO surface because of the significant difference of thicknesses between LCMO and LSAO ($d_1 \ll d_2$) according to (1).

4. Conclusions

In summary, we have observed the lateral photovoltaic effects in the LCMO thin film and LSAO substrate under the 248 nm pulse laser irradiation. The signal polarity inversion shows dependency of irradiation direction and electrode positions. That provides a potential application of the manganite film for photodetector.

Acknowledgments

This work has been supported by NCET, RFDP, Direct Grant from the Research Grants Council of the Hong Kong Special Administrative Region (Grant no. C001-2060295), and Foresight Fund Program from China University of Petroleum.

References

- [1] T. Choi, S. Lee, Y. J. Choi, V. Kiryukhin, and S. W. Cheong, "Switchable ferroelectric diode and photovoltaic effect in BiFeO_3 ," *Science*, vol. 324, no. 5923, pp. 63–66, 2009.
- [2] J. Badro, J. P. Rueff, G. Vankó, G. Monaco, G. Fiquet, and F. Guyot, "Electronic transitions in perovskite: possible nonconvecting layers in the lower mantle," *Science*, vol. 305, no. 5682, pp. 383–386, 2004.
- [3] C. C. Homes, T. Vogt, S. M. Shapiro, S. Wakimoto, and A. P. Ramirez, "Optical response of high-dielectric-constant perovskite-related oxide," *Science*, vol. 293, no. 5530, pp. 673–676, 2001.
- [4] D. D. Fong, G. B. Stephenson, S. K. Streiffer et al., "Ferroelectricity in ultrathin perovskite films," *Science*, vol. 304, no. 5677, pp. 1650–1653, 2004.
- [5] N. V. Volkov, C. G. Lee, P. D. Kim, E. V. Eremin, and G. S. Patrin, "Optically driven conductivity and magnetoresistance in a manganite-based tunnel structure," *Journal of Physics D*, vol. 42, no. 20, Article ID 205009, 2009.
- [6] H. B. Lu, K. J. Jin, Y. H. Huang et al., "Picosecond photoelectric characteristic in $\text{La}_{0.7}\text{Sr}_{0.3}\text{MnO}_3$ Si p-n junctions," *Applied Physics Letters*, vol. 86, no. 24, Article ID 241915, pp. 1–3, 2005.
- [7] X. M. Li, K. Zhao, H. Ni et al., "Voltage tunable photodetecting properties of $\text{La}_{0.4}\text{Ca}_{0.6}\text{MnO}_3$ films grown on miscut LaSrAlO_4 substrates," *Applied Physics Letters*, vol. 97, no. 4, Article ID 044104, 2010.
- [8] K. W. Liu, J. G. Ma, J. Y. Zhang et al., "Ultraviolet photoconductive detector with high visible rejection and fast photoresponse based on ZnO thin film," *Solid-State Electronics*, vol. 51, no. 5, pp. 757–761, 2007.
- [9] H. Ni, S. Q. Zhao, and K. Zhao, "Thickness-dependent photoresponse characteristics of miscut LaSrAlO_4 single crystals for ultraviolet detection," *Applied Optics*, vol. 49, no. 14, pp. 2635–2638, 2010.
- [10] S. Zeuner, W. Prettl, and H. Lengfellner, "Fast thermoelectric response of normal state $\text{YBa}_2\text{Cu}_3\text{O}_{7-\delta}$ films," *Applied Physics Letters*, vol. 66, pp. 1833–1835, 1995.
- [11] K. Zhao, H. B. Lu, M. He et al., "Anomalous photovoltaic effect in $\text{La}_{0.8}\text{Sr}_{0.2}\text{MnO}_3$ films grown on SrTiO_3 (001) substrates by laser molecular beam epitaxy," *The European Physical Journal*, vol. 35, no. 3, pp. 173–176, 2006.
- [12] H. Lengfellner, G. Kremb, A. Schnellbögl, J. Betz, K. F. Renk, and W. Prettl, "Giant voltages upon surface heating in normal $\text{YBa}_2\text{Cu}_3\text{O}_{7-\delta}$ films suggesting an atomic layer thermopile," *Applied Physics Letters*, vol. 60, no. 4, pp. 501–503, 1992.
- [13] H. S. Kwok and J. P. Zheng, "Anomalous photovoltaic response in $\text{YBa}_2\text{Cu}_3\text{O}_7$," *Physical Review B*, vol. 46, no. 6, pp. 3692–3695, 1992.

- [14] K. Takahashi, T. Kanno, A. Sakai, H. Adachi, and Y. Yamada, "Gigantic transverse voltage induced via off-diagonal thermoelectric effect in Ca_xCoO_2 thin films," *Applied Physics Letters*, vol. 97, no. 2, Article ID 021906, 2010.
- [15] A. Kyarad and H. Lengfellner, "Angle-dependent photovoltaic effect in Al-Si multilayers," *Applied Physics Letters*, vol. 87, no. 18, Article ID 182113, pp. 1–3, 2005.
- [16] K. Zhao, K. J. Jin, Y. Huang et al., "Ultraviolet fast-response photoelectric effect in tilted orientation SrTiO_3 single crystals," *Applied Physics Letters*, vol. 89, no. 17, Article ID 173507, 2006.

Research Article

Effect of p-Layer and i-Layer Properties on the Electrical Behaviour of Advanced a-Si:H/a-SiGe:H Thin Film Solar Cell from Numerical Modeling Prospect

Peyman Jelodarian and Abdolnabi Kosarian

Department of Electrical Engineering, Shahid Chamran University of Ahvaz, Ahvaz 61357-831351, Iran

Correspondence should be addressed to Peyman Jelodarian, p.jelodarian@yahoo.com

Received 9 August 2011; Revised 26 September 2011; Accepted 30 September 2011

Academic Editor: Leonardo Palmisano

Copyright © 2012 P. Jelodarian and A. Kosarian. This is an open access article distributed under the Creative Commons Attribution License, which permits unrestricted use, distribution, and reproduction in any medium, provided the original work is properly cited.

The effect of p-layer and i-layer characteristics such as thickness and doping concentration on the electrical behaviors of the a-Si:H/a-SiGe:H thin film heterostructure solar cells such as electric field, photogeneration rate, and recombination rate through the cell is investigated. Introducing Ge atoms to the Si lattice in Si-based solar cells is an effective approach in improving their characteristics. In particular, current density of the cell can be enhanced without deteriorating its open-circuit voltage. Optimization shows that for an appropriate Ge concentration, the efficiency of a-Si:H/a-SiGe solar cell is improved by about 6% compared with the traditional a-Si:H solar cell. This work presents a novel numerical evaluation and optimization of amorphous silicon double-junction (a-Si:H/a-SiGe:H) thin film solar cells and focuses on optimization of a-SiGe:H midgap single-junction solar cell based on the optimization of the doping concentration of the p-layer, thicknesses of the p-layer and i-layer, and Ge content in the film. Maximum efficiency of 23.5%, with short-circuit current density of 267 A/m² and open-circuit voltage of 1.13 V for double-junction solar cell has been achieved.

1. Introduction

Hydrogenated amorphous silicon-germanium alloys (a-SiGe:H) are widely used in multijunction solar cells, where their main advantage is the capability of shifting the optical band gap to lower energies by increasing the germanium concentration in the film [1–3]. In order to avoid drastic reduction of the short-circuit current (J_{SC}) in a cell with small thickness, it is necessary to increase absorbance of the material and optimize the cell structure [4]. Using a lower band-gap material such as a-SiGe in the active base region of the cell is a possible approach, owing to its compatibility with the mature Si-based cell process. An appreciable increase of photocurrent (J_{SC}) in the small band-gap a-SiGe material is highly expected, because of the increased absorption of photons. On the other hand, a drop of the open-circuit voltage (V_{OC}), due to the reduction of the SiGe band-gap with increasing Ge concentration [5, 6]. As a result, a compromise between the cell's parameters is necessary in the optimization procedure. The optimization of band-offset

between a-SiGe and a-Si either in the valence band (E_V) or in the conduction band (E_C) can help design a more effective back surface field, where the photogenerated carriers from the highly dislocated surfaces and interfaces are reflected, thus at the backside of the cell the recombination velocity is significantly decreased. The band offset of E_V and E_C at the a-Si/SiGe heterointerface is dependent on the Ge concentration in the film. In addition to less surface recombination velocity, the smaller band gap (E_g) in high Ge concentration SiGe film has a larger light absorption coefficient, which can lead to more electron-hole pair generation and higher J_{SC} . Both of them can result in higher cell efficiency of the a-SiGe-based solar cell [4]. The optimization process of a multijunction structure involves both the design of individual junction layers which produces an optimum output power and the design of a series stacked configuration of these junction layers which yields the highest possible overall output current. Figure 1 shows a double-junction structure for a p-i-n a-Si solar cell used in this work [7].

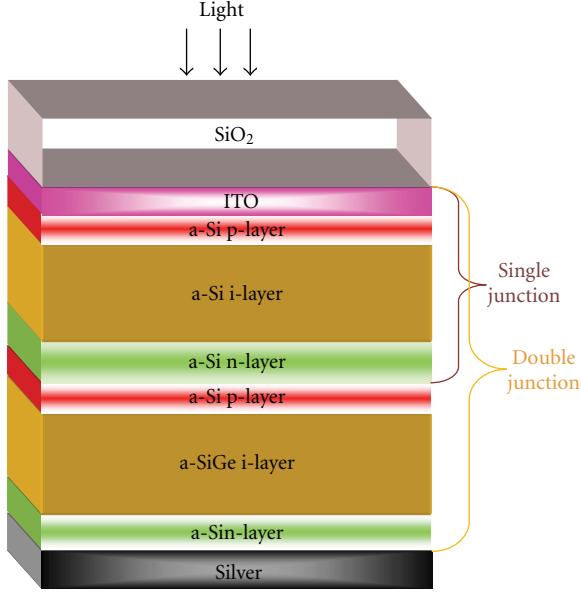


FIGURE 1: The structure of a double junction and the Layers material of simulated double-junction a-Si:H/a-SiGe:H solar cell.

2. Numerical Modeling

Referring to its I - V characteristics, the most important parameters of a solar cell are the short-circuit current (J_{SC}), the open-circuit voltage (V_{OC}), fill factor (FF), and efficiency (η). The short-circuit current is due to the generation and collection of light-generated carriers. So, ideally, it is equal to the light-generated current, and is the largest current that can flow through the solar cell. However, an appreciable fraction of the generated carriers recombine in the bulk and interface. The recombination losses are characterized by the diffusion length and the minority carrier lifetime in the active region.

Modeling of the device is based on the simultaneous solution of transport equations, such as, Poisson equations, continuity equations, and current density equations for holes and electrons [8]:

$$\begin{aligned} -\nabla \cdot \varepsilon \nabla \psi &= q\rho, \\ \nabla \cdot J_p &= q(G - R), \\ \nabla \cdot J_n &= -q(G - R), \end{aligned} \quad (1)$$

where ε is the dielectric constant, ψ is the homojunction hole potential, $-q$ is the electron charge, J_p and J_n are the current densities due to transport by hole and electron, respectively, G is the generation rate for carriers, and R is the recombination rate. The net charge carrier density ρ is given by the following expression:

$$\rho = p - n + n_T - p_T + N_{\text{tail}} + N_{\text{DS}}, \quad (2)$$

where p and n are the free hole and electron densities, n_T and p_T are the concentrations of ionized acceptor and donors, N_{tail} and N_{DS} are the net charge densities due to the trapping of holes and electrons in tail states and dangling bond states,

respectively. The value for n_T and p_T are calculated from the energy levels and total densities of donors and acceptors and from the spatially varying concentrations of free carriers in the solar cell.

Disordered materials like amorphous Silicon and Silicon-Germanium contain a large amount of defect states within the band gap of the material. To accurately model devices made of amorphous silicon, one should use a continuous density of states. The density of defect states (DOSs) is specified with a combination of Gaussian distributions of midgap states and exponentially decaying band tail states [8, 9].

Here, it is assumed that the total density of states (DOSs), $g(E)$, is combined of four components: two tail bands (an acceptor-like conduction band and a donor-like valence band), which are modeled by an exponential distribution, and two deep level bands (one donor-like and the other acceptor-like), which are modeled by a Gaussian distribution [9, 10]:

$$g(E) = g_{TD}(E) + g_{TA}(E) + g_{GD}(E) + g_{GA}(E), \quad (3)$$

where E is the trap energy. The subscripts (G, T, A, D) stand for Gaussian (deep level), tail, acceptor, and donor states, respectively, and [9, 10]

$$\begin{aligned} g_{TD}(E) &= N_{TD} \exp\left[\frac{E_V - E}{W_{TD}}\right], \\ g_{TA}(E) &= N_{TA} \exp\left[\frac{E - E_C}{W_{TA}}\right], \\ g_{GA}(E) &= N_{GA} \exp\left[-\left[\frac{E_{GA} - E}{W_{GA}}\right]^2\right], \\ g_{GD}(E) &= N_{GD} \exp\left[-\left[\frac{E - E_{GD}}{W_{GD}}\right]^2\right], \end{aligned} \quad (4)$$

where E is the trap energy, E_C is the conduction band energy, and E_V is the valence band energy.

For exponential tail distributions, the DOS is described by its conduction and valence band edge intercept densities (N_{TD} and N_{TA}) and by its characteristic decay energy (W_{TD} and W_{TA}). For Gaussian distributions, the DOS is described by its peak energy (E_{GD} and E_{GA}), its characteristic decay energy (W_{GA} and W_{GD}), and its total density of states (N_{GD} and N_{GA}).

The ionized densities of acceptor- and donor-like states (n_T and p_T , resp.) are given by:

$$\begin{aligned} n_T &= n_{TD} + n_{GD}, \\ p_T &= p_{TA} + p_{GA}, \end{aligned} \quad (5)$$

where p_{TA} , p_{GA} , n_{TD} , and n_{GD} are as below:

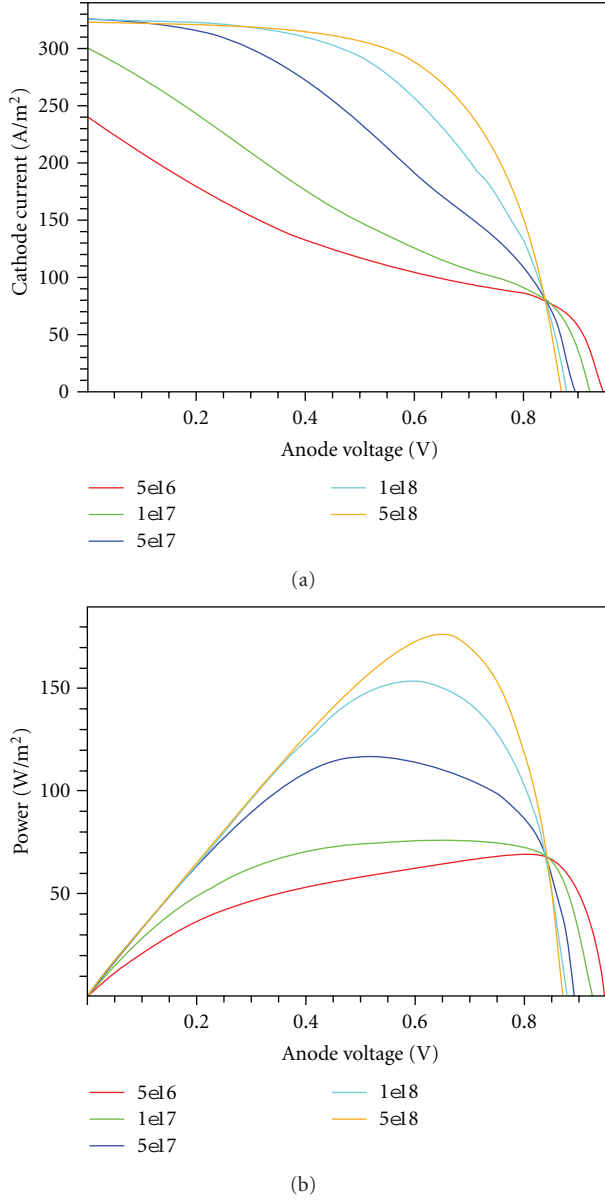


FIGURE 2: I - V and P - V curves of the a-SiGe:H single junction solar cell as a function of acceptor concentration in p-layer.

$$\begin{aligned}
 p_{TA} &= \int_{E_V}^{E_C} g_{TA}(E) \cdot f_{t_{TA}}(E, n, p) dE, \\
 p_{GA} &= \int_{E_V}^{E_C} g_{GA}(E) \cdot f_{t_{GA}}(E, n, p) dE, \\
 n_{TD} &= \int_{E_V}^{E_C} g_{TD}(E) \cdot f_{t_{TD}}(E, n, p) dE, \\
 n_{GD} &= \int_{E_V}^{E_C} g_{GD}(E) \cdot f_{t_{GD}}(E, n, p) dE.
 \end{aligned} \tag{6}$$

where $f_{t_{TA}}(E, n, p)$ and $f_{t_{GA}}(E, n, p)$ are the ionization probabilities for the tail and Gaussian acceptor DOS, while $f_{t_{TD}}(E, n, p)$ and $f_{t_{GD}}(E, n, p)$ are the ionization probabilities for the donors.

TABLE 1: The set of input parameters used in the simulation.

Layer	p-layer	i-layer	n-layer
Thickness [nm]	50	800	50
Doping concentration [/cm ³]	5×10^{18}	1×10^{14}	3×10^{18}
Mobility gap [eV]	1.8	1.5	1.8
Electron mobility [cm ² /Vs]	10	20	20
Hole mobility [cm ² /Vs]	1	2	2
Effective DOS in CB [/cm ³]	2.5×10^{20}	1×10^{20}	2.5×10^{20}
Effective DOS in VB [/cm ³]	2.5×10^{20}	1×10^{20}	2.5×10^{20}

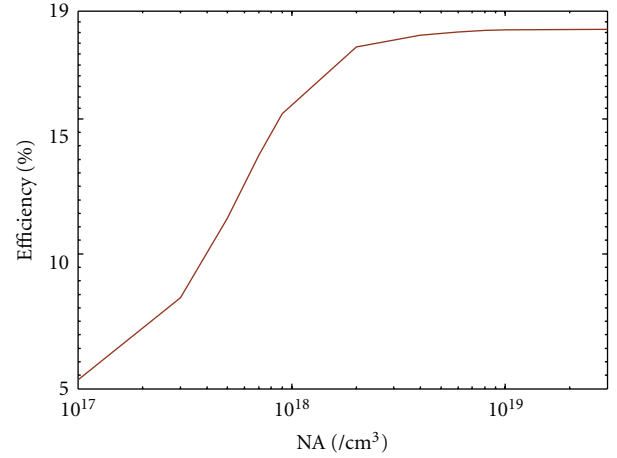


FIGURE 3: The a-SiGe:H solar cell efficiency as a function of concentration of acceptor in p-layer.

In the p-i-n structure of Figure 1 the p-type a-Si:H layer is highly doped, since its higher conductivity allows more light to pass through to the intrinsic layer. As a result, the open-circuit voltage as well as the short-circuit current could be improved. Moreover, this layer is made thinner than the other layers to give the carriers less opportunity and time to recombine before reaching the intrinsic layer.

Table 1 shows a set of input parameters, which are used in our simulation. The transparent conductive ITO layer has 75 nm thickness. For a-SiGe:H p-i-n solar cell, it is widely accepted that the most important parameters affecting the device properties are the gap states of the films.

In this work, the AM1.5 spectrum for illumination of samples was used.

3. Results and Discussion

The performance of a one-square-meter p-i-n single-junction a-SiGe:H solar cell (SiO₂/ITO/p-a-Si:H/i-a-SiGe:H/n-a-Si:H/Silver), such as short-circuit current (J_{SC}), open-circuit voltage (V_{OC}), fill factor (FF), conversion efficiency (η), and I - V curve, are obtained as a function of doping concentration, atomic percent of Ge in a-SiGe layer and thicknesses of i-layer and p-layer. Also variations of the electrical properties inside the solar cell such as the distribution of photo-generation and recombination rates, and electric field, with variation of layers properties are obtained.

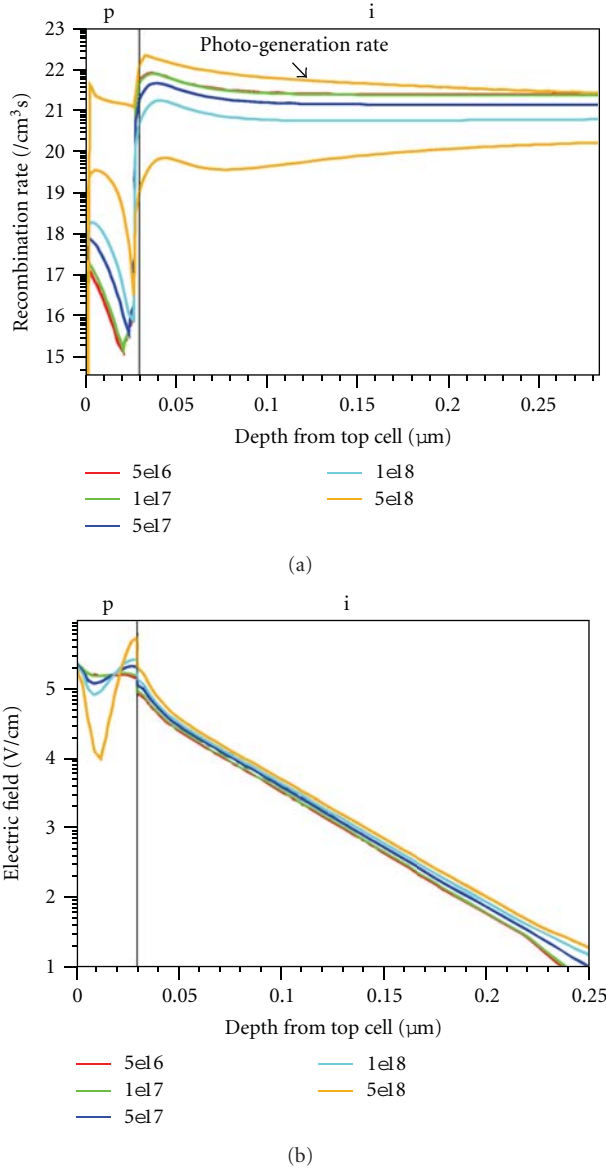


FIGURE 4: Recombination rate and electric field distribution of The a-SiGe:H solar cell device for different acceptor concentrations in p-layer.

In order to be able to collect the maximum number of electron-hole pairs generated by absorbed photons, the electric field at the p-i interface should be as high as possible; however, the recombination rate also increases with increasing the electric field, resulting in a reduction in the efficiency. So, there must be a compromise between the recombination rate and the electric field.

The a-SiGe:H solar cell I - V and P - V curves as a function of p-layer doping concentration are shown in Figure 2.

The a-SiGe:H solar cell efficiency as a function of p-layer doping concentration is shown in Figure 3. The other parameters are the same as in Table 1.

According to Figures 2 and 3, simulation indicates that for the p-layer concentrations larger than 10^{18} cm^{-3} , the cell has a high efficiency due to the drastic increase in

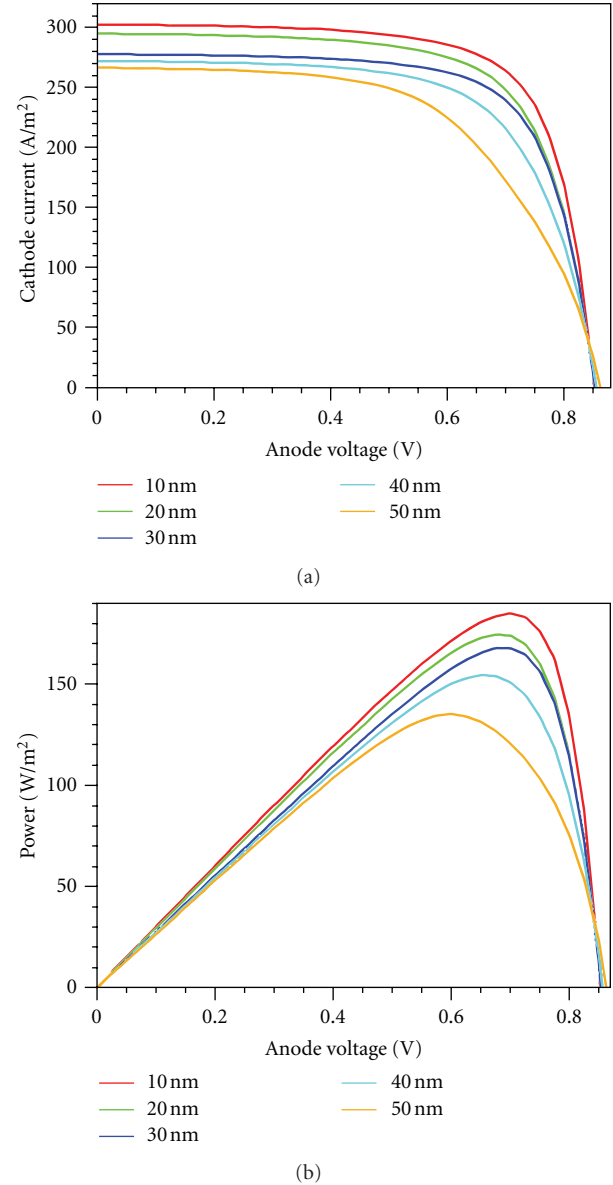


FIGURE 5: I - V and P - V curves of the a-SiGe:H single junction solar cell as function of thickness of p-layer.

short circuit current of the device. However, care is needed to achieve such a high acceptor concentration in the film without degrading the film quality.

Figure 4 shows the recombination rate and electric field distribution through the cell as a function of p-layer doping concentration. As shown in figure, $5 \times 10^{18} \text{ cm}^{-3}$ of p-layer concentration builds the highest electric field at the p-i interface that results more carriers collection by ITO layer, but it also has the highest recombination rate in i-layer.

The a-SiGe:H solar cell I - V and P - V curves as a function of p-layer thickness are shown in Figure 5.

The effect of p-layer thickness on the efficiency of the cell is shown in Figure 6. The other parameters used are the same as in Table 1. The thickness of the p-layer was changed from 10 to 90 nm.

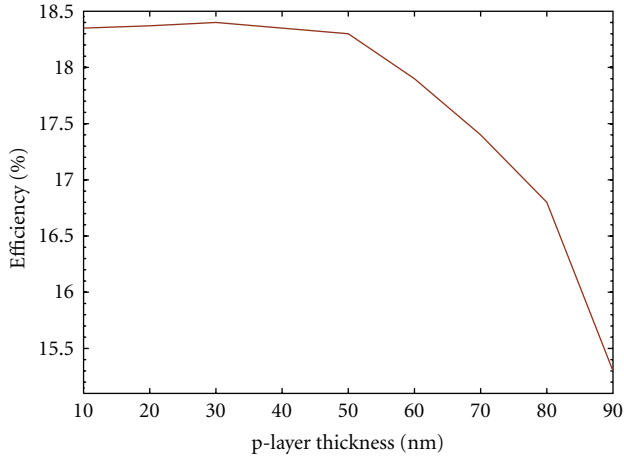


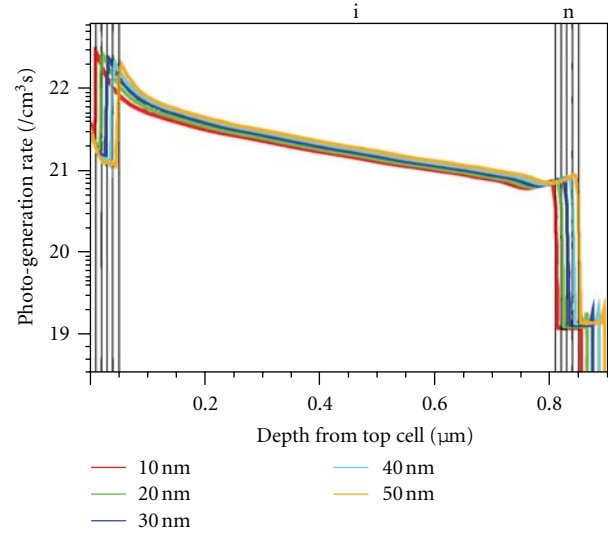
FIGURE 6: The a-SiGe:H solar cell efficiency as a function of thickness of p-layer.

The photogeneration rate and recombination rate and electric field distribution through the cell as a function of p-layer thickness are shown in Figures 7 and 8, respectively. These Figures show that the cell with thinner p-layer has lower recombination rate in p-layer and high electric field in p-i interface that results in higher current density.

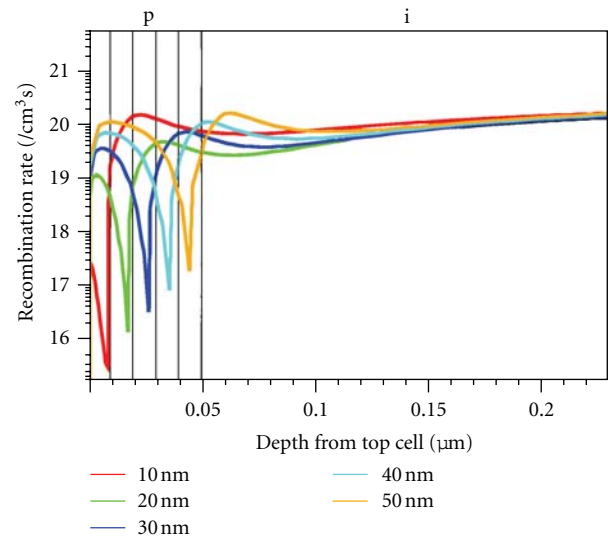
The SiGe band-gap, which is engineered by alteration of Ge concentration, is a critical parameter in the SiGe solar cell design. Introducing Ge atoms to the Si lattice in Si-based solar cells is an effective approach in improving their characteristics. In particular, current density of the cell can be enhanced without deteriorating its open-circuit voltage. The efficiency of the solar cell as a function of Ge concentration in SiGe layer is shown in Figure 9, where it is changed between 0 and 30 at %. The other parameters used are the same as in Table 1. Simulation shows that the maximum efficiency of 18.5% is obtained at the optimized value of Ge concentration of 17 at %, which shows 6% improvement in the overall efficiency of the cell compared with the common single-junction a-Si:H solar cell, Figure 9.

In amorphous thin film p-i-n solar cell, a thick absorber layer (i-layer) can absorb more light to generate electron and hole (carriers); however, a thicker i-layer degrades the drift electric field for carrier transport. On the other hand, a thin i-layer cannot absorb enough light. Thickness of i-layer is a key parameter that can limit the performance of amorphous thin film solar cells. The a-SiGe:H solar cell efficiency as a function of the i-layer thickness are shown in Figure 10. The other parameters used are the same as in Table 1. As shown in the figure, maximum efficiency is obtained at the 0.8 μm of thickness of i-layer.

Based on the optimized a-Si:H/SiGe:H single-junction solar cell, described previously, a double-junction solar cell (Figure 1) has been designed. *I-V* and *P-V* characteristics of the optimized single- and double-junction solar cells are shown in Figure 11. As you can see the current density of double-junction solar cell is lower than single-junction solar cell, because of current limitation of a-Si:H solar cell. The figures show that for double-junction cell the short-circuit



(a)



(b)

FIGURE 7: Photogeneration rate and recombination rate of The a-SiGe:H solar cell device for different thickness of p-layer.

current density, open-circuit voltage, maximum output power, and fill factor of 267 A/m^2 , 1.13 V, 235 W/m^2 , and 0.795 are obtained, respectively.

4. Conclusion

A two-dimensional computer simulation is presented here using the standard continuous density of state model for deep and shallow states in amorphous silicon band-gap for the optimization of the single- and double-junction-hydrogenated amorphous Silicon-Germanium solar cells. The simulation and modeling process indicate that it is possible to optimize the solar cell performance and improve the efficiency of the cell by appropriate selection of the thickness and doping concentration of the layers.

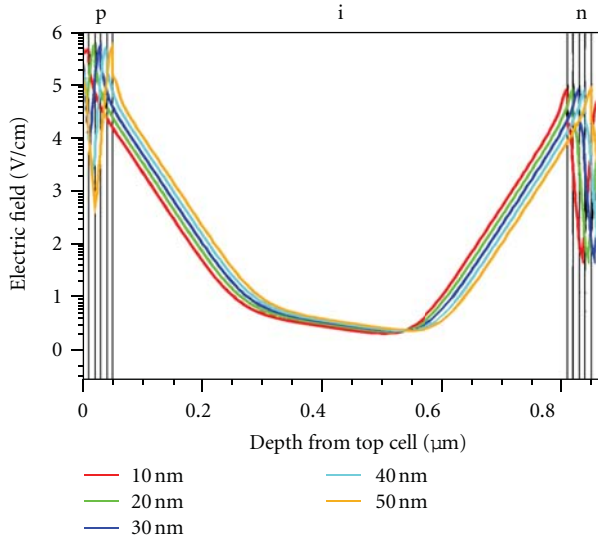


FIGURE 8: Electric field distribution of The a-SiGe:H solar cell device for different thickness of p-layer.

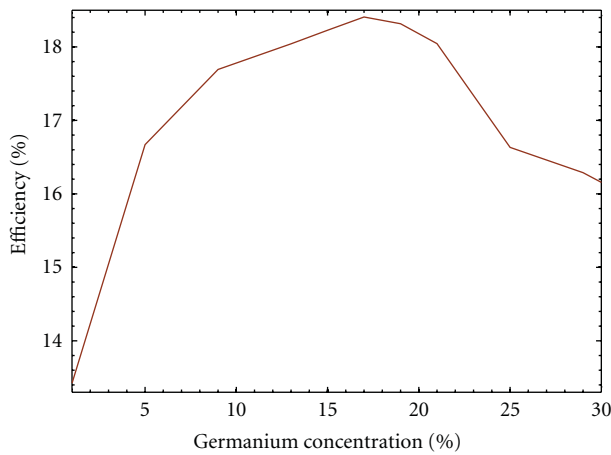


FIGURE 9: The a-SiGe:H solar cell efficiency as a function of Ge concentration in SiGe layer.

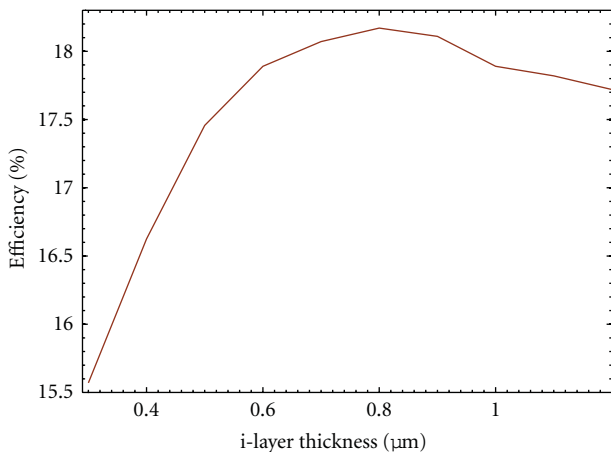
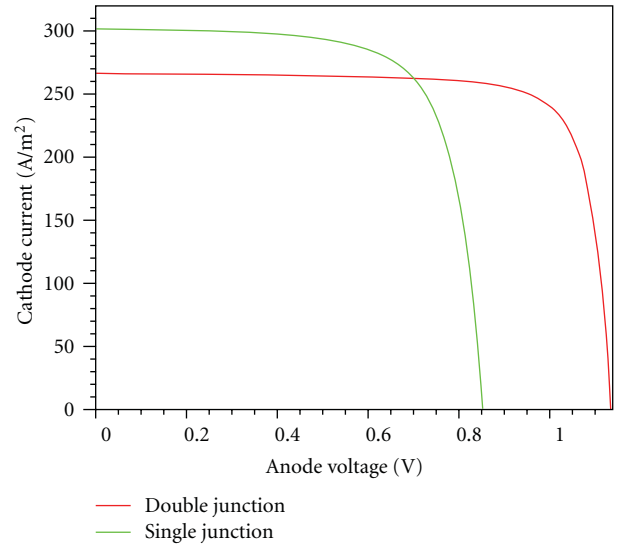
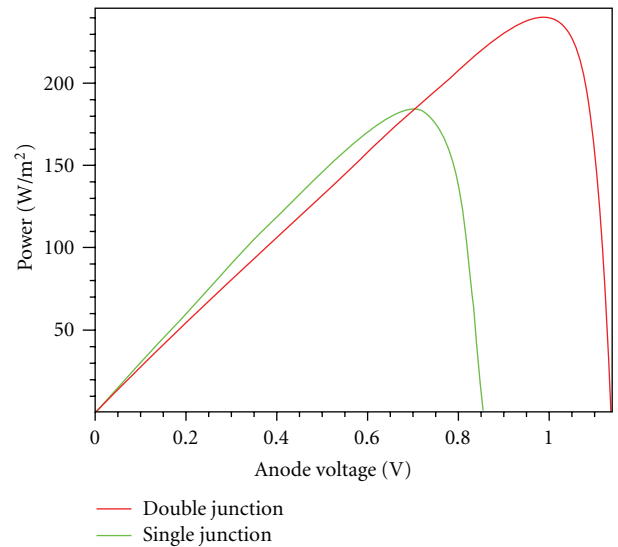


FIGURE 10: The a-SiGe:H solar cell efficiency as a function of i-layer thickness.



(a)



(b)

FIGURE 11: *I-V* and *P-V* curves of the optimized single- and double-junction solar cells.

Acknowledgments

This work was partly supported by Khuzestan Regional Electricity Company and Jundishapour Water and Energy Research Institute, Iran.

References

- [1] A. Gordijn, R. J. Zambrano, J. K. Rath, and R. E. I. Schropp, "Highly stable hydrogenated amorphous silicon germanium solar cells," *IEEE Transactions on Electron Devices*, vol. 49, no. 5, pp. 949–952, 2002.
- [2] S. Guha and J. Yang, "Science and technology of amorphous silicon alloy photovoltaics," *IEEE Transactions on Electron Devices*, vol. 46, no. 10, pp. 2080–2085, 1999.

- [3] A. Banerjee, K. Hoffman, X. Xu, J. Yang, and S. Guha, "Back reflector texture and stability issues in high efficiency multi-junction amorphous silicon alloy solar cells," in *Proceedings of the IEEE 1st World Conference on Photovoltaic Energy Conversion*, vol. 1, pp. 539–542, Waikoloa, Hawaii, USA, 1994.
- [4] M. H. Liao and C. H. Chen, "The investigation of optimal Si-sige hetero-structure thin-film solar cell with theoretical calculation and quantitative analysis," *IEEE Transactions on Nanotechnology*, vol. 10, no. 4, pp. 770–773, 2011.
- [5] C. Lee, H. Efstathiadis, J. E. Raynolds, and P. Haldar, "Two-dimensional computer modeling of single junction a-Si:H solar cells," in *Proceedings of the 34th IEEE Photovoltaic Specialists Conference, (PVSC '09)*, pp. 001118–001122, Philadelphia, Pa, USA, June 2009.
- [6] Z. Q. Li, Y. G. Xiao, and Z. M. S. Li, "Modeling of multi-junction solar cells by Crosslight APSYS," in *Proceedings of the High and Low Concentration for Solar Electric Applications*.
- [7] A. Kosarian and P. Jelodarian, "Optimization and characterization of advanced solar cells based on thin-film a-Si:H/SiGe hetero-structure," in *Proceedings of the 19th Iranian Conference on Electrical Engineering, (ICEE '11)*, pp. 1–5, 2011.
- [8] H. Tasaki, W. Y. Kim, M. Hallerdt, M. Konagai, and K. Takahashi, "Computer simulation model of the effects of interface states on high-performance amorphous silicon solar cells," *Journal of Applied Physics*, vol. 63, no. 2, pp. 550–560, 1988.
- [9] M. Kemp, M. Meunier, and C. G. Tannous, "Simulation of the amorphous silicon static induction transistor," *Solid State Electronics*, vol. 32, no. 2, pp. 149–157, 1989.
- [10] M. Hack and J. G. Shaw, "Numerical simulations of amorphous and polycrystalline silicon thin-film transistors," in *Proceedings of the Conference on Solid State Devices and Materials*, pp. 999–1002, Sendai, Japan, 1990.

Research Article

Performance of Dye-Sensitized Solar Cells with (PVDF-HFP)-KI-EC-PC Electrolyte and Different Dye Materials

M. M. Noor,^{1,2} M. H. Buraidah,² S. N. F. Yusuf,² M. A. Careem,³ S. R. Majid,² and A. K. Arof²

¹ Centre for Foundation Studies, International Islamic University Malaysia, Jalan Universiti, 46350 Petaling Jaya, Selangor, Malaysia

² Department of Physics, Centre for Ionics University Malaya, University of Malaya, 50603 Kuala Lumpur, Malaysia

³ Department of Physics, University of Peradeniya, 20400 Peradeniya, Sri Lanka

Correspondence should be addressed to A. K. Arof, akarof@um.edu.my

Received 8 July 2011; Revised 20 September 2011; Accepted 20 September 2011

Academic Editor: Leonardo Palmisano

Copyright © 2011 M. M. Noor et al. This is an open access article distributed under the Creative Commons Attribution License, which permits unrestricted use, distribution, and reproduction in any medium, provided the original work is properly cited.

A plasticized polymer electrolyte system composed of PVDF-HFP, potassium iodide (KI), and equal weight of ethylene carbonate (EC) and propylene carbonate (PC) has been used in a dye-sensitized solar cell (DSSC). The electrolyte with the composition 40 wt. % PVDF-HFP-10 wt. % KI-50 wt. % (EC + PC) exhibits the highest room temperature ionic conductivity of $1.10 \times 10^{-3} \text{ S cm}^{-1}$. A small amount of iodine crystal of about 10 wt. % of KI was added to the electrolyte in the liquid state to provide the redox couple for DSSC operation. The polymer electrolyte films were prepared by the solvent casting method. The DSSCs were fabricated with the electrolyte film sandwiched between a TiO_2 /dye photoelectrode and a Pt-counter electrode and characterized under 100 mW cm^{-2} white light. The DSSC performance with different dyes such as Ruthenizer 535 (N3), anthocyanin, chlorophyll, and a mixture of anthocyanin and chlorophyll ($v/v = 1$) has been compared. The DSSC with Ruthenizer 535 (N3) dye exhibits the best performance with a short-circuit current density of 8.16 mA cm^{-2} , open-circuit voltage of 0.76 V, fill factor of 0.35, and photoconversion efficiency of 2.2%.

1. Introduction

Solar cells are devices that utilize energy from the sun by converting solar radiation directly into electricity. The conventional solar cell device is silicon-based solar cells with efficiency as high as 30% under concentrated light. However, high manufacturing cost prevents the widespread use of silicon cells [1, 2]. Dye-sensitized solar cells (DSSCs) have attracted much attention as they can also offer high-energy conversion efficiencies. DSSCs are easy to fabricate, and manufacturing cost is lower compared to silicon solar cells [3–5]. The structure of the DSSC consists of a TiO_2 photoelectrode coated on conducting glass, dye sensitizer, an electrolyte containing redox couple, and a counter electrode [6]. Energy conversion in a DSSC is based on the injection of an electron from a photoexcited state of the dye into the conduction band of the TiO_2 photoelectrode [7]. Since the dye plays an important role in harvesting light and solar energy conversion to electricity, efforts have been focused on dye materials. The commercial synthetic ruthenium (II) polypyridyl complexes such as N719 and N3 are widely used in DSSCs

due to the satisfactory photoelectric conversion efficiency up to 10% [8, 9]. However, these dyes use metal compound complexes, which are expensive and produce environmental pollution [10]. Another approach is to use natural dyes, which is environmentally friendly, nontoxic, biodegradable, and cheaper compared to the synthetic dyes, but has yet to show good performance in terms of efficiency [11]. Natural sensitizing dyes include anthocyanins [12, 13]. In this study, the DSSCs were prepared with N3 dye or natural dyes. Anthocyanin from black rice extraction was used as the dye since anthocyanin has good chemical bonding with titanium dioxide [14]. Chlorophyll, a natural photosensitizer for photosynthesis in green plants, is another attractive potential compound as photosensitizer in the visible region for DSSC [15, 16].

2. Experimental

2.1. Materials. Poly(vinylidene fluoride-hexafluoropropylene) (PVDF-HFP) of MW 400,000 and potassium iodide (KI) salt were procured from Aldrich. High-purity (99%)

TABLE 1: Different compositions of PVDF-HFP polymer electrolyte.

Sample	Electrolyte composition in wt.% ratio		Weight (g)		Iodine (g) (10% of KI)
	(PVDF-HFP:KI):(EC/PC)	PVDF-HFP	KI	EC/PC	
S0	(50:0):50	1.00	0.00	1.00	0.00
S1	(45:5):50	0.90	0.10	1.00	0.01
S2	(40:10):50	0.80	0.20	1.00	0.02
S3	(35:15):50	0.70	0.30	1.00	0.03
S4	(30:20):50	0.60	0.40	1.00	0.04

acetone, ethylene carbonate (EC), and propylene carbonate (PC) were purchased from Fluka and TiO₂ paste PST-18NR from JGC Catalyst and Chemicals Ltd., Japan. Compact layer solution, *di-isopropoxytitanbis(acetylacetonate)* was purchased from Aldrich and was diluted with ethanol to obtain 0.38 M. Ruthenizer 535 (N3) dye, purchased from Solaronix, Switzerland was diluted to 0.003 M with ethanol and *chloroplatinic acid* was diluted to 0.005 M in 2-propanol prior to use. The *chloroplatinic acid* was purchased from Aldrich.

2.2. Preparation of Polymer Electrolytes. The electrolyte system using PVDF-HFP as polymer host, potassium iodide (KI) salt, and a mixture of ethylene carbonate (EC) and propylene carbonate (PC) at 1:1 weight ratio as plasticizers has been prepared for application in DSSC. Several compositions by weight % ratio of (polymer:salt):(plasticizer) were prepared as listed in Table 1. Acetone was used to dissolve the polymer, salt, and the plasticizer at 40°C, and the liquid solutions were cast to form electrolyte films. Electrochemical impedance spectroscopy (EIS) technique was used to determine the conductivity of each composition. The highest conducting electrolyte was used to fabricate the DSSC.

2.3. Preparation of Dye Materials. Three types of dyes were prepared for this study. First, chlorophyll dye was prepared from 20 g fresh leaves of fragrant screwpine (*Pandanus amaryllifolius*) or locally known as *pandan leaves*. The leaves were cleaned with distilled water, rinsed with ethanol, and were cut into small pieces and immersed in 200 mL ethanol. Second, anthocyanin dye solution was prepared from 100 g black rice immersed in 100 mL ethanol. Both solutions were kept for 24 hours in the dark before filtration to remove residues. Third, to obtain 0.003 M N3 dye, 10 mg Ruthenizer 535 (N3) dye powder was diluted in 5 mL ethanol and kept for 24 hours in the dark before use.

2.4. Preparation of Electrodes. The working electrode is a TiO₂ layer, and the counter electrode is a platinum layer. Indium tin oxide (ITO) glass was used as a substrate for both electrodes. To prepare the working electrode or photoanode, TiO₂ paste was doctor bladed on the ITO surface [17–19]. Prior to this, the ITO glass has been spin-coated with *diisopropoxytitanium bis(acetylacetonate)* at 3000 rpm for 10 seconds to improve adhesion of TiO₂ on the ITO glass and provide a larger TiO₂/ITO contact area. This compact layer also minimizes contact between the redox electrolyte and the conductive ITO surface. This is necessary to prevent electron

recombination in the DSSC and hence improve efficiency [20]. The layers were sintered at 450°C for 30 minutes after each process. The prepared TiO₂ electrode was immersed in each dye solution and left for 24 hours in the dark to allow the dye to attach to the TiO₂ surface. The TiO₂/dye electrode was washed in ethanol and dried before assembling the DSSC. The counter electrode was prepared by spin coating a thin layer of platinum (Pt) solution (*chloroplatinic acid* diluted to 0.005 M in 2-propanol) on the conducting surface of a cleaned ITO glass and sintered at 450°C for 30 minutes [21]. In this study, DSSCs were illuminated from the Pt counter electrode side. Hence the prepared Pt counter electrode should be highly transparent.

2.5. Preparation of DSSCs. The DSSCs were prepared using a photoelectrode with 0.16 cm² working area, a counter electrode of Pt-coated ITO glass, and an electrolyte film containing (PVDF-HFP), KI, a mixture of EC/PC plasticizer, and a small amount of iodine. The DSSCs were fabricated by sandwiching the electrolyte between the TiO₂ and Pt electrodes.

2.6. Characterization and Measurements. For the polymer electrolytes, electrochemical impedance spectroscopy (EIS) technique was used to determine the highest conducting composition. The impedance of the samples was measured using the HIOKI 3520 LCR Hi-Tester interfaced to a computer with frequency ranging from 50 Hz to 100 kHz at room temperature. Each sample was sandwiched between two stainless steel electrodes of diameter 2.0 cm before performing the measurement. The conductivity was calculated using equation

$$\sigma = \frac{l}{R_B A}. \quad (1)$$

Here R_B is the bulk resistance taken at the intersection of the Nyquist plot with the real impedance axis, l is the film thickness, and A is the surface area of the electrode/electrolyte contact. The absorption spectrum of the different dyes was taken with Shimadzu UV-1650PC UV-vis spectrophotometer. The photocurrent-voltage (I–V) characteristics of the DSSCs were measured under illumination from a xenon lamp at the intensity of 100 Mw cm⁻² using a Keithley 2400 electro meter. The fill factor (FF) was calculated using the equation

$$FF = \frac{I_{\max} V_{\max}}{I_{\text{SC}} V_{\text{OC}}}, \quad (2)$$

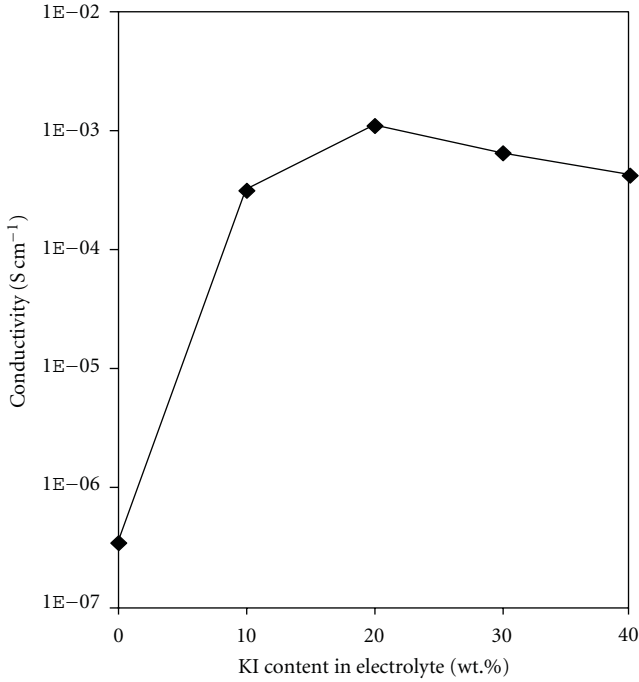


FIGURE 1: Conductivity of PVDF-HFP electrolyte with different salt contents.

where I_{\max} and V_{\max} are the maximum output value of current and voltage, respectively, and I_{SC} and V_{OC} are the short-circuit current and open-circuit voltage, respectively. The total energy conversion efficiency was calculated using the equation

$$\eta = \frac{I_{\text{SC}} V_{\text{OC}} \times \text{FF}}{P_{\text{in}}}, \quad (3)$$

where P_{in} is the power of incident light.

3. Results and Discussion

3.1. EIS of Polymer Electrolytes. The plot of room temperature conductivity of the electrolyte as a function of salt content is shown in Figure 1. The conductivity increases with the salt concentration, reaching a maximum value of $1.10 \times 10^{-3} \text{ S cm}^{-1}$ at 20 wt. % salt and gradually decreases thereafter. Conductivity increase is due to the increase of charge carriers or mobile ions when the salt content was increased. At high salt concentration, the distance between dissociated ions may become too close to each other enabling them to recombine into neutral ion-pairs which do not contribute to conductivity. Such phenomenon has been reported in the literature [22–24] and can be proven through Fourier transform impedance spectroscopy. The use of 50 wt. % EC/PC as plasticizers in the electrolyte helps to promote ion transfer and ion dissociation that enhances the conductivity. It is reported that the addition of plasticizers (up to 50 wt.%) enhances conductivity without compromising thermal, electrochemical, and dimensional stability of the electrolyte and the most employed plasticizers are low-molecular-weight

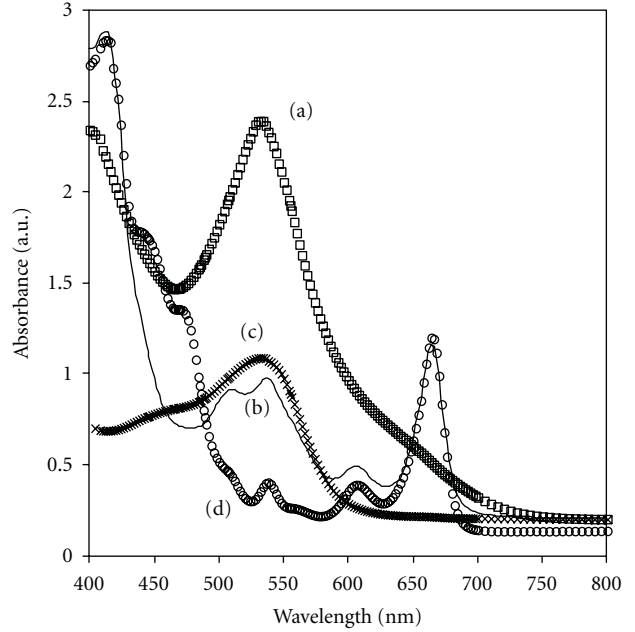


FIGURE 2: Absorption spectra of different dye materials. (a) Ruthenizer 535 (N3), (b) anthocyanin/chlorophyll mixture, (c) anthocyanin, (d) chlorophyll.

organic solvents such as propylene carbonate (PC) and ethylene carbonate (EC) [25, 26].

3.2. Characterizations of Natural Dye Sensitizers. Figure 2 shows the absorption spectra of Ruthenizer 535 (N3), anthocyanin, chlorophyll and a mixture of anthocyanin and chlorophyll, sensitizers at 1:1 volume ratio. The N3 dye exhibits maximum absorption at 535 nm, anthocyanin from black rice extraction at 532 nm, chlorophyll at 413 and 665 nm, and the mixture of black-rice and chlorophyll shows maximum peaks at 413, 536, and 665 nm. Since the sun's spectrum peaks at 550 nm, N3 and anthocyanin dyes should be able to absorb maximum sunlight and yield higher possibility of light harvesting [14]. Chlorophylls, which act as an effective photosensitizer in photosynthesis of green plant, has absorption maximum at 670 nm, thus, it is an attractive potential compound as a photosensitizer in the visible region [16]. It is also found that more absorption peaks are found when two natural dyes are mixed which shows that the absorption range is enhanced. This indicates the possibility of increasing the photoelectric conversion efficiency of a dye-sensitized solar cell with mixed dyes [27].

3.3. Characterizations of DSSCs. The photocurrent density-voltage graphs for DSSCs with different dyes material are shown in Figure 3. The values of open-circuit voltage (V_{OC}), short-circuit current density (I_{SC}), fill factor (FF), and conversion efficiency (η) obtained from Figure 3 are summarized in Table 2. Compared to the natural dye sensitizers, DSSC with Ruthenizer 535 (N3) dye shows the best overall performance with the short-circuit current density of 8.16 mA cm^{-2} , open-circuit voltage of 0.76 V, fill factor of

TABLE 2: The performance parameters of DSSCs with different dyes.

	N3	Anthocyanin	Chlorophyll	Anthocyanin + Chlorophyll
J_{sc} (mA cm^{-2})	8.16	3.02	1.61	3.26
V_{oc} (V)	0.76	0.36	0.36	0.36
FF	0.35	0.34	0.41	0.36
Efficiency (%)	2.17	0.37	0.24	0.42

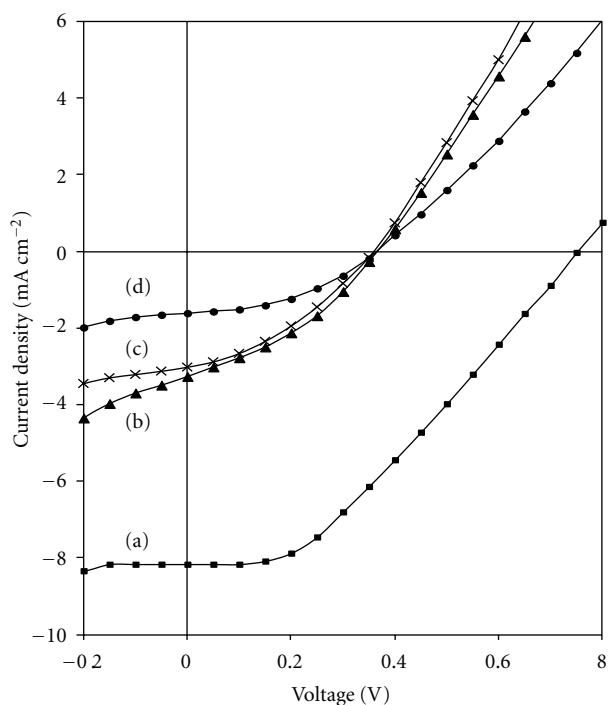


FIGURE 3: J - V curves for DSSCs with different dye materials. (a) Ruthenizer 535 (N3), (b) anthocyanin/chlorophyll mixture, (c) anthocyanin, (d) chlorophyll.

0.35, and photoconversion efficiency of 2.2%. For natural dyes, the mixed dye system shows better efficiency than dyes prepared using individual chlorophyll or anthocyanin extract. This suggests the possibility of utilizing multi-natural-dye mixture of different proportions and additives for the production of better absorbing dyes.

4. Conclusions

DSSCs have been fabricated using the highest conducting plasticized PVDF-HFP polymer electrolyte containing iodine/triiodide redox couple with N3, anthocyanin (from black rice extraction), and chlorophyll (from *pandan* extract) dyes as sensitizer. The DSSC using Ruthenizer 535 (N3) dye exhibits the best performance with a short-circuit current density of 8.16 mA cm^{-2} , open-circuit voltage of 0.76 V, fill factor of 0.35, and the highest photoconversion efficiency of 2.2%. As for the DSSC fabricated using natural dyes, the device with anthocyanin dye shows better performance compared to chlorophyll with a short-circuit current density of 1.07 mA cm^{-2} , open-circuit voltage 0.43 V, fill factor 0.33, and efficiency of 0.2% under the illumination of

100 mW cm^{-2} white light. However, the mixed dye system shows improved conversion efficiency suggesting that multi-dye mixtures may be more suitable for improving the efficiency of DSSCs.

Acknowledgments

The authors would like to thank University of Malaya for the financial support through Institute of Research Management and Consultancy of University Malaya, IPPP Grant (PS325/2009C) and (PS353/2009A) to carry out this research work. M. H. Buraidah and S. N. F. Yusuf thank the Ministry of Education Malaysia and University of Malaya for the scholarship and tutorship awarded, and M. M. Noor thanks the International Islamic University Malaysia (IIUM) for the study leave awarded.

References

- [1] B. Li, L. Wang, B. Kang, P. Wang, and Y. Qiu, "Review of recent progress in solid-state dye-sensitized solar cells," *Solar Energy Materials & Solar Cells*, vol. 90, no. 5, pp. 549–573, 2006.
- [2] G. P. Smestad, "Education and solar conversion: demonstrating electron transfer," *Solar Energy Materials & Solar Cells*, vol. 55, no. 1–2, pp. 157–178, 1998.
- [3] P. Wang, S. M. Zakeeruddin, and M. Grätzel, "Solidifying liquid electrolytes with fluorine polymer and silica nanoparticles for quasi-solid dye-sensitized solar cells," *Journal of Fluorine Chemistry*, vol. 125, no. 8, pp. 1241–1245, 2004.
- [4] Z. Liu, "Theoretical studies of natural pigments relevant to dye-sensitized solar cells," *Journal of Molecular Structure: THEOCHEM*, vol. 862, no. 1–3, pp. 44–48, 2008.
- [5] J. Wu, Z. Lan, J. Lin, M. Huang, and P. Li, "Effect of solvents in liquid electrolyte on the photovoltaic performance of dye-sensitized solar cells," *Journal of Power Sources*, vol. 173, no. 1, pp. 585–591, 2007.
- [6] S. R. Scully, M. T. Lloyd, R. Herrera, E. P. Giannelis, and G. G. Malliaras, "Dye-sensitized solar cells employing a highly conductive and mechanically robust nanocomposite gel electrolyte," *Synthetic Metals*, vol. 144, no. 3, pp. 291–296, 2004.
- [7] A. F. Nogueira, C. Longo, and M. A. De Paoli, "Polymers in dye sensitized solar cells: overview and perspectives," *Coordination Chemistry Reviews*, vol. 248, no. 13–14, pp. 1455–1468, 2004.
- [8] D. W. Kim, Y. B. Jeong, S. H. Kim, D. Y. Lee, and J. S. Song, "Photovoltaic performance of dye-sensitized solar cell assembled with gel polymer electrolyte," *Journal of Power Sources*, vol. 149, no. 1–2, pp. 112–116, 2005.
- [9] T. Asano, T. Kubo, and Y. Nishikitani, "Electrochemical properties of dye-sensitized solar cells fabricated with PVDF-type polymeric solid electrolytes," *Journal of Photochemistry and Photobiology A*, vol. 164, no. 1–3, pp. 111–115, 2004.

- [10] H. Chang, H. M. Wu, T. L. Chen, K. D. Huang, C. S. Jwo, and Y. J. Lo, "Dye-sensitized solar cell using natural dyes extracted from spinach and ipomoea," *Journal of Alloys and Compounds*, vol. 495, no. 2, pp. 606–610, 2010.
- [11] A. O. T. Patrocínio, S. K. Mizoguchi, L. G. Paterno, C. G. Garcia, and N. Y. M. Iha, "Efficient and low cost devices for solar energy conversion: efficiency and stability of some natural-dye-sensitized solar cells," *Synthetic Metals*, vol. 159, no. 21-22, pp. 2342–2344, 2009.
- [12] K. Wongcharee, V. Meeyoo, and S. Chavadej, "Dye-sensitized solar cell using natural dyes extracted from rosella and blue pea flowers," *Solar Energy Materials & Solar Cells*, vol. 91, no. 7, pp. 566–571, 2007.
- [13] S. Furukawa, H. Iino, T. Iwamoto, K. Kukita, and S. Yamauchi, "Characteristics of dye-sensitized solar cells using natural dye," *Thin Solid Films*, vol. 518, no. 2, pp. 526–529, 2009.
- [14] B. Yulianto, W. Septina, K. Fuadi, F. Fanani, L. Muliani, and Nugraha, "Synthesis of nanoporous TiO₂ and its potential applicability for dye-sensitized solar cell using antocyanine black rice," *Advances in Materials Science and Engineering*, vol. 2010, Article ID 789541, 2010.
- [15] Y. Amao, Y. Yamada, and K. Aoki, "Preparation and properties of dye-sensitized solar cell using chlorophyll derivative immobilized TiO₂ film electrode," *Journal of Photochemistry and Photobiology A*, vol. 164, no. 1–3, pp. 47–51, 2004.
- [16] H. Zhou, L. Wu, Y. Gao, and T. Ma, "Dye-sensitized solar cells using 20 natural dyes as sensitizers," *Journal of Photochemistry and Photobiology A*, vol. 219, no. 2-3, pp. 188–194, 2011.
- [17] C. Sima, C. Grigoriu, and S. Antohe, "Comparison of the dye-sensitized solar cells performances based on transparent conductive ITO and FTO," *Thin Solid Films*, vol. 519, no. 2, pp. 595–597, 2010.
- [18] D. Saikia, C. C. Han, and Y. W. Chen-Yang, "Influence of polymer concentration and dyes on photovoltaic performance of dye-sensitized solar cell with P(VdF-HFP)-based gel polymer electrolyte," *Journal of Power Sources*, vol. 185, no. 1, pp. 570–576, 2008.
- [19] Y. Ren, Z. Zhang, S. Fang, M. Yang, and S. Cai, "Application of PEO based gel network polymer electrolytes in dye-sensitized photoelectrochemical cells," *Solar Energy Materials & Solar Cells*, vol. 71, no. 2, pp. 253–259, 2002.
- [20] H. Yu, S. Zhang, H. Zhao, G. Will, and P. Liu, "An efficient and low-cost TiO₂ compact layer for performance improvement of dye-sensitized solar cells," *Electrochimica Acta*, vol. 54, no. 4, pp. 1319–1324, 2009.
- [21] Y. L. Lee, C. L. Chen, L. W. Chong, C. H. Chen, Y. F. Liu, and C. F. Chi, "A platinum counter electrode with high electrochemical activity and high transparency for dye-sensitized solar cells," *Electrochemistry Communications*, vol. 12, no. 11, pp. 1662–1665, 2010.
- [22] H. P. Singh and S. S. Sekhon, "Conductivity behaviour of proton conducting polymer gel electrolytes with PVdF-HFP," *European Polymer Journal*, vol. 39, no. 1, pp. 93–98, 2003.
- [23] M. F. Z. Kadir, S. R. Majid, and A. K. Arof, "Plasticized chitosan-PVA blend polymer electrolyte based proton battery," *Electrochimica Acta*, vol. 55, no. 4, pp. 1475–1482, 2010.
- [24] M. H. Buraidah, L. P. Teo, S. R. Majid, and A. K. Arof, "Ionic conductivity by correlated barrier hopping in NH₄I doped chitosan solid electrolyte," *Physica B*, vol. 404, no. 8–11, pp. 1373–1379, 2009.
- [25] S. Rajendran, M. Sivakumar, R. Subadevi, and M. Nirmala, "Characterization of PVA-PVdF based solid polymer blend electrolytes," *Physica B*, vol. 348, no. 1–4, pp. 73–78, 2004.
- [26] V. C. Nogueira, C. Longo, A. F. Nogueira, M. A. Soto-Oviedo, and M. A. D. Paoli, "Solid-state dye-sensitized solar cell: improved performance and stability using a plasticized polymer electrolyte," *Journal of Photochemistry and Photobiology A*, vol. 181, no. 2-3, pp. 226–232, 2006.
- [27] H. Chang and Y. J. Lo, "Pomegranate leaves and mulberry fruit as natural sensitizers for dye-sensitized solar cells," *Solar Energy*, vol. 84, no. 10, pp. 1833–1837, 2010.

Research Article

A Convenient Method for Manufacturing TiO₂ Electrodes on Titanium Substrates

Wei Qin,¹ Songtao Lu,² Xiaohong Wu,² and Song Wang²

¹ School of Materials Science and Engineering, Harbin Institute of Technology, Harbin 150001, China

² Department of Chemistry, Harbin Institute of Technology, Harbin 150001, China

Correspondence should be addressed to Wei Qin, qinwei@hit.edu.cn

Received 11 June 2011; Revised 15 September 2011; Accepted 15 September 2011

Academic Editor: Leonardo Palmisano

Copyright © 2011 Wei Qin et al. This is an open access article distributed under the Creative Commons Attribution License, which permits unrestricted use, distribution, and reproduction in any medium, provided the original work is properly cited.

Thin titanium dioxide films were successfully prepared on titanium plates in ammonium sulfate solution with the micro-plasma oxidation method. The thin TiO₂ films were sensitized with a *cis*-RuL₂(SCN)₂·2H₂O (L = *cis*-2, 2'-bipyridine-4, 4'-dicarboxylic acid) ruthenium complex, and implemented into a dye sensitized solar cell configuration. The influence of current density on the surface structure and photoelectric performance of the TiO₂ films was investigated. The results show that the thin TiO₂ films are porous, and the dye-sensitized solar cell based on the film prepared at 14 A/dm² has exhibited higher overall light-to-electricity conversion efficiencies of 0.095% under the illumination at 40 mW/cm².

1. Introduction

The dye-sensitized solar cell (DSSC) has attracted much attention as the next generation solar cell during the last decade [1, 2]. Remarkably, high enough efficiency and low cost of manufacturing are important characteristics to make the DSSC as a substitute of the conventional silicon and thin film photovoltaic devices. Various methods of preparing dye-sensitized solar cells have therefore been developed [3–5]. At present, the TiO₂ photoelectrode of DSSC is usually prepared by depositing a suspension or paste-containing TiO₂ nanoparticles with organic additives onto conductive glass substrates or polymer substrate [6, 7]. The deposited film is then subject to a posttreatment with the purpose of forming a continuous nanoparticle network with sufficient adherence and electrical contact to the substrate and between the nanoparticles. Although the conventional preparation method of using conductive glass substrate can achieve good interconnection between particles, a batch process must include heat treatments, which is not fast enough to produce the necessary devices. In addition, the use of glass substrates with fragility limits the manufacture process and the practical application of DSSCs. The use of plastic substrates is another choice of the TiO₂ suspension [8, 9]. However, these methods present a weak adherence of the films to the substrates, and obtain very thin films.

In this paper we, therefore, looked into the possibility of developing microplasma oxidation (MPO) method to prepare TiO₂ thin films on the thin light titanium substrates. This method is based on the anodic oxidation, which occurs at potentials above the breakdown voltage of the oxide film growing on the anode surface, such as Al, Mg, Ti, Nb, and Zr. As the process combines electrochemical oxidation with a high voltage spark treatment in an electrolyte bath, metal oxides are synthesized inside high voltage breakthrough channels across the former oxide layer. So the prepared thin oxide films have good adherence with substrate metal and can endure strong impact [10, 11]. In addition, the process of preparing thin films by MPO need very short time. In this paper, MPO in the ammonium sulfate solution with different current densities was used to prepare TiO₂ films on the surface of Ti substrate. The objective of this research was to investigate the structure and surface morphology of the films and measure their photoelectricity performance as photo anode of the DSSC.

2. Experimental

2.1. Preparation of Films. Plate samples of a titanium sheet (99.9% in purity) with a reaction dimension of 2 mm² were washed in 40% HF and 65% HNO₃ (1 : 1 in volume) aqueous solution. A home made-electrical source with the power at

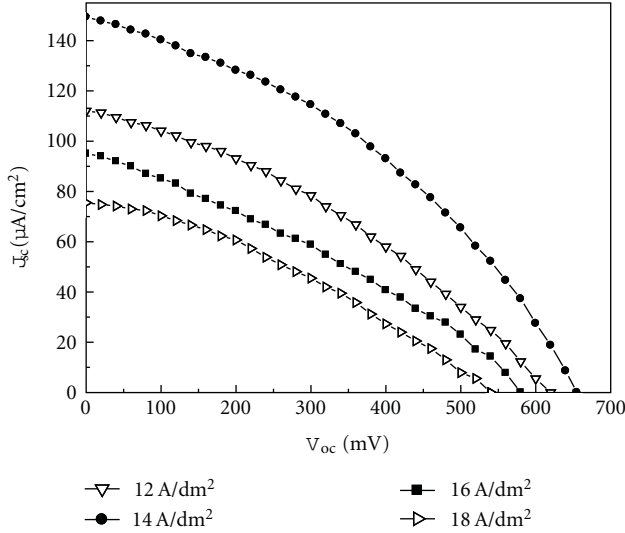


FIGURE 1: Results from I - V characteristics of TiO_2 electrodes prepared at different current density.

5 kW was used for microplasma oxidation of the samples in a water-cooled electrolyte, and a copper sheet serves as the counterelectrode. The reaction temperature was controlled to below 30°C by adjusting the cooling water flow. The electrolyte used in the experiment is ammonium sulfate solution (0.5 mol/L). The set-up scheme is shown in the past report [12]. The whole MPO process was carried out under different current densities (12, 14, 16, and 18 A/dm^2) for 10 min. After the treatment, the coated samples were flushed with water and dried in air. Then, these dried TiO_2 films were sensitized by $\text{cis-RuL}_2(\text{SCN})_2 \cdot 2\text{H}_2\text{O}$ in the anhydrous ethanol (3 mmol/L) at 40°C for 12 h.

2.2. Characterization of Films. The photoelectrochemical experiments were performed in two sandwich-type electrode cells. The dye-coated TiO_2 film was used as working electrode, and transparent conducting glass ($<20/\Omega$) as counter electrodes. A drop of electrolyte was then placed between the electrodes, and allowed to wet the surfaces of the electrodes by capillary action. The electrolyte was a solution of 0.5 M potassium iodide and 0.05 M iodine in a mixture of Ca. 80% acetonitrile and 20% glycol. For the photocurrent-photo-voltage measurements, the dye-sensitized TiO_2 films were illuminated through the conductive glass using a 500-W high pressure Xe lamp with a water IR filter, and a 420 nm long pass UV filter served as a light source as the simulating sunlight.

The surface morphology of the films was observed on an S-570 scanning electron microscope (SEM) from Hitachi. The X-ray diffraction (XRD) with a Cu K α source (D/max-r B from Ricoh) was applied to study the crystalline structure of the films with an accelerating voltage and an applied current of 40 kV and 30 mA, respectively. Surface roughness of the TiO_2 films were examined with a digital Instruments Nano-scope III atomic force microscope. The thickness of the films are measured by CTG-10.

TABLE 1: Results from I - V characteristics of TiO_2 electrodes prepared at different current density.

Type (A/dm^2)	V_{oc} (mV)	J_{sc} ($\mu\text{A}/\text{cm}^2$)	FF	(%)
12	619	112	0.35	0.061
14	652	149	0.39	0.095
16	581	95	0.32	0.044
18	542	76	0.33	0.034

3. Results and Discussion

3.1. Photoelectricity Properties of the Films. The distinct structure of TiO_2 films lead to dissimilar photoelectricity properties. A I - V curves between the TiO_2 films prepared with different current density are given in Figure 1. Table 1 shows the averaged data extracted from I - V curve measurement on dye-sensitized nanostructured TiO_2 electrode.

As is shown in Figure 1 and Table 1, the overall efficiency (η), open circuit voltage (V_{oc}), and short circuit current (J_{sc}) of the dye-sensitized solar cells firstly increase and then decrease with current density of MPO. The V_{oc} increases from 619 to 652 mV, while the J_{sc} increases from 112 to 149 $\mu\text{A}/\text{cm}^2$ when the current density increase from 12 A/dm^2 to 14 A/dm^2 . The J_{sc} and the V_{oc} reach maximum at 14 A/dm^2 and then decrease at the 16 and 18 A/dm^2 . The highest conversion efficiency of 0.095% has been achieved for the cell, employing the film prepared at 14 A/dm^2 .

3.2. Morphology of the Films. The TiO_2 films prepared at different current densities have different surface images (see Figure 2). It can be seen that the surface of prepared films are mesoporous and the microporous size increase with the current density. The mean roughness values of the TiO_2 films prepared at 12, 14, 16, and 18 A/dm^2 are 110.25, 138.65, 131.36, and 128.49 nm, respectively. When the current density is 14 A/dm^2 , the TiO_2 film obtains the largest roughness and then decreases with the increasing of the current density. The rough surface is propitious to absorb the sensitizer. The thickness of the films prepared at 12, 14, 16, and 18 A/dm^2 are 3.7 μm , 5.6 μm , 7.9 μm , 12.5 μm , respectively.

3.3. Structural Analysis of the Films. Figure 3 shows crystalline structures of the TiO_2 films. It can be noticed that the films consist of much rutile phase and less Ti substrates when current density is below 14 A/dm^2 . The content of rutile TiO_2 reaches almost 100% at the current density of 16 and 18 A/dm^2 . And the disappearance of Ti substrate peak could result from the increase of film thickness.

From I - V curve and SEM photographs, it can be seen that TiO_2 crystallite and pores are formed on the surface of the Ti substrate, and this kind of films have photoelectricity properties. From SEM photographs, the surface grain size and the density of the pores reach the maximum at 14 A/dm^2 . These changes could improve the photoelectricity properties of the films because more mesopores can absorb more OH^- to absorb the $\text{cis-RuL}_2(\text{SCN})_2 \cdot 2\text{H}_2\text{O}$, which can increase the utilization ratio of visible light. So, the overall efficiency, short circuit current and open circuit voltage of the TiO_2 film

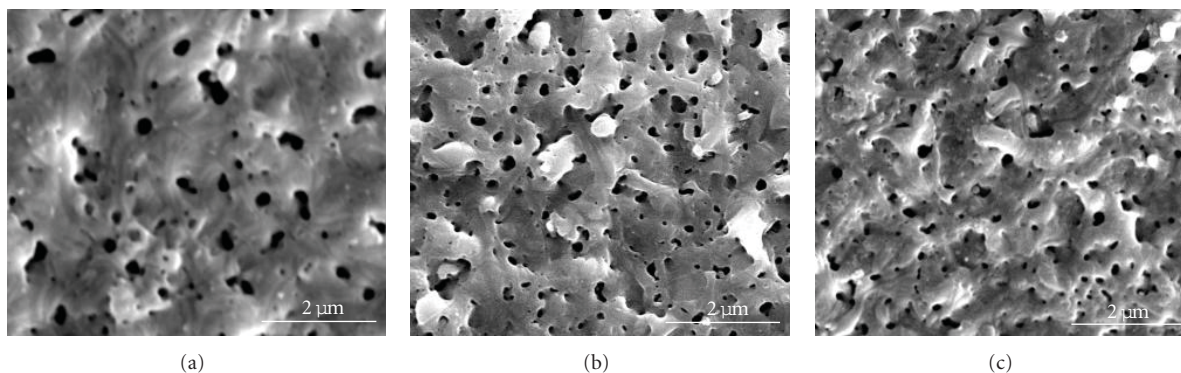


FIGURE 2: SEM images under different current densities: (a) 12 A/dm², (b) 14 A/dm², and (c) 16 A/dm².

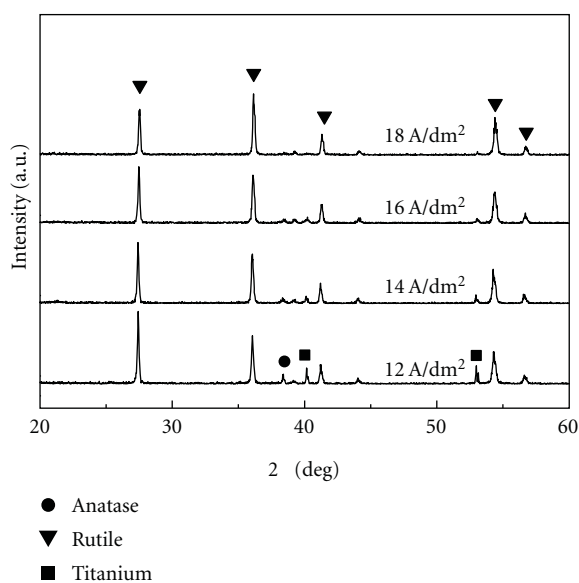


FIGURE 3: XRD of films prepared under different current densities.

prepared at 14 A/dm² are higher than that of the films prepared at 12 A/dm². When the current density of MPO is up to 16 A/dm², the efficiency of the fabricated cell decline. The reason is that the reaction temperature increases simultaneity with the increasing of the current density, and many bigger blocks TiO₂ are formed around the pores (see Figure 2). The sample showed inferior performance owing to the decreased surface area, the reduction in the pore size, which is related to the amount of dye adsorption.

4. Conclusion

In conclusion, uniform and porous thin TiO₂ films have been successfully prepared with the microplasma oxidation method in the (NH₄)₂SO₄ electrolyte solution. This method can prepare TiO₂ electrode conveniently. A higher photoelectric performance of TiO₂ electrode is obtained when the electrode is prepared by MPO under the current density of 14 A/dm². The dye-sensitized solar cell using this TiO₂ photoanode exhibited the overall conversion efficiency of 0.095% (AM-1.5, 40 mW/cm²).

Acknowledgments

The authors thank the National Natural Science Foundation of China (nos. 51173033, 51078101) the Program for New Century Excellent Talents in University (NCET-09-0064) and Heilongjiang Natural Science Foundation (no. B2007-04) for the financial support for this work.

References

- [1] B. O'Regan and M. Grätzel, "A low-cost, high-efficiency solar cell based on dye-sensitized colloidal TiO₂ films," *Nature*, vol. 353, no. 6346, pp. 737–740, 1991.
- [2] G. K. Mor, K. Shankar, M. Paulose, O. K. Varghese, and C. A. Grimes, "Use of highly-ordered TiO₂ nanotube arrays in dye-sensitized solar cells," *Nano Letters*, vol. 6, no. 2, pp. 215–218, 2006.
- [3] M. N. Liu, H. X. Wang, C. Yan, G. Will, and J. Bell, "One-step synthesis of titanium oxide with trilayer structure for dye-sensitized solar cells," *Applied Physics Letters*, vol. 98, article 133113, 2011.
- [4] S. Zhang, C. Ji, Z. Bian et al., "Single-wire dye-sensitized solar cells wrapped by carbon nanotube film electrodes," *Nano Letters*, vol. 11, no. 8, pp. 3383–3387, 2011.
- [5] J. R. Jennings, A. Ghicov, L. M. Peter, P. Schmuki, and A. B. Walker, "Dye-sensitized solar cells based on oriented TiO₂ nanotube arrays: transport, trapping, and transfer of electrons," *Journal of the American Chemical Society*, vol. 130, no. 40, pp. 13364–13372, 2008.
- [6] M. Koelsch, S. Cassaignon, C. Ta Thanh Minh, J. F. Guillemoles, and J. P. Jolivet, "Electrochemical comparative study of titania (anatase, brookite and rutile) nanoparticles synthesized in aqueous medium," *Thin Solid Films*, vol. 451-452, pp. 86–92, 2004.
- [7] G. Sauve, M. E. Cass, G. Coia et al., "High quantum yield sensitization of nanocrystalline titanium dioxide photoelectrodes with cis-dicyanobis(4,4'-dicarboxy-2,2'-bipyridine) osmium(II) or Tris(4,4'-dicarboxy-2,2'-bipyridine) osmium(II) complexes," *Journal of Physical Chemistry B*, vol. 104, no. 15, pp. 3488–3491, 2000.
- [8] C. Longo, J. Freitas, and M. D. Paoli, "Performance and stability of TiO₂/dye solar cells assembled with flexible electrodes and a polymer electrolyte," *Journal of Photochemistry and Photobiology A*, vol. 159, pp. 33–39, 2003.

- [9] H. Lindström, A. Holmberg, E. Magnusson, S. E. Lindquist, L. Malmqvist, and A. Hagfeldt, "A new method for manufacturing nanostructured electrodes on plastic substrates," *Nano Letters*, vol. 1, no. 2, pp. 97–100, 2001.
- [10] S. Ikonopisov, "Theory of electrical breakdown during formation of barrier anodic films," *Electrochimica Acta*, vol. 22, no. 10, pp. 1077–1082, 1977.
- [11] M. R. Bayati, F. Golestani-Fard, and A. Z. Moshfegh, "The effect of growth parameters on photo-catalytic performance of the MAO-synthesized TiO₂ nano-porous layers," *Materials Chemistry and Physics*, vol. 120, no. 2-3, pp. 582–589, 2010.
- [12] X. H. Wu, X. B. Ding, W. Qin, W. D. He, and Z. H. Jiang, "Enhanced photo-catalytic activity of TiO₂ films with doped La prepared by micro-plasma oxidation method," *Journal of Hazardous Materials*, vol. 137, no. 1, pp. 192–197, 2006.

Research Article

Optimization of Recombination Layer in the Tunnel Junction of Amorphous Silicon Thin-Film Tandem Solar Cells

Yang-Shin Lin,¹ Shui-Yang Lien,² Chao-Chun Wang,¹ Chia-Hsun Hsu,³ Chih-Hsiang Yang,² Asheesh Nautiyal,⁴ Dong-Sing Wu,¹ Pi-Chuen Tsai,⁵ and Shuo-Jen Lee⁴

¹ Department of Materials Science and Engineering, National Chung Hsing University, Taichung 402, Taiwan

² Department of Materials Science and Engineering, MingDao University, ChungHua 52345, Taiwan

³ Graduate Institute of Precision Engineering, National Chung Hsing University, Taichung 402, Taiwan

⁴ Department of Mechanical Engineering, Yuan Ze University, 135 Yuan-Tung Road, Chungli, 320 Taoyuan, Taiwan

⁵ Graduate Institute of Materials Science and Green Energy Engineering, National Formosa University, Huwei, Yunlin 632, Taiwan

Correspondence should be addressed to Shui-Yang Lien, syl@mdu.edu.tw

Received 1 June 2011; Accepted 10 September 2011

Academic Editor: Vincenzo Augugliaro

Copyright © 2011 Yang-Shin Lin et al. This is an open access article distributed under the Creative Commons Attribution License, which permits unrestricted use, distribution, and reproduction in any medium, provided the original work is properly cited.

The amorphous silicon/amorphous silicon (a-Si/a-Si) tandem solar cells have attracted much attention in recent years, due to the high efficiency and low manufacturing cost compared to the single-junction a-Si solar cells. In this paper, the tandem cells are fabricated by high-frequency plasma-enhanced chemical vapor deposition (HF-PECVD) at 27.1 MHz. The effects of the recombination layer and the i-layer thickness matching on the cell performance have been investigated. The results show that the tandem cell with a p⁺ recombination layer and i₂/i₁ thickness ratio of 6 exhibits a maximum efficiency of 9.0% with the open-circuit voltage (V_{oc}) of 1.59 V, short-circuit current density (J_{sc}) of 7.96 mA/cm², and a fill factor (FF) of 0.70. After light-soaking test, our a-Si/a-Si tandem cell with p⁺ recombination layer shows the excellent stability and the stabilized efficiency of 8.7%.

1. Introduction

Amorphous silicon (a-Si)/a-Si tandem solar cells have attracted extensive interest among solar cell because of the less light-induced degradation [1, 2] (Stabler-Wronski effect) compared to their single-junction solar cell counterparts. The n-p junction between the two subcells is often referred to as a tunnel junction but actually functions as a recombination junction in electrically connecting the two p-i-n junctions of the tandem structure. For high stabilized efficiency tandem cell applications, a good n/p junction must have very high recombination rates, negligible optical absorption, and an ohmic characteristic with a low series resistance in order to improve the carrier transport [3–6]. Various recombination layers, such as a-SiC:H [7], metal oxides [8], microcrystalline n⁺ layer [9], and n⁺/p⁺ recombination layer [10] have been introduced between the n and p layers to promote carrier recombination.

The thickness of intrinsic- (i-) layer of individual subcell is another key parameter because of the current matching limitation imposed by series connection. In addition, reducing

the i-layer thickness of top cell as possible as it is important to stabilize against light degradation [11, 12].

In this paper, we use a p⁺ recombination layer as the recombination layer inserted in a tandem solar cell to investigate the effect on the cell performance. Furthermore, the tandem cells with different i-layer thickness matching ratio are also fabricated and their photovoltaic characteristics are also discussed.

2. Experimental

In this study, we prepared double-junction (a-Si/a-Si) solar cells by high-frequency (27.1 MHz) plasma-enhanced chemical vapor deposition (HF-PECVD). The HF-PECVD reaction chamber is equipped with a load-lock for the transport and placement of the substrate into the chamber including a substrate holder, and a system with temperature control. The size of chamber was 20 × 20 cm², and the electrode distance ranged from 7 mm to 40 mm. We fabricated tandem cells without recombination layer (p₁-b₁-i₁-n₁-p₂-b₂-i₂-n₂),

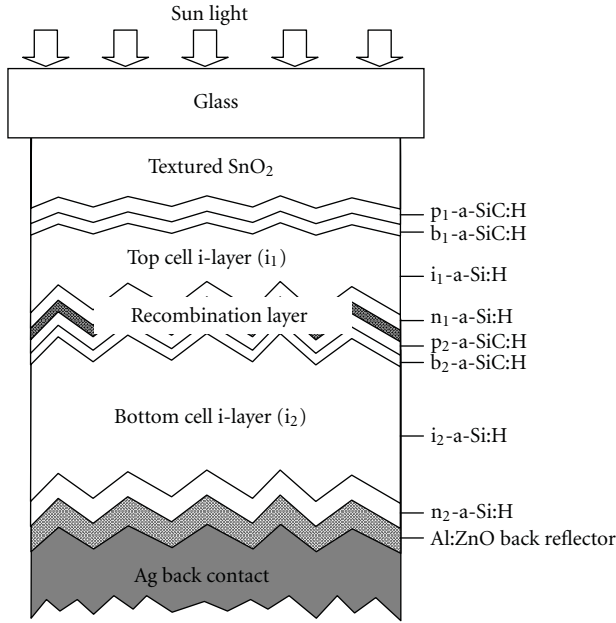
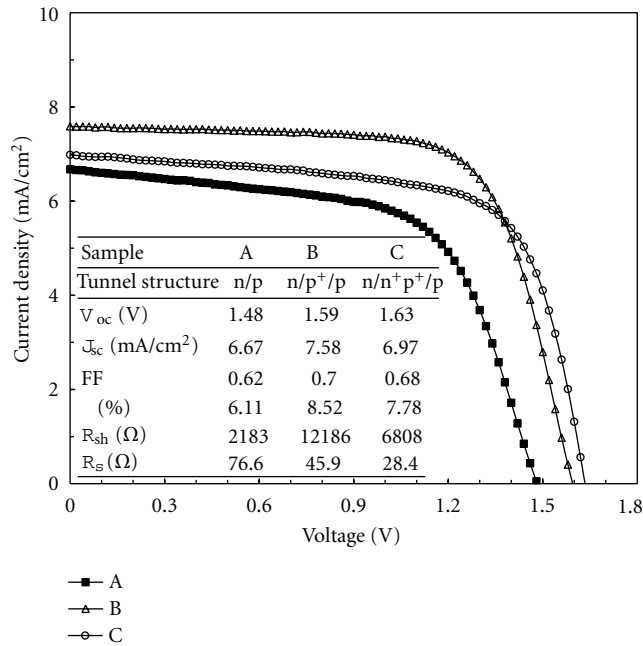
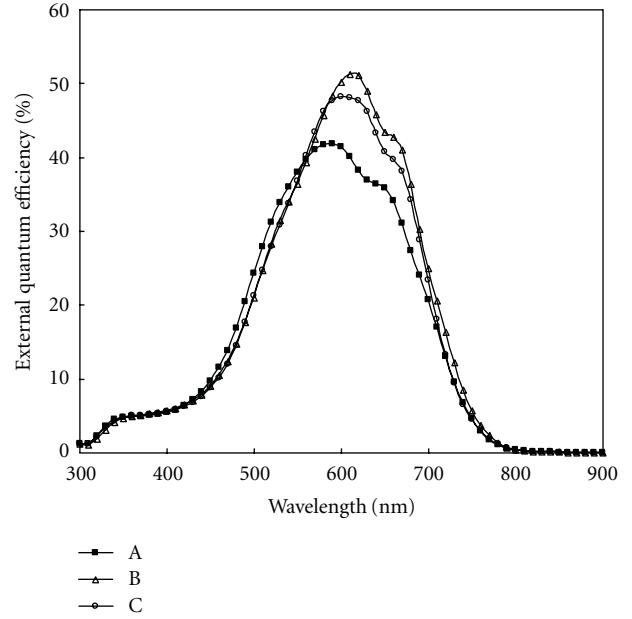
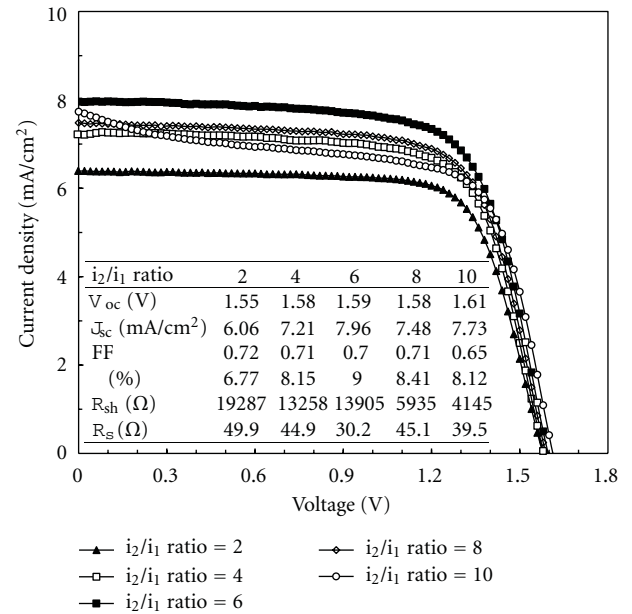


FIGURE 1: Schematic structure of an a-Si/a-Si tandem solar cell.

FIGURE 2: I - V characteristics of sample A, B, and C. Sample A is with the standard n/p junction; sample B has the p⁺ recombination layer; sample C has the n⁺/p⁺ double recombination layer.

with p⁺ recombination layer and with n⁺/p⁺ double recombination layers inserted between two subcells, which were designated as sample A, sample B, and sample C, respectively. The schematic structure is shown in Figure 1. The substrate used in this paper was SnO₂-coated glass (Asahi U-type). The substrate temperature was fixed at 200°C. The detailed process conditions are summarized in Table 1. An a-SiC:H buffer layer is necessary for making the energy band gap between

FIGURE 3: Measured QE of solar cells of sample A, B, and C. Sample A is with the standard n/p junction; samples B has the p⁺ recombination layer; sample C has the n⁺/p⁺ double recombination layer.FIGURE 4: I - V characteristics of a-Si/a-Si tandem solar cells with different i_2/i_1 ratio.

p-a-SiC:H layer and i-a-Si:H layer much smoother and reducing the recombination at the p/i interface to enhance the open-circuit voltage. To optimize the current matching, we set five thickness ratios of i-layer in the bottom cell to i-layer in the top cell of 2, 4, 6, 8, and 10 individually. The I - V characteristics of the device were measured under an AM1.5G solar simulator. Quantum efficiency (QE) was

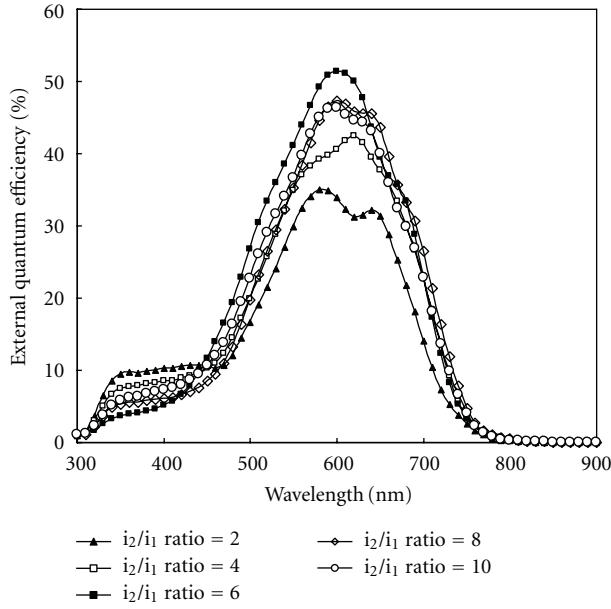


FIGURE 5: Measured QE of solar cells with different i_2/i_1 ratio.

TABLE 1: The deposition conditions of intrinsic layer of the tandem solar cell.

Parameter	Value
Power (W)	10
Pressure (Pa)	90
E/S distance (mm)	30
Substrate temperature ($^{\circ}$ C)	200
SiH ₄ flow rate (sccm)	40
H ₂ flow rate (sccm)	160
i_2/i_1 thickness ratio	2–10

measured for a wavelength range of 300 to 900 nm. Cross-section micrographs of the solar cell were obtained by transmission electron microscopy (TEM). The light soaking test was performed at the open circuit condition under one-sun light intensity using a metal halide lamp at 50 $^{\circ}$ C for 500 h.

3. Results and Discussion

Figure 2 shows the I - V characteristics of sample A, sample B, and sample C. It can be seen that the open-circuit voltage (V_{oc}) increases in the case of adding either p^+ recombination layer or n^+/p^+ double recombination layers. For the short-circuit current density (J_{sc}), the sample A, which is without recombination layer, does have a rectifying property, resulting in a reduction in J_{sc} [10]. The sample B shows the highest J_{sc} due to it not only has the smallest series resistance (R_s) offering a good ohmicity of the tunneling junction, but also the largest shunt resistance (R_{sh}). For the sample C, the n^+/p^+ double layer causes a buildup of trapped holes on the p^+ side and electrons on the n^+ side, and hence yields a lower J_{sc} compared to the sample B. From our result, the best cell

conversion efficiency of 8.52% occurs when the p^+ recombination layer is used.

The variation in the previous J_{sc} result is also reflected in the QE measurements, shown in Figure 3. The QE curves of these samples remain the same in the short-wavelength region but evidently vary in the long wavelength region, implying that the adding recombination layer could mainly improve the absorption at long wavelength.

Figure 4 shows the experimental I - V characteristics of the double-junction solar cells subject to different i_2/i_1 thickness ratio. It can be seen that the V_{oc} almost maintains a stable value of 1.59 V, approximately equaling to the sum of the V_{oc} of the two subcells, showing a good series connection. The J_{sc} increases from 6.06 to 7.96 mA/cm² with increasing the i_2/i_1 thickness ratio from 2 to 6, and then it drops to a lower value with further increasing the ratio. This result can be explained by the QE result, as shown in Figure 5. The tandem cell with an i_2/i_1 thickness ratio of 6 presents the highest QE response, showing the optimum current matching. By using the optimum i_2/i_1 thickness ratio, a conversion efficiency of 9% is obtained.

Figure 6(a) shows TEM cross-sectional images of the tandem cell with the p^+ recombination layer. The AZO back reflectors layer of 80 nm and Ag layer of 300 nm on the a-Si: H solar cell can be observed demonstrates the whole cross-section morphology. The photograph depicting the interface between p-layers and SnO₂ (TCO) of Asahi (U-type) substrate deposited the high-resolution TEM (HR-TEM) is shown in Figure 6(b), and Figure 6(c) demonstrates the TRJ ($n/p^+/p$) and recombination layer (p^+ -layer) between top and bottom cells. In general, a better interface treatment and uniform films are important factors for double-junction solar cells. It seems that each layer and interface of cells as shown Figure 6 is deposited densely and uniformly. Therefore carriers are able to travel longer path thus good for the conversion efficiency.

Figure 7 demonstrates the maximum output power of the a-Si/a-Si tandem solar cells with the p^+ recombination layer and the thickness ratio of 6 as a function of the exposure time. The relative power is also shown for the convenience of observing the degradation. Only very little decrease in power (less than 5% degradation) is observed, showing that the a-Si/a-Si tandem solar cell is more stable than a traditional single junction a-Si cell. This result can be attributed to a thinner i-layer (50 nm) of the top sub-cell compared to that 300 nm thickness i-layer of the single-junction solar cell, might leading to a reduction in escape of hydrogen atoms from Si matrix.

4. Conclusions

In this paper, the effects of the recombination layer and the i-layer thickness matching on the cell performance have been investigated. The results show that inserting the recombination layer can increase the V_{oc} and J_{sc} . Furthermore, the i-layer thickness ratio strongly affects the J_{sc} , and the i-layer of bottom sub-cell thicker than that of top sub-cell by a factor

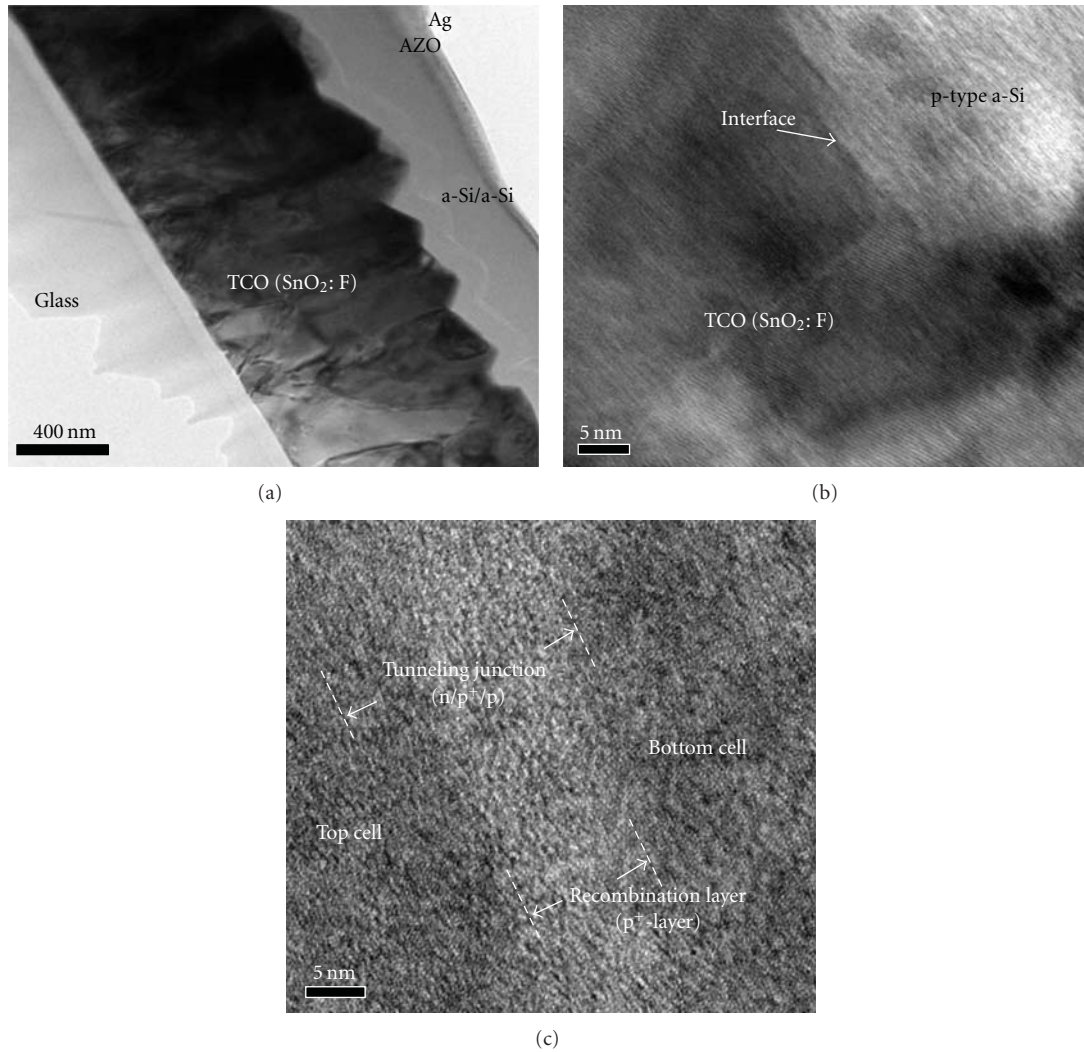


FIGURE 6: Cross-sectional transmission electron micrographs of (a) a-Si/a-Si tandem cell, (b) TCO/p interface, (c) n/δ(p⁺)/p junction.

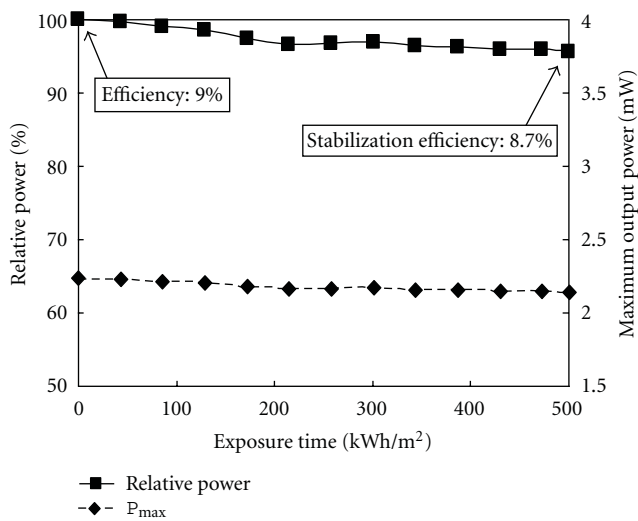


FIGURE 7: The maximum output power and relative power of the a-Si/a-Si tandem solar cells with the p⁺ recombination and the thickness ratio of 6 as a function of the exposure time.

of 6 is found to be the optimum thickness matching. Finally, an initial efficiency of 9.0% and the stabilized efficiency of 8.7% are obtained, showing the good stability compared to a typical single-junction a-Si:H solar cell.

Acknowledgments

This work is sponsored by Chung-Shan Institute of Science and Technology and the National Science Council of the Republic of China under Contracts nos. 99-2221-E-451-013, 99-2622-E-451-005-CC3, 99-2622-E-451-007-CC2, 99-2221-E-451-011 and 100-3113-E-451-001-CC2.

References

- [1] R. E. I. Schropp, M. B. V. Linden, J. D. Ouwens, and H. D. Gooijer, "Apparent "gettering" of the Staebler-Wronski effect in amorphous silicon solar cells," *Solar Energy Materials and Solar Cells*, vol. 34, no. 1–4, pp. 455–463, 1994.

- [2] V. Nádaždy, R. Durný, I. Thurzo, and E. Pinčík, "New experimental facts on the Staebler-Wronski effect," *Journal of Non-Crystalline Solids*, vol. 227–230, no. 1, pp. 316–319, 1998.
- [3] H. Jingya, X. Jianping, and K. Frank, "Non-local recombination in "tunnel junction" of multijunction amorphous si alloy solar cells," *Materials Research Society Symposium Proceedings*, vol. 336, pp. 717–722, 1994.
- [4] A. Kołodziej, C. R. Wronski, P. Krewniak, and S. Nowak, "Silicon thin film multijunction solar cells," *Opto-Electronics Review*, vol. 8, no. 4, pp. 339–345, 2000.
- [5] D. S. Shen, R. E. I. Schropp, H. Chatham, R. E. Hollingsworth, P. K. Bhat, and J. Xi, "Improving tunneling junction in amorphous silicon tandem solar cells," *Applied Physics Letters*, vol. 56, no. 19, pp. 1871–1873, 1990.
- [6] S. S. Hegedus, F. Kampas, and J. Xi, "Current transport in amorphous silicon np junctions and their application as "tunnel" junctions in tandem solar cells," *Applied Physics Letters*, vol. 67, no. 6, pp. 813–815, 1995.
- [7] J. Y. Hou, J. K. Arch, S. J. Fonash, S. Wiedeman, and M. Bennett, "An examination of the "tunnel junctions" in triple junction a-Si:H based solar cells: modeling and effects on performance," in *Proceedings of the Photovoltaic Specialists Conference*, pp. 1260–1264, October 1991.
- [8] J. K. Rath, F. A. Rubinelli, and R. E. I. Schropp, "Effect of oxide treatment at the microcrystalline tunnel junction of a-Si:H/a-Si:H tandem cells," *Journal of Non-Crystalline Solids*, vol. 266–269, pp. 1129–1133, 2000.
- [9] D. S. Shen, R. E. I. Schropp, H. Chatham, R. E. Hollingsworth, J. Xi, and P. K. Bhat, "High efficiency a-Si/a-Si tandem solar cells," in *Proceedings of the Photovoltaic Specialists Conference*, pp. 1471–1474, Bhat, May 1990.
- [10] N. Palit, A. Dasgupta, S. Ray, and P. Chatterjee, "Hole diffusion at recombination junction of thin film tandem solar cells and its effect on the illuminated current-voltage characteristic," *Journal of Applied Physics*, vol. 88, no. 5, pp. 2853–2861, 2000.
- [11] M. Zeman, J. A. Willems, L. L. A. Vosteen, G. Tao, and J. W. Metselaar, "Computer modelling of current matching in a-Si : H/a-Si : H tandem solar cells on textured TCO substrates," *Solar Energy Materials and Solar Cells*, vol. 46, no. 2, pp. 81–99, 1997.
- [12] A. Fantoni, M. Viera, and R. Martins, "Influence of the intrinsic layer characteristics on a-Si:H p-i-n solar cell performance analysed by means of a computer simulation," *Solar Energy Materials and Solar Cells*, vol. 73, no. 2, pp. 151–162, 2002.

Research Article

Three-Terminal Amorphous Silicon Solar Cells

Cheng-Hung Tai,¹ Chu-Hsuan Lin,¹ Chih-Ming Wang,¹ and Chun-Chieh Lin²

¹Institute of Opto-Electronic Engineering, National Dong Hwa University, Shoufeng, Hualien 97401, Taiwan

²Department of Electrical Engineering, National Dong Hwa University, Shoufeng, Hualien 97401, Taiwan

Correspondence should be addressed to Chu-Hsuan Lin, chlin0109@mail.ndhu.edu.tw

Received 15 June 2011; Accepted 5 September 2011

Academic Editor: Vincenzo Augugliaro

Copyright © 2011 Cheng-Hung Tai et al. This is an open access article distributed under the Creative Commons Attribution License, which permits unrestricted use, distribution, and reproduction in any medium, provided the original work is properly cited.

Many defects exist within amorphous silicon since it is not crystalline. This provides recombination centers, thus reducing the efficiency of a typical a-Si solar cell. A new structure is presented in this paper: a three-terminal a-Si solar cell. The new back-to-back p-i-n/n-i-p structure increased the average electric field in a solar cell. A typical a-Si p-i-n solar cell was also simulated for comparison using the same thickness and material parameters. The 0.28 μm -thick three-terminal a-Si solar cell achieved an efficiency of 11.4%, while the efficiency of a typical a-Si p-i-n solar cell was 9.0%. Furthermore, an efficiency of 11.7% was achieved by thickness optimization of the three-terminal solar cell.

1. Introduction

Amorphous silicon (a-Si) for photovoltaic applications can be deposited using the techniques of plasma-enhanced chemical vapor deposition (PECVD) [1–3], catalytic CVD (Cat-CVD) [4, 5], photo-CVD [6, 7], sputtering [8], and so forth. Since it is usually deposited at a low temperature, low-cost or flexible materials like glass, plastic, or stainless steel can be adopted as the substrate. Amorphous Si also has the advantages of an abundant supply on the earth and a high-absorption coefficient at visible wavelengths [9, 10]. These advantages make it promising for applications in thin-film photovoltaics. Amorphous Si can be applied to many types of solar cells, such as single-junction [11, 12], multijunction [13, 14], and HIT [15] (heterojunction with intrinsic thin layer) solar cells. In 2000, the stable efficiency of a single-junction a-Si solar cell (area of 1 cm^2) was 9.0% [16]. In 2009, a single-junction a-Si solar cell has achieved an efficiency of 10.1% [17]. Multijunction solar cells were usually able to achieve higher efficiencies. For example, the stable efficiency of a triple-junction solar cell (a-Si/a-Si/a-SiGe tandem solar cell) was 12.1% [18], and the efficiencies of micromorph Si solar cells (a-Si/ μc -Si tandem solar cells) were larger than 11% [19–21]. Multijunction solar cells are composed of two or more subcells. The working mechanism of multijunction solar cells is by way of tunnel-recombination junctions, and

the final efficiency is limited by the smallest photogenerated current among all subcells [22]. This is because each subcell of a multijunction solar cell must pass through the same current. Therefore, the defects inside the a-Si may reduce the efficiencies of solar cells whether for a single-junction cell or a multijunction cell. The efficiencies are reduced due to the recombination of photogenerated carriers via defects [23, 24]. In addition, carrier mobility in a-Si is quite low. Hence, the efficiencies of typical a-Si-based solar cells are limited.

We have designed and simulated a new structure of a three-terminal a-Si p-i-n/n-i-p solar cell. The new structure enhances the electric field in a-Si solar cells and reduces the recombination rate of photogenerated carriers in order to increase the efficiency. The three-terminal device structure also avoids the effect of current mismatch between subcells [25]. In this paper, we compare the two-terminal a-Si p-i-n solar cell (control cell) and the new three-terminal a-Si p-i-n/n-i-p solar cell with the same thickness and material parameters.

2. Device Structure

Figure 1 shows the device structures and doping concentrations of the single-junction a-Si p-i-n solar cell (labeled as control) and the three-terminal a-Si p-i-n/n-i-p solar cell

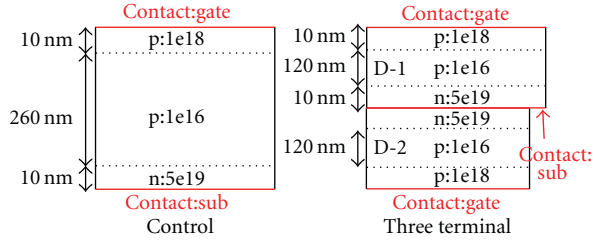


FIGURE 1: The structures of the two-terminal a-Si solar cell (labeled as control) and the three-terminal a-Si solar cell (labeled as three terminal). The thicknesses of the control cell and the three-terminal cell were both $0.28 \mu\text{m}$.

(labeled as three terminal). The simulation was carried out with the commercial simulation tool, ISE TCAD. The device structure and performance of the control cell were based on those in [16]. Sunlight irradiated the cells from the top of the device. In our simulation, all of the p-layers and n-layers had a thickness of $0.01 \mu\text{m}$, and both the control cell and the three-terminal cell were $0.28 \mu\text{m}$.

In order to contact “contact:sub” in the three-terminal solar cell, we should set the width of the subcell D-2 (see the definition in Figure 1) to be smaller than the width of the subcell D-1. Then, “contact:sub” could connect to the outer circuit. For a large area solar cell, the ratio of the contact region of “contact:sub” to the total area would be very small, and the influence due to the width decrease of the subcell D-2 could be neglected. On the other hand, the top “contact:gate” and bottom “contact:gate” of the three-terminal cell were joined and acted as the other terminal to the outer circuit.

For the control cell, most of the depletion region was in the intrinsic layer (i-layer). The photogenerated carriers were separated by an electric field of the depletion region and the electrons drifted to the “contact:sub,” while the holes drifted to the “contact:gate.” For the three-terminal cell, there are i-layers both in subcells D-1 and D-2. As with the control cell, most of the depletion region was in the i-layers. It is worth noting that the directions of the electric field in D-1 and D-2 are reversed. All of the photogenerated electrons in the three-terminal cell will drift to “contact:sub.” The photogenerated holes in D-1 will drift to the top “contact:gate,” and the photogenerated holes in D-2 will drift to the bottom “contact:gate.”

3. Results and Discussion

The key role in improving the efficiency of the three-terminal cell is the electric field in the i-layers. For a two-terminal cell, the built-in potential is distributed across the $0.28 \mu\text{m}$ -thick p-i-n structure. For a three-terminal cell, the same magnitude of the built-in potential is distributed across both the top p-i-n and bottom n-i-p structures. Hence, the average electric field of the three-terminal cell is larger than the control cell.

Figure 2 gives the I-V characteristics of the control cell and the three-terminal cell. In [16], the stable efficiency of a single-junction thin a-Si:H p-i-n solar cell was 9.0%, the

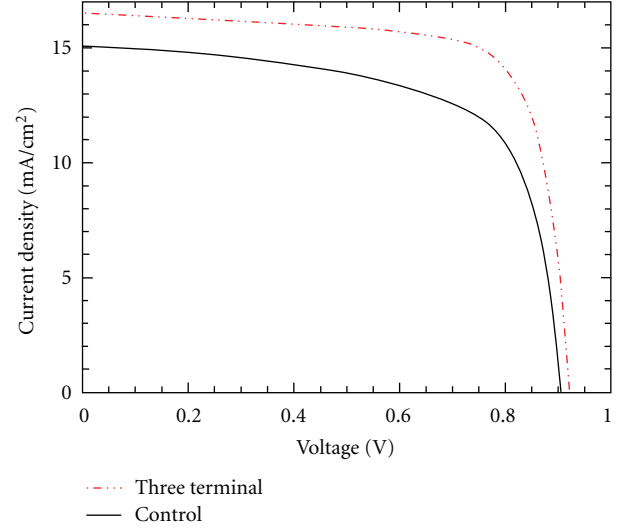


FIGURE 2: The I-V characteristics of the control cell and the three-terminal cell. The efficiency of the control cell was 9.0%, and the efficiency of three-terminal cell was 11.4%.

short-circuit current density (J_{SC}) was 15.8 mA/cm^2 , and the open-circuit voltage (V_{OC}) was 0.87 V . For the control cell in our simulation, the efficiency was 9.0%, the J_{SC} was 15.2 mA/cm^2 , and the V_{OC} was 0.91 V . It was proved that our simulation results were close to the practical conditions. For the three-terminal cell, the efficiency was 11.4%, the J_{SC} was 16.5 mA/cm^2 , and the V_{OC} was 0.92 V . The efficiency of the three-terminal a-Si solar cell was remarkably increased. A larger average electric field in the three-terminal cell could decrease the recombination of photogenerated carriers, and so that the efficiency was enhanced.

Figure 3 shows the generation rate ($1/(\text{cm}^3 \cdot \text{s})$) and recombination rate ($1/(\text{cm}^3 \cdot \text{s})$) of the control cell and the three-terminal cell. It could be observed that the control cell and the three-terminal cell had the same generation rate, but the three-terminal cell had a lower recombination rate than the control cell. The integral of the recombination rate over the depth was the amount of total bulk recombination. The integrals were $8.32 \times 10^{12} (1/(\text{cm}^2 \cdot \text{s}))$ and $23.27 \times 10^{12} (1/(\text{cm}^2 \cdot \text{s}))$ for the three-terminal cell and the control cell, respectively. The three-terminal cell had a smaller total bulk recombination, and so the efficiency of the three-terminal solar cell was higher than the control solar cell.

Figure 4 shows the band-edge diagram of the control cell and the three-terminal cell when sunlight irradiated from the left side of the band-edge diagram. With this band-edge diagram, it could be understood that, in the control cell, the photogenerated electrons would drift to the n-layer and the photogenerated holes would drift to the p-layer. In the control cell, “contact:sub” acted as the negative electrode of the solar cell, and “contact:gate” acted as the positive electrode. In the three-terminal cell, all of the photogenerated electrons would drift to the n-layer and connect to the outer circuit via “contact:sub” between the two n-layers. The photogenerated holes in the subcell D-1 would drift to the top p-layer and connect to the outer

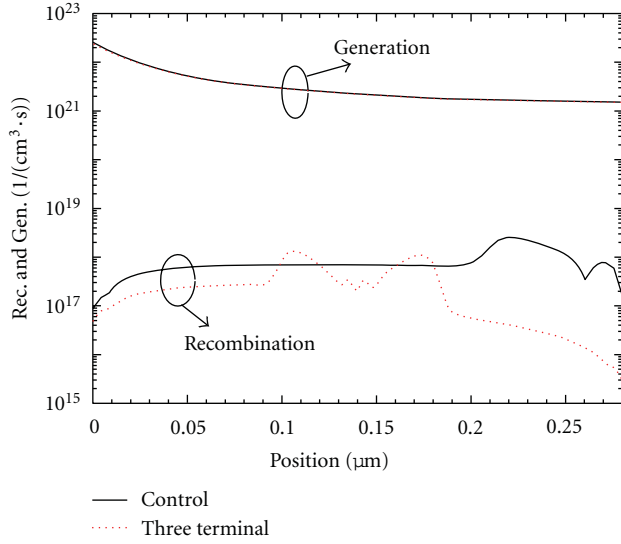


FIGURE 3: The generation and recombination rates of the control cell and the three-terminal cell. The control cell and the three-terminal cell have the same generation rate.

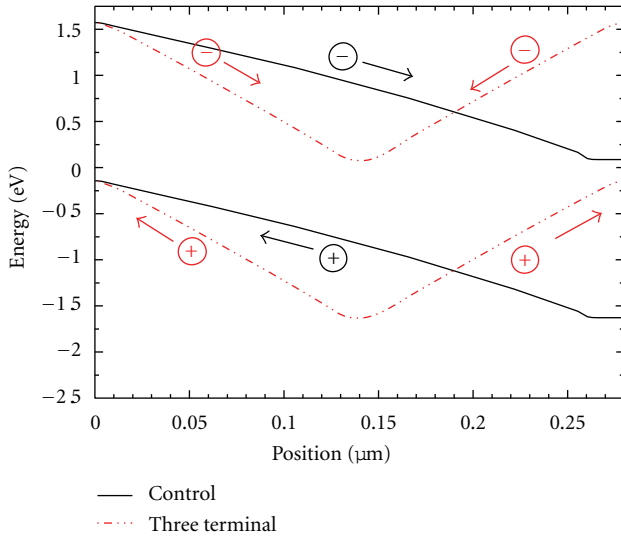


FIGURE 4: The band-edge diagram of the control cell and the three-terminal cell. The arrows show the drift directions of photogenerated carriers.

circuit via the top “contact:gate” on the top surface. The photogenerated holes in the subcell D-2 would drift to the bottom p-layer and connect to the outer circuit via the bottom “contact:gate.” Then, the top “contact:gate” and the bottom “contact:gate” were joined by metals. The directions of the photogenerated carrier flows of the three-terminal cell and the outer circuit were shown in Figure 5. Similar to the control cell, “contact:sub” in the three-terminal cell acted as the negative electrode, and two “contact:gates” acted as the positive electrode.

The thicknesses of the subcell D-1 and the subcell D-2 of the previous three-terminal cell were both 0.14 μm. We

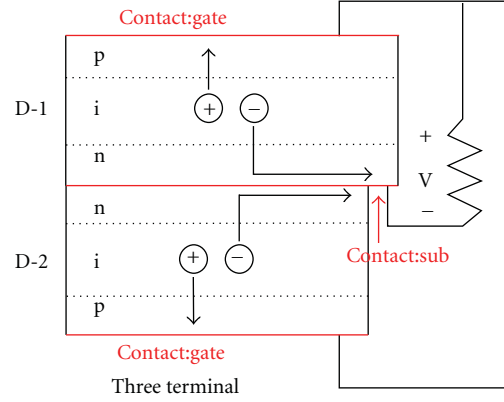


FIGURE 5: A simple diagram of the carrier flows and the outer circuit. The top “contact:gate” and the bottom “contact:gate” are assumed to be joined and act as the positive electrode of the three-terminal cell. The “contact:sub” acts as the negative electrode of the three-terminal cell.

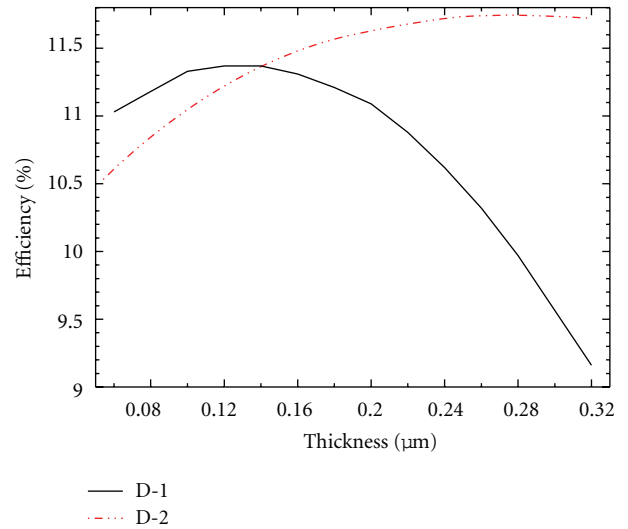


FIGURE 6: The efficiency as a function of the thickness of the subcell D-1 or the subcell D-2. The highest efficiency occurs when the thickness of the subcell D-1 is 0.14 μm.

optimized the three-terminal cell by adjusting the thickness of the subcell D-1 and the subcell D-2 (Figure 6). First, we kept the thickness of the subcell D-2 at 0.14 μm and adjusted the thickness of the subcell D-1 from 0.06 μm to 0.32 μm. We obtained the highest efficiency when the thickness of the subcell D-1 was 0.14 μm. Therefore, the thickness of the subcell D-1 was kept at 0.14 μm, and the thickness of the subcell D-2 was adjusted from 0.06 μm to 0.32 μm. The thicker the subcell D-2, the higher the efficiency. The efficiency almost saturated as the thickness became greater than 0.24 μm. From the simulation results, we obtain the following conclusions: (I) as the thickness of the subcell D-2 is fixed and the thickness of subcell D-1 is smaller than 0.14 μm, a thinner subcell D-1 will produce a lower J_{SC} in the three-terminal cell as a result of insufficient absorption, thus leading to a lower efficiency; (II) the thicker the subcell

D-1, the greater the overall J_{SC} , but the lower the overall V_{OC} . Therefore, the efficiency decreases if this subcell is too thick (thicker than $0.14\ \mu\text{m}$). The reason for decreasing in the overall V_{OC} as the thickness increases is discussed as follows. When the subcell D-1 is too thick, most of sunlight is absorbed by the subcell D-1, which leads to the decrease in absorption in the subcell D-2. This reduces the photogenerated current in the subcell D-2, and therefore the subcell D-2 has a lower V_{OC} than the subcell D-1. For a three-terminal cell, subcells D-1 and D-2 are connected in parallel to the circuit. Consequently, the reduced V_{OC} of the subcell D-2 will decrease the overall V_{OC} of the three-terminal cell; (III) on the other hand, as the thickness of the subcell D-1 is fixed, a thicker subcell D-2 absorbs more incident light, leading to the higher J_{SC} and efficiency.

4. Summary

We designed and simulated a new three-terminal a-Si solar cell. This structure improved the efficiency limitation that existed as a result of defects of a-Si solar cells. The efficiency of a $0.28\ \mu\text{m}$ -thick thin-film three-terminal a-Si solar cell achieved 11.4%. The efficiency of the three-terminal a-Si solar cell could reach $\sim 11.7\%$ with the optimized thickness.

Acknowledgments

The authors are grateful to the National Center for High-Performance Computing for computer time and facilities (ISE TCAD). This work is supported by the National Science Council of Taiwan. under Contract no. 97-2218-E-259-006 and no. 98-2221-E-259-002-MY3.

References

- [1] A. Matsuda, "Thin-film silicon—growth process and solar cell application," *Japanese Journal of Applied Physics*, vol. 43, no. 12, pp. 7909–7920, 2004.
- [2] P. Leempoel, P. Descamps, T. Kervyn de Meerendré et al., "Distributed electron cyclotron resonance plasma: a technology for large area deposition of device-quality a-Si:H at very high rate," *Thin Solid Films*, vol. 516, no. 20, pp. 6853–6857, 2008.
- [3] M. Brinza, J. K. Rath, and R. E. I. Schropp, "Thin film silicon n-i-p solar cells deposited by VHF PECVD at $100\ ^\circ\text{C}$ substrate temperature," *Solar Energy Materials and Solar Cells*, vol. 93, no. 6–7, pp. 680–683, 2009.
- [4] K. Chikusa, K. Takemoto, T. Itoh, N. Yoshida, and S. Nonomura, "Preparation of B-doped a-Si_{1-x}C_x:H films and heterojunction p-i-n solar cells by the Cat-CVD method," *Thin Solid Films*, vol. 430, no. 1–2, pp. 245–248, 2003.
- [5] K. Sugita, K. Koyama, K. Ohdaira, and H. Matsumura, "Relationship between textured structure of substrates and defect density of catalytic chemical vapor deposition amorphous silicon films," *Japanese Journal of Applied Physics*, vol. 46, no. 5, pp. 2852–2857, 2007.
- [6] S. Hiza, A. Yamada, and M. Konagai, "Low-temperature deposition of hydrogenated microcrystalline silicon thin films by photochemical vapor deposition technique and their application to thin film solar cells," *Japanese Journal of Applied Physics*, vol. 46, no. 4, pp. 1427–1431, 2007.
- [7] J. Kwak, S. W. Kwon, and K. S. Lim, "Fabrication of a n-p-p tunnel junction for a protocrystalline silicon multi-layer/amorphous silicon tandem solar cell," *Journal of Non-Crystalline Solids*, vol. 352, no. 9–20, pp. 1847–1850, 2006.
- [8] T. D. Moustakas, "Photovoltaic properties of amorphous silicon produced by reactive sputtering," *Solar Energy Materials*, vol. 13, no. 5, pp. 373–384, 1986.
- [9] B. Rech and H. Wagner, "Potential of amorphous silicon for solar cells," *Applied Physics A*, vol. 69, no. 2, pp. 155–167, 1999.
- [10] J. Yang, A. Banerjee, and S. Guha, "Amorphous silicon based photovoltaics—from earth to the 'final frontier,'" *Solar Energy Materials and Solar Cells*, vol. 78, no. 1–4, pp. 597–612, 2003.
- [11] T. Nishimoto, M. Takai, H. Miyahara, M. Kondo, and A. Matsuda, "Amorphous silicon solar cells deposited at high growth rate," *Journal of Non-Crystalline Solids*, vol. 299–302, no. 2, pp. 1116–1122, 2002.
- [12] A. Čampa, O. Isabella, R. van Erven et al., "Optimal design of periodic surface texture for thin-film a-Si:H solar cells," *Progress in Photovoltaics: Research and Applications*, vol. 18, no. 3, pp. 160–167, 2010.
- [13] H. Keppner, J. Meier, P. Torres, D. Fischer, and A. Shah, "Microcrystalline silicon and micromorph tandem solar cells," *Applied Physics A*, vol. 69, no. 2, pp. 169–177, 1999.
- [14] E. Maruyama, S. Okamoto, A. Terakawa, W. Shinohara, M. Tanaka, and S. Kiyama, "Toward stabilized 10% efficiency of large-area ($>5000\ \text{cm}^2$) a-Si/a-SiGe tandem solar cells using high-rate deposition," *Solar Energy Materials and Solar Cells*, vol. 74, no. 1–4, pp. 339–349, 2002.
- [15] M. Taguchi, E. Maruyama, and M. Tanaka, "Temperature dependence of amorphous/crystalline silicon heterojunction solar cells," *Japanese Journal of Applied Physics*, vol. 47, no. 2, pp. 814–818, 2008.
- [16] J. Meier, U. Kroll, S. Dubail et al., "Efficiency enhancement of amorphous silicon p-i-n solar cells by LP-CVD ZnO," in *Proceedings of the 28th IEEE Photovoltaic Specialists Conference*, p. 746, September 2000.
- [17] S. Benagli, D. Borrello, E. Vallat-Sauvain et al., "High-efficiency amorphous silicon devices on LPCVD-ZnO TCO prepared in industrial KAI TM-M R & D reactor," in *Proceedings of the 24th European Photovoltaic Solar Energy Conference*, p. 2293, 2009.
- [18] J. Yang, A. Banerjee, and S. Guha, "Triple-junction amorphous silicon alloy solar cell with 14.6% initial and 13.0% stable conversion efficiencies," *Applied Physics Letters*, vol. 70, no. 22, pp. 2975–2977, 1997.
- [19] J. Meier, S. Dubail, S. Golay et al., "Microcrystalline silicon and the impact on micromorph tandem solar cells," *Solar Energy Materials and Solar Cells*, vol. 74, no. 1–4, pp. 457–467, 2002.
- [20] M. Yoshimi, T. Sasaki, T. Sawada et al., "High efficiency thin film silicon hybrid solar cell module on 1m²-class large area substrate," in *Proceedings of the 3rd World Conference on Photovoltaic Energy Conversion*, pp. 1566–1569, May 2003.
- [21] P. D. Veneri, P. Aliberti, L. V. Mercaldo, I. Usatii, and C. Privato, "Influence of microcrystalline silicon bottom cell on micromorph tandem solar cell performance," *Thin Solid Films*, vol. 516, no. 20, pp. 6979–6983, 2008.
- [22] I. A. Yunaz, K. Sriprapha, S. Hiza, A. Yamada, and M. Konagai, "Effects of temperature and spectral irradiance on performance of silicon-based thin film multijunction solar cells," *Japanese Journal of Applied Physics*, vol. 46, no. 4, pp. 1398–1403, 2007.
- [23] S. Y. Myong, S. S. Kim, O. Chevaleevski, K. H. Jun, M. Konagai, and K. S. Lim, "Optimization of P-A-SiC:H/P-NC-SiC:H double layer structure for a high efficiency A-Si:H

based solar cell,” in *Proceedings of the 29th IEEE Photovoltaic Specialists Conference*, pp. 1226–1229, May 2002.

- [24] C.-H. Lin, “Si/Ge/Si double heterojunction solar cells,” *Thin Solid Films*, vol. 518, no. 6, supplement 1, pp. S255–S258, 2010.
- [25] T. Nagashima, K. Okumura, K. Murata, Y. Kimura et al., “Three-terminal tandem solar cells with a back-contact type bottom cell,” in *Proceedings of the 28th IEEE Photovoltaic Specialists Conference*, p. 1193, September 2000.

Research Article

Charge-Carrier Transport in Thin Film Solar Cells: New Formulation

Jesús E. Velazquez-Perez¹ and Yuri G. Gurevich²

¹Departamento de Física Aplicada, Universidad de Salamanca, 37008 Salamanca, Spain

²Departamento de Física, CINVESTAV del I.P.N., Apartado Postal 14-740, 07000 Mexico, DF, Mexico

Correspondence should be addressed to Jesús E. Velazquez-Perez, js@usal.es

Received 4 July 2011; Accepted 28 August 2011

Academic Editor: Leonardo Palmisano

Copyright © 2011 J. E. Velazquez-Perez and Y. G. Gurevich. This is an open access article distributed under the Creative Commons Attribution License, which permits unrestricted use, distribution, and reproduction in any medium, provided the original work is properly cited.

Solar cells rely on photogeneration of charge carriers in p-n junctions and their transport and subsequent recombination in the quasineutral regions. A number of basic issues concerning the physics of the operation of solar cells still remain obscure. This paper discusses some of those unsolved basic problems. In conventional solar cells, recombination of photogenerated charge carriers plays a major limiting role in the cell efficiency. High quality thin-film solar cells may overcome this limit if the minority diffusion lengths become large as compared to the cell dimensions, but, strikingly, the conventional model fails to describe the cell electric behavior under these conditions. A new formulation of the basic equations describing charge carrier transport in the cell along with a set of boundary conditions is presented. An analytical closed-form solution is obtained under a linear approximation. In the new framework given, the calculation of the open-circuit voltage of the solar cell diode does not lead to unphysical results.

1. Introduction

Charge carrier transport underlies the electrical behavior of any semiconductor device and, in particular, of solar cells. Despite efforts made over the years to correctly model charge-carrier transport in semiconductors, some important questions still remain unanswered. These questions need to be addressed in order to correctly model present and future devices.

One of these open questions is how to model carrier recombination. The mathematical expression routinely used to model the recombination rate [1] is basically incorrect. It has recently been demonstrated that it contradicts Maxwell's equations, and hence a new corrected model must be developed [2, 3]. This problem was partly addressed in previous works (see, e.g., [4]). Recombination is a key feature when describing carrier transport in solar cells because it strongly affects the electrical response of the semiconductor at all levels of external excitation. A remark that must be made about the need for a correct modeling of recombination is that in devices operating under a strong excitation

regime (the operation of solar cells lies in this regime), the importance of a correct formulation of the recombination terms is even more important.

Since in general the set of Poisson and transport equations cannot be solved analytically, some simplifications must be introduced to obtain a closed-form solution. One approximation commonly used to solve this system of equations is the assumption of quasineutrality (QN) [5]. The use of the QN approximation is acceptable if the sample's and the diffusion lengths are both larger than the Debye length. Although QN has been routinely used in semiconductor device modeling for many years, the role of space charge in the formation of the current-voltage ($I - V$) characteristic in a semiconductor is still controversial.

A very important question is the choice of the boundary conditions used when solving the carrier-transport equations. It should be noted that the expressions commonly used are valid only for semiconductor devices operating in open-circuit conditions (see, e.g., [6]). Since in normal operation a current flows at the terminals, the widespread use of boundary conditions for open-circuit conditions is

incorrect. For closed-circuit conditions, a different set of boundary conditions needs to be derived. This problem has only been addressed in the last few years [7–9].

All the abovementioned issues need to be addressed when modeling any semiconductor devices. Thin-film solar cells are one of the strongest technologies in the steadily growing photovoltaic market [10]. In this paper we will address a very basic problem encountered when modeling cells with large values of the minority diffusion lengths.

2. Problem Statement

The commonly accepted electrical model for the current density-voltage characteristic ($J - V$) of an ideal p-n junction is [11]

$$J = J_0 \left(e^{V/V_T} - 1 \right), \quad (1)$$

where J is the diode current density, V is the bias voltage, V_T is the thermal voltage, and J_0 the reverse-saturation current density that for a long abrupt diode is

$$J_0 = V_T \left(\frac{\sigma_p^n}{L_D^n} + \frac{\sigma_n^p}{L_D^p} \right), \quad (2)$$

σ_n^p (σ_p^n) is the electron (hole) conductivity of minority carriers in the p-side (n-side) of a junction diode; L_D^n and L_D^p are, respectively, the hole and electron minority carrier diffusion lengths of minority carriers in n- and p- sides defined as

$$L_D^n = \sqrt{D_p \tau_p}, \quad L_D^p = \sqrt{D_n \tau_n}, \quad (3)$$

D_n (D_p) is the electron (hole) diffusivity and τ_n (τ_p) is the electron (hole) minority carrier lifetime.

Equation (1) may be rewritten for a solar cell under illumination as [12]

$$-J = J_0 \left(e^{V/V_T} - 1 \right) + J_I, \quad (4)$$

where J_I is the photocurrent and J is additionally related to the generated voltage V through the external resistive load (R) in the circuit and the solar cell area (S) as shown in Figure 1:

$$J = \frac{V}{RS}. \quad (5)$$

For the sake of simplicity, let us examine the photocurrent generated in a slab of semiconductor of thickness L with incident light at $x = 0$. J_I may be obtained as the integral of the light intensity across the device $I(x)$ as

$$|J_I| = q\alpha\beta \int_0^L I(x) dx, \quad (6)$$

where q is the absolute value of the electron charge, α is the absorption coefficient of light, and β is the quantum efficiency,

$$\beta = \frac{\alpha - \alpha_0}{\alpha}. \quad (7)$$

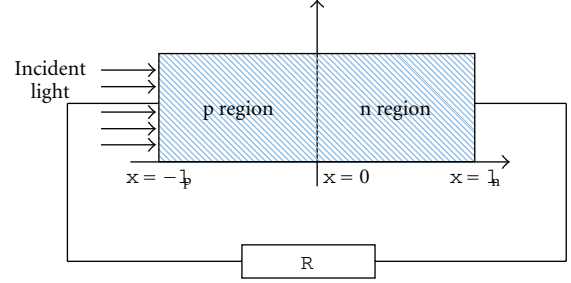


FIGURE 1: Solar cell diode with an external resistor load.

The light intensity inside the semiconductor slab will decrease following the law:

$$I = I_0 e^{-\alpha x}, \quad (8)$$

where I_0 is the light intensity (number of incident photons per unit time and unit area) at the plane of the incident light ($x = 0$) and the carrier generation rate due to photon-absorption can be written as

$$g = (\alpha - \alpha_0) I_0 e^{-\alpha x}. \quad (9)$$

The set of (4)–(9) may be extended or augmented with other equations for a finer modeling of a real technology [13], but this set constitutes the fundamental framework to describe the electrical behaviour of any diode-based solar cell. Let us assume a one-dimensional problem for a single-diode solar cell such as the one given in Figure 1. According to the values of diffusion lengths in Si, in a c-Si thin-film solar cell, or in a-Si ones of nanometer dimensions [14], the following inequality will hold:

$$l_{n,p} \ll L_D^{n,p}. \quad (10)$$

From (10) it follows that $L_D^{n,p} \rightarrow \infty$ and $\tau_{n,p} \rightarrow \infty$; therefore, recombination is negligible and according to (2) $J_0 \rightarrow 0$ and, moreover, from (4), the basic model leads to the unphysical result (see Figure 2(b)): $J \approx -J_I$, i.e., the p-n junction behaves as a current-source that translates photo-excitation into current at any value of the diode-voltage independently of the p-n junction properties.

From the above it follows that the framework of basic equations conventionally used to model solar cells fails in high-quality thin-film solar cells [15]. Regardless of its apparent simplicity, since this framework constitutes the foundations of any electrical modeling of a solar cell diode, the discussed problem will persist in any other model that one can build; therefore, it is crucial to identify the origin of the problem and modify the basic model to build a new framework free from unphysical errors. In this paper we will present a new model and we will analytically show in a simple case that this new framework does not fail to correctly describe the limiting case of a thin-film solar cell.

3. New Model for Thin-Film Solar Cells

Let us assume once again that inequality of (10) holds and, accordingly, the solar cell recombination is negligible. The

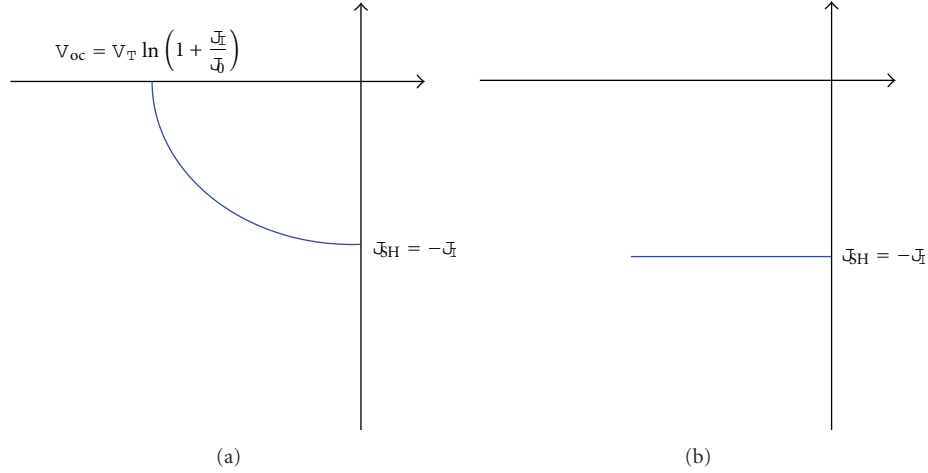


FIGURE 2: J - V characteristic of an ideal solar cell with the short- and open-circuit expressions for the axis-intercept points V_{oc} and J_{SH} , respectively, (a). J - V characteristic in the limiting case of a thin-film cell $l_{n,p} \ll L_D^{n,p}$ (b).

macroscopic description of the transport of nonequilibrium charge is done with the continuity equations for the electron (j_n) and hole (j_p) current densities [3]:

$$\begin{aligned} \frac{\partial n}{\partial t} &= g_n + \frac{1}{e} \operatorname{div} j_n - R_n, \\ \frac{\partial p}{\partial t} &= g_p - \frac{1}{e} \operatorname{div} j_p - R_p. \end{aligned} \quad (11)$$

In a stationary case and one-dimensional problem along the x -direction, normal to the p-n junction plane as in Figure 1, (11) becomes

$$\begin{aligned} \frac{dj_n}{dx} &= q(R_n - g_n), \\ \frac{dj_p}{dx} &= -q(R_p - g_p). \end{aligned} \quad (12)$$

Since volume recombination is negligible $R_n = R_p = 0$ and, accordingly, $g_n = g_p = g(x)$, that is, the recombination is band-to-band and the continuity equations reduce to

$$\begin{aligned} \frac{dj_n}{dx} &= -qg(x), \\ \frac{dj_p}{dx} &= qg(x). \end{aligned} \quad (13)$$

Additionally, it can be shown that in absence of recombination and under band-to-band generation, the density of charge in any impurity level remains constant [15], under all the above conditions the QN approximation reduces to $\delta n = \delta p$. In a general case, for a nondegenerate semiconductor, in a linear approximation δn and δp can be written in terms of the variations in their respective chemical potentials (μ_n and μ_p) as [16]

$$\begin{aligned} \delta n &= \frac{n_0}{T_0} \delta \mu_n, \\ \delta p &= \frac{p_0}{T_0} \delta \mu_p, \end{aligned} \quad (14)$$

where the subscript 0 stand for equilibrium value of the magnitude, and using the QN approximation the following relationship between the deviations from equilibrium of the chemical potentials holds

$$\delta \mu_p = \frac{n_0}{p_0} \delta \mu_n. \quad (15)$$

In order, to further simplify the mathematical problem, while ensuring no loss of generality of the physical one, we will assume a step-like profile for the light absorption instead of the model in (8):

$$I = \begin{cases} I_0 & -l_p < x < 0, \\ 0 & 0 < x < l_n. \end{cases} \quad (16)$$

Using (9) and (16), we may write the continuity equations, (13), as

$$\begin{aligned} \frac{dj_n^p}{dx} &= -qg_0, & \frac{dj_p^p}{dx} &= qg_0, \\ \frac{dj_n^n}{dx} &= 0, & \frac{dj_p^n}{dx} &= 0. \end{aligned} \quad (17)$$

Superscripts in current densities in (17) indicate the doping type of the region. The current densities may be written as [3]

$$\begin{aligned} j_n^n &= -\sigma_n^n \left(\frac{d\delta\varphi^n}{dx} - \frac{1}{q} \frac{d\delta\mu_n^n}{dx} \right), \\ j_p^n &= -\sigma_p^n \left(\frac{d\delta\varphi^n}{dx} + \frac{1}{q} \frac{d\delta\mu_p^n}{dx} \right), \\ j_n^p &= -\sigma_n^p \left(\frac{d\delta\varphi^p}{dx} - \frac{1}{q} \frac{d\delta\mu_n^p}{dx} \right), \\ j_p^p &= -\sigma_p^p \left(\frac{d\delta\varphi^p}{dx} + \frac{1}{q} \frac{d\delta\mu_p^p}{dx} \right), \end{aligned} \quad (18)$$

where we introduced the electric potential (φ). To solve (17) with (14), (15), and (18), we need to determine and impose enough boundary conditions at the semiconductor interfaces [8]. We will assume ideal metallic (ohmic) contacts placed at $x = -l_p$ and at $x = l_n$; therefore, the excess of carriers are null:

$$\delta n^p(-l_p) = \delta p^p(-l_p) = 0, \quad \delta n^n(l_n) = \delta p^n(l_n) = 0. \quad (19)$$

And, according to (19), we obtain the following four boundary conditions for the chemical potentials at the metal-semiconductor contacts:

$$\delta \mu_n^p(-l_p) = \delta \mu_p^p(-l_p) = 0, \quad \delta \mu_n^n(l_n) = \delta \mu_p^n(l_n) = 0. \quad (20)$$

Two additional boundary conditions may be imposed on the electric potential at the same metal-semiconductor contacts:

$$\delta \varphi^p(-l_p) = 0, \quad \delta \varphi^n(l_n) = V. \quad (21)$$

At the interface of the two semiconductor regions, since there is no recombination, we may write two additional boundary conditions at $x = 0$ [8]:

$$j_n^n(0) = j_n^p(0), \quad j_p^n(0) = j_p^p(0). \quad (22)$$

Two more boundary conditions are

$$\begin{aligned} \delta \varphi^p(0) - \frac{\delta \mu_p^p(0)}{q} &= \delta \varphi^n(0) - \frac{\delta \mu_n^n(0)}{q}, \\ \delta \varphi^p(0) + \frac{\delta \mu_p^p(0)}{q} &= \delta \varphi^n(0) + \frac{\delta \mu_n^n(0)}{q}. \end{aligned} \quad (23)$$

Using the obtained boundary conditions from the continuity of the Fermi quasilevels it is straightforward to solve the linear system of equations for the current densities (18) and obtain the solution

$$J \left(\frac{l_n}{\sigma_n^p} + \frac{l_p}{\sigma_p^p} \right) + V \left(\frac{l_p}{\sigma_n^p} + \frac{l_n}{\sigma_p^p} \right) + \frac{qg_0}{2} \left(\frac{l_p^2 l_n}{\sigma_n^p \sigma_p^p} \right) = 0. \quad (24)$$

In the third term of (24), we may identify the photocurrent density created under illumination

$$J_I = \frac{qg_0}{2} l_p. \quad (25)$$

Since we are under a small voltage-/current-linear approximation with the aim of obtaining an analytical closed form for the $J - V$ (24), we must compare the obtained equation with a linearization of (4):

$$J_I + V \left(\frac{J_0}{V_T} \right) = -J. \quad (26)$$

By rewriting (24) in a similar form we obtain

$$J_I + V \left(\frac{l_p}{\sigma_n^p} + \frac{l_n}{\sigma_p^p} \right) \left(\frac{\sigma_n^p \sigma_p^n}{l_p l_n} \right) = -J. \quad (27)$$

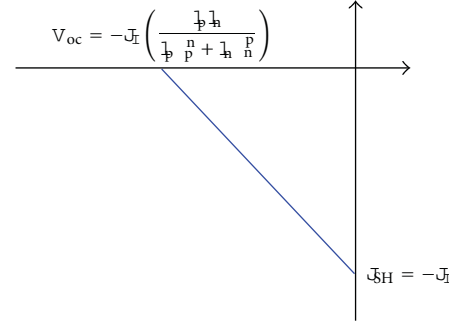


FIGURE 3: J - V characteristic of an ideal thin-film solar cell with the new expression for the x axis-intercept point V_{oc} .

This is a main result of this work, identifying the second terms in the left hand side of (26) and (27), we obtain a new expression for the current density J_0 :

$$J_0 = \left(\frac{l_p}{\sigma_n^p} + \frac{l_n}{\sigma_p^p} \right) \left(\frac{\sigma_n^p \sigma_p^n}{l_p l_n} \right) V_T. \quad (28)$$

This new expression does not exhibit an unphysical behavior ($J_0 \rightarrow \infty$) in thin-film solar cells (Figure 2(b)). Figure 3 gives the two axis-intercept points (V_{oc} and J_{SH}) of the $J - V$ characteristic, it can be trivially verified that the x -intercept point (V_{oc}) will remain at a finite value independently of the minority carriers diffusion lengths at each side of the junction and the diode dimensions. Since the analytical model presented in this paper was obtained by a linearization of the full model and some other approximations have been used to simplify the mathematical problem, the large-signal $J - V$ is not properly obtained (Figure 3), but the framework of transport equations and boundary conditions can be solved numerically to study any real solar cell diode.

4. Conclusions

Solar cells rely on photogeneration of charge carriers in p-n junctions and their subsequent recombination in the quasi-neutral regions. A number of basic issues concerning the physics of the operation of solar cells still remain obscure. In this paper we briefly discussed some of those unsolved basic problems: need for not unphysical models of the carrier recombination and revision of the QN concept. In conventional solar cells recombination of photogenerated charge carriers plays a major limiting role in the cell efficiency. High quality thin-film solar cells may overcome this limit if the minority diffusion lengths become large as compared to the cell dimensions, but, strikingly, the conventional model fails to describe the cell electric behavior under these conditions. A new formulation of the basic equations describing charge carrier transport in the cell along with a set of boundary conditions is presented. An analytical closed-form solution is obtained under a linear approximation. In the new framework given, the calculation of the open-circuit voltage of the solar cell diode does not lead to unphysical results.

Acknowledgments

J. E. Velázquez-Perez wants to thank Ministerio de Ciencia e Innovación (MICINN) and Junta de Castilla y León for partial financial support under Grants TEC2008-02281 and SA061A09. Yu. G. Gurevich wants to thank CONACYT-México for partial financial support.

References

- [1] P. T. Landsberg, *Recombination in Semiconductors*, Cambridge University, Cambridge, UK, 1991.
- [2] I. N. Volovichev, G. N. Logvinov, O. Y. Titov, and Y. G. Gurevich, "Recombination and lifetimes of charge carriers in semiconductors," *Journal of Applied Physics*, vol. 95, no. 8, pp. 4494–4496, 2004.
- [3] Yu. G. Gurevich, J. E. Velázquez-Perez, G. Espejo-Lopez, I. N. Volovichev, and O. Y. Titov, "Transport of nonequilibrium carriers in bipolar semiconductors," *Journal of Applied Physics*, vol. 101, no. 2, Article ID 023705, 8 pages, 2007.
- [4] Y. G. Gurevich and I. N. Volovichev, "Forgotten mechanism of nonlinearity in the theory of hot electrons," *Physical Review B*, vol. 60, no. 11, pp. 7715–7717, 1999.
- [5] I. N. Volovichev, J. E. Velázquez-Perez, and Yu. G. Gurevich, "Transport boundary condition for semiconductor structures," *Solid-State Electronics*, vol. 52, no. 11, pp. 1703–1709, 2008.
- [6] K. Seeger, *Semiconductor Physics*, Springer, Berlin, Germany, 1985.
- [7] O. Yu. Titov, J. Giraldo, and Yu. G. Gurevich, "Boundary conditions in an electric current contact," *Applied Physics Letters*, vol. 80, no. 17, p. 3108, 2002.
- [8] I. N. Volovichev, J. E. Velázquez-Perez, and Y. G. Gurevich, "Transport boundary conditions for solar cells," *Solar Energy Materials and Solar Cells*, vol. 93, no. 1, pp. 6–10, 2009.
- [9] Y. G. Gurevich, G. N. Logvinov, J. E. Velázquez, and O. Y. Titov, "Transport and recombination in solar cells: new perspectives," *Solar Energy Materials and Solar Cells*, vol. 91, no. 15-16, pp. 1408–1411, 2007.
- [10] M. A. Green, "Thin-film solar cells: review of materials, technologies and commercial status," *Journal of Materials Science*, vol. 18, supplement 1, pp. S15–S19, 2007.
- [11] J. Singh, *Semiconductor Devices: Basic Principles*, John Wiley & Sons, New York, NY, USA, 2000.
- [12] A. Luque and S. Hegedus, Eds., *Handbook of Photovoltaic Science and Engineering*, John Wiley & Sons, Chichester, UK, 2003.
- [13] *Sentaurus Device User Guide*, Synopsys, Mountain View, Calif, USA, 2009.
- [14] R. B. Bergmann, "Crystalline Si thin-film solar cells: a review," *Applied Physics A*, vol. 69, no. 2, pp. 187–194, 1999.
- [15] J. E. Velázquez-Pérez and Y. G. Gurevich, "Transport and recombination in solar cells, new boundary conditions and perspectives," in *Proceedings of the 25th European Photovoltaic Solar Energy Conference and Exhibition/5th World Conference on Photovoltaic Energy Conversion*, Valencia, Spain, September 2010.
- [16] Yu. G. Gurevich, G. N. Logvinov, I. N. Volovichev, G. Espejo, O. Yu. Titov, and A. Meriuts, "The role of non-equilibrium carriers in the formation of thermo-E.M.F. in bipolar semiconductors," *Physica Status Solidi B*, vol. 231, no. 1, pp. 278–293, 2002.

Research Article

Preparation and Characterization of Coevaporated $\text{Cd}_{1-x}\text{Zn}_x\text{S}$ Alloy Thin Films

Wei Li, Jiayi Yang, Zhen Sun, Lianghuan Feng, Jingquan Zhang, and Lili Wu

College of Materials Science and Engineering, Sichuan University, Chengdu 610064, China

Correspondence should be addressed to Wei Li, waylee2000@sohu.com

Received 30 April 2011; Accepted 30 August 2011

Academic Editor: Leonardo Palmisano

Copyright © 2011 Wei Li et al. This is an open access article distributed under the Creative Commons Attribution License, which permits unrestricted use, distribution, and reproduction in any medium, provided the original work is properly cited.

$\text{Cd}_{1-x}\text{Zn}_x\text{S}$ thin films have been prepared by the vacuum coevaporation method. The structural, compositional, and optical properties of $\text{Cd}_{1-x}\text{Zn}_x\text{S}$ thin films have been investigated using X-ray diffraction, X-ray fluorescence, and optical transmittance spectra. As-deposited $\text{Cd}_{1-x}\text{Zn}_x\text{S}$ thin films are polycrystalline and show the cubic structure for $x = 1$ and hexagonal one for $x < 1$ with the highly preferential orientation. The composition of $\text{Cd}_{1-x}\text{Zn}_x\text{S}$ thin films determined from Vegard's law and quartz thickness monitors agrees with that determined from the X-ray fluorescence spectra. Optical absorption edge of optical transmittance for $\text{Cd}_{1-x}\text{Zn}_x\text{S}$ thin films shows a blue shift with the increase of the zinc content. The band gap for $\text{Cd}_{1-x}\text{Zn}_x\text{S}$ thin films can be tuned nonlinearly with x from about 2.38 eV for CdS to 3.74 eV for ZnS. A novel structure for CuInS_2 -based solar cells with a $\text{Cd}_{0.4}\text{Zn}_{0.6}\text{S}$ layer is proposed in this paper.

1. Introduction

ZnS-based II-VI materials can form ternary alloys, such as $\text{Cd}_{1-x}\text{Zn}_x\text{S}$, with a direct fundamental band-gap range from 2.4 to 3.7 eV at room temperature. The energy position of the conduction band is changed primarily by varying the Zn content. Therefore, these materials have potential applications for efficient electron-confined structures, photovoltaic heterojunction, and electro-optical devices.

In photovoltaic system, the replacement of CdS with the higher band-gap $\text{Cd}_{1-x}\text{Zn}_x\text{S}$ has led to a decrease in window absorption losses and has resulted in an increase in the short-circuit current [1]. This $\text{Cd}_{1-x}\text{Zn}_x\text{S}$ ternary compound is also a useful buffer material for fabrication of p - n junctions without lattice mismatch [2].

$\text{Cd}_{1-x}\text{Zn}_x\text{S}$ thin films have been prepared by different techniques, which include evaporation [2–5], chemical bath deposition [1, 6, 7], and organic vapor deposition [8]. However, very little information is available on the ternary $\text{Cd}_{1-x}\text{Zn}_x\text{S}$ alloy films with the desired composition prepared by the vacuum evaporation technique. $\text{Cd}_{1-x}\text{Zn}_x\text{S}$ thin films, to our best knowledge, have been prepared by vacuum evaporation involved with three methods, one of which is the thin films being prepared by using a mechanically alloyed

mixture of CdS and ZnS [3]. It is obvious that a homogenous mixture of $\text{Cd}_{1-x}\text{Zn}_x\text{S}$ is difficult to obtain. So Kumar et al. [4] synthesized the fine powders of $\text{Cd}_{1-x}\text{Zn}_x\text{S}$ by solid-state reaction and then deposited $\text{Cd}_{1-x}\text{Zn}_x\text{S}$ thin films. Considering the large difference in the vapor pressures of CdS and ZnS, Torres and Gordillo [5] prepared $\text{Cd}_{1-x}\text{Zn}_x\text{S}$ thin films by evaporation, varying the diameter of the openings of the coaxial chambers which contain the CdS and ZnS precursors. However, homogenous $\text{Cd}_{1-x}\text{Zn}_x\text{S}$ thin films with desired content are not readily deposited by the evaporation mentioned above. In this work, $\text{Cd}_{1-x}\text{Zn}_x\text{S}$ ($0 \leq x \leq 1$) thin films have been prepared by using a coevaporation of CdS and ZnS from two horizontal sources, which allows independent control of the temperature and consequently control of the partial vapor pressures of both precursors. The structural, compositional, optical properties have been investigated.

2. Experimental Details

$\text{Cd}_{1-x}\text{Zn}_x\text{S}$ thin films were deposited by the vacuum coevaporation technique, as described elsewhere [9], to a thickness of ~ 300 nm at room temperature. The vacuum system had a base pressure of 10^{-4} Pa and was partitioned into two

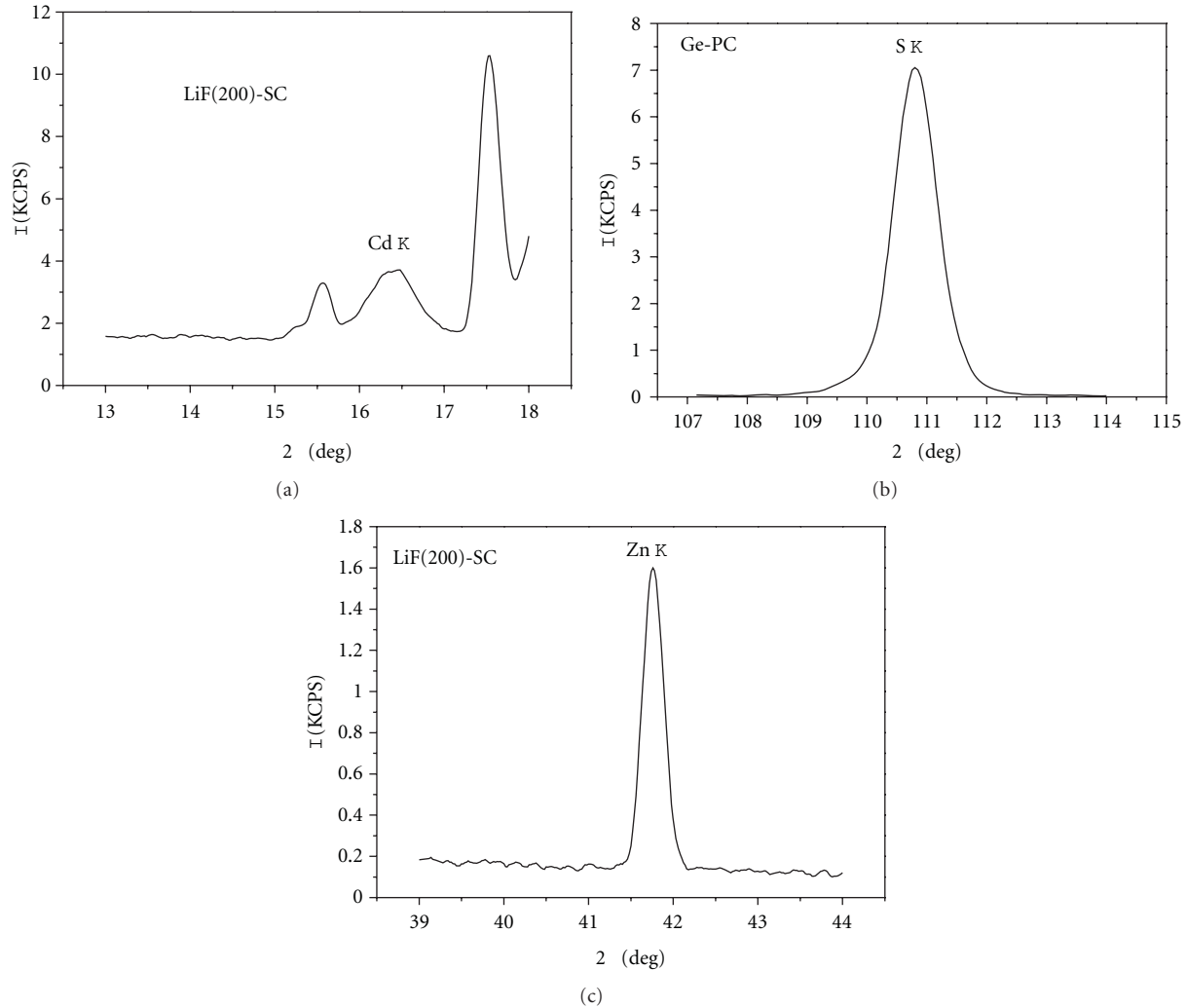


FIGURE 1: Typical XRF of $\text{Cd}_{1-x}\text{Zn}_x\text{S}$ ($x = 0.61$) thin films. (a) Cd- K_α , (b) S- K_α , and (c) Zn- K_α .

parts, one for a CdS powder source (5 N purity) and the other for a ZnS powder source (5 N purity). The CdS and ZnS deposition rates were measured by separate LHC-2 quartz monitors. The deposition rate of ZnS was adjusted to obtain different Zn concentrations in CdS thin films, varying between 0 and 1. The thickness was confirmed precisely by a surface profilometer. X-ray fluorescence (XRF) spectrometry was subsequently used to determine the composition of each sample. The crystallographic phase and lattice constants of each film were obtained by X-ray diffraction (XRD). Measurements of the optical transmittance were made over the wavelength range 200 ~ 800 nm with a data interval of 0.5 nm. Transmittance measurements were also made with the beam at near-normal incidence to the sample to prevent reflected light being returned to the monochromator.

3. Results and Discussion

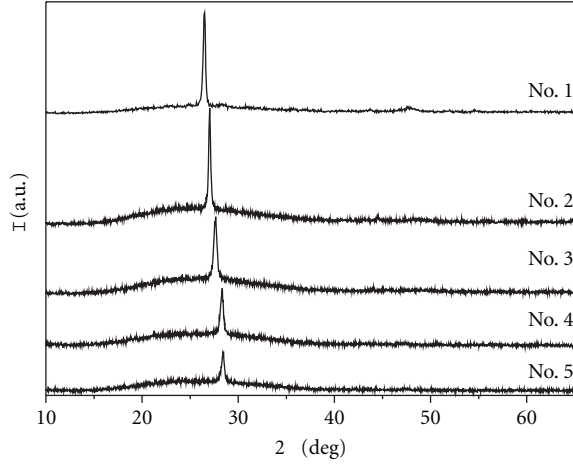
To accurately determine the composition of the $\text{Cd}_{1-x}\text{Zn}_x\text{S}$ alloys, X-ray fluorescence measurements of $\text{Cd}_{1-x}\text{Zn}_x\text{S}$ thin

films were also carried out (Figure 1). Table 1 shows composition of the $\text{Cd}_{1-x}\text{Zn}_x\text{S}$ thin films from XRF using the fundamental parameter (FP) method.

Figure 2 demonstrates X-ray diffraction spectra of $\text{Cd}_{1-x}\text{Zn}_x\text{S}$ ($0 \leq x \leq 1$) thin films obtained by using Cu K_α radiation, where only one diffraction peak with a 2θ value between 26.38 and 28.37° is present. The absence of diffraction peaks associated with CdS and ZnS suggests that those thin films are single-phase materials. The presence of sharp peaks in XRD patterns demonstrates the polycrystalline nature of these $\text{Cd}_{1-x}\text{Zn}_x\text{S}$ ($0 \leq x \leq 1$) thin films, which have a strong preferential orientation. From XRD patterns, one can see that the diffraction angle (2θ) shifts towards a slightly higher angle with increasing x (Zn content) in the thin films. This is due to the substitution of Zn^{2+} for Cd^{2+} , in which different ionic radius of Cd^{2+} (0.095 nm) and Zn^{2+} (0.074 nm) [10] leads to the increase of lattice constants of $\text{Cd}_{1-x}\text{Zn}_x\text{S}$ thin films. Figure 2 also shows that the intensity of XRD peaks decreases at higher concentration of Zn. The structure of $\text{Cd}_{1-x}\text{Zn}_x\text{S}$ thin films varies continuously from being cubic zincblende material with a preferred

TABLE 1: Composition of $\text{Cd}_{1-x}\text{Zn}_x\text{S}$ thin films.

	No. 1	No. 2	No. 3	No. 4	No. 5
From XRF	$\text{CdS}_{0.93}$	$\text{Cd}_{0.72}\text{Zn}_{0.28}\text{S}$	$\text{Cd}_{0.59}\text{Zn}_{0.61}\text{S}$	$\text{Cd}_{0.11}\text{Zn}_{0.89}\text{S}$	$\text{ZnS}_{1.12}$
From Vegard's law	CdS	$\text{Cd}_{0.723}\text{Zn}_{0.277}\text{S}$	$\text{Cd}_{0.42}\text{Zn}_{0.58}\text{S}$	$\text{Cd}_{0.1}\text{Zn}_{0.9}\text{S}$	ZnS
From monitors	CdS	$\text{Cd}_{0.7}\text{Zn}_{0.3}\text{S}$	$\text{Cd}_{0.4}\text{Zn}_{0.6}\text{S}$	$\text{Cd}_{0.1}\text{Zn}_{0.9}\text{S}$	ZnS

FIGURE 2: XRD patterns of as-deposited polycrystalline $\text{Cd}_{1-x}\text{Zn}_x\text{S}$ thin films.

orientation of (111) plane at the ZnS end to being hexagonal wurtzite with a preferential orientation of (002) plane when zinc content decreased.

Since the lattice constant of $\text{Cd}_{1-x}\text{Zn}_x\text{S}$ thin films follows Vegard's law, the composition of $\text{Cd}_{1-x}\text{Zn}_x\text{S}$ thin films can be determined by

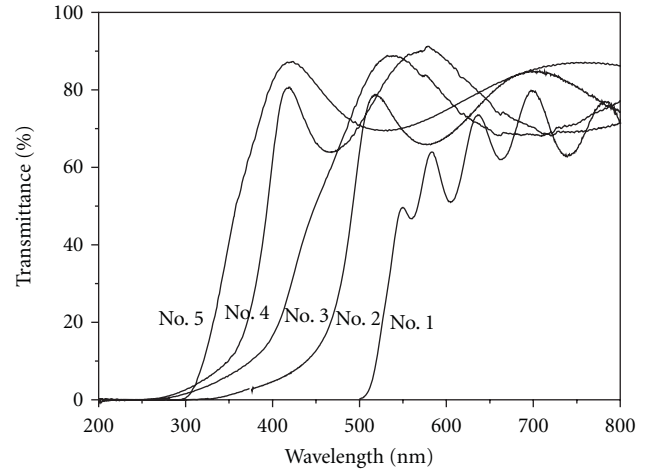
$$x_{\text{Cd}_{1-x}\text{Zn}_x\text{S}} = \frac{a_{\text{Cd}_{1-x}\text{Zn}_x\text{S}} - a_{\text{CdS}}}{a_{\text{ZnS}} - a_{\text{CdS}}} \times 100\%, \quad (1)$$

where $a_{\text{Cd}_{1-x}\text{Zn}_x\text{S}}$, a_{CdS} , and a_{ZnS} are, respectively, the lattice constants of $\text{Cd}_{1-x}\text{Zn}_x\text{S}$, CdS, and ZnS. From the d values of the X-ray diffraction spectra shown in Figure 2 the lattice constants can be calculated as follows:

$$d = \frac{a}{\sqrt{(4/3)(h^2 + hk + k^2) + (a/c)^2}}. \quad (2)$$

Therefore, from (1) and (2), one can obtain the composition of $\text{Cd}_{1-x}\text{Zn}_x\text{S}$ thin films as shown in Table 1. It can be seen that there is a good agreement among the three sets of x values. As for the low angle diffraction line the variation of the diffraction angle with the composition is small and the determined film composition is not so accurate. The error is estimated to be about 0.05 in x . The precision suggests that we can control the composition of $\text{Cd}_{1-x}\text{Zn}_x\text{S}$ thin films, which are prepared by coevaporation of CdS and ZnS. In addition, the comparison of calculated d values from the diffraction spectra (Figure 2) with the standard d^* values from the JCPDS XRD spectra data for $\text{Cd}_{1-x}\text{Zn}_x\text{S}$ is shown in Table 2.

The optical transmittance spectra of the $\text{Cd}_{1-x}\text{Zn}_x\text{S}$ films with different x values were obtained, and steep absorption

FIGURE 3: UV-visible transmission spectra of $\text{Cd}_{1-x}\text{Zn}_x\text{S}$ films.

edges were observed, demonstrating that the thin films are homogeneous (Figure 3). The optical transmittance of the $\text{Cd}_{1-x}\text{Zn}_x\text{S}$ films is typically 60% at wavelengths beyond the absorption edge. It can be seen that $\text{Cd}_{1-x}\text{Zn}_x\text{S}$ films show the blue shift in the absorption edge with the increase of the zinc content.

From the transmittance curves of Figure 3, the absorption coefficient α of the thin films is estimated. The absorption coefficient α with the energy of the photon $h\nu$ could be expressed by the following equation:

$$\alpha h\nu \propto (h\nu - E_g)^m, \quad (3)$$

where E_g is the optical band gap of the thin films, and the exponent m may take values, 1, 2, 3, 1/2, 3/2, depending on the electronic transitions in k -space. A linear fit is achieved for the $\text{Cd}_{1-x}\text{Zn}_x\text{S}$ films with $m = 1/2$, indicating that this material is a direct gap semiconductor. So $(\alpha h\nu)^2$ is plotted as a function of $h\nu$ for various zinc content (not shown there). The optical band energy gap can be determined from the intercept of the extrapolation of the straight portion to the $h\nu$ axis.

The band-gap dependence on composition is shown in Figure 4. It can be seen that the band gap varies with Zn content in a nonlinear way. This dependence can be determined by fitting the band-gap values to a parabolic form on the method of least square [11] and described as

$$E_g(x) = 2.38 + 0.69x + 0.67x^2. \quad (4)$$

It gives the bowing parameter (b) of 0.67 eV, which is much smaller than that reported on another $\text{Cd}_{1-x}\text{Zn}_x\text{S}$ alloy

TABLE 2: XRD results for $\text{Cd}_{1-x}\text{Zn}_x\text{S}$ thin films.

$\text{Cd}_{1-x}\text{Zn}_x\text{S}$	2θ	d	d^*	(hkl)	JCPDS
$x = 0$	26.442	3.3621	3.367	(002)	65-3414
$x = 0.28$	26.993	3.2972	3.290	(002)	40-0836
$x = 0.61$	27.613	3.2237	3.214 ^a	(002)	—
$x = 0.89$	28.347	3.1480	3.142 ^a	(002)	—
$x = 1$	28.533	3.1257	3.124	(111)	65-1691

^aCalculated from Vegard's law.

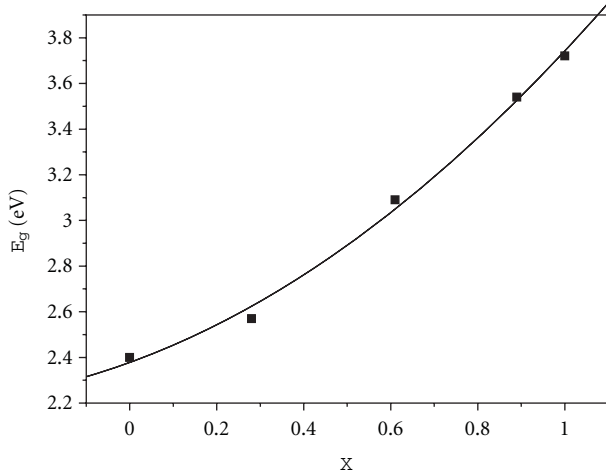


FIGURE 4: The variation of energy gap of the $\text{Cd}_{1-x}\text{Zn}_x\text{S}$ as a function of x .

system in thin films by Borse et al. [6] ($b = 0.85$ eV) and that in single crystal by Muhamad [12] ($b = 0.82$ eV), but agrees well with that in thin films by Yamaguchi et al. [1] ($b = 0.724$ eV). In the present case of $\text{Cd}_{1-x}\text{Zn}_x\text{S}$ thin films, E_g values vary from 2.38 to 3.74 eV for $x = 0$ to 1 in a nonlinear way. This change in the band gap of CdS by addition of Zn shows formation of a continuous series of solid solutions. Therefore, the band energy gap of $\text{Cd}_{1-x}\text{Zn}_x\text{S}$ can be adjusted in the range of the binary band gaps. And the energy position of the conduction band, that is, electron affinity χ , can be also adjusted by varying the zinc content [2].

For the photovoltaic solar cells, CuInS_2 has a desirable direct band gap of 1.5 eV, which is also well-matched with the solar spectrum. Efficiency of 11.4% for CuInS_2 -based solar cells has been successfully made [13]. However, further improvements on performance of CuInS_2 -based solar cells have been restricted by the conventional structure due to the lattice mismatch between ZnO and CuInS_2 . Therefore, an approach to overcome this problem is to introduce an effective buffer layer, $\text{Cd}_{1-x}\text{Zn}_x\text{S}$, in CuInS_2 -based solar cells.

Furthermore, according to Anderson's model, the band alignments with $\chi_{\text{absorber}} \leq \chi_{\text{buffer}} \leq \chi_{\text{window}}$ are desired to prevent the formation of a conduction band spike in the CuInS_2 -based solar cells. For Cu-rich films, electron affinity for CuInS_2 thin films is about 4.1 eV ($E_g \sim 1.53$ eV) [14, 15], and for ZnO thin films is about 4.2 eV ($E_g \sim 3.2$ eV), so the electron affinity of 4.1 eV for $\text{Cd}_{1-x}\text{Zn}_x\text{S}$ thin films (i.e., $x = 0.6$) [2] is taken into account. Based on these mentioned

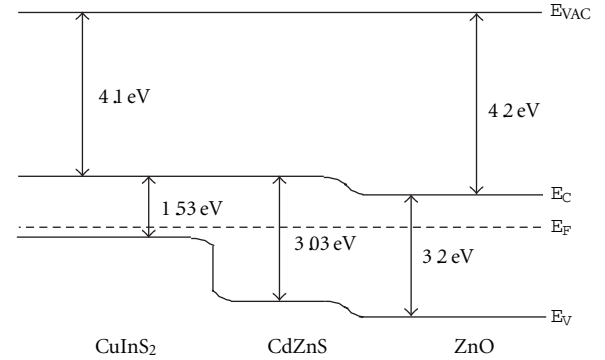


FIGURE 5: Flat band diagram of a $\text{CuInS}_2/\text{ZnO}$ heterojunction with a $\text{Cd}_{0.4}\text{Zn}_{0.6}\text{S}$ buffer layer.

above, we propose a modified structure of CuInS_2 -based solar cells. The energy band diagram of CuInS_2 -based solar cells is shown in Figure 5. $\text{Cd}_{0.4}\text{Zn}_{0.6}\text{S}$ thin films ($E_g \sim 3.03$ eV, from (4)) provide lattice constant matching to the absorber and reduce the interface state density between the p - and n -type materials, meanwhile, the conduction band and valence band spikes are eliminated too.

4. Conclusions

$\text{Cd}_{1-x}\text{Zn}_x\text{S}$ thin films with the required composition have been successfully deposited on glass substrates by the vacuum coevaporation method. The thin films are found to be cubic at the ZnS end and hexagonal for $x < 1$, which show the highly preferred orientation. The measurements of optical transmittance for $\text{Cd}_{1-x}\text{Zn}_x\text{S}$ films demonstrate the blue shift in the absorption edge, and the optical band gap increases from 2.38 to 3.74 eV in a nonlinear way as composition varies from $x = 0$ to 1. And the energy position of the conduction band can be tuned by varying the zinc content. Therefore, a buffer layer $\text{Cd}_{1-x}\text{Zn}_x\text{S}$ for $x = 0.6$ is introduced in the CuInS_2 -based solar cells to eliminate band spikes and provide lattice matching to the absorber.

Acknowledgments

Financial support from the National Basic Research Program of China (Grant no. 2011CBA007008), National Natural Science Foundation of China (Grant no. 61076058), and the Science and Technology Program of Sichuan Province, China (Grant no. 2008GZ0027) is gratefully acknowledged.

The authors thank Ms. Huiqin Sun, Analytical and Testing Center, Sichuan University, for optical transmittance spectra measurements.

References

- [1] T. Yamaguchi, Y. Yamamoto, T. Tanaka, and A. Yoshida, "Preparation and characterization of (Cd,Zn)S thin films by chemical bath deposition for photovoltaic devices," *Thin Solid Films*, vol. 343-344, no. 1-2, pp. 516-519, 1999.
- [2] R. Menner, B. Dimmler, R. H. Mauch, and H. W. Schock, "II-VI compound thin films for windows in heterojunction solar cells," *Journal of Crystal Growth*, vol. 86, no. 1-4, pp. 906-911, 1990.
- [3] D. Patidar, N. S. Saxena, and T. P. Sharma, "Structural, optical and electrical properties of CdZnS thin films," *Journal of Modern Optics*, vol. 55, no. 1, pp. 79-88, 2008.
- [4] P. Kumar, A. Misra, D. Kumar, N. Dhama, T. P. Sharma, and P. N. Dixit, "Structural and optical properties of vacuum evaporated $Cd_xZn_{1-x}S$ thin films," *Optical Materials*, vol. 27, no. 2, pp. 261-264, 2004.
- [5] J. Torres and G. Gordillo, "Photoconductors based on $Zn_xCd_{1-x}S$ and $CdSe_{1-y}S_y$ thin films, fabricated with multi-layer structure," *Thin Solid Films*, vol. 310, no. 1-2, pp. 310-316, 1997.
- [6] S. V. Borse, S. D. Chavhan, and R. Sharma, "Growth, structural and optical properties of $Cd_{1-x}Zn_xS$ alloy thin films grown by solution growth technique (SGT)," *Journal of Alloys and Compounds*, vol. 436, no. 1-2, pp. 407-414, 2007.
- [7] G. K. Padam, G. L. Malhotra, and S. U. M. Rao, "Studies on solution-grown thin films of $Zn_xCd_{1-x}S$," *Journal of Applied Physics*, vol. 63, no. 3, pp. 770-774, 1988.
- [8] S. Yamaga, A. Yoshikawa, and H. Kasai, "Growth and properties of $Zn_{1-x}Cd_xS$ films on GaAs by low-pressure MOVPE," *Journal of Crystal Growth*, vol. 99, no. 1-4, pp. 432-436, 1990.
- [9] W. Li, L. H. Feng, L. L. Wu et al., "Preparation and properties of polycrystalline CdS_xTe_{1-x} thin films for solar cells," *Wuli Xuebao/Acta Physica Sinica*, vol. 54, no. 4, pp. 1879-1884, 2005.
- [10] R. D. Shannon, "Revised effective ionic radii and systematic studies of interatomic distances in halides and chalcogenides," *Acta Crystallographica Section A*, vol. 32, pp. 751-767, 1976.
- [11] R. Hill, "Energy-gap variations in semiconductor alloys," *Journal of Physics C*, vol. 7, no. 3, article 009, pp. 521-526, 1974.
- [12] M. R. Muhamad, "Excitonic electroabsorption in solid solution of $Cd_xZn_{1-x}S$ single crystals," *Japanese Journal of Applied Physics, Part 1*, vol. 32, no. 8, pp. 3385-3390, 1993.
- [13] D. Braunger, D. Hariskos, T. Walter, and H. W. Schock, "An 11.4% efficient polycrystalline thin film solar cell based on $CuInS_2$ with a Cd-free buffer layer," *Solar Energy Materials and Solar Cells*, vol. 40, no. 2, pp. 97-102, 1996.
- [14] R. Hunger, C. Pettenkofer, and R. Scheer, "Surface properties of (111), (001), and (110)-oriented epitaxial $CuInS_2/Si$ films," *Surface Science*, vol. 477, no. 1, pp. 76-93, 2001.
- [15] J. L. Lin, J. T. Lue, M. H. Yang, and H. L. Hwang, "Pulsed electron beam annealing of phosphorus-implanted $CuInS_2$," *Applied Physics Letters*, vol. 48, no. 16, pp. 1057-1059, 1986.

Research Article

Efficiency Considerations and Application Limits of Single-Phase Active Power Filter with Converters for Photoenergy Applications

Saša Sladić,¹ Srđan Skok,¹ and David Nedeljković²

¹ Faculty of Engineering, University of Rijeka, Vukovarska 58, 51000 Rijeka, Croatia

² Faculty of Electrical Engineering, University of Ljubljana, Tržaška 25, 1000 Ljubljana, Slovenia

Correspondence should be addressed to David Nedeljković, davidn@fe.uni-lj.si

Received 30 June 2011; Revised 11 August 2011; Accepted 29 August 2011

Academic Editor: Vincenzo Augugliaro

Copyright © 2011 Saša Sladić et al. This is an open access article distributed under the Creative Commons Attribution License, which permits unrestricted use, distribution, and reproduction in any medium, provided the original work is properly cited.

A new way of connecting PV sources to adaptive voltage active power filter (AV APF) has been compared with classic approach including active power filter (APF). In standard active power filter applications a relatively high DC link voltage (500 V or even more) with a buck converter or lower voltage (approx. 100 V) with boost converter can be used. These two converters appear also in adaptive voltage circuit of AV APF, but in this case it is possible to achieve many different connections of DC source. Benefit of this approach is that the same circuit is used for improving switching conditions in APF and for connection of solar cells. It appears that these two functions support each other and a large variety of DC voltages and currents can be connected to AC mains. Experimental results confirm expectations of increased energy transfer from additional DC source to network, especially for DC voltages being lower than DC link voltage.

1. Introduction

Renewable energy sources have variable output voltages and time-dependent output power. These unpredictable conditions demand flexible, high-efficiency converter [1]. Further demand of such a converter is high quality of delivered power. That means low-power energy sources should operate at near-unity power factor. It follows that additional DC sources can be connected to active power filter (APF). Basically, APF is a current generator which is intended for power factor improvement, but it can be used for connection of renewable energy sources to electric network, as well. Classic active power filter can operate at different levels of DC link (filter capacitor) voltage, which is usually controlled to be constant. The question, which filter capacitor voltage level is the most suitable for APF in sense of current distortion, has no conclusive answer [2]. However, DC link voltage has to be higher than maximal line voltage (>400 V) in order to ensure proper APF operation. Such approach has been used for decades [3–11]. Consequently, to obtain sufficient voltage for connection of PV source to DC link of classic APF, even in modern solutions, it is necessary to connect large number of solar cells in series [12].

Adaptive voltage approach is quite rare in active power filtering [13, 14], and adaptive voltage active power filter has not been widely investigated in sense of PV source connection [14]. Circuitry for filter capacitor voltage adaptation could additionally provide energy delivery from PV source, thus optimizing use of hardware. With this approach, beside the benefits of adaptive voltage APF (improved line current waveform and reduced APF switching losses), more energy from a renewable DC source could be transferred to the supply network. Generally, single-phase active power filter can be used for that purpose either with buck or boost DC/DC converter. Buck-converter approach enables high efficiency of DC/DC conversion [4, 12], but it is not suitable in cases when the DC source has voltage lower than DC link voltage (usually around 500 V). Boost converter is suitable for lower voltages (around 100 V, when the DC link voltage is around 500 V). Its main drawback is that its efficiency decreases as the step-up ratio increases [7]. In this paper several topologies are introduced and various possibilities of connections of renewable energy sources to active power filter are discussed and compared in sense of their efficiency for different voltage levels.

TABLE 1: Selection of active switches in single-phase shunt APF.

	$v_S < 0$	$v_S > 0$
S_1	1	0
S_2	0	1
	$i_{Sr} > i_S$	$i_{Sr} < i_S$
S_3	0	1
S_4	1	0

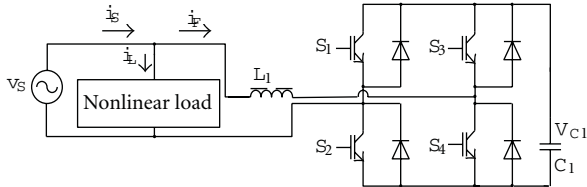


FIGURE 1: Single-phase shunt (H-bridge) active power filter.

2. Efficiency Consideration of Classic Active Power Filter

In order to determine APF efficiency, a practical model of APF was used, as shown in Figure 1. Active power filter with constant filter capacitor voltage consists of four switches (S_1 – S_4). H-bridge acts as a current drain when the neighbouring switches are active, for example, S_2 and S_4 . On the other hand, H-bridge acts as a current source in case when the diagonal switches are conducting, for example, S_2 and S_3 . The combination of conducting switches is selected according to the sign of supply network voltage v_S and the sign of supply current reference error (i.e., the difference between supply current reference i_{Sr} and its actual value i_S), as shown in Table 1.

Therefore, always one transistor in a transistor leg is conducting; transistor switching conditions are rather hard, because its switching voltage is determined by DC link voltage V_{C1} . This voltage is quite high (>320 V, typically 500 V [2]) for an APF connected to classic 230 V, 50 Hz electric network. That means DC (PV) source voltage has to be high, at least 500 V.

Typical experimental waveforms during APF operation, including DC link voltage, are shown in Figure 2. It can be noted that DC link voltage was about 600 V [2, 15]. That means photovoltage of connected solar cells would have to be higher than this DC link voltage, oppositely energy transmission to AC network would not be possible. Consequently, a large number of solar cells have to be connected in series and eventual shadowing of one section of solar array can stop energy transfer of the whole system.

In order to increase capability of energy transfer to AC mains, energy transfer has to be enabled for lower voltages (<100 V), as well. Tests were conducted with DC voltage of 33 V (DC source, or one module of solar cells). That means a boost converter, shown in Figure 3, has to be used, or some other step-up converter, possibly with electric transformer [5].

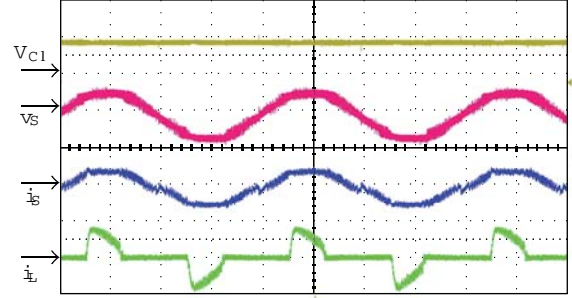
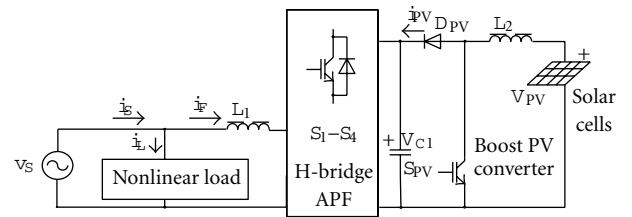
FIGURE 2: Measured waveforms of active power filter (APF), filter capacitor voltage (V_{C1}), line voltage (v_S), line current (i_S), and load current (i_L); THD(i_S) = 7.1%, THD(i_L) = 92%, (5 A/div., 500 V/div., 5 ms/div.).

FIGURE 3: Single-phase shunt active power filter with boost converter and PV source [7].

DC source voltage V_{PV} is quite low compared to DC link voltage V_{C1} , which makes energy transfer demanding [10], so DC link voltage has to be reduced in order to obtain significant energy transfer.

It was noticed that energy transfer from DC source to electric network strongly depends on DC link voltage. In the test, shown in Figure 4, the lowest possible DC link voltage was chosen, and it was recorded that 145 W was transferred from PV source to AC network. In spite of flexibility of this approach, it can be noted in the literature that buck converter is more frequent [8]. Intention of further work was to increase efficiency of APF system and to enable connection of lower voltages to APF. Furthermore, transmitted power should be increased.

3. Efficiency Consideration of Adaptive Voltage Active Power Filter

One possible approach to adaptive voltage active power filter (AV APF) is shown in Figure 5. This topology is obtained in frame of adaptive voltage converter which is used for adaptation of filter capacitor voltage to the conditions in electric network. This approach can be found in inverters [13, 16], but it is quite rare in APF applications [14]. It is important to notice that for discharging of filter capacitor a boost converter has been used and a buck converter for its charging. In this case an efficiency improvement can be expected since voltage adaptation improves the switching conditions in active power filter (H-bridge). It is important to mention that for such a result switching frequency of

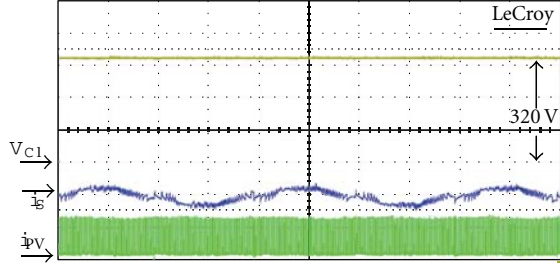


FIGURE 4: Measured filter capacitor voltage (V_{C1}), line current (i_s), and boost converter output current (i_{pv}) for maximal power ($P = 145$ W) for given DC source (33 V) and constant filter-capacitor voltage (100 V/div., 5 A/div.).

adaptive voltage circuit (S_5 and S_6) was set to 5 kHz [14] in order to limit the switching losses of adaptive voltage converter, shown in Figure 5.

Adaptive filter capacitor voltage has influence on both harmonic distortion (THD) of line current (i_s) and switching conditions of entire PV system (H-bridge and DC/DC converter). Filter capacitor reference voltage is formed on basis of absolute line voltage. When the APF DC link is being discharged, filter capacitor voltage (V_{C1}) demands higher voltage; otherwise filter capacitor voltage has to be close to absolute line voltage. In this way, source current (i_s) ripple is decreased compared to classic approach [14]. Mathematically, filter capacitor reference voltage can be expressed as

$$\begin{aligned} v_{Cr} &= k_1 |v_S| + k_2 \cdot \text{sign}(i_F) \cdot (-v_S), \\ v_{Cr} &= k_1 |v_S| + k_2 \cdot i_{fk}. \end{aligned} \quad (1)$$

Constant k_1 has to be slightly higher than 1, and k_2 has resistive character. Its value should be around 10Ω or higher. Current i_{fk} is defined as a current which is supplied from the APF when the APF acts as a current source. This current is continuous, which is different from the current which is supplied from the filter capacitor, which is discontinuous. Experimental results for AV APF are shown in Figure 6. During the intervals within the cycle, when the AV APF is acting as a current source (action of current i_{fk}), filter capacitor voltage V_{C1} is higher than 600 V. For other intervals, when AV APF is acting as a current drain, voltage V_{C1} is reduced to around 200 V. When the filter capacitor voltage is controlled to be constant, as shown in Figure 2, its value has to be constantly high (600 V) in order to avoid converter saturation.

Since the line voltage is sinusoidal, it crosses zero twice a cycle. When the line voltage is so low, filter capacitor voltage could be much lower than 600 V, for example, 200 V, but compensation of nonlinear load will still be possible. Since permanently high-voltage V_{C1} means higher voltage stress (hard switching) for all switches in APF, adaptive voltage V_{C1} leads to improved efficiency in spite of larger number of switches, as it was measured and shown in Figure 7.

It was confirmed that intervals of lower filter capacitor voltages support the energy transfer of photovoltaic energy.

Experimental results were recorded for the power of 80 W received from PV side of converter, see Figure 8. This figure illustrates the influence of filter capacitor (DC link) voltage to maximal power received from DC/DC converter (e.g., MPPT converter). A value of 80 W represents the mean power transmitted to AC side of AV APF. Within this test, adaptive voltage of filter capacitor increases the transmitted power from PV source to the AC network approximately by factor two (at this power level), because minimal output current from DC/DC converter represents less than half of its maximal value. Therefore the same converter (boost) can transmit more power to the AC network for the same PV voltage and equal DC/DC converter duty cycle, by adaptive voltage approach.

Adaptive filter capacitor voltage obtains different waveforms for different nonlinear loads, but AV APF filter capacitor always involves intervals of decreased filter capacitor voltage.

4. Efficiency Consideration of Buck Converter

Buck converter from Figure 9 can be used for PV energy injection [4, 8] both in APF and AV APF applications because its conversion is highly efficient. However, energy transfer is not possible for the PV cells/module voltage being too low.

Buck converter efficiency depends on its output resistance R_e . It could be written as

$$\begin{aligned} \eta &= \frac{P_O}{P_O + P_{\text{loss}}} = \frac{V_O^2/R_e}{(V_O^2/R_e) + I_L^2 \cdot r_L} \\ &= \frac{V_O^2/R_e}{(V_O^2/R_e) + [V_O/R_e]^2 \cdot r_L} = \frac{1}{1 + (r_L/R_e)}. \end{aligned} \quad (2)$$

In (2), the only losses in inductor parasitic resistance were taken into account. It can be seen that efficiency η of buck converter depends on the ratio of inductor parasitic resistance (r_L) and equivalent resistance (R_e). In the case of variable output voltage, output current tends to flow more through diode D rather than through transistor T (same output current) for the same output power. Since diode D has lower voltage drop than transistor, slightly higher efficiency can be achieved with adaptive filter capacitor voltage, rather than with constant filter capacitor voltage. With adaptive filter capacitor voltage, lower input voltage of buck converter can be used, as well.

From the theorem on maximal power, it follows that maximal power given to the load (R_e) equals the power on parasitic resistance r_L ,

$$P_{O\text{max}} = \frac{1}{2} P_{\text{IN}}. \quad (3)$$

Since the same current flows through inductor L and the load, it could be written

$$r_L = R_e. \quad (4)$$

From (4) it follows that maximal power appears with efficiency of 50%.

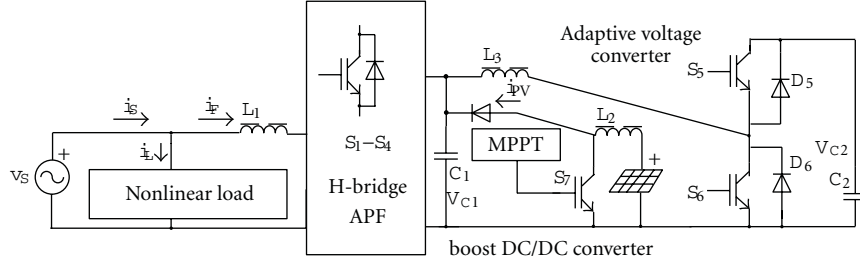


FIGURE 5: Single-phase adaptive voltage active power filter with PV source directly connected to filter capacitor.

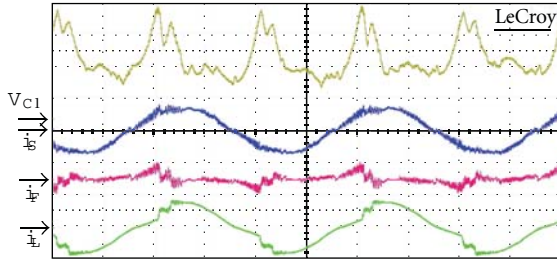


FIGURE 6: Measured waveforms of adaptive voltage active power filter: filter capacitor voltage (V_{C1}), line voltage (v_s), line current (i_s), and load current (i_L); $\text{THD}(i_s) = 4.9\%$, $\text{THD}(i_L) = 30\%$, (5 A/div., 200 V/div., 5 ms/div.).

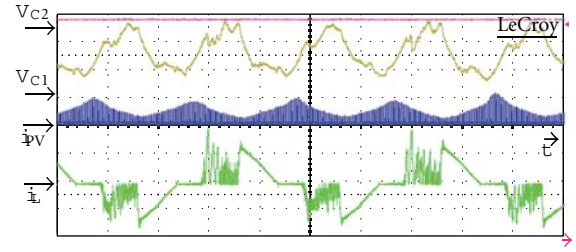


FIGURE 8: Injection of PV current i_{PV} with adaptive filter-capacitor voltage V_{C1} (200 V/div, $P_{PV} = 80$ W, 5 A/div, 5 ms/div.).

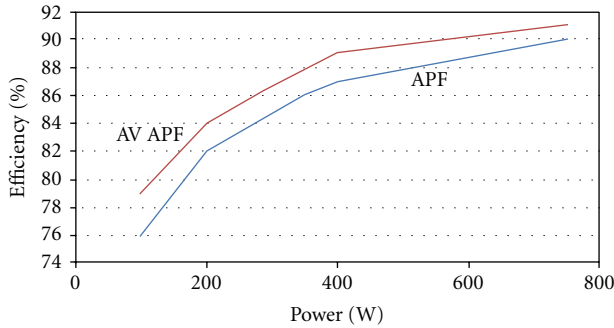


FIGURE 7: Efficiency of APF compared to AV APF efficiency.

Decreased filter capacitor voltage indicates that equivalent resistance

$$R_e = \frac{V_{C1}}{i_{PV}} \quad (5)$$

decreases, as well. DC/DC converters are usually designed in order to ensure high efficiency, which means $R_e \gg r_L$. Reduced equivalent output resistance meets condition (3) at higher output current. That means power transmitted to AC network is increased by periodical voltage drop. Efficiency of buck converter (2) is generally high; however, it is desirable that voltage difference between input and output voltage is as low as possible [17], especially for higher switching frequencies. High periodic change of voltage difference between input and output voltage has negative influence on its switching losses; hence for the design of buck converter in

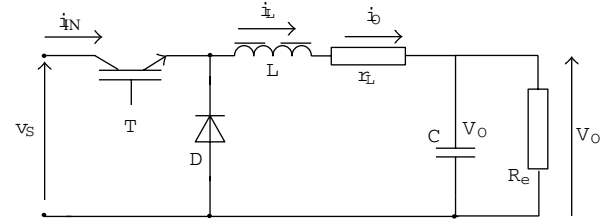


FIGURE 9: Buck converter with its parasitic resistance r_L .

AV APF application, it is preferable that buck converter has lower switching frequency.

5. Efficiency Consideration of Boost Converter

Boost converter, shown in Figure 10, can be used in applications where PV voltage has to be increased. Its efficiency depends not only on ratio between inductor resistance and equivalent resistance, but also on converter duty cycle,

$$\begin{aligned} \eta &= \frac{P_O}{P_O + P_{\text{loss}}} = \frac{V_O^2/R_e}{(V_O^2/R_e) + I_L^2 \cdot r_L} \\ &= \frac{V_O^2/R_e}{V_O^2/R_e + [V_O/(R_e \cdot (1-D))]^2 \cdot r_L} \\ &= \frac{1}{1 + (r_L/(R_e \cdot (1-D)^2))}. \end{aligned} \quad (6)$$

Equation (6) indicates strong relation between duty cycle D of transistor T and boost converter efficiency. Obviously,

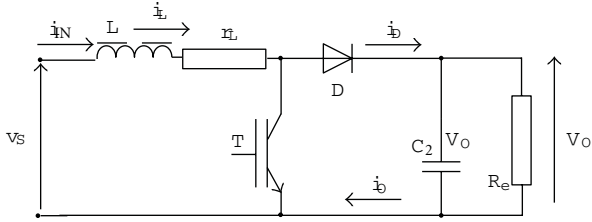


FIGURE 10: Boost converter equivalent circuit.

it is desirable to transfer energy with as low-duty cycle as possible, since input and output voltages are related by

$$V_O = \frac{V_S}{1-D}. \quad (7)$$

It means that efficiency will be higher for lower step-up ratio of input (V_S) and output voltages (V_O). In case when the filter capacitor voltage (V_{C1}) is lower or equal to the boost converter output voltage, higher efficiency of boost converter can be achieved.

Equivalent resistance R_e is defined like in buck converter by (5). It decreases as filter capacitor voltage (periodically) decreases, which means its value is approaching to condition (3). Furthermore, increase of output boost converter current additionally reduces equivalent resistance. Consequently, power transmitted to AC mains is increased by periodical voltage drop. An increase of transmitted power from DC source to AC network means that the same output power will be achieved with lower-duty cycle of DC/DC converter. According to (6), that leads to higher efficiency of boost converter and lower transistor current for the same output power. It can be stated that periodic voltage drop improves the boost converter performance, making it more competitive to buck converter in sense of efficiency since influence of its duty cycle is reduced.

In order to confirm positive effect of filter capacitor voltage adaptation to boost converter, the duty cycle equation (7) for nonideal case can be used

$$D = \frac{V_O - V_S}{V_O} \cdot \eta. \quad (8)$$

Measurement of boost output current, shown in Figure 8, was repeated for different load levels (duty cycles of boost converter). In one case output resistance was a constant and in other case output resistance was a periodic function. In both cases nonlinear load was successfully compensated by APF. In case of constant filter capacitor voltage, the maximal power was recorded for $D = 0.65$. In second case same power was recorded for $D = 0.55$. Further increase of duty cycle in second case increases the DC power transfer. So the maximal transferred power is larger in case of AV APF than for classic APF. Measurements were conducted for low DC power level. Measured transferred power was 145 W for constant filter capacitor voltage and 190 W for adaptive voltage approach. In both cases the same converter with 33 V DC source was used.

This simple measurement illustrates the way in which a boost converter increases its low-input voltage power

capability, so it can operate with low-duty cycle in order to obtain high efficiency, according to (6). In this way, theoretical expectations are confirmed practically. It can be concluded that variable output voltage of boost converter decreases the transistor current for the same output power and increases the boost converter efficiency.

6. Two-Direction Buck-Boost (TDB) Converter and Its Application Limits

Adaptive voltage circuit [13, 16] can be used in many ways in order to connect an additional DC source, and some approaches are already reported [18].

Solar cells can be connected to AC network without additional inductor by two-direction boost-buck adaptive voltage active power filter (TDB AV APF) which is shown in Figure 11. This approach has not been discussed in the literature, so far. It consists of classic H-bridge, adaptive voltage circuit and additional transistor, and diode, and DC source. It can be noted that adaptive voltage converter shares the same inductor (with terminal in its middle) with TDB converter. Adaptive voltage converter charges (action of switch S_5) and discharges (action of switch S_6) the filter capacitor (C_1).

Adaptive filter capacitor voltage improves the switching conditions both for H-bridge and for DC/DC converter because of lower switching voltages. Lower voltages mean lower switching losses and higher efficiency. Quasi-resonant approach in APF, especially in single-phase APFs, is quite rare [14]. More sophisticated approach, offering the synergy between recharging of filter capacitor and connection of additional sources, has been proposed in [18]. Application of this circuit could possibly arise in automotive industry, where two or even more different voltage systems coexist (e.g., 12 V and 42 V) and additional energy sources (e.g., solar cells) tend to partially replace energy from fossil fuels.

Inductances L_{21} and L_{22} are the only parts of inductance L_2 . First question, which arises when the inductance should be divided, is ratio of its division. Two main factors influence the final decision for the division ratio of inductance L_2 : first, PV voltage which (usually) has to be stepped up and second, converter efficiency (which is generally higher for buck comparing to boost converter). However, experiments show that 50:50 ratio is most appropriate, because adaptive-voltage converter dynamics demands fast changes and relatively low inductance.

This approach has several advantages compared to solution with constant filter capacitor voltage, since solar cells can release their energy to capacitors C_1 or C_2 or to both of them in desired ratio (action of S_7 selects the interval of energy transfer), according to PV voltage or APF operation needs. It is known that in both converters, boost and buck, load current flows also when an appropriate switch (S_5 or S_6) is not conducting. This is a consequence of energy accumulated in their inductors. Figure 12 shows equivalent schemes for both cases (boost and buck) for intervals when the S_5 and S_6 are not conducting.

Redirecting of flyback current, when the energy is supplied from DC link (can be capacitor either C_1 or

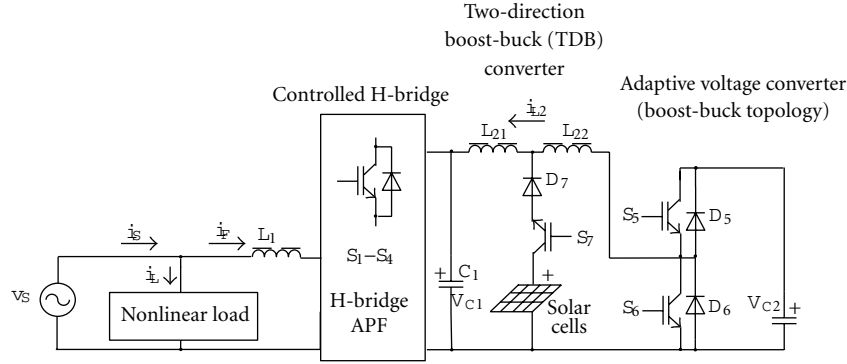


FIGURE 11: Single-phase APF with TDB converter in adaptive voltage circuit (magnetically coupled inductances).

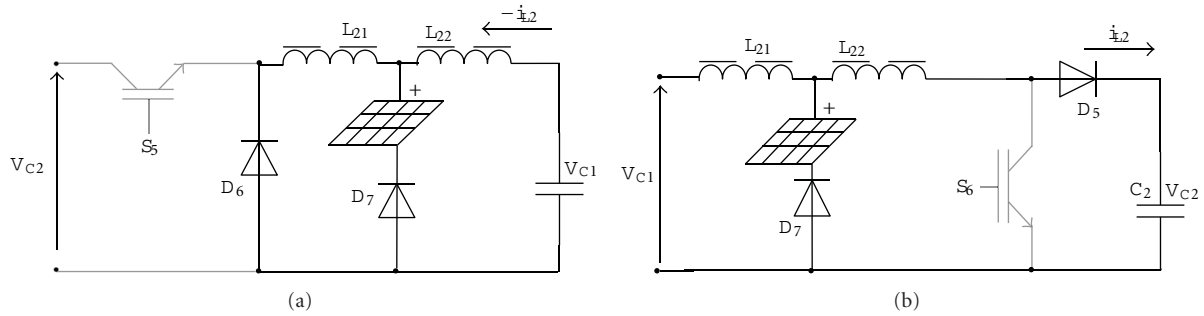


FIGURE 12: Buck (a) and boost (b) converters (interval $(1-D)T$): simplified TDB converter operation.

C_2), means that quasi-resonant circuit (adaptive voltage converter) action supports the current through the solar cells. Current could flow through PV cells even when their voltage is lower than voltages on capacitors C_1 and C_2 .

In the case of boost converter, current flows through the path: diode D_7 , DC source, inductor (L_{22}), and in the case of buck converter, current flows through the so-called flyback diode (D_6) or through DC source and diode D_7 . In both cases, current is decreasing. In TDB converter, these currents are commutated to PV source even for very low DC voltages (e.g., 10 V). It is useful to observe mentioned intervals in experimentally recorded waveform of current i_{L2} (current through inductor L_2), as shown in Figure 13.

Waveforms of filter capacitor voltage (V_{C1}), current through inductor L_2 (i_{L2}) and load current were measured at 110 V of supply voltage. When the i_{L2} is positive, capacitor C_1 is being charged, and when it is negative, C_1 is being discharged. Charging of C_1 is related with the buck action from the capacitor C_2 , and discharging is related with the boost action, when the capacitor C_2 (DC link) is being charged. Condition for solar cells to retake decreasing current is to have positive voltage (buck operation) and to have positive voltage higher than V_{C1} (boost operation). Energy between two capacitors (C_1 and C_2) is circulating even when the AV APF is unplugged ($I_F = 0$), so the solar cell can cover APF losses at low loads.

In spite of its advantages, TDB approach is less suitable for low PV voltages than boost converter approach, because TDB internal boost converter transmits energy to higher

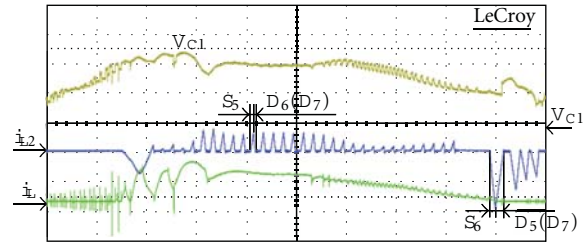


FIGURE 13: Measured waveforms of filter capacitor voltage (V_{C1}), current through L_2 (i_{L2}), and load current (i_L) at 110 V source voltage and approximately 300 W load power (100 V/div, 2 A/div, 1 ms/div).

voltage (V_{C2}) than the boost converter, connected to adaptive voltage (V_{C1}). However, this disadvantage can be partially removed in cases when the filter capacitor voltage obtains values close to zero. Measured waveforms for such a case are given in Figure 14, where PV energy can be transmitted to the filter capacitor even when the PV voltage is extremely low.

Intervals with low filter capacitor voltage, as previously stated, reduce the switching losses in H-bridge. Furthermore, distortion (THD) of line current (i_s) can be also reduced in comparison with constant voltage APF operation, as was previously reported [14, 18]. It can be stated that TDB connection, as well as direct AV APF connection, increases the energy transfer from secondary DC source. The cause for PV current increase in TDB configuration is a combined action of DC link capacitor and PV source. The percentage

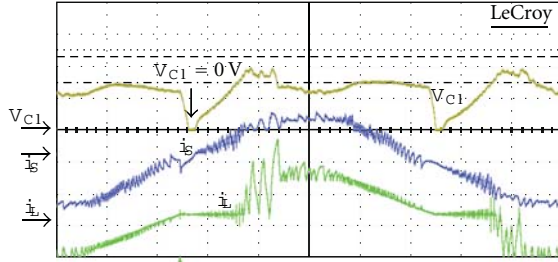


FIGURE 14: AV APF operation and voltage adaptation with multiple nonlinear loads; measured filter-capacitor voltage (V_{C1}), source current (i_s), and load current (i_L) at 110 V source voltage and approximately 300 W load power (100 V/div, 2 A/div, 2 ms/div.).

TABLE 2: Comparison of different APF converter types in sense of switch and inductor number in addition to the possibility of connection of low DC voltages and efficiency.

	Number of switches	Inductors (mass)	PV voltage	Efficiency
APF	4	1	—	+
AV APF	6	2	—	++
APF + buck	5	2	-	+
APF + boost	5	2	+	-
AV APF + buck	7	3	+/-	+
AV APF + boost	7	3	++	+
TDB AV APF	7	2	+	+/-

of this increase depends on filter capacitor voltage and DC source voltage. For 110 V of supply voltage, intervals appear when filter capacitor voltage reaches zero. In this case any DC voltage could transfer energy to filter capacitor.

At low loads and lower supply voltages, voltage V_{C1} could reach zero voltage, but with power approaching 1 kW, adaptive voltage tends to the waveform from Figure 8. In each case, energy from the solar cells could be transferred to AC mains. It can be noted that numerous connections of additional DC sources can be obtained. Some of them are compared in Table 2. Topologies were tested at flexible prototype based on TMS320LF2407.

7. Conclusion

Renewable energy sources are usually of uncertain or low voltage, and their connection to AC mains is rather difficult, especially because high efficiency is demanded. To solve this complex problem, active power filter (APF) can be used. However, adaptive voltage active power filter (AV APF) has lower losses because of soft switching. Besides, adaptive voltage converter can be used to support connection of low-voltage DC source. That makes AV APF very attractive for different renewable energy applications. In this paper two emerging connection types were compared in sense of their performances. Both solutions that were analyzed, direct connection of additional DC source to filter capacitor and two-direction boost-buck (TDB) converter, enable

application of lower voltages than in case of classic, constant voltage APF. Energy transferred to AC mains is increased compared to the case of APF with constant filter capacitor voltage. Improvement in case of direct connection of boost converter to AV APF is higher than in case of TDB converter (measurements were conducted with 33 V DC source), but TDB converter has lower number of inductors and can be lighter.

References

- [1] M. Taherbaneh, A. H. Rezaie, H. Ghafoorifard, K. Rahimi, and M. B. Menhaj, "Maximizing output power of a solar panel via combination of sun tracking and maximum power point tracking by fuzzy controllers," *International Journal of Photoenergy*, vol. 2010, Article ID 312580, 13 pages, 2010.
- [2] D. A. Torrey and A. M. A. M. Al-Zamel, "Single-phase active power filters for multiple nonlinear loads," *IEEE Transactions on Power Electronics*, vol. 10, no. 3, pp. 901–908, 1995.
- [3] T. Al Chaer, J.-P. Gaubert, L. Rambault, and M. Najjar, "Linear feedback control of a parallel active harmonic conditioner in power systems," *IEEE Transactions on Power Electronics*, vol. 24, no. 3, pp. 641–653, 2009.
- [4] T. F. Wu, H. S. Nien, C. L. Shen, and T. M. Chen, "A single-phase inverter system for PV power injection and active power filtering with nonlinear inductor consideration," *IEEE Transactions on Industry Applications*, vol. 41, no. 4, pp. 1075–1083, 2005.
- [5] J. Wang, F. Z. Peng, J. Anderson, A. Joseph, and R. Buffenbarger, "Low cost fuel cell converter system for residential power generation," *IEEE Transactions on Power Electronics*, vol. 19, no. 5, pp. 1315–1322, 2004.
- [6] G. R. Walker and P. C. Sernia, "Cascaded DC-DC converter connection of photovoltaic modules," *IEEE Transactions on Power Electronics*, vol. 19, no. 4, pp. 1130–1139, 2004.
- [7] N. Patcharaprakiti, S. Premrudeepreechacharn, and Y. Sriuthaisirivong, "Maximum power point tracking using adaptive fuzzy logic control for grid-connected photovoltaic system," *Renewable Energy*, vol. 30, no. 11, pp. 1771–1788, 2005.
- [8] T. F. Wu, H. S. Nien, H. M. Hsieh, and C. L. Shen, "PV power injection and active power filtering with amplitude-clamping and amplitude-scaling algorithms," *IEEE Transactions on Industry Applications*, vol. 43, no. 3, pp. 731–741, 2007.
- [9] S. B. Kjaer, J. K. Pedersen, and F. Blaabjerg, "A review of single-phase grid-connected inverters for photovoltaic modules," *IEEE Transactions on Industry Applications*, vol. 41, no. 5, pp. 1292–1306, 2005.
- [10] D. D. C. Lu and V. G. Agelidis, "Photovoltaic-battery-powered DC bus system for common portable electronic devices," *IEEE Transactions on Power Electronics*, vol. 24, no. 3, pp. 849–855, 2009.
- [11] R. W. Erickson and D. Maksimović, *Fundamentals of Power Electronics*, Kluwer Academic, Boston, Mass, USA, 2nd edition, 2001.
- [12] Y. Chen and K. M. Smedley, "A cost-effective single-stage inverter with maximum power point tracking," *IEEE Transactions on Power Electronics*, vol. 19, no. 5, pp. 1289–1294, 2004.
- [13] D. M. Divan and G. Skibinski, "Zero-switching-loss inverters for high-power applications," *IEEE Transactions on Industry Applications*, vol. 25, no. 4, pp. 634–643, 1989.
- [14] S. Sladić, B. Barišić, and M. Soković, "Cost-effective power converter for thin film solar cell technology and improved

- power quality,” *Journal of Materials Processing Technology*, vol. 201, no. 1–3, pp. 786–790, 2008.
- [15] Q. Li and P. Wolfs, “A review of the single phase photovoltaic module integrated converter topologies with three different DC link configurations,” *IEEE Transactions on Power Electronics*, vol. 23, no. 3, pp. 1320–1333, 2008.
- [16] S. Behera, S. P. Das, and S. R. Doradla, “Quasi-resonant inverter-fed direct torque controlled induction motor drive,” *Electric Power Systems Research*, vol. 77, no. 8, pp. 946–955, 2007.
- [17] M. S. Rahman, *Buck converter design issues*, M.S. thesis, Linköping Institute of Technology, Linköping, Sweden, 2007, LiTH-ISY-EX—06/3854—SE.
- [18] S. Sladić, P. Zajec, and D. Nedeljković, “Transformerless connections of low voltage DC sources to single-phase shunt active power filter with adaptive filter capacitor voltage,” in *Proceedings of the International Symposium on Power Electronics, Electrical Drives, Automation and Motion (SPEEDAM '10)*, pp. 1537–1540, Pisa, Italy, June 2010.

Research Article

TiO₂/Chitosan-NH₄I(+I₂)-BMII-Based Dye-Sensitized Solar Cells with Anthocyanin Dyes Extracted from Black Rice and Red Cabbage

M. H. Buraidah,¹ L. P. Teo,¹ S. N. F. Yusuf,¹ M. M. Noor,^{1,2} M. Z. Kufian,¹ M. A. Careem,³ S. R. Majid,¹ R. M. Taha,⁴ and A. K. Arof¹

¹ Centre for Ionics University Malaya, Department of Physics, University of Malaya, 50603 Kuala Lumpur, Malaysia

² Centre for Foundation Studies, International Islamic University Malaysia, Jalan Universiti, 46350 Petaling Jaya, Selangor, Malaysia

³ Department of Physics, University of Peradeniya, 20400 Peradeniya, Sri Lanka

⁴ Institute of Biological Sciences, University of Malaya, 50603 Kuala Lumpur, Malaysia

Correspondence should be addressed to A. K. Arof, akarof@um.edu.my

Received 8 July 2011; Revised 26 August 2011; Accepted 2 September 2011

Academic Editor: Gaetano Di Marco

Copyright © 2011 M. H. Buraidah et al. This is an open access article distributed under the Creative Commons Attribution License, which permits unrestricted use, distribution, and reproduction in any medium, provided the original work is properly cited.

Dye sensitized solar cells (DSSCs) were fabricated using anthocyanin dye and polymer electrolyte with ammonium iodide (NH₄I) salt. The study was designed to focus on increasing the efficiency of the DSSC. DSSC using 26.9 wt. % chitosan-22 wt. % NH₄I(+2.2 wt. % I₂)-48.9 wt. % IL solid electrolyte, black rice anthocyanin with Pt counter electrode showed J_{sc} of 172 $\mu\text{A cm}^{-2}$ and V_{oc} of 195 mV. The performance of the cell with Pt electrode was further improved by coating a blocking layer on the indium tin oxide (ITO) substrate. The black rice DSSC using 11 wt. % (chitosan:PEO, wt. ratio 30:70)-9 wt. % NH₄I-80 wt. % BMII gel electrolyte exhibited J_{sc} of 1213 $\mu\text{A cm}^{-2}$, V_{oc} of 400 mV, FF of 0.47, and η of 0.23%. The red cabbage anthocyanin DSSC containing (phthaloyl chitosan-PEO)-NH₄I-BMII gel electrolyte using tartaric acid to adjust the pH of anthocyanin solution showed the best performance with the fill factor of 0.39, J_{sc} of 3503 $\mu\text{A cm}^{-2}$, V_{oc} of 340 mV, and an overall conversion efficiency of 0.46%.

1. Introduction

Dye-sensitized solar cells (DSSCs) have gained much interest as energy converters since they are inexpensive compared to conventional silicon solar cells, easy to fabricate, and can achieve high solar energy conversion efficiency [1]. Dye-sensitized solar cell (DSSC) which is a type of photoelectrochemical cell utilizing electrolyte as a medium for charge transport comprises a transparent conducting oxide (TCO) glass, semiconductor as photoelectrode, dye-sensitized agent, electrolyte containing redox mediator, and counter electrode. Titanium dioxide (TiO₂) is most commonly used as photoanode in DSSC application since it is nontoxic, inert, and has a large energy bandgap (E_g of ~ 3 eV) as well as good optical and electrical properties and, thus, can be efficiently sensitized by a dye [2].

Other than photoelectrode, counter electrode is also one of the main constituents in DSSC which makes it worthy

of investigation. The function of counter electrode is to transfer electrons received from the external circuit into the electrolyte and enable the reduction of the oxidized charge mediator. The selection of material as counter electrode requires the material to possess low charge-transfer resistance, good chemical and electrochemical stability in the electrolyte/electrode interface, and capability to catalyze the reduction of redox mediator [3]. Platinum (Pt) and carbon-based materials are two most popular choices to serve as counter electrode. Others include conducting polymers, that is, poly(3,4-ethylenedioxythiophene) (PEDOT) [4], polypyrrole (PPy) [5], and polyaniline (PANI) [6]. Some examples of carbon-based materials include graphite [7], activated carbon [8], carbon black [9], and carbon nanotube [10, 11]. However, Pt is more suitable to serve as counter electrode than carbon-based materials due to its excellent catalytic activity and low charge-transfer resistance [12]. Pt exhibits excellent catalyst behaviour, high electrical conductivity, low

charge-transfer resistance, and light reflecting properties [3, 13]. Hence, Pt was employed as counter electrode in the present study. Herein, Pt was deposited on indium tin oxide (ITO) glass substrate via thermal decomposition method which is an easy and cheaper way of preparation compared to sputtering technique.

The function of dye is to absorb light, inject electrons into the TiO_2 conduction band, and then accept electrons from the redox mediator in the electrolyte. Although the ruthenium (II) polypyridyl complexes are the most popular synthetic dye-sensitizing agent [14–17], it has several disadvantages including high cost, long-term unavailability, and complex process of synthesis and is environmentally unfriendly due to the heavy metal it contains [18]. As an alternative, natural dye can be used as sensitizer for DSSC. Natural dye is readily available and cheap, thus, making it environmental friendly and can reduce the cost of DSSC devices.

Anthocyanins are natural compounds commonly found in flowers, fruits, and leaves of plants such as the canary bird flower (*Rosa xanthina*) [19], blue pea (*Clitoria ternatea*) flowers [20], strawberries [21], blackberries [22], pomegranate fruits [23, 24], and maple leaves [25]. Anthocyanin used in this study was extracted from black rice (*Oryza sativa*) and red cabbage (*Brassica oleracea*) both of which have been reported to exhibit antioxidant property [26–28]. Black rice was chosen as it shows the best sensitization as reported by Hao and coworkers [19]. Anthocyanin from red cabbage is used mainly in food coloring and beverage industries as well as in making sweets and chewing gum [29, 30]. The utilization of red cabbage as sensitizer is worthwhile investigating since up to now only Zhang's [31] and Furukawa's groups [32] employed anthocyanin dye from red cabbage as sensitizer in DSSC.

Polymer electrolytes (PEs) that offer many advantages such as fast ion transport, electrochemical stability, and good mechanical properties [33] have replaced the use of liquid electrolytes in semiconductor/electrolyte junction solar cells [34, 35]. Intensive efforts have been geared towards increasing the conductivity of the polymer electrolytes in order to improve the performance of the solar cells. These efforts include blending of polymers [36–38], adding plasticizers [39–41] and ionic liquid (IL) [42–44] into the polymer electrolyte. Ionic liquids (IL) are nonvolatile and nonflammable materials. They have high thermal stability, high ionic conductivity, and wide potential windows [45–47]. Gel polymer electrolytes exhibit both the cohesive property of a solid and also diffusive nature of a liquid which results in high ionic conductivity, long-term stability, and superior interfacial contact between electrodes and electrolyte [48].

In our earlier work [49], 50 wt. % ionic liquid 1-butyl-3-methylimidazolium iodide (BMII) was added into a chitosan ammonium iodide (NH_4I) polymer electrolyte. A TiO_2 DSSC was fabricated with ITO as counter electrode using anthocyanin extracted from black rice and betacyanin from the callus of *Celosia plumosa*, respectively, as sensitizer. In this work, DSSC is fabricated from a combination of relatively cheap materials containing TiO_2 photoelectrode, natural dye, polymer electrolyte containing I^-/I_3^- redox mediator, and

TABLE 1: Various electrolyte composition.

Chitosan (wt. %)	Phthaloyl chitosan (wt. %)	PEO (wt. %)	NH_4I (wt. %)	BMII (wt. %)
27.5	—	—	22.5	50
11	—	—	9	80
3.3	—	7.7	9	80
—	11	—	9	80
—	3.3	7.7	9	80

counter electrode. In this study, chitosan- NH_4I electrolytes containing different amounts of IL were prepared in solid and gel forms, and the relationship between conductivity of the polymer electrolytes and DSSC performance (short-circuit current density) was examined. To the best of the authors' knowledge, all the natural dye DSSCs reported in the literature are using liquid electrolyte.

2. Experimental

2.1. Preparation and Characterization of the Electrolyte. The composition of the electrolytes is shown in Table 1. The electrolyte film consisting of chitosan- NH_4I -BMII and (chitosan-PEO)- NH_4I -BMII were prepared by the solution cast technique. The appropriate amounts of chitosan, PEO, NH_4I , and BMII were dissolved in 50 mL 1% acetic acid solution at room temperature. The solutions were then cast in different petri dishes, and the solvent was allowed to evaporate to form films. Gel polymer electrolytes for that composition were prepared by reducing the solvent to 20 mL.

For the preparation of electrolyte containing phthaloyl chitosan- NH_4I -BMII and phthaloyl chitosan-PEO- NH_4I -BMII, 10 mL dimethylformamide (DMF) was used as solvent. 0.04 g of iodine (I_2) crystals was added into the electrolytes in order to provide I^-/I_3^- redox couple for DSSC applications. Impedance of the electrolytes was measured by the complex impedance technique using the HIOKI 3531-01 LCR Hi-Tester in the frequency range from 50 Hz to 1 MHz.

2.2. Preparation of Anthocyanin Extracts. The natural colorant-containing anthocyanin was extracted from black rice and red cabbage, respectively. 100 g black rice was immersed in 80 mL ethanol solution (95%) and kept at room temperature without exposing to light. 100 g red cabbage was soaked in 120 mL ethanol, and the red cabbage was replaced after 5 hours in order to obtain concentrated solution. The residues were removed by filtration, and the pH of the dye was adjusted by adding hydrochloric acid (HCl) or tartaric acid. The absorption characteristics of the anthocyanin containing natural colorant at different pHs in the range 400 to 700 nm were determined using a Shimadzu PC3101 UV-Vis NIR spectrophotometer.

2.3. Preparation of the TiO_2 /Dye Electrode. The ITO glass ($2.5 \times 2.5 \text{ cm}^2$) was cleaned with distilled water and acetone to remove impurities. The cleaned ITO surface was coated

with commercially available nanocrystalline TiO_2 paste using the doctor-blade method. The ITO/ TiO_2 electrodes were sintered at 500°C for 1 hour. The thickness of the TiO_2 layer was controlled using adhesive tape of thickness $100\ \mu\text{m}$. When the temperature of the TiO_2 electrodes reached 100°C during cooling, the electrodes were immersed in the anthocyanin dye solution for 24 hours. The white TiO_2 film will change color when dye is absorbed. The TiO_2 /dye electrode was washed with water to remove impurities and then with ethanol to remove trapped water from the initial washing.

2.4. Preparation of Pt Counter Electrode. To prepare platinum catalyst coated on ITO glass substrate, $5\ \text{mmol L}^{-1}$ hexachloroplatinic acid solution in isopropanol was spread on the ITO conducting surface. The Pt-coated ITO counter electrode was then heated in a furnace at $723\ \text{K}$ for 30 minutes.

2.5. Fabrication of Natural Colorant-Sensitized Solar Cells (DSSCs). Natural colorant-sensitized solar cells with active area about $0.16\ \text{cm}^2$ were fabricated by sandwiching the electrolyte between TiO_2 /dye electrode and Pt counter electrode. The J - V characteristics of the dye-sensitized solar cells were obtained under white light illumination ($100\ \text{mW cm}^{-2}$) using Keithley 2400 source meter.

3. Results and Discussion

3.1. Characteristics of DSSCs Using Dye of Black Rice

3.1.1. UV-Vis Studies of Black Rice. Figure 1 shows the absorption spectra of bare TiO_2 electrode, anthocyanin solution extracted from black rice and that of the TiO_2 electrode after being soaked in anthocyanin solution. The absorption spectrum for the anthocyanin dye in solution shows peak at wavelength $\lambda = 535\ \text{nm}$. It can be observed that the absorption band of anthocyanin/ TiO_2 is red shifted towards higher wavelength ($\lambda = 538\ \text{nm}$) compared to that of the anthocyanin in solution. The shift towards lower energy can be attributed to complexation between anthocyanin and metal ions, Ti^{4+} [50]. Similar behavior has also been observed by Sirimanne and Soga [51]. It can be observed that TiO_2 does not strongly absorb in the visible region. Absorbance of TiO_2 increases as the ultraviolet region is approached. After soaking TiO_2 with black rice anthocyanin, absorbance significantly increased, but the absorbance of the TiO_2 /anthocyanin complex is lower than that of the untreated anthocyanin solution. This shows that TiO_2 is sensitized by the anthocyanin dye.

It is known that anthocyanin extracted from black rice contains cyanidin-3-glucoside and peonidin-3-glucoside [52]. The chemical structure of anthocyanin mainly present in black rice is illustrated in Figure 2(a). Figure 2(b) shows that the complexation occurs between anthocyanin molecule and TiO_2 particles. It can be seen that TiO_2 particles can form bonding with hydroxyl group in cyanidin-3-glucoside and both hydroxyl and methoxy groups in peonidin-3-glucoside.

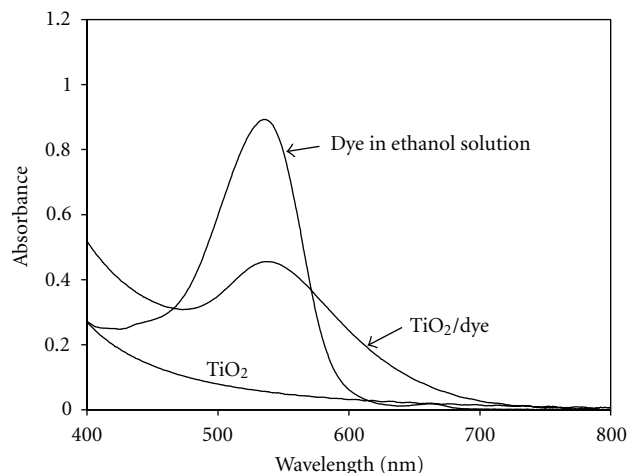


FIGURE 1: The absorption spectra of TiO_2 electrode, anthocyanin solution from black rice, and anthocyanin adsorbed onto TiO_2 electrode.

Anthocyanins are glycosylated polyhydroxyl derivatives of 2-phenylbenzopyrylium salts or better known as flavylium salts. They are made up of three six-membered rings, that is, an aromatic ring bonded to heterocyclic aromatic ring that contains oxygen and carbon which is also bonded to another aromatic ring. It is said that anthocyanins can exist in various chemical forms, that is, quinonoidal base, flavylium cation, carbinol or pseudobase, and chalcone, which depend on the pH of the solution [53]. Figure 3 depicts an example of different molecular structures of cyanidin-3-glucoside which are pH dependent. At pH 1, anthocyanins mainly present as flavylium cations which are red in colour whereas quinonoidal base in blue colour exists at pH values between 2 and 4. At pH values between 4 and 6, anthocyanins can exist in four chemical forms, that is, flavylium cation, anhydrous quinonoidal base, carbinol base, and chalcone. Carbinol base has no colour whereas the colour of chalcone is pale yellow. The equilibrium between the quinonoidal bases and carbinol has to take place via the flavylium cation. Carbinol pseudobase and chalcone are two main species present at pH values between 5 and 6. The absence of conjugated double bond between the second and the third aromatic ring in the carbinol form does not allow it to absorb visible light. Degradation of anthocyanins occurs at pH above 7. The stability of anthocyanins is dependent on pH [54]. According to the literature [21, 55], it is known that the flavylium cation is the stable form of anthocyanin. The oxonium ion in flavylium form is said to assist in the absorption of photons in the visible range [56]. This is supported by the absorption spectra of black rice anthocyanin in solution as depicted in Figure 4(a). From the figure, the highest absorption peak intensity can be seen at wavelength of $535\ \text{nm}$ for the anthocyanin solution with pH 1. Consequently, it can be concluded that the flavylium ion is predominant and more stable at pH 1 compared to other pH values. Figure 4(b) presents the absorption spectra of black rice extract adsorbed on TiO_2 electrode at various pHs. The results obtained are in accordance with the absorption

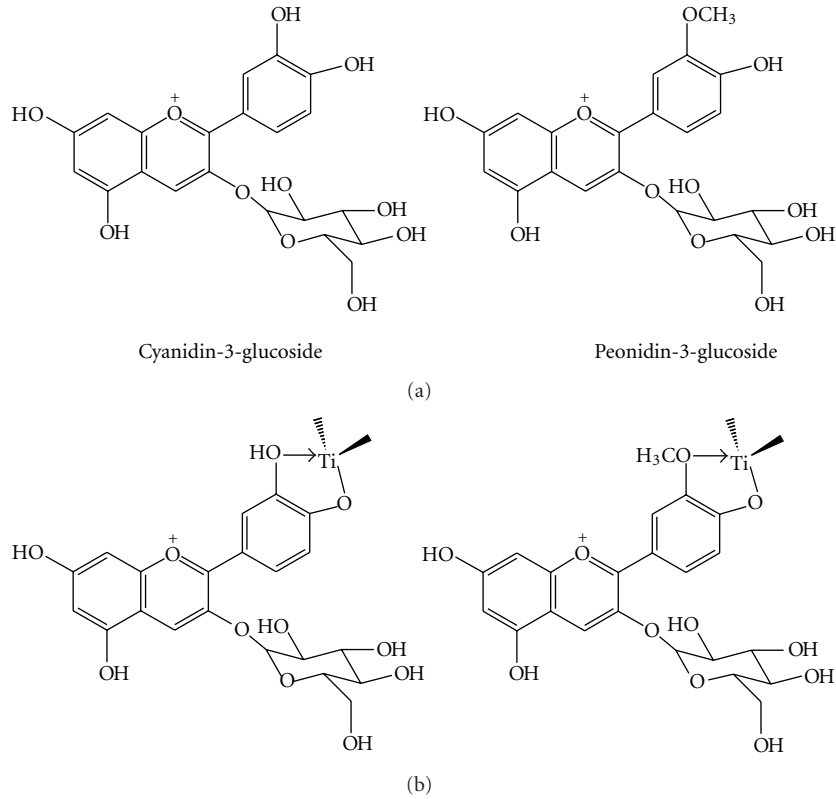


FIGURE 2: (a) Chemical structure of cyanidin-3-glucoside and peonidin-3-glucoside present in black rice. (b) The binding between anthocyanin molecule and TiO_2 particle.

TABLE 2: V_{oc} , J_{sc} , FF , and η of DSSC with platinum as counter electrode for black rice dye solution at pH 1. Electrolyte is 26.9 wt. % chitosan-22 wt. % NH_4I (+ 2.2 wt. % I_2) + 48.9 wt. % IL.

	V_{oc} (mV)	J_{sc} ($\mu\text{A cm}^{-2}$)	FF (%)	η (%)
No blocking layer	195	172	31	0.01
With blocking layer	270	288	44	0.03

spectra of anthocyanin in solution (Figure 4(a)). It is noted that, at pH = 1, the black-rice-sensitized TiO_2 has the maximum absorbance at $\lambda = 538$ nm. This indicates that the flavylium ion can form bonding with Ti^{4+} ion more effectively [57]. Hence, anthocyanin extract of black rice solution at pH 1 was used to soak the TiO_2 photoelectrode overnight. The soaked TiO_2 photoelectrode was then used in the fabrication of ITO/ TiO_2 /anthocyanin dye/polymer electrolyte/counter electrode junction solar cell.

3.1.2. DSSCs Utilizing Black Rice Dye. The performance of DSSCs using Pt as the counter electrode, with and without compact blocking layer, is tabulated in Table 2. In the literature [58, 59], Ti(IV) bis(ethyl acetoacetato)-diisopropoxide has been used to prepare the blocking TiO_2 layer, and it is reported that this layer prevents electron recombination losses to the oxidized electrolyte. Recombination of electrons in the TiO_2 conduction band and electrolyte will cause the

occurrence of dark current at the electrode-electrolyte interface and deteriorate the performance of DSSC. In addition, it is understood that recombination of electrons in TiO_2 with the oxidized dye has significant effect on the performance of natural DSSC [57, 60]. In this work, diisopropoxytitanium bis(acetylacetonate) is used to prepare the blocking layer. From Table 2, it can be observed that the DSSC with blocking layer coating exhibits better performance with efficiency of 0.03% compared to that without the blocking layer ($\eta = 0.01\%$). According to Calandra et al. [61], platinum which is very compatible to I^-/I_3^- redox couple helps to ensure fast reduction of the triiodide, I_3^- ion, and, thus, making the dye regeneration process more efficient. Also, platinum is said to help in reducing the overpotential for the triiodide-iodide reduction and thereby minimizes the energy loss [62]. Calogero and co-workers [57] reported the improvement on performance for DSSC based on eggplant sensitizer with blocking layer compared to that without blocking layer.

The highest J_{sc} and efficiency of DSSC obtained using Pt counter electrode and anthocyanin dye extracted from black rice are $288 \mu\text{A cm}^{-2}$ and 0.034%, respectively. Hao et al. [19] has reported J_{sc} of 1.14 mA cm^{-2} for DSSC sensitized by anthocyanin dyes (extracted from black rice) with liquid electrolyte. This is about four times higher compared to that in the present work. The low performance of DSSCs in this work may be due to the low ionic conductivity of the electrolyte which is only $3.43 \times 10^{-5} \text{ S cm}^{-1}$. Other than

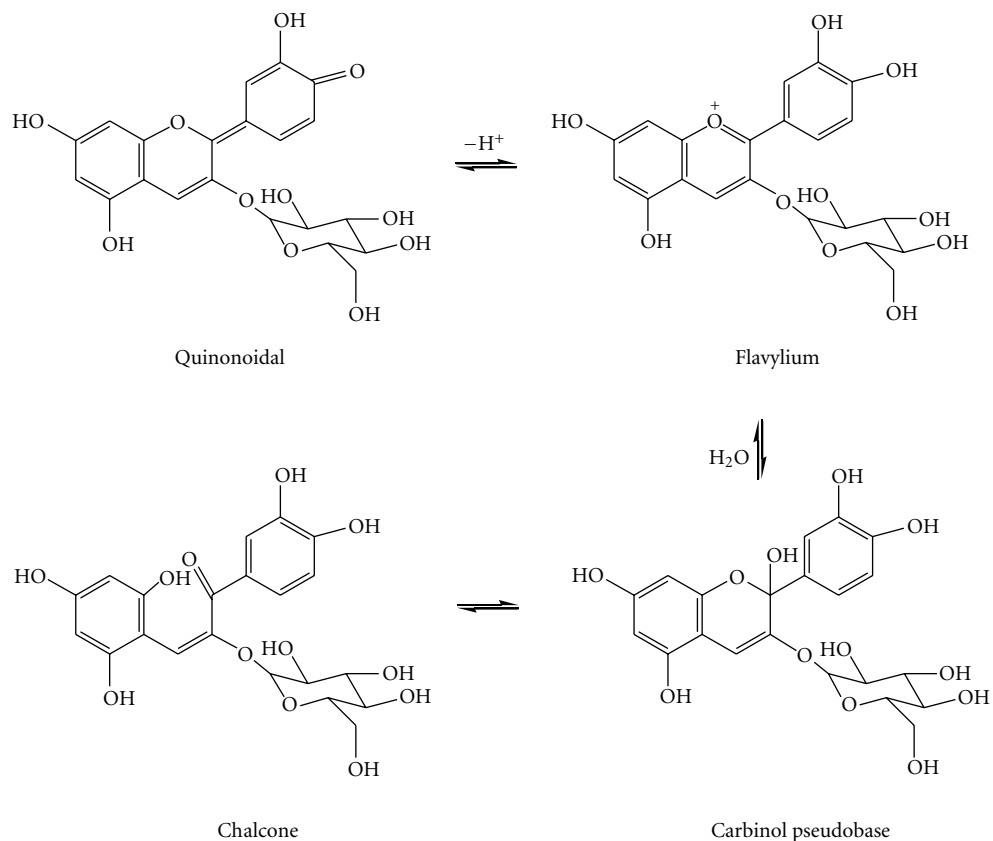


FIGURE 3: Various chemical forms of cyanidin-3-glucoside.

that, the contact issue at the electrode-electrolyte interface is also another probable reason why the performance of DSSCs in the present study is low. To improve the electrode-electrolyte contact, the electrolyte was prepared in gel form for application in DSSC. A better contact is expected between the electrode and electrolyte in gel form. Conductivity of the electrolyte in gel form has also been further improved by increasing the IL content up to 80 wt. % and by blending chitosan with PEO. The conductivity of 27.5 wt. % chitosan-22.5 wt. % NH_4I -50 wt. % BMII gel electrolyte doubled upon the addition up to 80 wt. % BMII. The conductivity of chitosan-based gel electrolyte with 80 wt. % BMII increased by about four times when blending chitosan and PEO in wt. ratio 30:70. Figure 5 shows the J - V characteristics of DSSCs fabricated using various compositions of electrolyte in gel form. J_{sc} of $762 \mu\text{A cm}^{-2}$ and V_{oc} of 380 mV were obtained. Parameters such as V_{oc} , J_{sc} , FF , and η of DSSC employing different compositions of electrolyte in gel form are tabulated in Table 3. The conductivity of 27.5 wt. % chitosan-22.5 wt. % NH_4I -50 wt. % BMII in gel form is increased by one order of magnitude compared to that of the solid electrolyte with the same composition. From Table 3, it can be noted clearly that V_{oc} , J_{sc} , FF , and η of DSSCs have significantly been increased with the use of electrolyte in gel form.

3.2. Characteristics of DSSCs Using Dye of Red Cabbage

3.2.1. UV-Vis of Red Cabbage. For the sake of comparison, the pH of red cabbage anthocyanin was also set to 1. The absorption spectra of anthocyanin extracted from red cabbage in solution and adsorbed onto the TiO_2 electrode are depicted in Figure 6. An absorption peak at about 550 nm is observed. Similar absorption peak has been reported by Furukawa et al. [63]. The absorption peak for TiO_2 -anthocyanin absorbance shifted towards lower energy indicating that complexation has occurred between the anthocyanin and TiO_2 . The carbonyl and hydroxyl groups in anthocyanin molecule can be bound to the surface of TiO_2 film as proposed by Hao and coauthors [19]. It can be observed that the absorption intensity for the TiO_2 photoelectrode soaked with red cabbage anthocyanin is only slightly lower than the intensity of absorption for the anthocyanin solution.

Figures 7(a) and 7(b) exhibit the chemical structure of anthocyanin mainly present in red cabbage and its complexation with TiO_2 particles. Cyanidin-3-(sinapoyl)diglucoside-5-glucoside is the prime species found in red cabbage [29]. As can be seen from Figure 7(b), the cyanidin-3-(sinapoyl)diglucoside-5-glucoside structure in red cabbage is able to interact with two Ti^{4+} ions.

TABLE 3: V_{oc} , J_{sc} , FF , and η of black rice anthocyanin DSSCs using various compositions of electrolyte in gel form.

Composition	Conductivity, σ ($S\ cm^{-1}$)	J_{sc} ($\mu A\ cm^{-2}$)	V_{oc} (mV)	FF (%)	η (%)
27.5 wt. % chitosan-22.5 wt. % NH_4I -50 wt. % BMII	1.51×10^{-4}	762	380	48	0.14
11 wt. % chitosan-9 wt. % NH_4I -80 wt. % BMII	3.02×10^{-4}	900	365	45	0.15
11 wt. % (chitosan : PEO, wt. ratio 30 : 70)-9 wt. % NH_4I -80 wt. % BMII	5.52×10^{-4}	1213	400	47	0.23

TABLE 4: V_{oc} , J_{sc} , FF , and η of DSSC employing red cabbage anthocyanin and different electrolytes in gel form.

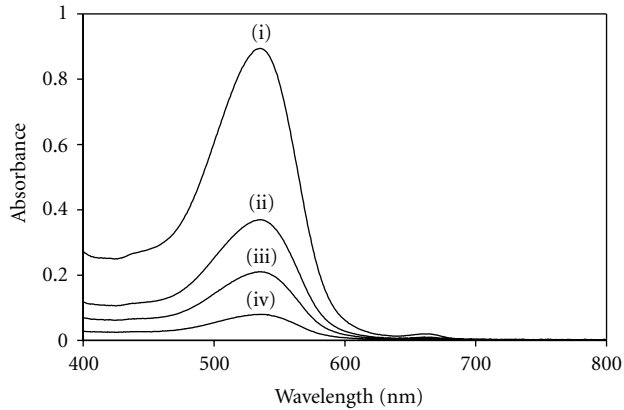
DSSCs	Acid	Composition	Conductivity, σ ($S\ cm^{-1}$)	J_{sc} ($\mu A\ cm^{-2}$)	V_{oc} (mV)	FF (%)	η (%)
a	HCl	27.5 wt. % chitosan-22.5 wt. % NH_4I -50 wt. % BMII	1.51×10^{-4}	1421	305	45	0.20
b	Tartaric	27.5 wt. % chitosan-22.5 wt. % NH_4I -50 wt. % BMII		1429	475	32	0.22
c	HCl	11 wt. % chitosan-9 wt. % NH_4I -80 wt. % BMII	3.02×10^{-4}	1588	450	41	0.29
d	Tartaric	11 wt. % chitosan-9 wt. % NH_4I -80 wt. % BMII		2090	610	30	0.38
e	Tartaric	11 wt. % (chitosan : PEO, wt. ratio 30 : 70)-9 wt. % NH_4I -80 wt. % BMII	5.52×10^{-4}	2523	395	39	0.39
f	Tartaric	11 wt. % phthaloyl chitosan-9 wt. % NH_4I -80 wt. % BMII	5.86×10^{-4}	3472	365	34	0.43
g	Tartaric	11 wt. % (phthaloyl chitosan : PEO, wt. ratio 30 : 70)-9 wt. % NH_4I -80 wt. % BMII	6.24×10^{-4}	3503	340	39	0.46

TABLE 5: DSSC properties sensitized with natural dyes.

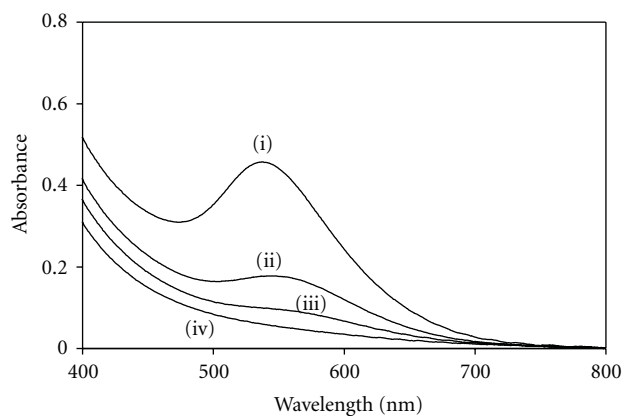
Dye	Electrolyte	J_{sc} ($\mu A\ cm^{-2}$)	V_{oc} (mV)	P_{max} ($mW\ cm^{-2}$)	FF (%)	η (%)	Ref.
Blue pea	Liquid	1630	404	—	57	0.05	[20]
Rosella	Liquid	370	372	—	33	0.37	[20]
Red cabbage	Liquid	4700	525	1.51	61	—	[31]
Red cabbage	Liquid	680	520	0.25	70	0.5	[63]
Black rice	Liquid	1140	551	0.327	52	—	[19]
Black rice	Liquid	1287	550	0.24	33	0.24	[64]
Blackberries	Liquid	10600	330	1.469	42	1.46	[10]
Red yeast rice	Liquid	6100	570	2.29	66	2.3	[65]
Spinach leaves	Liquid	9400	530	—	—	2.6	[57]
Red turnip	Liquid	9500	480	—	—	1.75	[57]
Skin of eggplant	Liquid	3400	350	0.48	40	0.48	[50]
Wild Sicilian prickly pear	Liquid	9400	350	—	38	1.26	[60]
Skin of jaboticaba	Liquid	2600	660	1.10	62	—	[66]
Fructus lycii	Liquid	530	689	—	46.6	0.17	[67]
Marigold	Liquid	510	542	—	83.1	0.23	[67]
Chinese rose	Liquid	900	483	—	61.9	0.27	[67]

3.2.2. *DSSCs Utilizing Red Cabbage Dye.* All the black rice anthocyanin DSSCs were fabricated with dyes prepared using hydrochloric acid (HCl) to adjust pH of the anthocyanin solution. The performance of DSSCs using HCl and tartaric acid to adjust pH of anthocyanin solution extracted from red cabbage is tabulated in Table 4, and Figure 8 depicts the J - V characteristics of DSSCs. For all the DSSCs utilizing red cabbage anthocyanin, electrolytes in the form of gel

were used. From Table 4, the red cabbage anthocyanin DSSC employing 27.5 wt. % chitosan-22.5 wt. % NH_4I -50 wt. % BMII gel electrolyte and HCl as the agent to adjust pH exhibits higher J_{sc} and η compared to black rice anthocyanin DSSC with the same electrolyte composition in gel form and HCl as pH adjuster (see Table 3). The better performance of the DSSC employing red cabbage anthocyanin may be due to the structural differences between



(a)



(b)

FIGURE 4: The absorption spectra of anthocyanin (a) in ethanol solution and (b) on TiO_2 extracted from black rice at pH (i) 1, (ii) 2, (iii) 3, and (iv) 4.

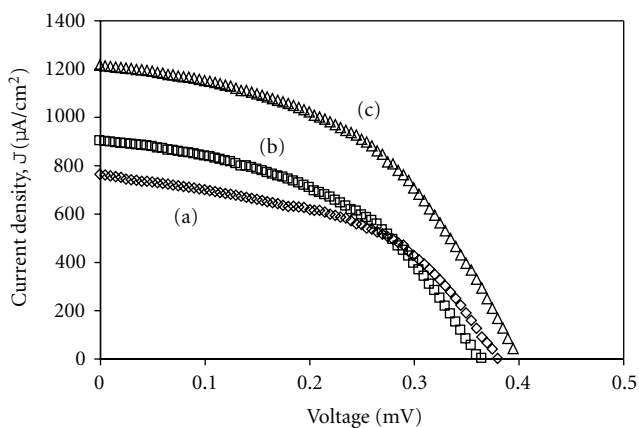


FIGURE 5: J - V characteristics of black rice DSSC with electrolytes having (a) 27.5 wt. % chitosan-22.5 wt. % $\text{NH}_4\text{I}(\text{I}_2)$ + 50 wt. % IL (b) 11 wt. % chitosan-9 wt. % NH_4I -80 wt. % BMII, and (c) 11 wt. % (chitosan : PEO, wt ratio 30 : 70)-9 wt. % NH_4I -80 wt. % BMII electrolyte (in gel form).

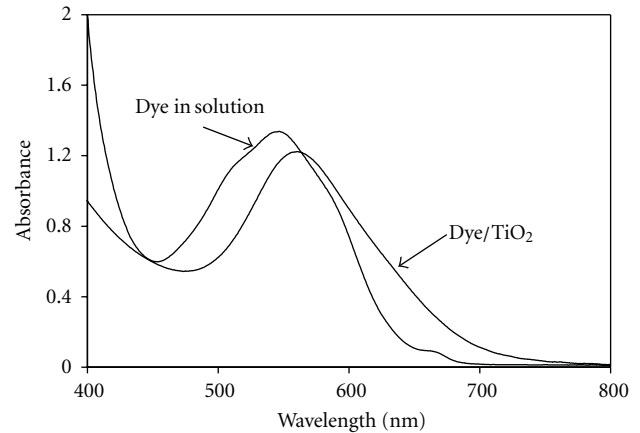


FIGURE 6: The absorption spectra of anthocyanin extracted from red cabbage.

anthocyanins from the two sources. It is understood that there is an increased charge density at the catechol end of anthocyanin molecule upon complexation with Ti^{4+} ion and, thus, enables electronic coupling for charge injection [57]. As can be seen in Figure 7(b), the molecular structure of cyanidin-3-(sinapoyl)diglucoside-5-glucoside in red cabbage provides two binding sites with Ti^{4+} ions compared to cyanidin-3-glucoside or peonidin-3-glucoside found in black rice (Figure 2(b)). Therefore, it can be inferred that the strong electronic coupling for charge injection occurs in cyanidin-3-(sinapoyl)diglucoside-5-glucoside of red cabbage which leads to better performance.

Other than blending chitosan with PEO, modification of chitosan by the method of phthaloylation can increase the ionic conductivity of the electrolyte which in turn improves the DSSC performance. The conductivity of 11 wt. % chitosan-9 wt. % NH_4I -80 wt. % BMII gel electrolyte is almost doubled for the same gel electrolyte composition, but using phthaloyl chitosan as polymer host. The J_{sc} of DSSC employing 11 wt. % phthaloyl chitosan-9 wt. % NH_4I -80 wt. % BMII gel electrolyte is ~ 1.7 times higher than J_{sc} of DSSC utilizing 11 wt. % chitosan-9 wt. % NH_4I -80 wt. % BMII gel electrolyte. Efficiency of the former DSSC is also higher than that of the latter. From the table, it can be observed that the use of tartaric acid as pH adjustment agent resulted in higher efficiency of DSSCs. It can be seen clearly that DSSC using tartaric acid as pH adjustment agent and phthaloyl chitosan-PEO blend electrolyte in gel form exhibits the highest short-circuit current density and efficiency. The V_{oc} and J_{sc} of DSSC with red cabbage as sensitizer and phthaloyl chitosan-PEO blend electrolyte in this work are comparable to the V_{oc} (525 mV) and J_{sc} ($4700 \mu\text{A cm}^{-2}$) of DSSC employing red cabbage and liquid electrolyte obtained by Calogero and Marco [50]. Furukawa et al. [63] reported that η of 0.50% was achieved by red cabbage DSSC under illumination of 50 mW cm^{-2} .

Tartaric acid is one of the most concentrated naturally occurring organic acids in grapes and wine. It mainly acts as an acidity adjuster in foods. Since tartaric acid is a diprotic

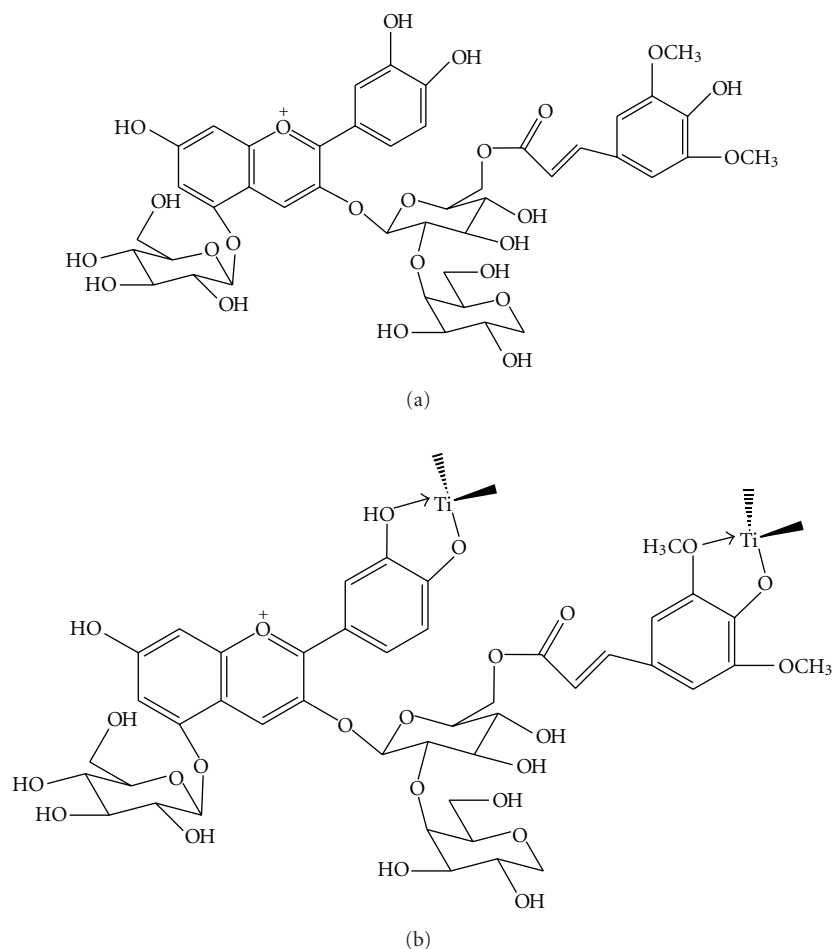


FIGURE 7: (a) Molecular structure of cyanidin-3-(sinapoyl)diglucoside-5-glucoside mainly found in red cabbage and (b) complexation between anthocyanin molecule and TiO_2 particles.

organic acid, it is able to donate two protons, H^+ , per acid molecule when dissolved in solvent. Tartaric acid has twice the number of available hydronium ions compared to that of hydrochloric acid which helps in the absorption of photons in the visible region. Hence, tartaric acid is more suitable to serve as pH adjuster. Since ethanol was used in the solvent extraction of anthocyanin and being an organic acid, tartaric acid is more soluble in ethanol compared to HCl. This is an added advantage to tartaric acid as a pH adjuster.

To gauge the performance of the best DSSC obtained from this work, comparison with reported DSSCs using natural dyes was carried out. Table 5 lists the performance parameters of various DSSCs using natural dye found in the literature. Although the best DSSC obtained from this work uses gel polymer electrolyte of conductivity $\sim 10^{-4} \text{ S cm}^{-1}$, its efficiency is comparable to some of the reported DSSCs using liquid electrolyte.

4. Conclusions

UV-Vis studies show the shift of the absorption band of TiO_2 immersed in anthocyanin solution indicating the occurrence of complexation between anthocyanin and Ti^{4+} ions.

Absorption spectrum also shows that anthocyanin dye from black rice is found to be highly absorbing at pH 1, and; thus, the TiO_2 photoelectrode was soaked in anthocyanin dye at this pH. The conductivity of the electrolyte influences short-circuit current density of the cell. Anthocyanin (from black rice) dye-sensitized solar cell with platinum as counter electrode exhibited the J_{sc} of $172 \mu\text{A cm}^{-2}$ and V_{oc} of 195 mV. The performance of ITO/ TiO_2 /anthocyanin dye/26.9 wt. % chitosan-22 wt. % NH_4I (+2.2 wt. % I_2) + 48.9 wt. % IL/Pt cell was improved by coating a diisopropoxytitanium bis(acetylacetonate) layer on the ITO glass. J_{sc} increased from $172 \mu\text{A cm}^{-2}$ to $288 \mu\text{A cm}^{-2}$. The utilization of electrolyte in gel form improves the performance of DSSC. Black rice anthocyanin DSSC employing gel electrolyte of composition chitosan-PEO blend (wt. ratio 30:70) doped with 9 wt. % NH_4I (+ I_2) and 80 wt. % IL exhibited J_{sc} of $1213 \mu\text{A cm}^{-2}$, V_{oc} of 0.4 V, and η of 0.23%. A similar DSSC, but using red cabbage anthocyanin at the same pH (also adjusted with HCl), exhibited better performance with efficiency of 0.29%. The better performance of the red cabbage anthocyanin DSSC compared to black rice DSSC is attributed to the structural differences between the two anthocyanins. The cell fabricated using red cabbage anthocyanin as dye sensitizer

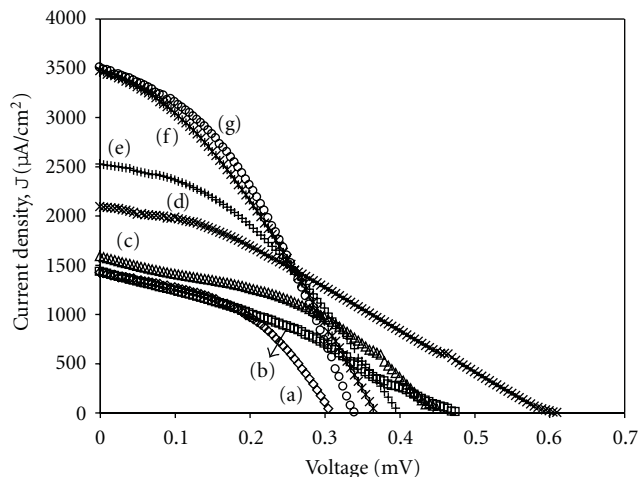


FIGURE 8: J - V characteristics of the red cabbage DSSCs for sample (a) HCl as pH adjuster and 27.5 wt. % chitosan-22.5 wt. % NH_4I -50 wt. % BMII gel electrolyte, (b) tartaric acid as pH adjuster and 27.5 wt. % chitosan-22.5 wt. % NH_4I -50 wt. % BMII gel electrolyte, (c) HCl as pH adjuster and 11 wt. % chitosan-9 wt. % NH_4I -80 wt. % BMII gel electrolyte, (d) tartaric acid as pH adjuster and 11 wt. % chitosan-9 wt. % NH_4I -80 wt. % BMII gel electrolyte, (e) tartaric acid as pH adjuster and 11 wt. % (chitosan:PEO, wt. ratio 30:70)-9 wt. % NH_4I -80 wt. % BMII gel electrolyte, (f) tartaric acid as pH adjuster and 11 wt. % phthaloyl chitosan-9 wt. % NH_4I -80 wt. % BMII gel electrolyte and (g) tartaric acid as pH adjuster and 11 wt. % (chitosan : PEO, wt ratio 30:70)-9 wt. % NH_4I -80 wt. % BMII gel electrolyte.

and phthaloyl chitosan-PEO blend electrolyte in gel form as the electrolyte exhibits a J_{sc} of $3503 \mu\text{A cm}^{-2}$ and η of 0.46%. The use of tartaric acid to adjust pH on red cabbage anthocyanin improves the DSSC performance. This may be due to its diprotic nature.

Acknowledgments

The authors would like to thank the University of Malaya for the financial support through PS353/2009A and PS325/2009C Grants to carry out this research work. M. H. Buraidah and S. N. F. Yusuf thank the Ministry of Education Malaysia and the University of Malaya for the scholarship and tutorship awards, and M. M. Noor thanks the International Islamic University Malaysia (IIUM) for the study leave awarded.

References

- [1] M. Grätzel, "Dye-sensitized solar cells," *Journal of Photochemistry and Photobiology C*, vol. 4, no. 2, pp. 145–153, 2003.
- [2] S. Karuppuchamy, J. M. Jeong, D. P. Amalnerkar, and H. Minoura, "Photoinduced hydrophilicity of titanium dioxide thin films prepared by cathodic electrodeposition," *Vacuum*, vol. 80, no. 5, pp. 494–498, 2006.
- [3] C. Longo and M. A. De Paoli, "Dye-sensitized solar cells: a successful combination of materials," *Journal of the Brazilian Chemical Society*, vol. 14, no. 6, pp. 889–901, 2003.
- [4] K. M. Lee, W. H. Chiu, H. Y. Wei et al., "Effects of mesoscopic poly(3,4-ethylenedioxythiophene) films as counter electrodes for dye-sensitized solar cells," *Thin Solid Films*, vol. 518, no. 6, pp. 1716–1721, 2010.
- [5] J. Wu, Q. Li, L. Fan et al., "High-performance polypyrrole nanoparticles counter electrode for dye-sensitized solar cells," *Journal of Power Sources*, vol. 181, no. 1, pp. 172–176, 2008.
- [6] Q. Li, J. Wu, Q. Tang et al., "Application of microporous polyaniline counter electrode for dye-sensitized solar cells," *Electrochemistry Communications*, vol. 10, no. 9, pp. 1299–1302, 2008.
- [7] T. Denaro, V. Baglio, M. Girolamo et al., "Investigation of low cost carbonaceous materials for application as counter electrode in dye-sensitized solar cells," *Journal of Applied Electrochemistry*, vol. 39, no. 11, pp. 2173–2179, 2009.
- [8] K. Imoto, K. Takahashi, T. Yamaguchi, T. Komura, J. I. Nakamura, and K. Murata, "High-performance carbon counter electrode for dye-sensitized solar cells," *Solar Energy Materials and Solar Cells*, vol. 79, no. 4, pp. 459–469, 2003.
- [9] T. N. Murakami and M. Grätzel, "Counter electrodes for DSC: application of functional materials as catalysts," *Inorganica Chimica Acta*, vol. 361, no. 3, pp. 572–580, 2008.
- [10] H. Zhu, H. Zeng, V. Subramanian, C. Masarapu, K. H. Hung, and B. Wei, "Anthocyanin-sensitized solar cells using carbon nanotube films as counter electrodes," *Nanotechnology*, vol. 19, no. 46, Article ID 465204, 2008.
- [11] G. Calogero, F. Bonaccorso, O. M. Maragò, P. G. Gucciardi, and G. Di Marco, "Single wall carbon nanotubes deposited on stainless steel sheet substrates as novel counter electrodes for ruthenium polypyridine based dye sensitized solar cells," *Dalton Transactions*, vol. 39, no. 11, pp. 2903–2909, 2010.
- [12] M. Y. Yen, C. Y. Yen, S. H. Liao et al., "A novel carbon-based nanocomposite plate as a counter electrode for dye-sensitized solar cells," *Composites Science and Technology*, vol. 69, no. 13, pp. 2193–2197, 2009.
- [13] G. Calogero, P. Calandra, A. Irrera, A. Sinopoli, I. Citro, and G. Di Marco, "A new type of transparent and low cost counter-electrode based on platinum nanoparticles for dye-sensitized solar cells," *Energy and Environmental Science*, vol. 4, no. 5, pp. 1838–1844, 2011.
- [14] K. Kalyanasundaram and M. Grätzel, "Applications of functionalized transition metal complexes in photonic and optoelectronic devices," *Coordination Chemistry Reviews*, vol. 177, no. 1, pp. 347–414, 1998.
- [15] M. K. Nazeeruddin, S. M. Zakeeruddin, J. J. Lagref et al., "Stepwise assembly of amphiphilic ruthenium sensitizers and their applications in dye-sensitized solar cell," *Coordination Chemistry Reviews*, vol. 248, no. 13-14, pp. 1317–1328, 2004.
- [16] C. Klein, M. K. Nazeeruddin, P. Liska et al., "Engineering of a novel ruthenium sensitizer and its application in dye-sensitized solar cells for conversion of sunlight into electricity," *Inorganic Chemistry*, vol. 44, no. 2, pp. 178–180, 2005.
- [17] P. Wang, B. Wenger, R. Humphry-Baker et al., "Charge separation and efficient light energy conversion in sensitized mesoscopic solar cells based on binary ionic liquids," *Journal of the American Chemical Society*, vol. 127, no. 18, pp. 6850–6856, 2005.
- [18] Y. Amao and T. Komori, "Bio-photovoltaic conversion device using chlorine-e6 derived from chlorophyll from Spirulina adsorbed on a nanocrystalline TiO_2 film electrode," *Biosensors and Bioelectronics*, vol. 19, no. 8, pp. 843–847, 2004.
- [19] S. Hao, J. Wu, Y. Huang, and J. Lin, "Natural dyes as photosensitizers for dye-sensitized solar cell," *Solar Energy*, vol. 80, no. 2, pp. 209–216, 2006.

- [20] K. Wongcharee, V. Meeyoo, and S. Chavadej, "Dye-sensitized solar cell using natural dyes extracted from rosella and blue pea flowers," *Solar Energy Materials and Solar Cells*, vol. 91, no. 7, pp. 566–571, 2007.
- [21] Ø. M. Andersen, T. Fossen, K. Torskangerpoll, A. Fossen, and U. Hauge, "Anthocyanin from strawberry (*Fragaria ananassa*) with the novel aglycone, 5-carboxypyranopelargonidin," *Phytochemistry*, vol. 65, no. 4, pp. 405–410, 2004.
- [22] A. Olea, G. Ponce, and P. J. Sebastian, "Electron transfer via organic dyes for solar conversion," *Solar Energy Materials and Solar Cells*, vol. 59, no. 1, pp. 137–143, 1999.
- [23] Q. Dai and J. Rabani, "Unusually efficient photosensitization of nanocrystalline TiO₂ films by pomegranate pigments in aqueous medium," *New Journal of Chemistry*, vol. 26, no. 4, pp. 421–426, 2002.
- [24] P. M. Sirimanne, M. K. I. Senevirathna, E. Premalal, P. K. D. D. P. Pitigala, V. Sivakumar, and K. Tennakone, "Utilization of natural pigment extracted from pomegranate fruits as sensitizer in solid-state solar cells," *Journal of Photochemistry and Photobiology A*, vol. 177, no. 2-3, pp. 324–327, 2006.
- [25] A. A. Gitelson, M. N. Merzlyak, and O. B. Chivkunova, "Optical properties and nondestructive estimation of anthocyanin content in plant leaves," *Photochemistry and Photobiology*, vol. 74, no. 1, pp. 38–45, 2001.
- [26] S. H. Nam, S. M. Chang, and M. Y. Kang, "Screening of mutagenicity and antimutagenic activity against chemical direct mutagens of ethanolic extracts from colored rice bran," *Journal of the Korean society of Agricultural Chemistry and Biotechnology*, vol. 45, pp. 195–202, 2002.
- [27] C. Hu, J. Zawistowski, W. Ling, and D. D. Kitts, "Black rice (*Oryza sativa* L. *indica*) pigmented fraction suppresses both reactive oxygen species and nitric oxide in chemical and biological model systems," *Journal of Agricultural and Food Chemistry*, vol. 51, no. 18, pp. 5271–5277, 2003.
- [28] Z. Xu, J. Wu, Y. Zhang, X. Hu, X. Liao, and Z. Wang, "Extraction of anthocyanins from red cabbage using high pressure CO₂," *Bioresour. Technology*, vol. 101, no. 18, pp. 7151–7157, 2010.
- [29] G. J. McDougall, S. Fyffe, P. Dobson, and D. Stewart, "Anthocyanins from red cabbage—stability to simulated gastrointestinal digestion," *Phytochemistry*, vol. 68, no. 9, pp. 1285–1294, 2007.
- [30] N. Chigurupati, L. Saiki, C. Gayser, and A. K. Dash, "Evaluation of red cabbage dye as a potential natural color for pharmaceutical use," *International Journal of Pharmaceutics*, vol. 241, no. 2, pp. 293–299, 2002.
- [31] D. Zhang, N. Yamamoto, T. Yoshida, and H. Minoura, "Natural dye-sensitized solar cells," *Transactions of the Materials Research Society of Japan*, vol. 27, no. 4, pp. 811–814, 2002.
- [32] S. Furukawa, H. Iino, K. Kukita, and K. Kaminosono, "Effects of pH of dyes on characteristics of dye-sensitized solar cells," *IEEE Transactions on Fundamentals and Materials*, vol. 130, no. 2, pp. 136–140, 2010.
- [33] O. A. Ileperuma, M. A. K. L. Dissanayake, S. Somasunderam, and L. R. A. K. Bandara, "Photoelectrochemical solar cells with polyacrylonitrile-based and polyethylene oxide-based polymer electrolytes," *Solar Energy Materials and Solar Cells*, vol. 84, no. 1–4, pp. 117–124, 2004.
- [34] A. Fujishima and K. Honda, "Electrochemical photolysis of water at a semiconductor electrode," *Nature*, vol. 238, no. 5358, pp. 37–38, 1972.
- [35] H. Gerischer, "Electrochemical photo and solar cells principles and some experiments," *Journal of Electroanalytical Chemistry*, vol. 58, no. 1, pp. 263–274, 1975.
- [36] J. Wu, P. Li, S. Hao, H. Yang, and Z. Lan, "A polyblend electrolyte (PVP/PEG+KI+I₂) for dye-sensitized nanocrystalline TiO₂ solar cells," *Electrochimica Acta*, vol. 52, no. 17, pp. 5334–5338, 2007.
- [37] S. A. Mohamad, M. H. Ali, R. Yahya, Z. A. Ibrahim, and A. K. Arof, "Photovoltaic activity in a ZnSe/PEO-chitosan blend electrolyte junction," *Ionics*, vol. 13, no. 4, pp. 235–240, 2007.
- [38] S. A. Mohamad, R. Yahya, Z. A. Ibrahim, and A. K. Arof, "Photovoltaic activity in a ZnTe/PEO-chitosan blend electrolyte junction," *Solar Energy Materials and Solar Cells*, vol. 91, no. 13, pp. 1194–1198, 2007.
- [39] V. C. Nogueira, C. Longo, A. F. Nogueira, M. A. Soto-Oviedo, and M. A. D. Paoli, "Solid-state dye-sensitized solar cell: improved performance and stability using a plasticized polymer electrolyte," *Journal of Photochemistry and Photobiology A*, vol. 181, no. 2-3, pp. 226–232, 2006.
- [40] S. A. Haque, E. Palomares, H. M. Upadhyaya et al., "Flexible dye sensitised nanocrystalline semiconductor solar cells," *Chemical Communications*, vol. 9, no. 24, pp. 3008–3009, 2003.
- [41] O. A. Ileperuma, M. A. K. L. Dissanayake, and S. Somasundaram, "Dye-sensitized photoelectrochemical solar cells with polyacrylonitrile based solid polymer electrolytes," *Electrochimica Acta*, vol. 47, no. 17, pp. 2801–2807, 2002.
- [42] P. Wang, S. M. Zakeeruddin, J. E. Moser, and M. Grätzel, "A new ionic liquid electrolyte enhances the conversion efficiency of dye-sensitized solar cells," *Journal of Physical Chemistry B*, vol. 107, no. 48, pp. 13280–13285, 2003.
- [43] N. Yamanaka, R. Kawano, W. Kubo et al., "Dye-sensitized TiO₂ solar cells using imidazolium-type ionic liquid crystal systems as effective electrolytes," *Journal of Physical Chemistry B*, vol. 111, no. 18, pp. 4763–4769, 2007.
- [44] D. Kuang, P. Wang, S. Ito, S. M. Zakeeruddin, and M. Grätzel, "Stable mesoscopic dye-sensitized solar cells based on tetracyanoborate ionic liquid electrolyte," *Journal of the American Chemical Society*, vol. 128, no. 24, pp. 7732–7733, 2006.
- [45] Q. Dai, D. B. Menzies, D. R. MacFarlane et al., "Dye-sensitized nanocrystalline solar cells incorporating ethylmethylimidazolium-based ionic liquid electrolytes," *Comptes Rendus Chimie*, vol. 9, no. 5-6, pp. 617–621, 2006.
- [46] D. R. MacFarlane, P. Meakin, J. Sun, N. Amini, and M. Forsyth, "Pyrrolidinium imides: a new family of molten salts and conductive plastic crystal phases," *Journal of Physical Chemistry B*, vol. 103, no. 20, pp. 4164–4170, 1999.
- [47] E. I. Cooper and E. J. M. O'Sullivan, *Proceedings of the Eight International Symposium on Molten Salts*, R. J. Gale, G. Blomgren, and H. Kojima, Eds., The Electrochemical Society Proceedings Series, The Electrochemical Society, Pennington, NJ, USA, 1992.
- [48] J. Wu, Z. Lan, S. Hao et al., "Progress on the electrolytes for dye-sensitized solar cells," *Pure and Applied Chemistry*, vol. 80, no. 11, pp. 2241–2258, 2008.
- [49] A. K. Arof, M. H. Buraidah, L. P. Teo, S. R. Majid, R. Yahya, and R. M. Taha, "Characterizations of chitosan-based polymer electrolyte photovoltaic cells," *International Journal of Photoenergy*, vol. 2010, Article ID 805836, 7 pages, 2010.
- [50] G. Calogero and G. D. Marco, "Red Sicilian orange and purple eggplant fruits as natural sensitizers for dye-sensitized solar cells," *Solar Energy Materials and Solar Cells*, vol. 92, no. 11, pp. 1341–1346, 2008.
- [51] P. M. Sirimanne and T. Soga, "Fabrication of a solid-state cell using vitamin C as sensitizer," *Solar Energy Materials and Solar Cells*, vol. 80, no. 3, pp. 383–389, 2003.

- [52] S. N. Ryu, S. Z. Park, and C. T. Ho, "High performance liquid chromatographic determination of anthocyanin pigments in some varieties of black rice," *Journal of Food and Drug Analysis*, vol. 6, no. 4, pp. 729–736, 1998.
- [53] A. Bakowska, A. Z. Kucharska, and J. Oszmiański, "The effects of heating, UV irradiation, and storage on stability of the anthocyanin-polyphenol copigment complex," *Food Chemistry*, vol. 81, no. 3, pp. 349–355, 2003.
- [54] A. Castañeda-Ovando, Ma. d. L. Pacheco-Hernández, Ma. E. Pérez-Hernández, J. A. Rodríguez, and C. A. Galán-Vidal, "Chemical studies of anthocyanins: a review," *Food Chemistry*, results obtained are in accordance with vol. 113, no. 4, pp. 859–871, 2009.
- [55] G. Fan, Y. Han, Z. Gu, and F. Gu, "Composition and colour stability of anthocyanins extracted from fermented purple sweet potato culture," *Food Science and Technology*, vol. 41, no. 8, pp. 1412–1416, 2008.
- [56] J. M. R. C. Fernando and G. K. R. Senadeera, "Natural anthocyanins as photosensitizers for dye-sensitized solar devices," *Current Science*, vol. 95, no. 5, pp. 663–666, 2008.
- [57] G. Calogero, G. Di Marco, S. Caramori, S. Cazzanti, R. Argazzi, and C. A. Bignozzi, "Natural dye sensitizers for photoelectrochemical cells," *Energy and Environmental Science*, vol. 2, no. 11, pp. 1162–1172, 2009.
- [58] J. H. Kim, M. S. Kang, Y. J. Kim, J. Won, and Y. S. Kang, "Poly(butyl acrylate)/NaI/I₂ electrolytes for dye-sensitized nanocrystalline TiO₂ solar cells," *Solid State Ionics*, vol. 176, no. 5–6, pp. 579–584, 2005.
- [59] P. K. Singh, K. W. Kim, and H. W. Rhee, "Development and characterization of ionic liquid doped solid polymer electrolyte membranes for better efficiency," *Synthetic Metals*, vol. 159, no. 15–16, pp. 1538–1541, 2009.
- [60] G. Calogero, G. Di Marco, S. Cazzanti et al., "Efficient dye-sensitized solar cells using red turnip and purple wild Sicilian prickly pear fruits," *International Journal of Molecular Sciences*, vol. 11, no. 1, pp. 254–267, 2010.
- [61] P. Calandra, G. Calogero, A. Sinopoli, and P. G. Gucciardi, "Metal nanoparticles and carbon-based nanostructures as advanced materials for cathode application in dye-sensitized solar cells," *International Journal of Photoenergy*, vol. 2010, Article ID 109495, 15 pages, 2010.
- [62] C. H. Yoon, R. Vittal, J. Lee, W. S. Chae, and K. J. Kim, "Enhanced performance of a dye-sensitized solar cell with an electrodeposited-platinum counter electrode," *Electrochimica Acta*, vol. 53, no. 6, pp. 2890–2896, 2008.
- [63] S. Furukawa, H. Iino, T. Iwamoto, K. Kukita, and S. Yamauchi, "Characteristics of dye-sensitized solar cells using natural dye," *Thin Solid Films*, vol. 518, no. 2, pp. 526–529, 2009.
- [64] B. Yulianto, W. Septina, K. Fuadi, F. Fanani, L. Muliani, and Nugraha, "Synthesis of nanoporous TiO₂ and its potential applicability for dye-sensitized solar cell using antocyanine black rice," *Advances in Materials Science and Engineering*, vol. 2010, Article ID 789541, 6 pages, 2010.
- [65] S. Ito, T. Saitou, H. Imahori, H. Uehara, and N. Hasegawa, "Fabrication of dye-sensitized solar cells using natural dye for food pigment: Monascus yellow," *Energy and Environmental Science*, vol. 3, no. 7, pp. 905–909, 2010.
- [66] A. S. Polo and N. Y. Murakami Iha, "Blue sensitizers for solar cells: natural dyes from Calafate and Jaboticaba," *Solar Energy Materials and Solar Cells*, vol. 90, no. 13, pp. 1936–1944, 2006.
- [67] H. Zhou, L. Wu, Y. Gao, and T. Ma, "Dye-sensitized solar cells using 20 natural dyes as sensitizers," *Journal of Photochemistry and Photobiology A*, vol. 219, no. 2–3, pp. 188–194, 2011.

Research Article

Indium-Doped Zinc Oxide Thin Films as Effective Anodes of Organic Photovoltaic Devices

Ziyang Hu, Baochen Jiao, Jianjun Zhang, Xiaodan Zhang, and Ying Zhao

Key Laboratory of Photo-Electronics Thin Film Devices and Technique of Tianjin, Institute of Photo-Electronic Thin Film Device and Technique of Nankai University, Key Laboratory of Opto-Electronic Information Science and Technology for Ministry of Education, Tianjin 300071, China

Correspondence should be addressed to Jianjun Zhang, jjzhang@nankai.edu.cn

Received 29 June 2011; Revised 31 August 2011; Accepted 5 September 2011

Academic Editor: Gaetano Di Marco

Copyright © 2011 Ziyang Hu et al. This is an open access article distributed under the Creative Commons Attribution License, which permits unrestricted use, distribution, and reproduction in any medium, provided the original work is properly cited.

Indium-doped zinc oxide (IZO) thin films were prepared by low-cost ultrasonic spray pyrolysis (USP). Both a low resistivity ($3.13 \times 10^{-3} \Omega \text{ cm}$) and an average direct transmittance (400~1500 nm) about 80% of the IZO films were achieved. The IZO films were investigated as anodes in bulk-heterojunction organic photovoltaic (OPV) devices based on poly(3-hexylthiophene) and [6,6]-phenyl C_{60} -butyric acid methyl ester. The device fabricated on IZO film-coated glass substrate showed an open circuit voltage of 0.56 V, a short circuit current of 8.49 mA cm^{-2} , a fill factor of 0.40, and a power conversion efficiency of 1.91%, demonstrating that the IZO films prepared by USP technique are promising low In content and transparent electrode candidates of low-cost OPV devices.

1. Introduction

Organic photovoltaics (OPVs) have attracted considerable attentions for use as the next generation of renewable energy sources, due to their simple cell structure, ease of fabrication, low cost, and flexibility [1–3]. To fabricate cost-efficient and large area OPVs, it is imperative to develop low-cost transparent conducting oxide (TCO) electrodes, which can substitute for the conventional indium tin oxide (ITO) electrodes and a highly efficient TCO deposition process. Considering the cost advantage of OPVs, ITO film is not a desirable anode material, due to the high cost and shortage of indium [4]. Therefore, extensive efforts are being dedicated to finding low/non-In TCOs which are inexpensive but have higher conductivity and a broader transparency window than ITO [5–12]. In addition, the conventional sputtering process is not acceptable in low-cost OPVs due to its low target usage, clumsy equipments, and necessity of vacuum-based condition. Recently, ultrasonic spray pyrolysis (USP) has received extra-attentions because of its simplicity, suitability for product industrialization, and atmospheric-pressure solution deposition routes [13–16]. Wienke et al. have used USP to fabricate IZO thin film, which were

used in amorphous silicon solar cells as transparent anodes. However, there have been few studies on investigation of the fabrication of OPVs on the USP-deposited IZO electrodes, which would be beneficial for the low-cost production of OPVs [17].

In this work, we report the electrical and optical properties of low indium IZO electrodes prepared by USP technique. An efficient OPV device fabricated on the IZO-coated glass was achieved. The performance of OPV device fabricated on both commercial ITO and USP-deposited IZO are compared.

2. Experimental Details

IZO thin films were prepared on glass substrates (Corning eagle 2000) by USP. A 0.2 mol/L solution of zinc acetate dehydrate $[\text{Zn}(\text{CH}_3\text{COO})_2 \cdot 2\text{H}_2\text{O}]$ diluted in ethanol, and deionized water (3:1) was used for the film, and indium acetate $[\text{In}(\text{CH}_3\text{COO})_3]$ was added to initial solution for indium doping. The In/Zn ratio was 1.5 at %. The glacial acetic acid was added into the precursor solution at 18 vol. % content. After the glass substrate was heated to 480°C , the aerosol of initial solution was nebulized by an ultrasonic

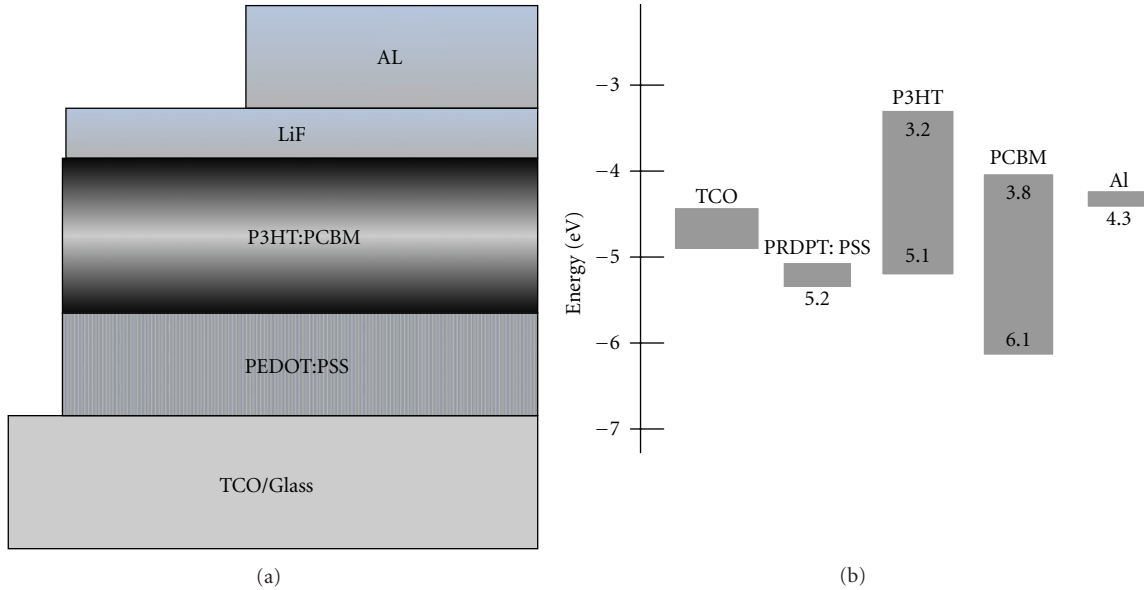


FIGURE 1: (a) Device structure and (b) energy diagram of OPVs.

agitation with 1.7 MHz and transported into the growth chamber by air at a flow rate of 11 L/min. The IZO film with ~ 600 nm thicknesses was measured by step profilometer (AMBIOS-XP2) and field emission scanning electron microscope (FE-SEM, JSM-6700F). The electrical properties were obtained by Hall-effect measurements using Van der Pauw method (Accent HL5500 PC). The surface morphology was observed by SEM. The direct transmittances of thin films were evaluated by UV-visible-NIR spectrometer (Cary 5000 UV-VIS produced by Varian Company). The root mean square roughness (RMS) was taken in a contact mode with an atomic force microscope (AFM, SPA-400 SPM UNIT product by Seiko Instruments Inc.).

Conventional OPVs were fabricated on the USP-grown IZO electrode to investigate the effect of the sheet resistance, transmittance and work function of the USP-grown IZO electrode on the performance of the OPVs. To fabricate the OPVs, IZO electrodes were cleaned with detergent, ultrasonicated in acetone and isopropyl alcohol, and subsequently dried in an oven overnight. Conducting PEDOT:PSS (Baytron P VP AI 4083) was spin-cast (5000 rpm) with thickness about 40 nm from aqueous solution (after passing a $0.45 \mu\text{m}$ filter). A blend solution of 15 mg of poly(3-hexylthiophene) (P3HT) and 12 mg of [6,6]-phenyl C_{61} -butyric acid methyl ester (PCBM) in 1 mL of chlorobenzene was spin-coated on top of the respective PEDOT:PSS layers. Subsequently, the devices were pumped down in vacuum (10^{-4} Pa), and an LiF(1 nm)/Al (100 nm) film used as the cathode was deposited on top of the active layer. The reference devices were fabricated on commercial ITO glass substrates in the same manner. OPVs with a structure of TCO/PEDOT:PSS/P3HT:PCBM/LiF/Al were completed. The schematic diagram is shown in Figure 1(a). The active area of the devices was 0.08 cm^2 defined by the shade mask. Device current density-voltage (J - V) characteristics were measured

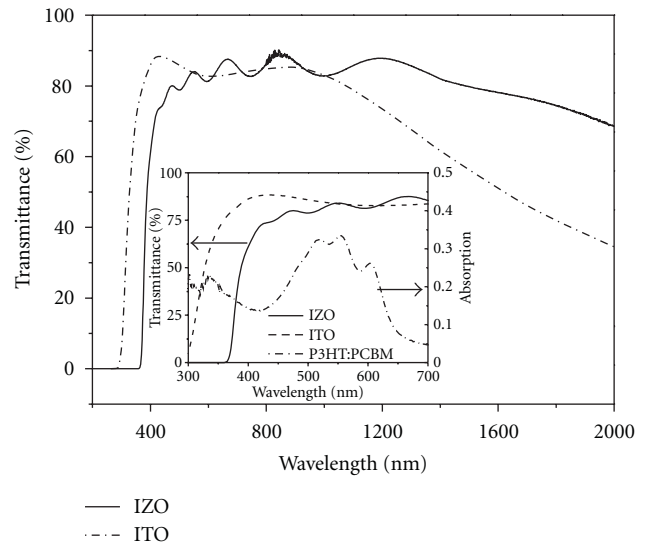


FIGURE 2: Transmittance of IZO- and ITO-coated glass substrates from ultraviolet to near-infrared region. Inset indicates transmittance of IZO- and ITO-coated glass substrates with respect to the absorbance of the P3HT:PCBM films.

using a Keithley 2420 under 100 mW/cm^2 simulated AM 1.5 G solar illumination calibrated using a Si photodetector. All of the measurements were fabricated and tested in ambient conditions in air.

3. Results and Discussions

As shown in Figure 2, the transparency of IZO-coated glass extends well into the near infrared region (NIR) and exhibits transmittance $>80\%$ around 1500 nm. The high transparency of IZO film in the NIR suggests the potential

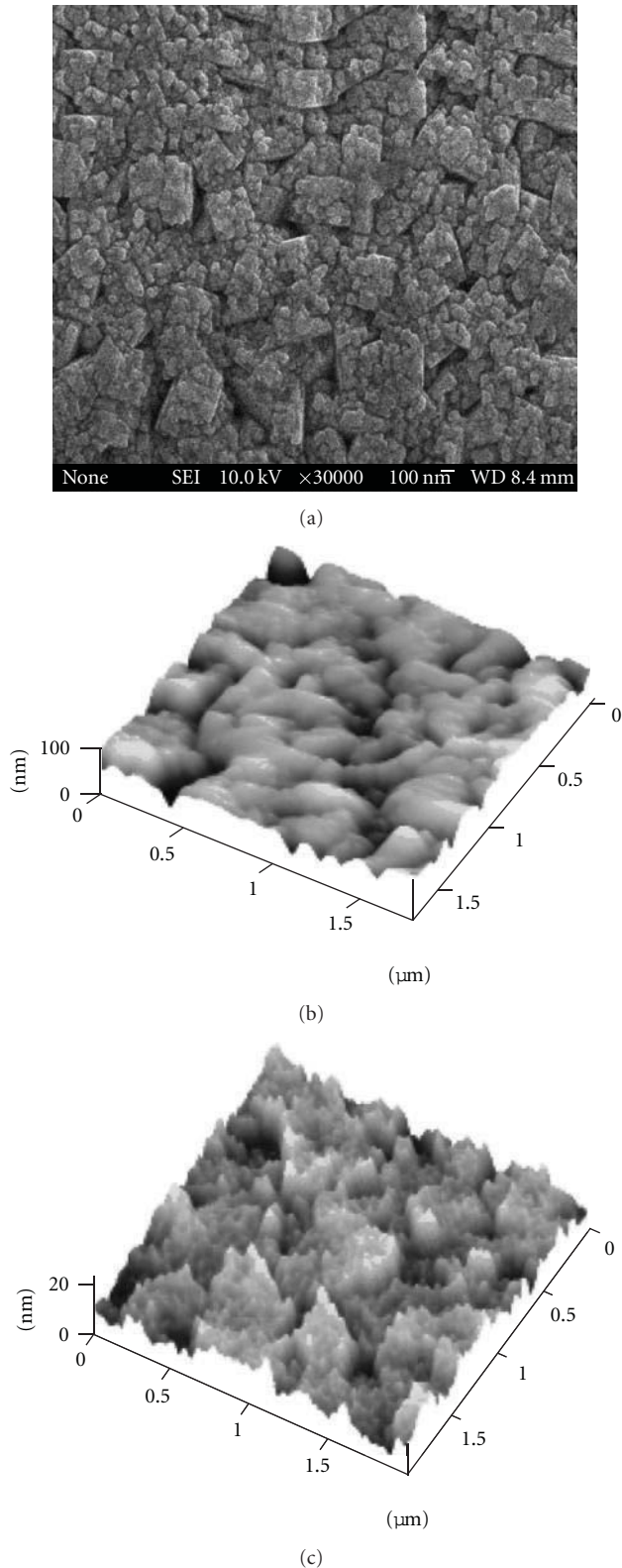


FIGURE 3: (a) Scanning electron microscope (SEM) image of IZO film prepared by ultrasonic spray pyrolysis. The topography of (b) IZO-coated glass and (c) ITO-coated glass substrates measured using atomic force microscopy (AFM). The root mean square surface roughness is 12.37 nm for IZO and 2.41 nm for ITO.

application in stacked cell where high NIR transmittance is required. In contrast, the transmittance of commercial ITO-coated glass decreases in the NIR (<1000 nm) due to the high degree of free-carrier absorption [18]. From Figure 2, it is perceptible that the transmission window of the IZO-coated glass is significantly larger than that of the ITO-coated glass. The high transparency is ascribed to the lower carrier density ($1.54 \times 10^{20} \text{ cm}^{-3}$) according to the Drude model [19]. The measured resistance of IZO-coated glass is $3.14 \times 10^{-3} \Omega \text{ cm}$, higher than that of commercial ITO-coated glass ($4.58 \times 10^{-4} \Omega \text{ cm}$). These optical and electrical characteristics of the IZO films make this material suitable for solar cell applications.

A comparison of the surface roughness between the IZO- and ITO-coated glass substrates is shown in Figures 3(b) and 3(c), respectively. The AFM images reveal that the IZO film forms large irregular crystals, resulting in a surface root mean square (RMS) roughness of 12.37 nm as shown in Figure 3(b). In contrast, the ITO film forms small crystal grains and has a comparatively smooth surface with a RMS roughness of 2.41 nm as shown in Figure 3(c). Although the rough surface of the IZO may induce direct contact between the oxide anode and the Al cathode, spin-coating a ~ 40 nm thick PEDOT:PSS buffer layer on the IZO film surface prior to spin-coating of the active layer smooths the rough surface and eliminates these shorts.

Device A with the structure of IZO/PEDOT:PSS/P3HT:PCBM/LiF/Al and Device B with the structure of ITO/PEDOT:PSS/P3HT:PCBM/LiF/Al were fabricated, respectively. The J - V curves in the dark and under simulated AM 1.5 conditions (100 mW/cm^2) of the devices A and B are shown in Figure 4. Under illumination, the device A yields a V_{oc} of 0.56 V, a J_{sc} of 8.49 mA/cm^2 , an FF of 0.40, and a power conversion efficiency (PCE) of 1.91%, which is inferior to the performance of the device B with an efficiency of 3.24%. The slopes at the short circuit point and at the open circuit voltage are the inverse values of the shunt resistance (R_{sh}) and the series resistance (R_s) of the equivalent circuit scheme of a solar cell, respectively. The estimated values of R_s and R_{sh} are presented in Table 1.

The measured short circuit currents of the devices A and B were nearly identical, from which we may conclude that there was little change in the optical field distribution, or in charge collection efficiency. From the inset of Figure 2, it can be seen that the absorption domain of the blend of P3HT:PCBM, the photoconductive films of the organic cells, is mainly situated in the region of large transparency of IZO-coated glass. The average of transmittance of IZO is appreciably less than that of ITO in the range of 350~650 nm, which may result in the lower current density than that of device B.

The device made with IZO exhibited similar V_{oc} than did those made with ITO. The value of V_{oc} is also similar to the previous results. If both electrodes establish ohmic contacts with the active layer, V_{oc} in these bulk-heterojunction cells is related directly to the energy difference between the HOMO level of the donor (P3HT) and the LUMO level of the acceptor (PCBM) components. As shown in Figure 1(b),

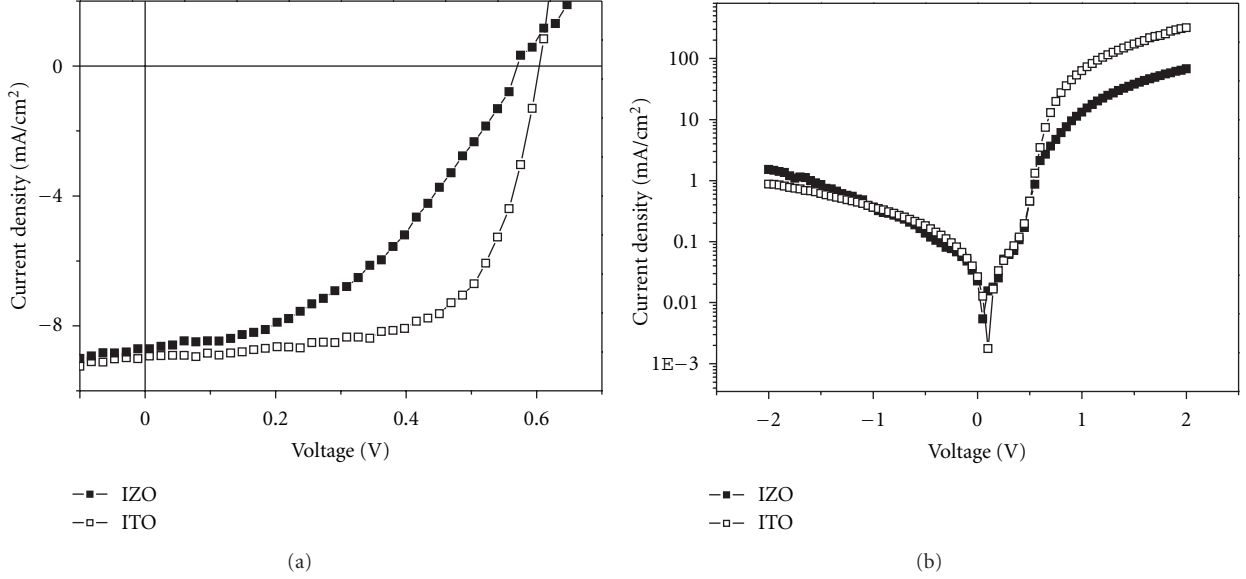


FIGURE 4: Current density-voltage (J - V) characteristics of FTO/PEDOT:PSS/P3HT:PCBM/LiF/Al and ITO/PEDOT:PSS/P3HT:PCBM/LiF/Al photovoltaic devices (a) under simulated AM 1.5 conditions and (b) in the dark.

TABLE 1: Detailed performance parameters of the OPVs fabricated on the IZO- and ITO-coated glass substrates.

Device	Anode	J_{sc} (Ma cm^{-2})	V_{oc} (V)	FF (%)	PCE (%)	R_s ($\Omega \text{ cm}^2$)	R_{sh} ($\Omega \text{ cm}^2$)
A	IZO	8.49	0.56	40	1.91	32.25	284.45
B	ITO	8.95	0.59	61	3.24	8.08	584.79

the introduction of high work function of PEDOT:PSS as a buffer layer, ohmic contacts between TCO and active layer are achieved, resulting in better hole extraction. Therefore, PEDOT:PSS buffer layer not only planarizes the IZO surface, but also induces the ohmic contact between TCO and active layer. Slight variation in V_{oc} values may arise from pinholes, which short-circuits the photovoltaic cell resulting in large leak current. For a conventional p - n junction solar cell the V_{oc} is given by the formula

$$V_{oc} = \left(\frac{nkT}{q} \right) \ln \left(\frac{J_{sc}}{J_s} + 1 \right), \quad (1)$$

where J_s is the saturation current density, q is the elementary charge, k is Boltzmann's constant, T is temperature, and n is the ideality factor, J_{sc} is the short circuit current density. The values of V_{oc} derived from experimental light J - V curves of devices A and B fit to the above equation agree with the measured values well.

In Figure 4(b), the dark J - V characteristics of the devices A and B are shown on a logarithmic scale. The devices A and B almost present the same reverse biased current, which suggest the smooth effect of PEDOT:PSS on relatively rough IZO-coated glass. The influence of the buffer layer can be observed in the J - V curves under lower bias in the dark. The J - V curves were first symmetric, and then reached the injection limit at forward bias. At further increase of forward bias the current approached a space charge limited condition and the difference among the J - V curves of the diodes with different buffer layers is small. This is because the current in

this region mainly depends on the mobility of charge carriers in the active layers. Under forward bias, the difference of ohmic contributions and injection limit in diodes reflect the hole injection from anode to active layer via the buffer layer, because the electron injection conditions are the same in the devices A and B. This indicates that the injection capabilities of these buffer layers are the same as well. At high forward bias, the current density of device B is obviously larger than that of device A, which is ascribed to the lower resistance of ITO films, indicating superior FF of device B [2]. To overcome FF losses in solar cells, future research should concentrate on increasing the layer conductivity and enhancing the surface smoothness of the films without losing the transmittance.

4. Conclusion

In summary, this study investigates atmospheric-pressure solution deposition routes as an alternative to these traditional high-vacuum techniques. Solution processing is attractive due to its ease and potential to lower device-manufacturing costs. We demonstrated that USP-grown IZO electrodes are promising low-cost anode materials. Due to the relatively low resistivity and high transmittance extended to NIR, which is a critical benefit for the fabrication of low-cost OPVs. More importantly, considering the materials cost and process efficiency, it is believed that low In IZO electrodes grown by the USP method are better suited to cost-efficient OPVs than the batch-type grown ITO electrodes.

Furthermore, it was found that the performance of the OPV fabricated on the UPS-grown IZO electrodes depends mainly on the sheet resistance and surface morphology of the IZO electrodes, regardless of the work function, due to the existence of a PEDOT:PSS ohmic layer connecting the anode and the active layer. The presented results demonstrate that USP is a promising method for the deposition of IZO thin films and can be used as replacement for the ITO electrode. In addition, the IZO film with high transparency in the NIR appears very promising in stacked solar cells with absorption of full wavelength spectrum. This may lead to higher efficiency organic multijunction photovoltaic cells.

Acknowledgments

This work was supported by the National Basic Research Program of China (Grants no. 2011CBA00705, 2011CBA00706, and 2011CBA00707), and the National High-tech R&D Program (Grant no. 2009AA050602).

References

- [1] W. Ma, C. Yang, X. Gong, K. Lee, and A. J. Heeger, "Thermally stable, efficient polymer solar cells with nanoscale control of the interpenetrating network morphology," *Advanced Functional Materials*, vol. 15, no. 10, pp. 1617–1622, 2005.
- [2] J. Xue, S. Uchida, B. P. Rand, and S. R. Forrest, "Asymmetric tandem organic photovoltaic cells with hybrid planar-mixed molecular heterojunctions," *Applied Physics Letters*, vol. 85, no. 23, pp. 5757–5759, 2004.
- [3] G. Chidichimo and L. Filippelli, "Organic solar cells: problems and perspectives," *International Journal of Photoenergy*, vol. 2010, Article ID 123534, 11 pages, 2010.
- [4] T. Minami, "Transparent conducting oxide semiconductors for transparent electrodes," *Semiconductor Science and Technology*, vol. 20, no. 4, pp. S35–S44, 2005.
- [5] E. J. J. Martin, M. Yan, M. Lane, J. Ireland, C. R. Kannewurf, and R. P. H. Chang, "Properties of multilayer transparent conducting oxide films," *Thin Solid Films*, vol. 461, no. 2, pp. 309–315, 2004.
- [6] J. Ni, H. Yan, A. Wang et al., "Synthesis and characterization of volatile zinc MOCVD precursors and their implementation in growth of highly transparent, conducting zinc- and tin-doped indium oxide anodes for polymer light-emitting diodes," *Journal of the American Chemical Society*, vol. 127, no. 15, pp. 5613–5624, 2005.
- [7] Y. Yang, L. Wang, H. Yan, S. Jin, T. J. Marks, and S. Li, "Highly transparent and conductive double-layer oxide thin films as anodes for organic light-emitting diodes," *Applied Physics Letters*, vol. 89, no. 5, pp. 051116–051118, 2006.
- [8] Z. Hu, J. Zhang, Z. Hao, Q. Hao, X. Geng, and Y. Zhao, "Highly efficient organic photovoltaic devices using F-doped SnO₂ anodes," *Applied Physics Letters*, vol. 98, no. 12, pp. 123302–123304, 2011.
- [9] J. A. Jeong, H. K. Kim, and S. I. Na, "Low resistance and high transparent amorphous IZTO electrode cosputtered by linear facing target sputtering for organic photovoltaics," *Electrochemical and Solid-State Letters*, vol. 12, no. 9, pp. J80–J82, 2009.
- [10] V. Bhosle, J. T. Prater, F. Yang, D. Burk, S. R. Forrest, and J. Narayan, "Gallium-doped zinc oxide films as transparent electrodes for organic solar cell applications," *Journal of Applied Physics*, vol. 102, no. 2, pp. 023501–023505, 2007.
- [11] G. B. Murdoch, S. Hinds, E. H. Sargent, S. W. Tsang, L. Mordoukhovski, and Z. H. Lu, "Aluminum doped zinc oxide for organic photovoltaics," *Applied Physics Letters*, vol. 94, no. 21, pp. 213301–213303, 2009.
- [12] F. Yang and S. R. Forrest, "Organic solar cells using transparent SnO₂-F anodes," *Advanced Materials*, vol. 18, no. 15, pp. 2018–2022, 2006.
- [13] M. D. L. L. Olvera, H. Gómez, and A. Maldonado, "Doping, vacuum annealing, and thickness effect on the physical properties of zinc oxide films deposited by spray pyrolysis," *Solar Energy Materials and Solar Cells*, vol. 91, no. 15–16, pp. 1449–1453, 2007.
- [14] J. Wienke and A. S. Booi, "ZnO: in deposition by spray pyrolysis—influence of the growth conditions on the electrical and optical properties," *Thin Solid Films*, vol. 516, no. 14, pp. 4508–4512, 2008.
- [15] J. M. Bian, X. M. Li, X. D. Gao, W. D. Yu, and L. D. Chen, "Deposition and electrical properties of N-In codoped p-type ZnO films by ultrasonic spray pyrolysis," *Applied Physics Letters*, vol. 84, no. 4, pp. 541–543, 2004.
- [16] H. Gomez, A. Maldonado, M. D. L. L. Olvera, and D. R. Acosta, "Gallium-doped ZnO thin films deposited by chemical spray," *Solar Energy Materials and Solar Cells*, vol. 87, no. 1–4, pp. 107–116, 2005.
- [17] J. Wienke, B. van der Zanden, M. Tijssen, and M. Zeman, "Performance of spray-deposited ZnO: in layers as front electrodes in thin-film silicon solar cells," *Solar Energy Materials and Solar Cells*, vol. 92, no. 8, pp. 884–890, 2008.
- [18] M. Yang, J. Feng, G. Li, and Q. Zhang, "Tungsten-doped In₂O₃ transparent conductive films with high transmittance in near-infrared region," *Journal of Crystal Growth*, vol. 310, no. 15, pp. 3474–3477, 2008.
- [19] T. J. Coutts, D. L. Young, and X. Li, "Characterization of transparent conducting oxides," *MRS Bulletin*, vol. 25, no. 8, pp. 58–65, 2000.

Research Article

Load-Resistance- and Voltage-Tunable Photovoltaic Effect in Tilting Manganite Films

X. L. Han,^{1,2} H. Ni,² K. Zhao,^{1,2,3,4} Y.-C. Kong,³ H. K. Wong,³ and S. Q. Zhao²

¹ State Key Laboratory of Heavy Oil Processing, China University of Petroleum, Beijing 102249, China

² College of Science, China University of Petroleum, Beijing 102249, China

³ Department of Physics, The Chinese University of Hong Kong, Hong Kong

⁴ International Center for Materials Physics, Chinese Academy of Sciences, Shenyang 110016, China

Correspondence should be addressed to K. Zhao, zhk@cup.edu.cn

Received 24 April 2011; Accepted 30 August 2011

Academic Editor: Vincenzo Augugliaro

Copyright © 2011 X. L. Han et al. This is an open access article distributed under the Creative Commons Attribution License, which permits unrestricted use, distribution, and reproduction in any medium, provided the original work is properly cited.

The photovoltaic properties of miscut $\text{La}_{2/3}\text{Ca}_{1/3}\text{MnO}_3$ films were systematically investigated with different bias voltage (V_b) and load resistance (R_S). The photoresponse depended strongly on V_b and R_S and was improved greatly by increasing V_b and R_S . The maximum photovoltaic sensitivity reached 62.5 mV/mJ. The present results suggested the promising potential of increasing V_b and R_S in high-sensitivity detectors.

1. Introduction

Hydrocarbon resource is important and strategic for the national modernization, defense, and security. Present concept of Digital Oilfield suggests that an optical detector in oil well can operate at high temperature upto $\sim 500^\circ\text{C}$ and high pressure upto ~ 100 MPa with high-speed response. Recently there have been active studies of the photoresponse characteristics in the manganite thin films which can work in a harsh environment (features such as thermal instability and high pressure). Technological interest has centered on bolometers [1], while more basic issues have involved quasiparticle generation and carrier relation times [2–6]. Ultrafast photovoltaic effect has been observed in manganite oxide with a picosecond response time, which was due to a combination mechanism of photoinduced carriers and Seebeck effect [7–9].

In this work, to improve the photosensitivity of manganite films and meet the needs of oil and gas optical engineering, we focused on load-resistance- (R_S -) and bias-voltage- (V_b -) tunable lateral photovoltages of $\text{La}_{2/3}\text{Ca}_{1/3}\text{MnO}_3$ (LCMO) films grown on miscut LaSrAlO_4 (LSAO) substrates with 10° tilted to [001] direction of LSAO. The laser-induced voltage (LIV) depended strongly on V_b and R_S . Under an

irradiation of 248 nm ultraviolet laser, when V_b is changed from 30 to -30 V, the LIV peak sensitivity can be tuned from -10.8 to 12.5 mV/mJ and from -52.1 to 62.5 mV/mJ at $R_S = 10$ and 72 Ω , respectively.

2. Experimental

A LCMO (120 nm) thin film was deposited by facing-target sputtering technique on the LSAO substrate cut along the (001) surface with an intentional 10° vicinal angle toward the [010] direction [10, 11]. The substrate temperature was kept at 680°C with the oxygen pressure of 30 mTorr during deposition. After the deposition, the vacuum chamber was immediately backfilled with 1 atm oxygen. The LCMO film was then cooled to room temperature with the substrate heater power cutoff.

Figure 1 shows the schematic circuit of the photoresponse measurement. Before the measurement, the sample was carefully cleaned using alcohol and acetone. Two colloidal silver electrodes of $1\text{ mm} \times 2.5\text{ mm}$ area were prepared on LCMO surface. Compex 50 excimer-pulsed laser was used as the light source, operating at a wavelength of 248 nm with 20 ns duration at a repetition rate of 1 Hz. The on-sample

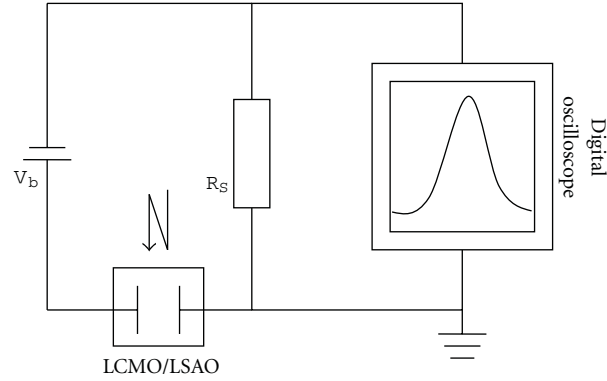


FIGURE 1: The schematic circuit of the sample measurement.

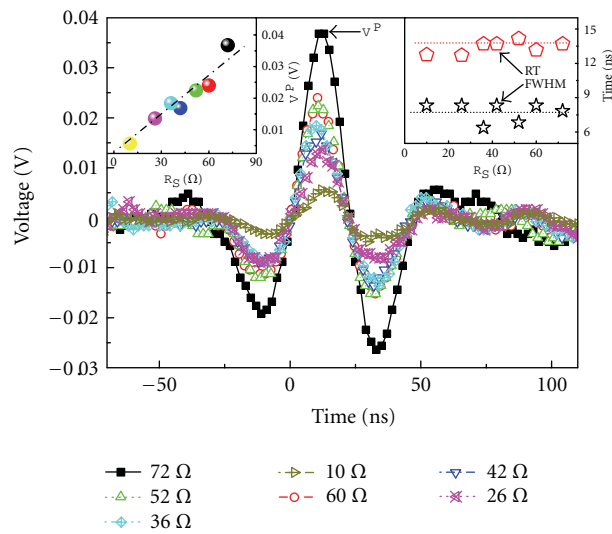


FIGURE 2: Waveforms for different load resistance R_S at $V_b = 0$ V under the 248 nm laser illumination. The left inset shows the dependence of V^P on R_S . The right inset displays the RT and FWHM as functions of R_S .

laser pulse energy is 2.88 mJ. The waveforms were recorded by a sampling oscilloscope with an input impedance of 1 M Ω . All the measurements were carried out at room temperature.

3. Results and Discussion

Figure 2 shows a typical voltage transient of LCMO film under the 248 nm laser irradiation without bias ($V_b = 0$ V). The rise time (RT) and full width at half-maximum (FWHM) are independent of R_S and 7 ns and 13 ns, respectively. As reviewed in the left inset of Figure 2, the peak voltage signal V^P has a linear relationship with the R_S from 10 to 72 Ω .

The laser-induced voltage waveform is plotted in Figures 3(a) and 3(b) as a function of time, and the photovoltage peak value V^P increases monotonously from -0.15 to 0.18 V

and from -0.031 to 0.036 V with V_b from 30 to -30 V at $R_S = 72$ and 10 Ω . Figure 3(c) reviews V^P as a function of applied bias voltage V_b , which depended linearly on V_b and showed no saturation for selected R_S . In addition, V^P is also very sensitive to the load resistance R_S and shows a higher value for a larger R_S . As shown in Figure 3(d), the 10–90% rise time RT of the photovoltaic signals nearly keeps constant with varying R_S , while the response speed is faster for the lower bias and the RT difference between $V_b = 0$ and 30 V is about 10 ns.

Figure 4 summarizes the spatial distribution of the V^P as a function of R_S and V_b . $|V^P|$ shows a higher value for a larger V_b while a lower value for a smaller V_b and increases with increasing load resistance R_S . The result indicates the potential possibility to improve the photovoltage sensitivity by introducing the load resistance and applying bias voltage.

Since the photon energy of 248 nm wavelength (4.86 eV) is above the bandgap of LCMO (~ 1.2 eV), electron-hole pairs

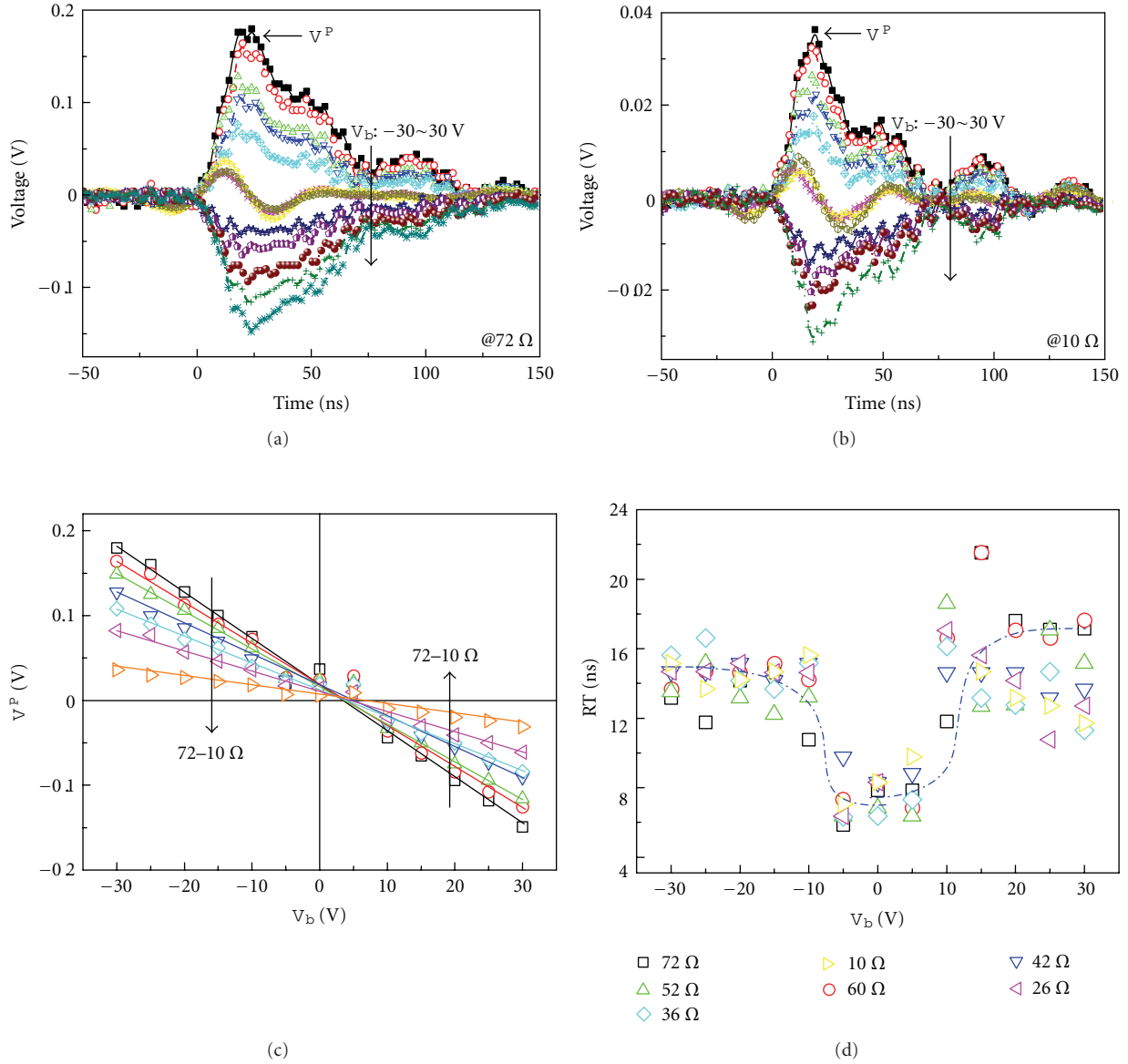


FIGURE 3: Photovoltage as a function of time with (a) $R_S = 72 \Omega$ and (b) $R_S = 10 \Omega$ under 248 nm laser pulses at different bias voltage V_b . (c) V^P and (d) rise time RT as a function of V_b .

are generated in the LCMO film. In our case, the laser we used is a 248 nm KrF excite laser beam in duration of 20 ns, so the amount of laser-induced carriers should be comparable with or even much larger than that of the majority carriers in the LCMO; on the other hand, there exists no built-in field which exists in the p-n junction to separate holes and electrons. Therefore, both the electrons and holes play an important role in the photovoltaic. Under the external bias, the carriers are sped up and the photoresponse is enhanced.

From the basic laws of circuit networks, the readout voltage V_S from the oscilloscope can be calculated from $V_S = (V_b - V_0)R_S / (R_S + R_0)$, where V_0 is the voltage signal generated in the sample and R_0 is the sample impedance. In our case, the load resistance is small and $R_S \ll R_0$. Thus, V_S can be

presented as $V_S \approx (V_b - V_0)R_S / R_0 \propto R_S$ as shown in Figures 2 and 4.

4. Conclusions

In summary, the bias and load resistance-dependent photovoltaic effects in LCMO thin film grown on miscut LSAO were studied systematically. With the increase in V_b and R_S , the peak photovoltage signals increase monotonically and a maximum of 0.18 V was achieved at $R_S = 72 \Omega$, $V_b = 30$ V. The experimental results showed that increasing V_b and R_S is an effective method for improving the photovoltage sensitivity in manganite, suggesting the potential for optoelectronic detection applications.

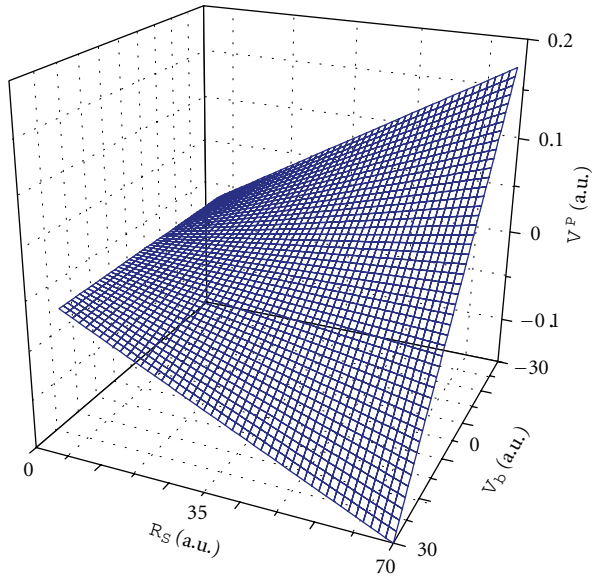


FIGURE 4: Three-dimensional plot for V^P as a function of R_S and V_b .

Acknowledgments

This work has been supported by NCET, NSFC, RFDP, and Direct Grant from the Research Grants Council of the Hong Kong Special Administrative Region (Grant no. C001-2060295).

References

- [1] M. Rajeswari, C. H. Chen, A. Goyal et al., "Low-frequency optical response in epitaxial thin films of $\text{La}_{0.67}\text{Ca}_{0.33}\text{MnO}_3$ exhibiting colossal magnetoresistance," *Applied Physics Letters*, vol. 68, no. 25, pp. 3555–3557, 1996.
- [2] Y. G. Zhao, J. J. Li, R. Shreekala et al., "Ultrafast laser induced conductive and resistive transients in $\text{La}_{0.7}\text{Ca}_{0.3}\text{MnO}_3$: charge transfer and relaxation dynamics," *Physical Review Letters*, vol. 81, no. 6, pp. 1310–1313, 1998.
- [3] R. D. Averitt, A. I. Lobad, C. Kwon, S. A. Trugman, V. K. Thorsmølle, and A. J. Taylor, "Ultrafast conductivity dynamics in colossal magnetoresistance manganites," *Physical Review Letters*, vol. 87, no. 1, Article ID 017401, pp. 1–4, 2001.
- [4] K. Zhao, K. J. Jin, H. Lu et al., "Transient lateral photovoltaic effect in p-n heterojunctions of $\text{La}_{0.7}\text{Sr}_{0.3}\text{MnO}_3$ and Si," *Applied Physics Letters*, vol. 88, no. 14, Article ID 141914, 2006.
- [5] K. Zhao, K. J. Jin, H. B. Lu et al., "Electrical-modulated magnetoresistance in multi- p-n heterojunctions of $\text{La}_{0.9}\text{Sr}_{0.1}\text{MnO}_3$ and oxygen-vacant $\text{SrTiO}_{3-\delta}$ on Si substrates," *Applied Physics Letters*, vol. 93, no. 25, Article ID 252110, 2008.
- [6] H. Liu, K. Zhao, N. Zhou et al., "Photovoltaic effect in micrometer-thick perovskite-type oxide multilayers on Si substrates," *Applied Physics Letters*, vol. 93, no. 17, Article ID 171911, 2008.
- [7] K. Zhao, K. J. Jin, Y. H. Huang et al., "Laser-induced ultrafast photovoltaic effect in $\text{La}_{0.67}\text{Ca}_{0.33}\text{MnO}_3$ films at room temperature," *Physica B*, vol. 373, no. 1, pp. 72–75, 2006.
- [8] K. Zhao, M. He, G. Z. Liu, and H. B. Lu, "Photo-induced voltage characteristics of $\text{La}_{0.9}\text{Sr}_{0.1}\text{MnO}_3$ films epitaxially

grown on vicinal SrTiO_3 (001) substrates," *Journal of Physics D*, vol. 40, no. 18, pp. 5703–5706, 2007.

- [9] K. Zhao, Y. H. Huang, H. B. Lu et al., "Anomalous photovoltaic effect in $\text{La}_{0.8}\text{Sr}_{0.2}\text{MnO}_3$ films grown on SrTiO_3 (001) substrates by laser molecular beam epitaxy," *EPJ Applied Physics*, vol. 35, no. 3, pp. 173–176, 2006.
- [10] X. T. Zeng and H. K. Wong, "Epitaxial growth of single-crystal (La,Ca) MnO_3 thin films," *Applied Physics Letters*, vol. 66, no. 24, pp. 3371–3373, 1995.
- [11] Z. J. Yue, K. Zhao, H. Ni et al., "Photo-induced magnetoresistance enhancement in manganite heterojunction at room temperature," *Journal of Physics D*, vol. 44, Article ID 095103, 2011.

Review Article

Achievements and Challenges of CdS/CdTe Solar Cells

Zhou Fang, Xiao Chen Wang, Hong Cai Wu, and Ce Zhou Zhao

Department of Electrical and Electronic Engineering, Xi'an Jiaotong-Liverpool University, Suzhou 215123, China

Correspondence should be addressed to Ce Zhou Zhao, cezhou.zhao@xjtlu.edu.cn

Received 28 June 2011; Revised 8 August 2011; Accepted 8 August 2011

Academic Editor: Leonardo Palmisano

Copyright © 2011 Zhou Fang et al. This is an open access article distributed under the Creative Commons Attribution License, which permits unrestricted use, distribution, and reproduction in any medium, provided the original work is properly cited.

Thin film CdS/CdTe has long been regarded as one promising choice for the development of cost-effective and reliable solar cells. Efficiency as high as 16.5% has been achieved in CdS/CdTe heterojunction structure in laboratory in 2001, and current techniques for CdS/CdTe solar cells gradually step toward commercialization. This paper reviews some novel techniques mainly within two years to solve this problem from aspects of promotion of fabrication technology, structural modification, and choice of back contact materials.

1. Introduction

As the world is suffering from impending death of fossil fuels and serious pollution resulted from the fuels, solar energy is now regarded as one promising solution to the global energy crisis. Among various means for generating energy from the sun, solar cells are an effective approach to convert solar energy into practical electrical energy. In 2009, the global production of photovoltaic cells and modules in 2009 was 12.3 GW [1], and it increased to over 20 GW one year later [2]. Many kinds of solar cells based on Si [3], thin film [4, 5], or even organic materials [6, 7] are gradually developed these years. According to the US Department of Energy, solar energy should only be economically viable for large-scale production if the cost can be reduced to \$0.33/Wp (Wp = watt peak) [8].

Thin-film cadmium telluride (CdTe) is now regarded as one leading material for the development of cost-effective photovoltaics (PV), and it is also the first PV technology with the price for Wp below \$1 (\$0.85) [9]. CdTe has a band gap of ~1.5 eV, which is close to the ideal value for photovoltaic conversion efficiency. Meanwhile, high optical absorption coefficient and high chemical stability also appear in CdTe. All of them make CdTe a very attractive material for thin-film solar cells. The theoretical efficiency of CdTe thin-film solar cells is expected to be 28%–30% [10, 11]. Currently, First Solar has announced a new world record this year for CdTe PV solar cell efficiency of 17.3% with a test cell constructed using commercial-scale manufacturing equipment

and materials, and its average efficiency of modules produced in the first quarter of 2011 was 11.7% [12].

One of best choices for CdTe cells are heterojunction structures with n-type cadmium sulfide (CdS) as a transparent window layer, and they are generally fabricated in a superstrate configuration (Figure 1). Despite the lattice mismatch of 10% between CdTe and CdS, the formed heterojunction has an excellent electrical behavior, leading to a high fill factor of 0.77 in produced solar cells [13]. Therefore, this structure is favored by a variety of world-leading corporates. For example, First Solar has launched one project to double its manufacturing capacity of CdS/CdTe solar cells from 1.5 GW at the beginning of 2011 to nearly 3 GW by the end of 2012 [14]. Calyxo also expended their capacity up to 25 MWp in 2008 and expects to finish their second production line with capacity of 110 MWp in 2011 [15]. In CdS/CdTe heterojunction structure, efficiency up to 16.5% has been achieved in lab as early as 2001 [16], while the best commercial modules are approximately 10%–11% [17]. However, these are still much lower than the theoretical value. There are currently several challenges for further making CdS/CdTe thin-film solar cells more competitive: (1) short minority carrier lifetime due to the recombination of electron-hole pairs at the defect centers in CdTe layers and at the interface between CdS and CdTe, (2) insufficient transparency of transparent conductive oxide (TCO) and CdS window layers, (3) lack of good ohmic contact between CdTe layers and back contacts, and (4) possibility in doping p-type CdTe films in a stable way. Techniques coming up

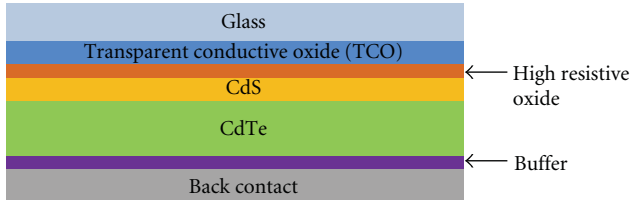


FIGURE 1: An example of the structure of standard CdS/CdTe thin-film solar cells.

in recent years are mainly concentrated on the first three challenges above.

Instead of summarizing the history, this paper aims to review the progress of CdS/CdTe photovoltaics by evaluating some current techniques to deal with first three challenges above from three aspects: fabrication technology, structural design, and choice of back contact, respectively.

2. Promotion in Fabrication Techniques

Fabrication methods for CdS/CdTe layers could have a significant effect on cell efficiency and cost. Samples have been obtained successfully by several common techniques: radio frequency sputtering (R. F. Sputtering) [18], close-spaced sublimation (CSS) [19], and chemical bath deposition (CBD) [20] for CdS preparation, while electrodeposition (ED) [21], screen printing (SP) [22], and CSS [23–25] for CdTe thin-film formation. However, these methods are still not sufficient good due to their inherent drawbacks. For example, R. F. Sputtering for preparing CdS window layer can be rather fast but with poor quality that reduces the cell efficiency, while CBD could provide a dense and smooth CdS layer but the solution waste recycling and management cause extra cost. Therefore, the techniques should be carefully chosen with the consideration of high quality thin-film structure (high efficiency), proper pollution control, and commercial production prospect. Currently, the emerging problems related to fabrication mainly focus on (1) the short circuit of TCO and the CdTe layer caused by the partial grain covering and pinholes in CdS with extremely small thickness and (2) short minority carrier life time due to the defects inside the CdTe layer. Fortunately, several modifications to conventional methods and new techniques have been explored to improve the problems above these years [26–36].

2.1. Sputtering in Ar + CHF₃ Atmosphere. One excellent improvement to the fabrication of CdS layers is employing R. F. sputtering in the atmosphere of argon (Ar) containing ~3% of CHF₃ [11, 26–29]. This gas is decomposed and ionized during the sputtering discharge, delivering electronegative fluorine (F) to the substrate. Although it has been proved that F does not reduce the resistance of CdS layers [11, 27, 29], compared with undoped CdS, F-doped CdS still exhibits a larger forbidden gap [26], a stronger photoconductivity, and, most importantly, gives higher-efficiency solar cells [27]. This phenomenon probably results from the presence of F.

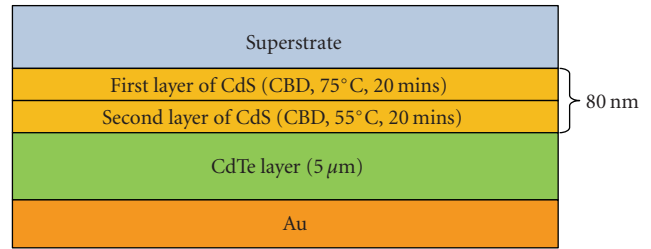


FIGURE 2: The structure of CdS/CdTe thin-film solar cell with bilayer CdS.

On one hand, it strongly reduces the growth rate of CdS and bombards the CdS films during the growth, which can eliminate the excess of Cd and S, hence producing a dense film with excellent thickness and quality control [28, 29]. On the other hand, it also promotes the formation of CdF₂, which could passivate the grain boundaries and forming good CdS/CdTe junctions [11, 28, 29]. Efficiency as high as 15%–15.8% has been obtained by Bosio et al. [11] in this approach. Therefore, this technique can be treated as a good choice for the fabrication of CdS layers in industrial production of photovoltaic modules.

2.2. Bilayer CdS Thin-Film Preparation. The structure of the bilayer CdS thin-film solar cell is shown in Figure 2. In this technology, the first CdS layer is made by standard CBD process with reduced time (compared with standard structure shown in Figure 1), and then the second CdS layer is deposited by CBD at lower temperature (55°C). Approximately 14.6 nm's roughness was observed in atomic force microscopy (AFM) for standard CBD of CdS thin film, while it could be reduced to 7.2 nm in bilayer case (see in Figures 3(a) and 3(b), resp.). Then smaller grain size would be obtained since the bilayer structure could provide the compact and uniform CdS layers without pinholes and cracks among grain boundaries. The dense and smooth CdS thin films could generate isolation between TCO and CdTe layers, which could solve the shunt problem between these two layers. Moreover, thinner CdS film results in higher short-circuit current (Figure 4) and improved the efficiency by around 6.1% with less demand of material (only 80 nm thickness of CdS layer shown in Figure 2) compared with standard CBD process [30, 31].

2.3. Low-Temperature Deposition Method. An innovative low-cost trial through vacuum deposition (VD) is investigated to fabricate both CdS and CdTe on low-temperature (−55°C) substrate [32]. The substrate holder was cooled by liquid nitrogen, while a secondary heater can adjust the temperature in a desired range. This process could provide higher optical transparency of CdS thin film and similar grain size (average 300 nm) for both layers (see in Figures 5(a) and 5(b)) compared with conventional techniques. As the performance of the solar cell is closely related to the quality of the interface between CdS and CdTe, the similar grain size does favor to good intermixture of these

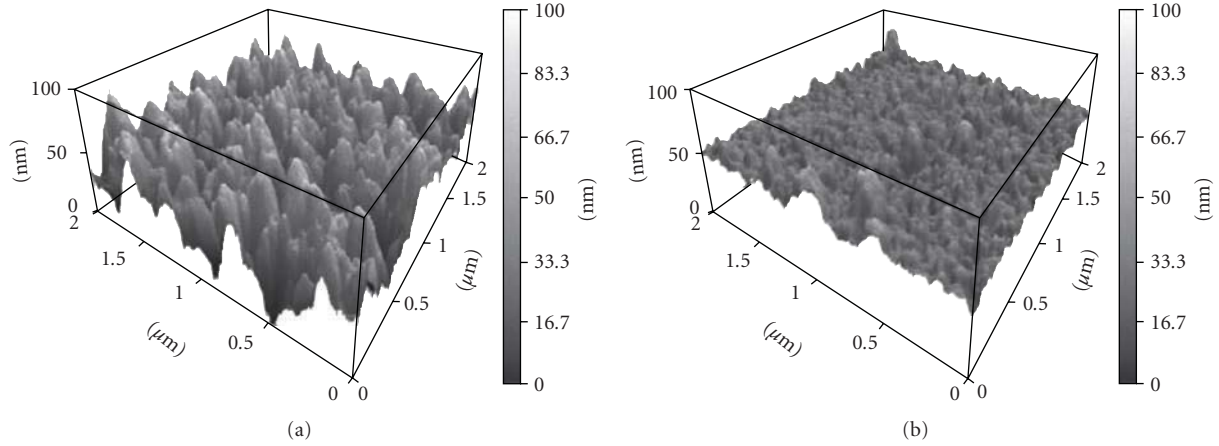


FIGURE 3: AFM of (a) standard CBD CdS with roughness of 12.2 nm, (b) CBD CdS with CdCl₂ annealing treatment at 300°C with roughness of 14.6 nm, (c) bilayer CdS with total 80 nm thickness with roughness of 7.2 nm. Figures are taken from [30].

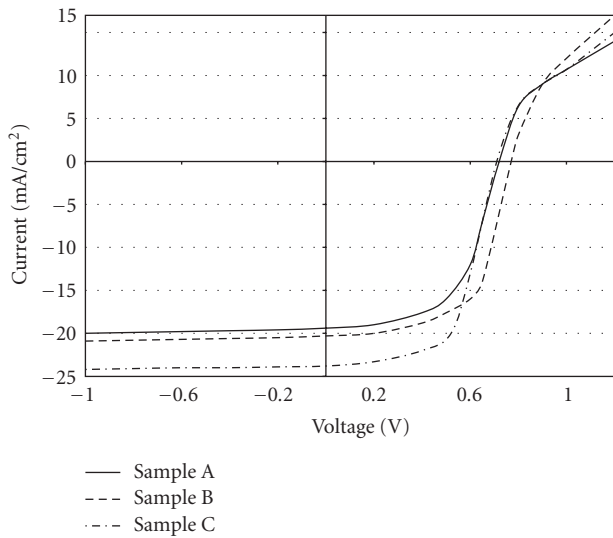
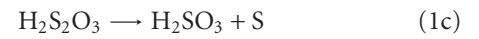
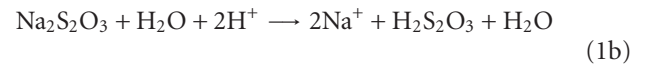


FIGURE 4: J-V characteristics of CdS/CdTe solar cells with different CdS films: Sample A: standard CBD CdS; Sample B: CBD CdS with CdCl₂ annealing treatment at 300°C; Sample C: bilayer CdS with total 80 nm thickness. Figures are taken from [30].

two materials and could dramatically decrease the defects inside interface. The resulted conversion efficiency >14% is rather high since it is the first successful operation of CdS/CdTe-based solar cell prepared by low-temperature deposition, and more work should be done to optimize the process before actually applying for commercial purpose [33].

2.4. All-Electrodeposited Method. In the all-electrical-deposition (AE) processing for CdS thin film, a graphite anode and a glass/fluorine-doped tin oxide (FTO) cathode are applied to pass an electric current through the electrolyte with CdCl₂ and Na₂S₂O₃ dissolved in (pH = 1.40) as shown in Figure 6. Both Cd- and S-containing cations are deposited on the cathode surface with electrically discharging and chemically

reaction. The formation of CdS on the cathode can be represented by following mechanisms:



Daily waste of toxic Cd-contained solution during the production could be avoided since the bath for ED-CdS can be used for at least 18 months without discarding the electrolyte compared with CBD process. Furthermore, the CdS/CdTe thin-film solar cells achieve a similar or superior performance by applying ED-CdS instead of CBD-CdS, because the crystal structure is hexagonal for former and cubic for latter. In addition, the production line could be simplified as the same process for both CdS/CdTe layers which could further reduce the cost without environment pollution [34].

2.5. Dry CdCl₂ Treatment for CdTe Recrystallization. Conventionally, CdS/CdTe samples are immersed into the solution containing CdCl₂ and heated at 400–500°C in order to enlarge the grains inside the CdTe layers and eliminate defects to increase the minority carrier lifetime. However, it seems to be unsuitable for large area manufacture considering industrial production and the residue of the solute may not be thoroughly cleared up. To solve this problem, Lee's work [35] shows that the dry CdCl₂ treatment by physical vapor deposition (PVD) on the sputtered CdTe layer. This method reveals effective process since no vacuum breaks are involved in production line, which agrees with commercial prospects. Furthermore, the average lower transmittance than wet treatment reflects its better light absorption property (Figure 7, the curve for dry CdCl₂ treatment is obviously below the wet one) [35].

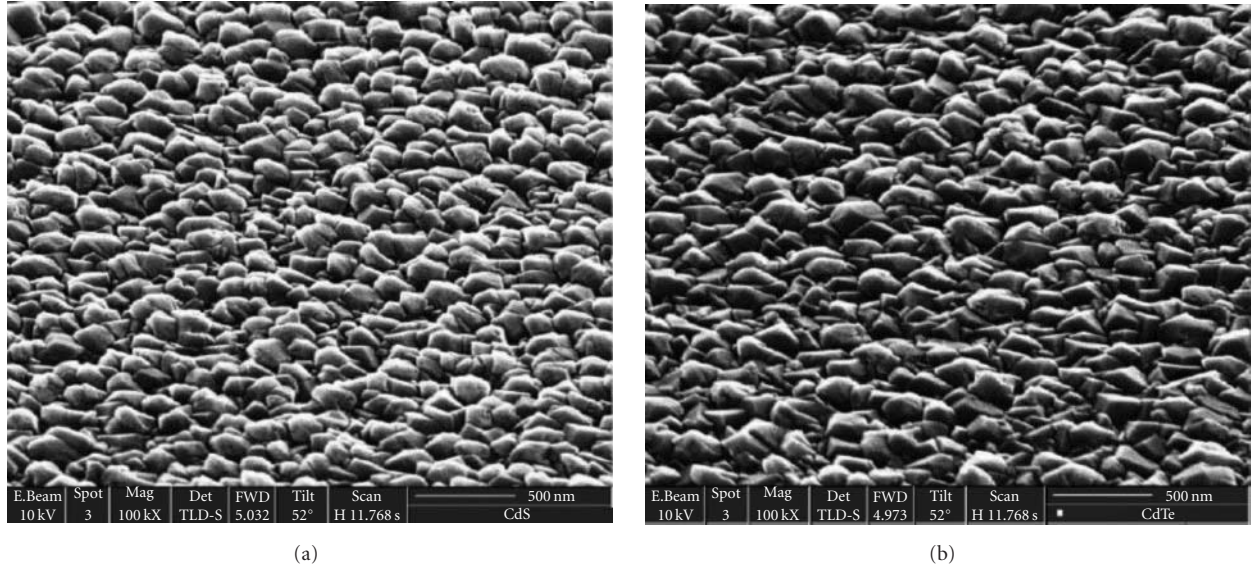


FIGURE 5: SEM photomicrographs of (a) CdS thin films prepared at 218 K substrate temperature, (b) CdTe thin films prepared at 218 K substrate temperature. Figures are taken from [33].

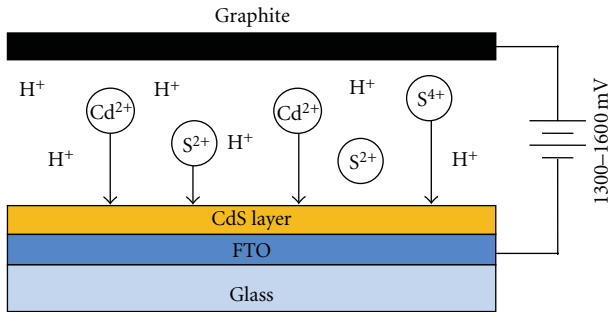


FIGURE 6: Electrodeposition process of CdS with graphite anode and glass/FTO cathode.

2.6. Nontoxic Chlorine Ambient Treatment. As the heat treatment with CdCl₂ would bring both pollutions to environment and toxic threats to operators, nontoxic process is expected to be explored while retaining the efficiency of solar cells. Romeo et al. [29] provide a solution: to anneal the CdS/CdTe structure in mixture of 100–500 mbar of Ar and 20–50 mbar of nontoxic gas containing Cl₂ such as difluorochloromethane (HCF₂Cl) for 5–10 minutes at 400°C. HCF₂Cl is stable, inert, and nontoxic at room temperature, and it would be decomposed as Cl₂ and other products during annealing. Hence, the reactions below are supposed to happen:



The resultant CdTe solid in second chemical reaction (2b) would have larger grain size than the one in first reaction (2a) since annealing process in chlorine ambient assists the recrystallization of CdTe grains. The merits of this method are

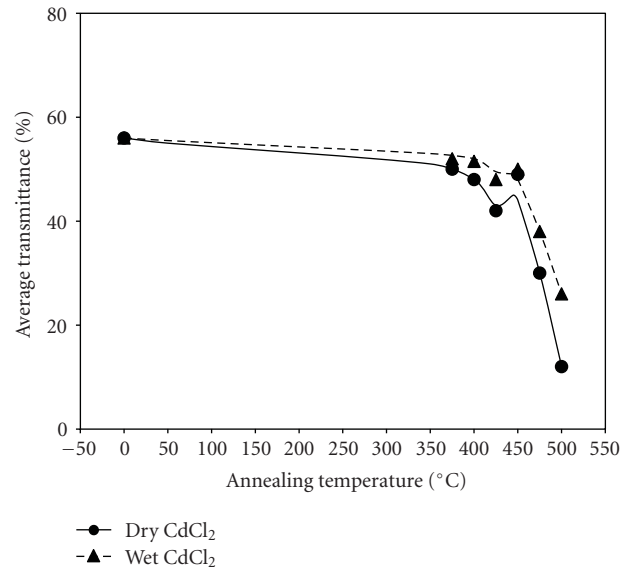


FIGURE 7: Average transmittance in the range of 800–100 nm for CdTe films annealed at different temperatures with dry and wet CdCl₂ treatment. The films were deposited on ITO-coated glass substrate instead of CdS/ITO/glass substrate. Figure is taken from [35].

that it provides an effective way of producing high-quality CdTe layers with large grains and few defects (Figures 8(a) and 8(b)) to obtain less possibility of electron-hole recombination. The highest cell efficiency has reached 15.8%. In addition, any gas of Freon family can be applied for carrying Cl₂. Although the Freon gas with Cl is harmful to the ozone belt, the recovering machines are already commercially available. This process has been patented by Romeo et al. [36].

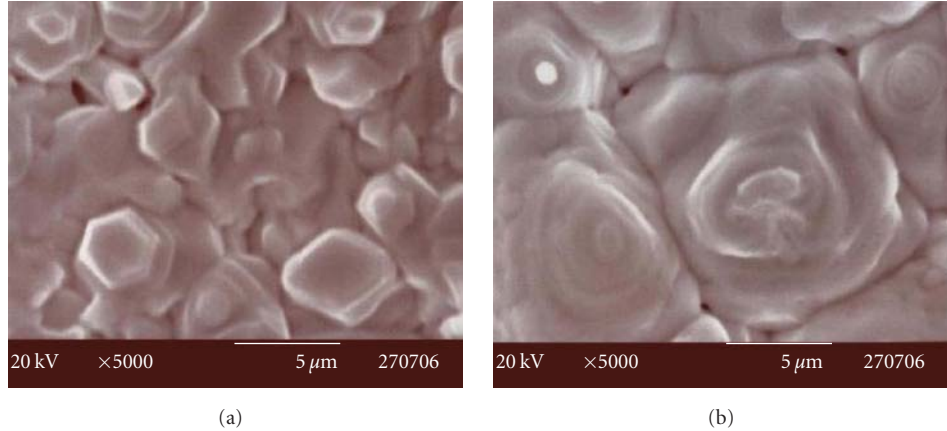


FIGURE 8: SEM photomicrographs of the surface of CdTe films: morphology of an untreated CdTe film deposited by the CSS method (a) before and (b) after thermal treatment in Ar + HCF₂Cl atmosphere at a temperature of 400°C for 5 min. Figure is taken from [29].

3. Structural Modification

The second approach to improve efficiency is to modify the configuration of CdS/CdTe solar cells. The favorable formation enthalpy and good chemical stability of CdS/CdTe heterojunction have allowed many routes to be explored in novel device architectures. In this part, two of them, namely nanostructure and tandem cells, are discussed.

3.1. Nanostructured Geometries. Nanostructured geometries are believed to be the most promising method to achieve high efficiency and low cost from structural aspect [37, 38]. By employing nanopillar instead of planar CdS layer, on one hand, this provide excellent transparency of CdS layer, since the size of nanopillars is much smaller than the wavelength of visible light. On the other hand, light absorption is enhanced simultaneously due to quantum confinement effect. In addition, this approach also offers more flexibility, since the optical gap can be tuned by size variation of nanopillars. Currently, power conversion efficiency of 6.5% has been achieved by Liu et al. in this kind of structure [37], and it is expected to reach >20% after further optimization [38].

The nanopillars can be directly built on or even embedded into CdTe with several methods (details in reference [39]), and one popular way is to employ anodized aluminum membrane (AAM) as the molds [37–39]. An excellent work of one three-dimensional (3D) nanopillar-array CdS/CdTe solar cell done by Fan et al. [40] is shown in Figure 9(a). A $\sim 2\ \mu\text{m}$ AAM with near-perfect ordering after anodization is built on Al substrate (Figure 9(b)), followed by a barrier thinning process to branch out the pore channels and reduce the AAM film to a few nanometers. After electrodepositing a thin layer of Au at the bottom of the channel, the nanopillar structure of CdS is then carried out in a quartz tube furnace with two resistive heating. In the third step, the AAM layer is partially etched by NaOH (Figure 9(c)) and a p-type CdTe film with $\sim 1\ \mu\text{m}$ is deposited by chemical vapor deposition (CVD). Finally, Cu/Au bilayer is grown on CdTe film

by thermal evaporation to achieve low-barrier contact. This fabrication method can achieve high-density, single-crystal nanopillar array with good geometric control. This is an excellent breakthrough since it is difficult to keep high-quality single-crystal structure when moving into nanometer level, and single crystal is usually required for high-efficiency solar cells to maintain high density of e-h pairs. Furthermore, it is also suggested that 3D nanopillar array can also improve the light absorption while enhancing the carrier collection efficiency [40]. The main limitation on its performance is the poor transparency of Cu/Au layer (currently 50% only). Conversion efficiency of $\sim 6\%$ has been reported in the initial design. To improve the efficiency, future research should focus on both the creation of high-quality single-crystal nanopillar and understanding on pillar distribution and recombination rate of carriers in this structure.

3.2. Bifacial and Tandem Structure. Another popular structural solution of increasing efficiency is to build tandem cells. Bifacial configuration, the base of tandem connection, was developed in 1980s and then obtained renewed interests with intensive research after 2004 [41–44]. The basic idea is to replace conventional Cu/Au with transparent indium tin oxide (ITO) as back contact layers. In this way, the solar cells can be illuminated from both sides, and, more importantly, the long-term stability can be improved due to the absence of bulk Cu layer [20]. The equivalent circuit of bifacial cells is now modeled as two opposite illuminated diodes representing main separating barrier and the barrier near the back contact, respectively [45]. Current efficiency achieved in CdS/CdTe bifacial structure has exceeded 10% and 3% on the front side and back side illumination, respectively [43]. It has also been shown that a very thin Cu layer can be added between CdTe and ITO to decrease the series resistance but still keeping the transparency [43, 45]. If further reducing the thickness of CdTe layers in bifacial configuration, tandem cells can be built to increase the efficiency by absorbing a broader part of solar spectrum, though intensive researches are still required to make it into practice [45, 46].

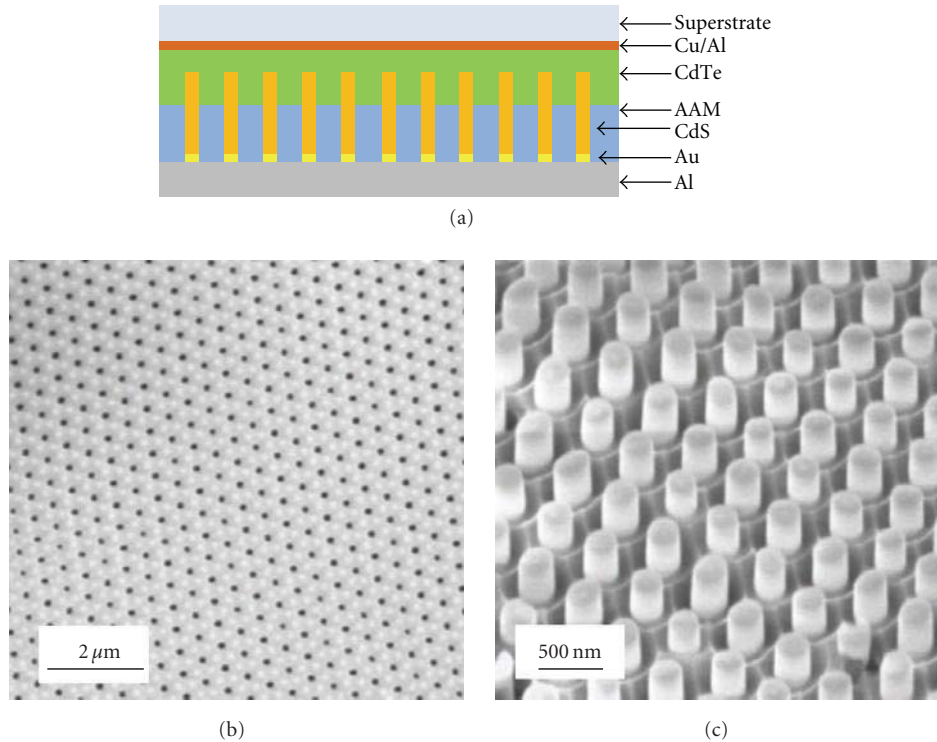


FIGURE 9: (a) Cross-sectional schematic diagram of the solar nanopillar cell. (b) SEM images of an as-made AAM with perfectly ordered pores and (c) a CdS nanopillar array after partial etching of the AAM. Figures (b) and (c) are taken from [40].

4. Choice of Back Contact

Due to the high electron affinity of p-type CdTe, the Fermi level pinning would be formed between the absorption layer and the metal layer. A reverse-biased potential would be formed at the CdTe-metal interface to limit the holes' transport and would seriously reduce the cells' efficiency. Hence, an ohmic contact or tunneling contact is seriously required. Conventionally, an etching with nitric-phosphoric (NP) acid is applied to obtain Te-rich layers on the top of CdTe before copper deposition [11], so that a diffusion layer of Cu_xTe alloy can be formed during the annealing after Cu deposition. Since Cu_xTe exhibits p-type characteristics, a large amount of holes appear in Cu_xTe , and this offers a good ohmic contact with CdTe layers. Although it does help to provide tunneling contact and improve the cell performance, the roll over phenomenon can still not be avoided. Instead, a new etching technique employing nitric-acetic (NA) acid can be applied to avoid roll over phenomenon in J-V curve (Figure 10) and generate better ohmic contact with lower series resistance ($4.3 \Omega\text{cm}^2$) than that of NP acid etching method ($6.5 \Omega\text{cm}^2$) as well as higher fill factor [47].

Several novel techniques have been explored to suppress the large Schottky barrier and reduce the contact resistance at the CdTe-metal interface. One popular solution is to use ZnTe as a buffer layer between the CdTe layer and the Cu back contact. ZnTe has a similar lattice parameter with CdTe, and the insertion of ZnTe layer produces an electrical field to reduce recombination loss of minority carriers at back contact surface [48, 49]. Kim et al. [50] also shows that

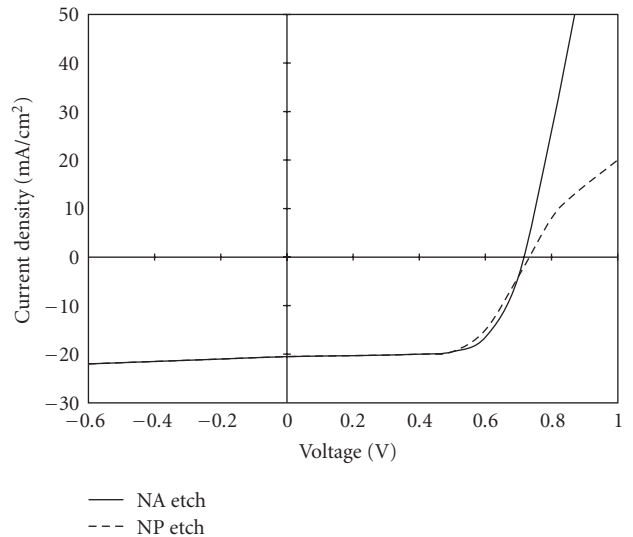


FIGURE 10: J-V characteristics of CdTe solar cells with different etching solutions applied. Figure is taken from [47].

double-layer structure with Cu doped ZnTe (ZnTe:Cu) buffer and Cu_xTe back contact can be very attractive for back contact fabrication, since ZnTe:Cu offers a good alignment of the valence band with CdTe, while Cu_xTe , produced by bilayer deposition method, has an excellent crystallinity and contact with CdTe:Cu. Park et al. [51] have also reported that doping ZnTe:Cu with Na_2Te can further improve

the performance by decreasing the film resistance of ZnTe layer to $<1\ \Omega\text{cm}$. In addition, the stability can also be improved to a large extent if replacing the back contact metal of Cu into Al [52].

The use of Cu may reduce the long-term stability of solar cells, since Cu would gradually diffuse through grain boundaries reaching the interface of the junction and cause the shunt problem. Alternatively, some metals, such as Ni, Al, Mo, and W, can be employed to extend cell lifetime. Similarly, ohmic contact and metal diffusion barrier can be realized by a buffer layer inserted between CdTe and metal. Sb_2Te_3 is considered as a low-resistivity p-type material ($10^{-4}\ \Omega\ \text{cm}$) [29] that suitable for buffer layer with Mo or W metal contact to provide stable high-efficiency solar cell [11]. However, the performance highly depends on process condition and material purity, and the doping effect of Te into Sb_2Te_3 can be complicated [11]. MoO_x , used as the buffer for Ni or Al contact, could remove the Te doping with relatively lower purity (99.95%) and ultrathin CdTe cells, and efficiency of $>10\%$ has been obtained [53]. An innovative way of $\text{As}_2\text{Te}_3/\text{Cu}/\text{Mo}$ bilayer buffer structure provides efficiency as high as 16%, since the Cu_xTe compound raises the conductivity in p-type material. As As_2Te_3 is directly deposited onto CdTe layer, no etching process is required. Moreover, an extremely thin Cu layer (2–20 nm) is inserted to get a low contact resistance without varying the stability. The controlled affinity of $x \leq 1.4$ ensures cell stability without rectification [29].

5. Conclusion

This paper has summarized the latest research and techniques to solve the efficiency problem in CdS/CdTe solar cells from aspects of fabrication, structure, and back contact materials. Although there is no impressive progress for efficiency improvement these years, those techniques above offer some novel ideas for further development. Based on the previous analysis, we still believe that CdS/CdTe solar cell will be a crucial candidate for global low-cost solar cells market in future.

Acknowledgments

This research was funded in part from the National Natural and Science Foundation of China under Grant no. 60976075, the Suzhou Science and Technology Bureau of China under Grant SYG201007, and SIP Service industry guiding funding.

References

- [1] W. P. Hirshman, "Surprise, surprise (cell production 2009: survey)," *Photon International*, pp. 176–199, 2010.
- [2] A. Sharma, "PV demand database—quarterly," IMS Research, 2011.
- [3] B. Yan, G. Yue, X. Xu, J. Yang, and S. Guha, "High efficiency amorphous and nanocrystalline silicon solar cells," *Physica Status Solidi A*, vol. 207, no. 3, pp. 671–677, 2010.
- [4] M. A. Green, "Thin-film solar cells: review of materials, technologies and commercial status," *Journal of Materials Science in Electronics*, vol. 18, no. 10, supplement 1, pp. S15–S19, 2007.
- [5] V. Fthenakis, "Sustainability of photovoltaics: the case for thin-film solar cells," *Renewable and Sustainable Energy Reviews*, vol. 13, no. 9, pp. 2746–2750, 2009.
- [6] T. Kietzke, "Recent advances in organic solar cells," *Advances in OptoElectronics*, vol. 2007, Article ID 40285, 2007.
- [7] L. Ren and S. Wang, "Progress of organic photovoltaic materials," *Recent Patents on Materials Science*, vol. 3, no. 1, pp. 26–39, 2010.
- [8] T. P. Kimbis, "Solar energy technology program," US Department of Energy, 2011, http://www1.eere.energy.gov/solar/pdfs/solar_program_mypp_2008-2012.pdf.
- [9] V. Avrutin, N. Izyumskaya, and H. Morko, "Semiconductor solar cells: recent progress in terrestrial applications," *Superlattices and Microstructures*, vol. 49, no. 4, pp. 337–364, 2011.
- [10] S. M. Sze, "Physics of semiconductor devices (2nd edition), Wiley, Amsterdam (1981)," *Microelectronics Journal*, vol. 13, no. 4, p. 44, 1982.
- [11] A. Bosio, N. Romeo, S. Mazzamuto, and V. Canevari, "Polycrystalline CdTe thin films for photovoltaic applications," *Progress in Crystal Growth and Characterization of Materials*, vol. 52, no. 4, pp. 247–279, 2006.
- [12] First Solar, "First solar sets world record for CdTe solar PV efficiency," 2011, <http://investor.firstsolar.com/releasedetail.cfm?ReleaseID=593994>.
- [13] X. Wu, "High-efficiency polycrystalline CdTe thin-film solar cells," *Solar Energy*, vol. 77, no. 6, pp. 803–814, 2004.
- [14] S. Leone, "\$4.5 Billion in loans to support three first solar projects," *Renewable Energy World*, 2011, <http://www.renewableenergyworld.com/rea/news/article/2011/07/4-5-in-loans-to-support-three-first-solar-projects>.
- [15] C. Neumann, "CALYXO CdTe excellent yield per W_p of the PV technologies," 2010, <http://www.votum.cz/pdf/workshop/Neumann%20-%20Calyxo-%20Vynikajici%20vyteznost%20na%20Wp.pdf>.
- [16] X. Wu, J. C. Keane, R. G. Dhere et al., "16.5%-efficient CdS/CdTe polycrystalline thin-film solar cells," in *Proceedings of the 17th European Photovoltaic Solar Energy Conference and Exhibition (PVSEC '01)*, pp. 995–1000, 2001.
- [17] M. Powalla and D. Bonnet, "Thin-film solar cells based on the polycrystalline compound semiconductors CIS and CdTe," *Advances in OptoElectronics*, vol. 2007, Article ID 97545, 2007.
- [18] N. Romeo, A. Bosio, V. Canevari, M. Terheggen, and L. Vaillant Roca, "Comparison of different conducting oxides as substrates for CdS/CdTe thin film solar cells," *Thin Solid Films*, vol. 431–432, pp. 364–368, 2003.
- [19] C. S. Ferekides, V. Ceekala, K. M. Dugan et al., "Reduction of recombination current in CdTe/CdS solar cells," *Applied Physics Letters*, vol. 67, no. 13, pp. 1896–1898, 1995.
- [20] G. Khrypunov, A. Romeo, F. Kurdesau, D. L. Bätzner, H. Zogg, and A. N. Tiwari, "Recent developments in evaporated CdTe solar cells," *Solar Energy Materials and Solar Cells*, vol. 90, no. 6, pp. 664–677, 2006.
- [21] G. C. Morris and S. K. Das, "Some fabrication procedures for electrodeposited CdTe solar cells," *International Journal of Solar Energy*, vol. 12, no. 1–4, pp. 95–108, 1992.
- [22] S. Ikegami, "CdS/CdTe solar cells by the screen-printing-sintering technique: fabrication, photovoltaic properties and applications," *Solar Cells*, vol. 23, no. 1–2, pp. 89–105, 1988.
- [23] T. L. Chu and S. S. Chu, "High efficiency thin film CdS/CdTe solar cells," *International Journal of Solar Energy*, vol. 12, no. 1–4, pp. 121–132, 1992.

- [24] N. Romeo, A. Bosio, R. Tedeschi, A. Romeo, and V. Canevari, "Highly efficient and stable CdTe/CdS thin film solar cell," *Solar Energy Materials and Solar Cells*, vol. 58, no. 2, pp. 209–218, 1999.
- [25] J. Britt and C. Ferekides, "Thin-film CdS/CdTe solar cell with 15.8% efficiency," *Applied Physics Letters*, vol. 62, no. 22, pp. 2851–2852, 1993.
- [26] N. Romeo, A. Bosio, and V. Canevari, "The role of CdS preparation method in the performance of CdTe/CdS thin film solar cells," in *Proceedings of the 3rd World Conference on Photovoltaic Energy Conversion*, vol. 1, pp. 469–470, Osaka, Japan, 2003.
- [27] N. Romeo, A. Bosio, V. Canevari, and A. Podestà, "Recent progress on CdTe/CdS thin film solar cells," *Solar Energy*, vol. 77, no. 6, pp. 795–801, 2004.
- [28] A. Podestà, N. Armani, N. Romeo, A. Bosio, G. Salviati, and M. Prato, "Influence of the fluorine doping on the optical properties of CdS thin films for photovoltaic applications," *Thin Solid Films*, vol. 511–512, pp. 448–452, 2006.
- [29] N. Romeo, A. Bosio, and A. Romeo, "An innovative process suitable to produce high-efficiency CdTe/CdS thin-film modules," *Solar Energy Materials and Solar Cells*, vol. 94, no. 1, pp. 2–7, 2010.
- [30] J. Han, C. Spanheimer, G. Haindl et al., "Optimized chemical bath deposited CdS layers for the improvement of CdTe solar cells," *Solar Energy Materials and Solar Cells*, vol. 95, no. 3, pp. 816–820, 2011.
- [31] M. E. Calixto, M. Tufiño-Velázquez, G. Contreras-Puente et al., "Study of chemical bath deposited CdS bi-layers and their performance in CdS/CdTe solar cell applications," *Thin Solid Films*, vol. 516, no. 20, pp. 7004–7007, 2008.
- [32] E. Bacaksiz, B. M. Basol, M. Altunbaş, V. Novruzov, E. Yanmaz, and S. Nezir, "Effects of substrate temperature and post-deposition anneal on properties of evaporated cadmium telluride films," *Thin Solid Films*, vol. 515, no. 5, pp. 3079–3084, 2007.
- [33] V. D. Novruzov, N. M. Fathi, O. Gorur et al., "CdTe thin film solar cells prepared by a low-temperature deposition method," *Physica Status Solidi A*, vol. 207, no. 3, pp. 730–733, 2010.
- [34] D. G. Diso, G. E. A. Muftah, V. Patel, and I. M. Dharmadasa, "Growth of CdS layers to develop all-electrodeposited CdS/CdTe thin-film solar cells," *Journal of the Electrochemical Society*, vol. 157, no. 6, pp. H647–H651, 2010.
- [35] J. Lee, "Effects of heat treatment of vacuum evaporated CdCl₂ layer on the properties of CdS/CdTe solar cells," *Current Applied Physics*, vol. 11, no. 1, pp. S103–S108, 2011.
- [36] N. Romeo, A. Bosio, and A. Romeo, "Process for large scale production of CdTe/CdS thin film solar cells," Patent No. US2004248340 (A1).
- [37] P. Liu, V. P. Singh, C. A. Jarro, and S. Rajaputra, "Cadmium sulfide nanowires for the window semiconductor layer in thin film CdS-CdTe solar cells," *Nanotechnology*, vol. 22, no. 14, 2011.
- [38] R. Kapadia, Z. Fan, and A. Javey, "Design constraints and guidelines for CdS/CdTe nanopillar based photovoltaics," *Applied Physics Letters*, vol. 96, no. 10, Article ID 103116, 2010.
- [39] V. V. Kislyuk and O. P. Dimitriev, "Nanorods and nanotubes for solar cells," *Journal of Nanoscience and Nanotechnology*, vol. 8, no. 1, pp. 131–148, 2008.
- [40] Z. Fan, H. Razavi, J. W. Do et al., "Three-dimensional nanopillar-array photovoltaics on low-cost and flexible substrates," *Nature Materials*, vol. 8, no. 8, pp. 648–653, 2009.
- [41] T. Nakada, Y. Hirabayashi, T. Tokado, D. Ohmori, and T. Mise, "Novel device structure for Cu(In,Ga)Se₂ thin film solar cells using transparent conducting oxide back and front contacts," *Solar Energy*, vol. 77, no. 6, pp. 739–747, 2004.
- [42] A. N. Tiwari, G. Khrypunov, F. Kurdzesau, D. L. Bätzner, A. Romeo, and H. Zogg, "CdTe solar cell in a novel configuration," *Progress in Photovoltaics: Research and Applications*, vol. 12, no. 1, pp. 33–38, 2004.
- [43] A. Romeo, G. Khrypunov, S. Galassini, H. Zogg, and A. N. Tiwari, "Bifacial configurations for CdTe solar cells," *Solar Energy Materials and Solar Cells*, vol. 91, no. 15–16, pp. 1388–1391, 2007.
- [44] S. Marsillac, V. Y. Parikh, and A. D. Compaan, "Ultra-thin bifacial CdTe solar cell," *Solar Energy Materials and Solar Cells*, vol. 91, no. 15–16, pp. 1398–1402, 2007.
- [45] A. V. Meriuts, G. S. Khrypunov, T. N. Shelest, and N. V. Deyneko, "Features of the light current-voltage characteristics of bifacial solar cells based on thin CdTe layers," *Semiconductors*, vol. 44, no. 6, pp. 801–804, 2010.
- [46] I. M. Dharmadasa, "Latest developments in CdTe, CuInGaSe₂ and GaAs/AlGaAs thin film PV solar cells," *Current Applied Physics*, vol. 9, no. 2, pp. e2–e6, 2009.
- [47] J. Han, C. Fan, C. Spanheimer et al., "Electrical properties of the CdTe back contact: a new chemically etching process based on nitric acid/acetic acid mixtures," *Applied Surface Science*, vol. 256, no. 20, pp. 5803–5806, 2010.
- [48] N. Amin, K. Sopian, and M. Konagai, "Numerical modeling of CdS/CdTe and CdS/CdTe/ZnTe solar cells as a function of CdTe thickness," *Solar Energy Materials and Solar Cells*, vol. 91, no. 13, pp. 1202–1208, 2007.
- [49] J. Sites and J. Pan, "Strategies to increase CdTe solar-cell voltage," *Thin Solid Films*, vol. 515, no. 15, pp. 6099–6102, 2007.
- [50] S. H. Kim, J. H. Ahn, H. S. Kim, H. M. Lee, and D. H. Kim, "The formation of ZnTe:Cu and Cu_xTe double layer back contacts for CdTe solar cells," *Current Applied Physics*, vol. 10, no. 3, pp. S484–S487, 2010.
- [51] K. C. Park, E. S. Cha, and B. T. Ahn, "Sodium-doping of ZnTe film by close-spaced sublimation for back contact of CdTe solar cell," *Current Applied Physics*, vol. 11, no. 1, pp. S109–S112, 2011.
- [52] M. A. Matin, M. Mannir Aliyu, A. H. Quadery, and N. Amin, "Prospects of novel front and back contacts for high efficiency cadmium telluride thin film solar cells from numerical analysis," *Solar Energy Materials and Solar Cells*, vol. 94, no. 9, pp. 1496–1500, 2010.
- [53] H. Lin, W. Xia, H. N. Wu, and C. W. Tang, "CdS/CdTe solar cells with MoO_x as back contact buffers," *Applied Physics Letters*, vol. 97, no. 12, Article ID 123504, 2010.

Research Article

Theoretical Insight into the Spectral Characteristics of Fe(II)-Based Complexes for Dye-Sensitized Solar Cells—Part I: Polypyridyl Ancillary Ligands

Xiaoqing Lu,¹ Shuxian Wei,² Chi-Man Lawrence Wu,¹ Ning Ding,¹ Shaoren Li,² Lianming Zhao,² and Wenyue Guo²

¹Department of Physics and Materials Science, City University of Hong Kong, Hong Kong

²College of Physics Science and Technology, China University of Petroleum, Dongying, Shandong 257061, China

Correspondence should be addressed to Chi-Man Lawrence Wu, lawrence.wu@cityu.edu.hk

Received 22 May 2011; Revised 7 July 2011; Accepted 25 July 2011

Academic Editor: Gaetano Di Marco

Copyright © 2011 Xiaoqing Lu et al. This is an open access article distributed under the Creative Commons Attribution License, which permits unrestricted use, distribution, and reproduction in any medium, provided the original work is properly cited.

The design of light-absorbent dyes with cheaper, safer, and more sustainable materials is one of the key issues for the future development of dye-sensitized solar cells (DSSCs). We report herein a theoretical investigation on a series of polypyridyl Fe(II)-based complexes of $\text{FeL}_2(\text{SCN})_2$, $[\text{FeL}_3]^{2+}$, $[\text{FeL}'(\text{SCN})_3]^-$, $[\text{FeL}_2']^{2+}$, and $\text{FeL}''(\text{SCN})_2$ ($L = 2,2'$ -bipyridyl-4,4'-dicarboxylic acid, $L' = 2,2',2''$ -terpyridyl-4,4',4''-tricarboxylic acid, $L'' = 4,4''$ -dimethyl-2,2':6',2'' :6'',2'''-quaterpyridyl-4',4''-biscarboxylic acid) by density functional theory (DFT) and time-dependent DFT (TD-DFT). Molecular geometries, electronic structures, and optical absorption spectra are predicted in both the gas phase and methyl cyanide (MeCN) solution. Our results show that polypyridyl Fe(II)-based complexes display multitransition characters of $\text{Fe} \rightarrow$ polypyridine metal-to-ligand charge transfer and ligand-to-ligand charge transfer in the range of 350–800 nm. Structural optimizations by choosing different polypyridyl ancillary ligands lead to alterations of the molecular orbital energies, oscillator strength, and spectral response range. Compared with Ru(II) sensitizers, Fe(II)-based complexes show similar characteristics and improving trend of optical absorption spectra along with the introduction of different polypyridyl ancillary ligands.

1. Introduction

Due to the features of low cost and high conversion efficiency, dye-sensitized solar cells (DSSCs) based on organic/inorganic hybrid materials have attracted extensive attention as an alternative to the conventional Si-based solar cells [1–3]. As crucial light-harvesting elements in DSSCs, the photo-excited sensitizers can inject electrons from their excited states into the semiconductor conduction band, and are recharged by an electrolyte to their initial states [4–6]. Early design of sensitizers had focused on transition metal coordinated complexes because of their unique richness of electronic properties for light absorption as well as photochemical and photophysical behaviors, especially for the photoredox activities [7]. These behaviors were originated from the nature of the coordinated complexes, involving the metal-to-ligand charge transfer (MLCT) character and

intervening spin-orbit coupling attached to the presence of metal cations with large atomic numbers [7]. Metal coordinated complexes also facilitate the fine tuning of electronic properties by means of the proper choice of both polypyridyl ancillary ligands and metal cations. Up to now, polypyridyl Ru(II)-based complexes are proven to be the most efficient sensitizers employed in DSSCs. Among them, the tetraprotonated $\text{Ru}(4,4'$ -dicarboxy-2,2'-bipyridine) $_2(\text{NCS})_2$ complex (coded as **N3**) [8] and its doubly protonated analog (coded as **N719**) [9] exhibit outstanding properties, that is, broad visible light absorption spectrum, high photo-, electro-, thermal and chemical stability, and strong adsorption on the semiconductor surfaces. Using **N3** as sensitizers, a solar-to-electric energy conversion efficiency of 10% was first attained for DSSCs. Therefore, **N3** is usually considered as a reference dye for DSSCs and is used as a base for designing other sensitizers. At present, the maximum efficiency of DSSCs is

12.1% using Ru(II)-based complex of **C106** as a sensitizer [10].

However, considering the high cost and limited availability of Ru, novel dyes using cheaper, safer, and more sustainable metal materials are desirable for next-generation DSSCs. Although Fe and Ru are in the same column of the periodic table, Fe is a first row transition metal and is environmental-friendly and inexpensive. It is therefore of an interest to determine whether Fe can be used to replace Ru in sensitizers to exhibit similar photophysical and photochemical properties. Recent studies on Fe(II)-based complexes have been reported [7, 11–20], in which the geometries and absorption spectra were analyzed. However, better understanding of the electronic structures and spectra characteristics of Fe(II)-based complexes for DSSCs is still scarce. In this work, we present a theoretical study on a series of polypyridyl Fe(II)-based complexes of $\text{FeL}_2(\text{SCN})_2$, $[\text{FeL}_3]^{2+}$, $[\text{FeL}'(\text{SCN})_3]^-$, $[\text{FeL}_2']^{2+}$, and $\text{FeL}''(\text{SCN})_2$ ($L = 2,2'$ -bipyridyl-4,4'-dicarboxylic acid, $L' = 2,2',2''$ -terpyridyl-4,4',4''-tricarboxylic acid, $L'' = 4,4'''$ -dimethyl-2,2':6',2'' : 6'',2'''-quaterpyridyl-4',4''-biscarboxylic acid) that follow straightforward design strategies applied to Ru(II) sensitizers, by means of DFT/TD-DFT calculations. The molecular geometries, electronic structures, and spectral characteristics are elaborated in both the gas phase and MeCN solution.

2. Computational Methods

All calculations were performed using the Gaussian 09 program package [21]. The geometrical optimizations for all Fe(II)-based complexes were carried out using the B3LYP exchange correlation functional in conjunction with the pure 6-31G* and mixed DZVP/3-21G* basis sets, in both the gas phase and MeCN solution. The reason why we chose two basis sets was to eliminate the errors caused by improper selection of basis set. In the pure 6-31G* basis set, all atoms were described in the same basis set. In the mixed DZVP/3-21G* basis set, the DZVP set [22] supplemented with three sets of uncontracted pure angular momentum f functions was chosen for Fe, and the 3-21G* basis set for nonmetal atoms. For Ru(II)-based complexes, the B3LYP functional in conjunction with the pure 3-21G* and mixed SDD/6-31G* basis sets was employed in the geometrical optimizations. The SDD set along with the quasirelativistic MWB (28 core electrons) pseudopotential [23, 24] was chosen for Ru and the 6-31G* basis set for the remaining nonmetal atoms. For simplicity, B3LYP/DZVP was used to stand for the B3LYP functional in conjunction with the mixed DZVP/3-21G* basis set and B3LYP/SDD for the B3LYP functional in conjunction with the mixed SDD/6-31G* basis set.

TD-DFT calculations were used to investigate the optical properties of the sensitizers. The lowest vertical excitation energy of the system at the ground state geometry can be accurately and efficiently calculated by TD-DFT [25, 26]. The 70 lowest transitions, up to the energy level of at least 4.50 eV, were taken into account in the calculations of the absorption spectra. The solvent effects were evaluated

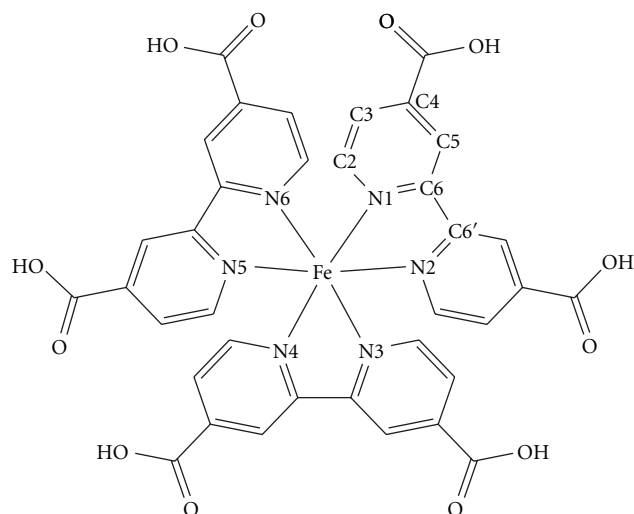


FIGURE 1: Sketch of chemical structures of the $[\text{FeL}_3]^{2+}$ complex ($L = 2,2'$ -bipyridyl-4,4'-dicarboxylic acid) with the atom numbering scheme.

using the nonequilibrium implementation of the conductor-like polarizable continuum model (C-PCM) [27–30]. In particular, optimized structures and solvation energies were computed by a cavity model [31] coupled to C-PCM [30]. This approach provides results very close to those obtained by the original dielectric model for high dielectric constant solvents but is significantly more effective in geometry optimizations and less prone to numerical errors arising from the small part of the solute electron cloud lying outside the cavity [30].

3. Results and Discussion

In the following sections, we first establish the accuracy for the chosen levels of theory. Then, we present the results of molecular geometries, molecular orbitals and electronic structures, electronic excitations, and absorption spectra of Fe(II)-based complexes, as well as the comparison with those of Ru(II)-based complexes.

3.1. Calibration. It is essential to calibrate the quality of the geometries obtained at different levels because the accuracy of the calculations of electronic structures used to produce reliable absorption spectra depends highly on the geometrical parameters. However, since there is no optimized complex which corresponds exactly to an experimental result, the closest complex $[\text{FeL}_3]^{2+}$ ($L = 2,2'$ -bipyridyl-4,4'-dicarboxylic acid) is chosen for comparison with the experimental complex, $[\text{Fe}(\text{bpy})_3]^{2+}$ [11, 13]. Table 1 lists the selected theoretical and experimental parameters of the ground state structures, and the corresponding labeling scheme is given in Figure 1.

The bond length of Fe–N in the gas-phase $[\text{FeL}_3]^{2+}$ is 1.997 Å calculated at the B3LYP/6-31G* level and 1.992 Å at the B3LYP/DZVP level (see Table 1), in good agreement with the solid-state distances of 1.965–1.967 Å [11, 13].

TABLE 1: Comparisons between calculated geometrical parameters of the $[\text{FeL}_3]^{2+}$ using B3LYP at different basis sets in the gas phase with experimental values^a.

Parameters	B3LYP				Expt.		
	DZVP	6-31G*	TZVP ^b	6-311 + G** ^b	DZVP ^c	Reference [11]	Reference [13]
R _{Fe-N1}	1.992	1.997	2.027	2.022	2.017	1.967	1.965
R _{N-C2}	1.359	1.347	1.342	1.344	1.347	1.338	1.353
R _{N-C6}	1.373	1.363	1.356	1.358	1.361	1.359	1.352
R _{C2-C3}	1.390	1.391	1.386	1.389	1.394	1.358	1.380
R _{C3-C4}	1.395	1.396	1.389	1.391	1.396	1.380	1.377
R _{C4-C5}	1.392	1.394	1.387	1.389	1.394	1.374	1.385
R _{C5-C6}	1.391	1.394	1.394	1.396	1.400	1.377	1.384
R _{C6-C6'}	1.466	1.472	1.473	1.475	1.478	1.471	1.473
∠N1-Fe-N2	81.5	81.3	80.3	80.5	80.8	81.8	81.5
∠N1-Fe-N3	88.4	88.2			88.7		90.7
∠N1-Fe-N5	95.1	95.3			95.4		94.1

^aBond lengths are in angstroms and angles are in degrees.

^bResults from [13].

^cResults from [19].

The bond lengths of C–N and C–C in the N1 containing pyridine ring are in the range of 1.347–1.373 Å and 1.390–1.396 Å, compared to the experimental values of 1.338–1.359 Å and 1.358–1.385 Å, respectively. The bite-angles of the bpy-domains, ∠N1–Fe–N2, is 81.3° obtained at the B3LYP/6-31G* level and 81.5° at the B3LYP/DZVP level, very close to the experimental values of 81.5–81.8° [11, 13]. Moreover, a maximum skewing of 2.5° of the calculated interbpy angles (∠N1–Fe–N3 and ∠N1–Fe–N5) is in good agreement with the available experimental data. In addition, previous calculations using the B3LYP functional with pure DZVP [19], TZVP [13], and 6-311 + G** [13] basis sets are also listed in Table 1 for comparison. The deviations are less than 3% between our results and the experimental and previous calculated values. Considering that our study is performed in the gas phase and does not account for the packing and counter-ion effects that are present in the solid state, our calculated geometries match excellently with experimental results. The good agreements demonstrate the reliability of the chosen model and level of theory.

Considering that TD-DFT excitation energies are dependent on the DFT functionals, benchmark calculations of the absorption spectra using the CAM-B3LYP functional are also provided for Fe(II)-based complex of **1** in both the gas phase and MeCN solution. Seen from Figure S1 (in Supplementary Material available online at doi: 10.1155/2011/316952), these two DFT functionals indeed give consistent absorption spectra. These results justify the reliability of our model and levels of theory. In addition, benchmark calculations containing diffusion functions (e.g., 6-31 + G*) were performed, and the results were very similar to those without the diffusion functions. This is in good agreement with our previous studies on Ru(II)-based complexes [24]. Because the results of Fe(II)-based complexes calculated at the B3LYP/6-31G* and B3LYP/DZVP levels are very close to each other, only the B3LYP/6-31G* results will be used for clarification, unless otherwise stated. In the case of Ru(II)-based complexes, the

B3LYP/SDD results will be chosen to compare with Fe(II)-based complexes.

3.2. Molecular Geometries. The optimized molecular structures of the polypyridyl Fe(II)-based complexes of $\text{FeL}_2(\text{SCN})_2$, $[\text{FeL}_3]^{2+}$, $[\text{FeL}'(\text{SCN})_3]^-$, $[\text{FeL}_2']^{2+}$, and $\text{FeL}''(\text{SCN})_2$ are shown in Figure 2, together with the atom numbering scheme. Table 2 summarizes the selected geometrical parameters of the fully optimized Fe(II)-based complexes at the B3LYP/6-31G* level and **N3** at the B3LYP/DZVP level in MeCN solution.

Fe coordination complexes in its Fe(II) form have septet ground state with d^5s^1 configuration, which allows it to bind to six neighboring nitrogen ions to form octahedral complexes. The geometry of **1** with a cis arrangement of the thiocyanate is optimized to be a pseudooctahedral C_2 symmetry, while the geometry of the trans isomer **1'** exhibits an almost D_2 symmetry, as shown in Figure 2. For **1** and **1'**, the bond lengths of Fe–N (thiocyanate) are calculated to be almost the same, while the Fe–N (bpy) bond lengths are ~ 1.98 Å and ~ 2.02 Å, respectively. The bite angles of the bpy-domains (∠N1–Fe–N2 and ∠N3–Fe–N4) show a deviation of 1.2° between these two isomers (see Table 2). These differences of both bond lengths and angles correspond to the difference that the trans isomer **1'** is 12.90 kcal mol⁻¹ higher in the binding energy than the corresponding cis isomer **1**. To evaluate the protonation/deprotonation effect as appearing between **N3** and its analog **N719**, the H⁺ cations on carboxylic groups are substituted by methyl (**1** → **2**). This substitution has slight effect on the geometries, especially for the skeleton parameters (see Table 2). Thiocyanate ligands are usually chosen as the electron-donating groups in the most efficient Ru(II)-based sensitizers. However, from a chemical point of view, the thiocyanate seems to be the weakest part [6]. This situation can be improved by substituting thiocyanate in **1** with a dc bpy ligand (**1** → **3**).

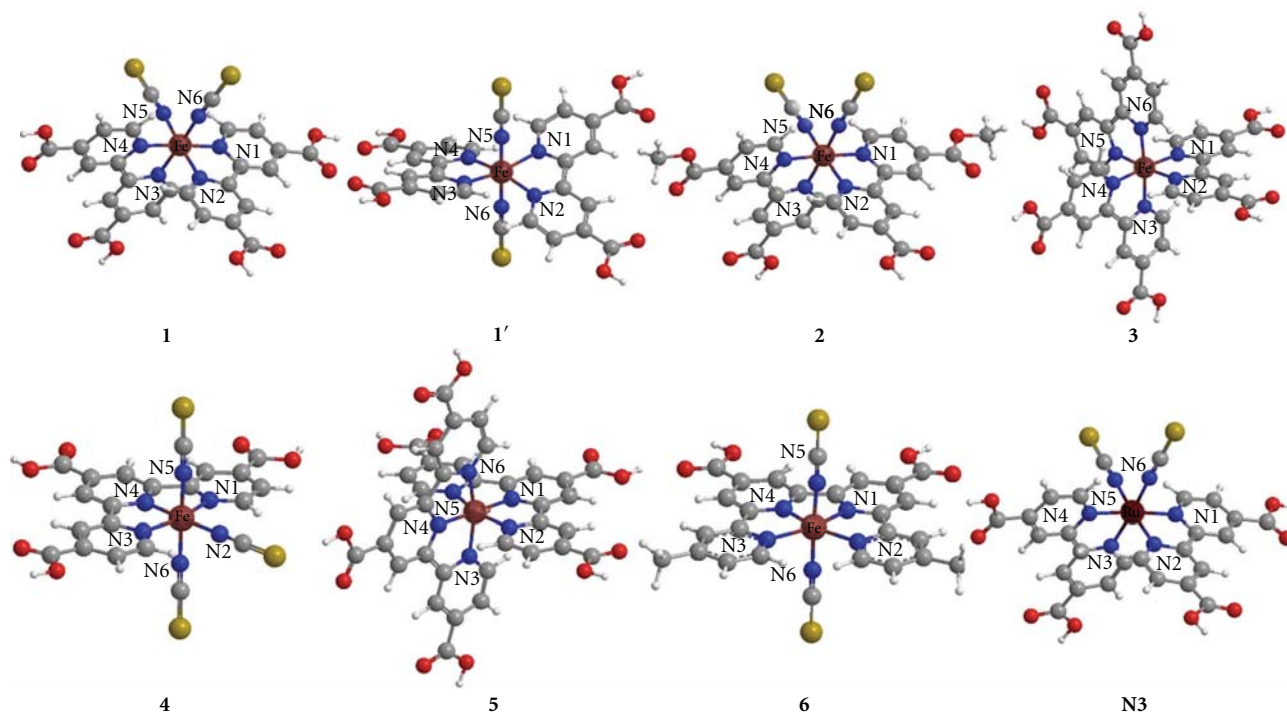


FIGURE 2: Optimized structures of polypyridyl Fe(II)-based complexes and N3 with the atom numbering scheme.

TABLE 2: Selected geometrical parameters of the polypyridyl Fe(II)-based complexes calculated at the B3LYP/6-31G* level in MeCN solution and N3 calculated at the B3LYP/SDD level in MeCN solution^{a,b}.

Parameters	1	1'	2	3	4	5	6	N3
R_{M-N1}	1.981	2.018	1.984	1.992	1.990	1.897	1.881	2.083
R_{M-N2}	1.979	2.018	1.981	1.991	1.954	2.000	2.062	2.076
R_{M-N3}	1.979	2.019	1.981	1.991	1.991	1.999	2.063	2.076
R_{M-N4}	1.980	2.019	1.984	1.992	1.877	1.897	1.880	2.083
R_{M-N5}	1.945	1.945	1.947	1.992	1.946	1.999	1.933	2.066
R_{M-N6}	1.945	1.944	1.947	1.991	1.947	2.000	1.933	2.066
$\angle N1-M-N2$	81.5	80.3	81.5	81.3	98.3	81.0	80.5	78.6
$\angle N2-M-N3$	91.0	101.6	90.9	88.2	98.3	91.4	116.8	92.7
$\angle N3-M-N4$	81.5	80.3	81.5	81.4	81.7	81.0	80.5	78.6
$\angle N5-M-N6$	91.0	179.9	90.8	81.3	178.6	91.4	173.4	90.1
$\angle N1-N2-N3-N4$	-111.2	22.8	-111.4	-110.8	-0.1	-106.0	0.1	-112.6

^a Bond lengths are in angstroms, and angles are in degrees.

^b M presents Fe in Fe(II)-based complexes and Ru in N3.

The interbpy angle in **3** is distorted somewhat, as indicated by the alteration of $\angle N2-Fe-N3$ (2.8°). Relatively, distortions are very small for both bond lengths and bite angles of **3** with respect to those of **1**.

The optimized geometry of **4** shows almost a C_2 symmetric arrangement of the ligands, and the octahedral dispositions of the N atoms around the Fe center are distorted due to the different nature of thiocyanate and tricarboxylic terpyridine (tctpy) ligands. The difference in bond lengths of Fe–N (thiocyanate: 1.946–1.954 Å) and Fe–N (bpy: 1.877–1.991 Å) confirms this point (see Table 2). However, the dihedral angle of $\angle N1-N2-N3-N4$ (-0.1°) mirrors the fact that the involved N atoms are almost

in the same plane, quite different from that of the trans isomer **1'** (22.8°). Substituting tctpy for thiocyanates makes the complex **5** a C_2 symmetry, in which the geometrical parameters including the bond lengths and angles related to two tctpy ligands are exactly the same with each other.

For the dicarboxylic quaterpyridine (dcqpy) containing Fe(II)-based complex, **6**, the Fe–N (dcqpy) bond lengths are in the range of 1.880–2.063 Å calculated at the 6-31G* level in MeCN solution. A comparison of the optimized parameters shows that complex **6** has shorter Fe–N (thiocyanate) distances with respect to that in **1'** (1.933 versus 1.944–1.945 Å). This may result from the weaker interaction between Fe and a tetradentate ligand with respect to that

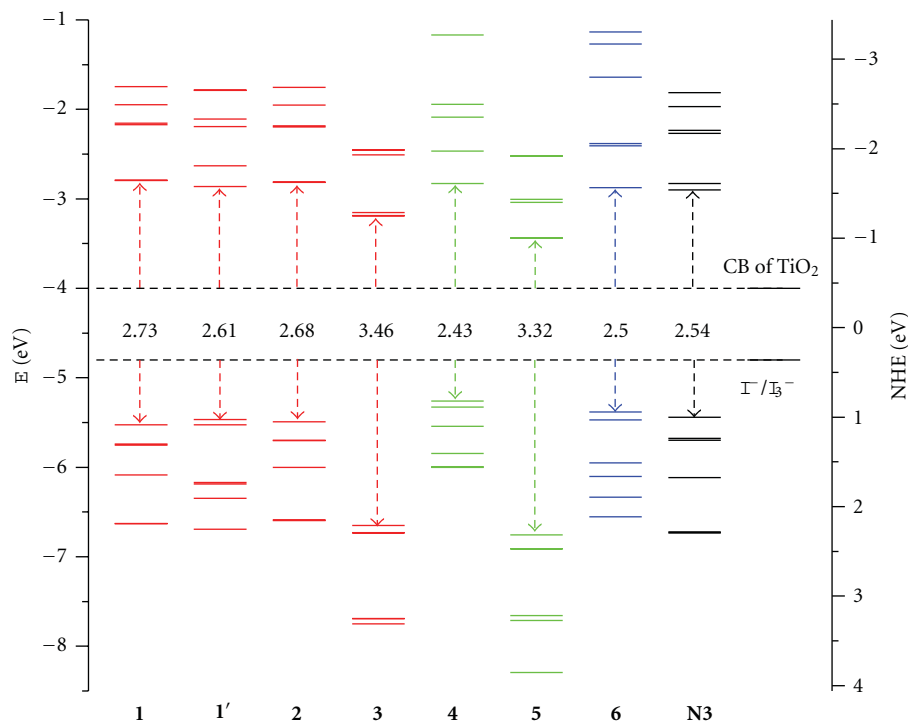


FIGURE 3: Energy levels and HOMO-LUMO gaps of Fe(II)-based complexes calculated at the B3LYP/6-31G* level in MeCN solution.

between Fe and two bidentate ligands, and thus the stronger interaction between Fe and thiocyanate ligands shortens the Fe–N (thiocyanate) distances. Similar phenomena also appear for the Ru(II)-based complexes when comparing dcqpy containing complex **N886** with dcbpy containing complex **N3** [32].

3.3. Molecular Orbitals and Electronic Structures. Since the crucial electronic excitations occur from the highest occupied molecular orbitals (HOMOs) to the lowest unoccupied molecular orbitals (LUMOs), it is therefore important to form efficient charge-separated states with the HOMOs localized on the donor subunit and the LUMOs on the acceptor subunit. The molecular orbital energy levels and the HOMO-LUMO gaps of Fe(II)-based complexes are depicted in Figure 3. In view of the distributions of frontier orbital energies, similar molecular orbital shapes would be envisaged for the complexes with the same ancillary ligand. Therefore, **1**, **4**, and **6** are chosen to exhibit the electron distributions of the frontier molecular orbitals, as shown in Figure 4.

For **1** in MeCN solution, the three highest HOMOs (from HOMO to HOMO–2) are a set of quasi degenerate orbitals, originating from the combination of Fe t_{2g} orbitals (d_{xy} , d_{xz} , and d_{yz}) with the 2p orbital and lone pairs of the thiocyanate ligands. The following HOMO–3 shows similar orbital compositions from thiocyanate ligands but without the contributions from the Fe t_{2g} orbitals with respect to the first three HOMOs (see Figure 4(a)). Compared with those in **N3** [33], the first four HOMOs in Fe(II)-based complexes **1** show very close orbital compositions and percentages. Not

only that, Fe also shows similar field splitting in **1** to that of Ru in **N3**, mirrored by the molecular orbital energy levels of HOMOs shown in Figure 3. The four lowest LUMOs (from LUMO to LUMO+3) of **1**, lying at least 2.73 eV about the HOMO in the range of 0.64 eV, result mainly from the π^* combinations of the C and N atoms localized on the dcbpy ligands (see Figure 4(a)). Since the carboxylic group of the dcbpy ligands has a strong electron-withdrawing ability, the LUMOs are mainly localized on the dcbpy ligands. The anchoring groups involved in those LUMOs would facilitate the electron injection from the excited state of the sensitizers into the semiconductor. Here, it would be specially mentioned that six HOMOs and LUMOs are presented but less levels are observed in Figure 3 due to the degeneracy. For instance, HOMO–1, HOMO–4, LUMO, and LUMO+2 of **1** correspond to HOMO–2, HOMO–5, LUMO+1, and LUMO+3 in energies; thus only eight levels can be observed in Figure 3. In fact, this situation also appears in all the other Fe(II)-based complexes (see Figure 3).

It can be seen from Figure 3 that the energy levels of **2** are very close to those of **1**, indicating that the protonated/deprotonation effect is slight for Fe(II)-based complexes in MeCN solution. However, the isomerization effect has larger influence on the frontier molecular orbitals, mirrored by the alteration of both the energy levels and energy gap. The most obvious alteration between **1** and **1'** is the degenerate orbitals of HOMOs. The first set for **1** is composed of the three highest HOMOs (from HOMO to HOMO–2) in the range of 0.22 eV, while that for **1'** is composed of the two highest HOMOs in the range of 0.06 eV. This points out the difference of the field splitting of Fe

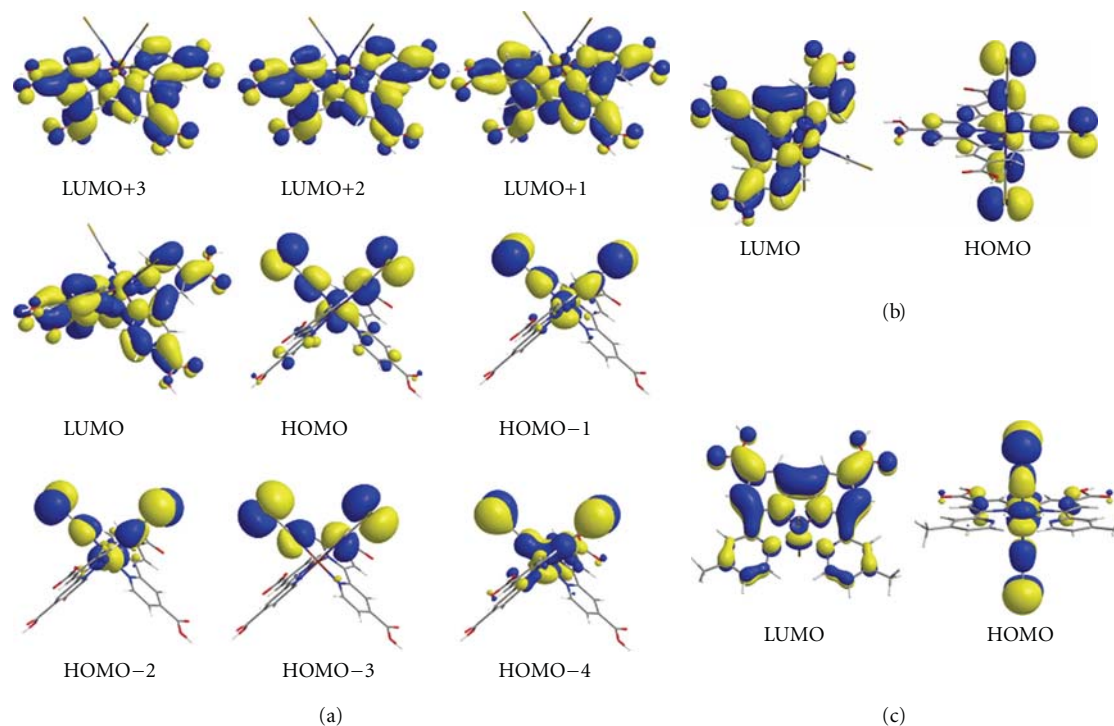


FIGURE 4: Selected frontier molecular orbitals of the complexes **1** (a), **4** (b), and **6** (c) calculated at the B3LYP/6-31G* level in MeCN solution. Isodensity contour: 0.02.

between **1'** and **1**. Due to the alteration of orbital levels, the HOMO-LUMO gap of **1'** reduces to 2.61 eV with respect to 2.73 eV in **1**. Substitution of the thiocyanates in **1** with a dcby ligand (**1** \rightarrow **3**) has great influence on the energy levels and the HOMO-LUMO gap, as shown in Figure 3. All the molecular orbital energies of **3** are downshifted but the HOMOs are stabilized much more than the LUMOs. Accordingly, the HOMO-LUMO gap of **3** is increased to 3.46 eV.

For **4** in MeCN solution, the HOMO shows mainly contributions from the combination of Fe center and three thiocyanate ligands, while the LUMO shows contributions from the tctpy ligand, as shown in Figure 4(b). Compared with **1**, the six highest HOMOs of **4** are unshifted and lie in a smaller range of 0.74 eV, while the LUMO is close to that of **1** but the six lowest LUMOs lie in a larger range of 2.84 eV. Accordingly, the HOMO-LUMO gap of **4** is calculated to be 2.43 eV. The smaller HOMO-LUMO gap would help decrease the excitation energy, and this is beneficial for the absorption spectrum to shift towards the longer wavelength of the visible region. Substitution of the thiocyanates in **4** with a tctpy ligand (**4** \rightarrow **5**) shows the same trend on the energy levels as **1** \rightarrow **3** substitution. As seen from Figure 3, both the HOMO and LUMO levels of **5** are lower than those of **4**, and the HOMO-LUMO gap of **5** is 0.89 eV smaller than that of **4**. Obviously, both the energy levels and HOMO-LUMO gaps of the thiocyanate-substituted complexes (**3** and **5**) are less favorable than those unsubstituted complexes (**1** and **4**) with respect to the reference dye **N3**.

For **6** in MeCN solution, the HOMO also shows main contributions from the combination of Fe center orbital and two thiocyanate ligands, while the LUMO shows contributions from the dcqpy ligand, as shown in Figure 4(c). Fe shows slightly different field splitting in **6** compared with that in **1**, which leads to slightly different energy levels of the HOMOs, as shown in Figure 3. The great difference in energy levels of LUMOs between **1** and **6** correspond to the great structural difference in the polypyridyl ancillary ligands of dcby and dcqpy. The HOMO-LUMO gap of **6** is calculated to be 2.50 eV.

3.4. Electronic Excitations and Absorption Spectra. Figure 5 presents the simulated absorption spectra of Fe(II)-based complexes at the B3LYP/6-31G* level and **N3** at the B3LYP/SDD level in MeCN solution. Table 3 lists excitation energies, oscillator strengths, and relative orbital contributions of the optical transitions between 350 and 800 nm for **1**, **4**, and **6**, in which only oscillator strengths larger than 0.01 and orbital percentages larger than 10% are presented. The gas phase absorption spectra and transitions information of **1'**, **2**, **3**, and **5** are provided in Figure S2 and Table S1, respectively. As seen from Figure S2, the band shapes of spectra obtained in the gas phase are qualitatively similar to those in MeCN solution, but the oscillator strengths are stronger for most spectra in MeCN solution at the longer wavelength range. In order to depict the real environmental, the results obtained in MeCN solution will be used for analysis.

TABLE 3: Selected excitation energies (E , nm), oscillator strength (f), and relative orbital contributions of the absorption spectra of Fe(II)-based complexes calculated at the B3LYP/6-31G* level in MeCN solution.

E	f	Compositions
1		
633.5	0.022	H-0 \rightarrow L + 1 (87%)
594.4	0.029	H-1 \rightarrow L + 0 (76%)
559.4	0.054	H-2 \rightarrow L + 1 (84%)
445.3	0.060	H-3 \rightarrow L + 0 (55%) H-0 \rightarrow L + 3 (41%)
442.9	0.033	H-3 \rightarrow L + 1 (66%) H-0 \rightarrow L + 2 (23%)
431.1	0.023	H-1 \rightarrow L + 2 (82%)
415.6	0.022	H-2 \rightarrow L + 3 (95%)
395.1	0.070	H-4 \rightarrow L + 0 (61%)
361.2	0.032	H-3 \rightarrow L + 2 (33%) H-6 \rightarrow L + 1 (21%)
4		
766.8	0.017	H-1 \rightarrow L + 0 (93%)
693.0	0.026	H-0 \rightarrow L + 0 (87%) H-1 \rightarrow L + 1 (11%)
609.4	0.031	H-0 \rightarrow L + 1 (96%)
473.4	0.064	H-0 \rightarrow L + 2 (84%)
471.1	0.054	H-1 \rightarrow L + 2 (92%)
422.5	0.016	H-6 \rightarrow L + 0 (86%)
6		
724.5	0.014	H-1 \rightarrow L + 0 (93%)
682.4	0.018	H-0 \rightarrow L + 0 (85%)
561.5	0.048	H-0 \rightarrow L + 1 (90%)
507.0	0.020	H-4 \rightarrow L + 8 (34%) H-2 \rightarrow L + 8 (34%) H-1 \rightarrow L + 2 (26%)
493.4	0.018	H-1 \rightarrow L + 1 (64%) H-0 \rightarrow L + 0 (12%)
396.2	0.023	H-0 \rightarrow L + 3 (96%)
350.1	0.024	H-7 \rightarrow L + 0 (28%) H-0 \rightarrow L + 5 (25%) H-1 \rightarrow L + 4 (22%)

^aOnly oscillator strength $f > 0.01$ and orbital percentage $>10\%$ are reported, where H stand for HOMO and L for LUMO.

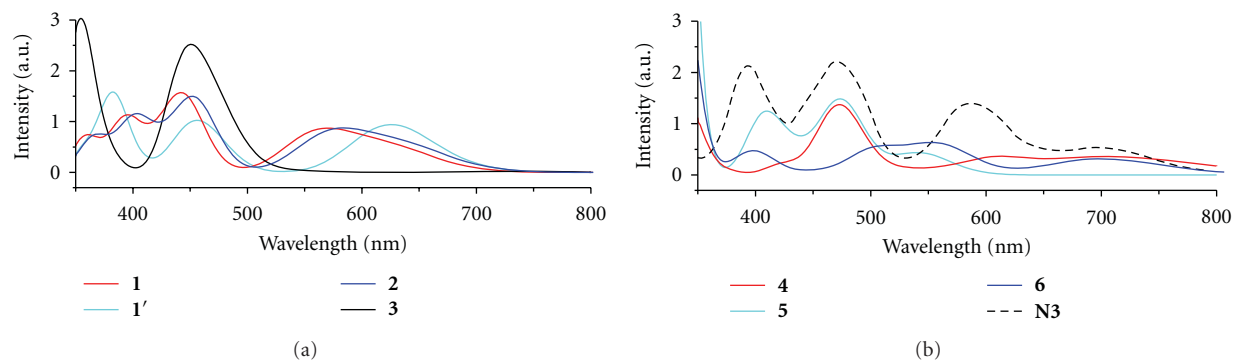


FIGURE 5: Simulated absorption spectra of Fe(II)-based complexes (solid lines) at the B3LYP/6-31G* level and N3 (dash line) at the B3LYP/SDD level in MeCN solution.

In the energy range investigated, there are four bands that clearly appear with the intensity maxima centered at ~ 362 , ~ 395 , ~ 442 , and ~ 571 nm for **1** (see Figure 5). At ~ 362 nm, the band originates from the starting orbitals of HOMO-3/HOMO-6 combination to the arriving orbitals of LUMO+1/LUMO+2 with the oscillator strength of 0.032. As seen from Figure 4(a), the HOMO-3 \rightarrow LUMO+2 transition shows the interligand $\pi \rightarrow \pi^*$ transition from

the thiocyanate ligands to the dcbpy ligands, a typical LLCT character. At ~ 395 nm, the HOMO-4 \rightarrow LUMO (61%) transition shows the strongest oscillator strength of 0.070 involving the Fe(II) center to the dcbpy ligand and interligand $\pi \rightarrow \pi^*$ transitions, a multitransition character of MLCT and LLCT. As shown in Table 3, the band at ~ 442 nm of **1** is composed of a series of peaks from 415.6 nm to 445.3 nm. Among them, the peak at 445.3 nm includes

the transitions of HOMO/HOMO-3 as the starting orbitals and LUMO/LUMO+3 as the arriving orbitals, exhibiting a multitransition character of LLCT and MLCT. At ~ 571 nm, a broad absorption band is observed with the peaks ranging from 559.4 nm to 633.5 nm. The first vertical excitation occurs at 633.5 nm ($f = 0.022$), originated from the HOMO \rightarrow LUMO+1 (87%) transition with the multitransition character of MLCT and LLCT.

As shown in Figure 5, the calculated absorption spectrum of the derivative **2** is quantitatively similar to that of **1** but with a slight blueshift. This corresponds to the minor alterations of the energy levels caused by the slight structural changes. It can also be confirmed by comparing the excitations of **2** with those of **1** in Tables S1 and 3. The absorption spectrum of isomer **1'** is quite different from that of **1** due to the great difference in geometry. As seen from Figure 5, three bands are found to center at ~ 382 , ~ 457 , and ~ 625 nm for **1'** in the energy range investigated. The bands at ~ 625 nm are composed of two peaks, involving the HOMO-1 \rightarrow LUMO transition ($f = 0.063$) at 630.8 nm and the combinations of HOMO/HOMO-1 \rightarrow LUMO/LUMO + 9 transition ($f = 0.024$) at 603.6 nm (see Table S1). The oscillator strength of the first vertical excitation of **1'** is stronger than that of **1**, but the band of **1'** at the longer wavelength region is not as broad as that of **1**. Substitution of the thiocyanates with a dcby ligand (**1** \rightarrow **3**) shrinks the effective spectral response range sharply, corresponding to the enlarged HOMO-LUMO gaps. Only one band is observed at ~ 450 nm in the energy range investigated, originated from the combinations of HOMO-1/HOMO-2 \rightarrow LUMO+2 transitions. Compared with Ru(II)-based complex **N3**, the absorption spectra of **1** and its derivative **2** have similar band shape. However, the bands in the range of 400–600 nm are only two-thirds as much oscillator strength as those of **N3**.

For **4** in MeCN solution, the calculated absorption spectrum is shifted towards the near-infrared region, which can be comparable with the region that the black dye can reach [34]. Three bands are observed with the intensity maxima centered at ~ 472 , ~ 609 , and ~ 704 nm in the energy range investigated (see Figure 5). At ~ 472 nm, the bands are composed of two peaks, originated from HOMO-1 \rightarrow LUMO+2 (92%) transition at 471.1 nm and HOMO \rightarrow LUMO+2 (84%) transition at 473.4 nm. The oscillator strengths reach 0.054 and 0.064, respectively. An analysis of both transitions shows the multitransition character of MLCT and LLCT involving the Fe center to the tctpy ligand and interligand $\pi \rightarrow \pi^*$ transitions. At ~ 609 nm, the HOMO \rightarrow LUMO+1 (96%) transition has the oscillator strength of 0.031, exhibiting a multitransition character of MLCT and LLCT. The band at ~ 704 nm is composed of two peaks at 693.0 and 766.8 nm. The peak at 766.8 nm corresponds to the first vertical excitation, originated from the HOMO-1 \rightarrow LUMO transition with the oscillator strength of 0.017. This extension towards the longer wavelength region would be greatly beneficial for the sensitizers to absorb the low-energy photons and thus improves the DSSCs spectral response range. The substitution of the thiocyanates with a tctpy ligand (**4** \rightarrow **5**) renders the absorption spectrum of **5** to be redshifted sharply, similar to the effect of

substitution of the thiocyanates with a dcby ligand (**1** \rightarrow **3**). The longest wavelength region of the bands for **5** is at ~ 543 nm, composed of two peaks from the transitions of HOMO \rightarrow LUMO and HOMO \rightarrow LUMO + 1.

For **6** in the energy range investigated, three separated absorption bands are found to center at ~ 396 , ~ 552 , and ~ 699 nm (see Figure 5). At ~ 396 nm, the band is composed of the transition of HOMO \rightarrow LUMO + 3 ($f = 0.023$). At ~ 552 nm, the band is mainly composed of transitions in the range of 493.4–561.5 nm, originated from the starting orbitals of the HOMO/HOMO + 1/HOMO+2/HOMO+4 combinations to the arriving orbitals of LUMO/LUMO + 1/LUMO+2/LUMO+8 (see Table 3). An analysis of these transition shows that excitations correspond to electron transfer from the Fe 3d orbitals to the unoccupied π^* orbitals of the dcqpy ligand and from the occupied orbitals of the thiocyanate ligands to the unoccupied π^* orbitals of the dcqpy ligand, that is, a mixture of MLCT and LLCT transitions. At ~ 699 nm, the band is mainly composed of the transitions of HOMO \rightarrow LUMO (85%) at 682.4 nm ($f = 0.018$) and HOMO-1 \rightarrow LUMO (93%) at 724.5 nm ($f = 0.014$), showing primary MLCT and LLCT characters (see Figure 4(c)). Compared with **1**, the absorption spectrum of dcqpy containing complex **6** is blueshifted towards the longer wavelength range, similar to the phenomenon that occurs for Ru(II)-based sensitizers when going from **N3** to dcqpy containing complex **N886** [32].

3.5. Fe(II)-Based Complexes versus Ru(II)-Based Complexes.

Benefiting from the introduction of different polypyridyl ancillary ligands, the performance of Ru(II)-based complexes has been improved in some respects. For example, when going from dcby containing **N3** to tctpy containing black dye, the spectral response range is highly extended and thus the efficiency of DSSCs is enhanced [34]. How do these ligands affect the performance of Fe(II)-based complexes and to what extent can it be confirmed by comparing these complexes with different polypyridyl ancillary ligands? The key factors for confirmation include energy levels, absorption bands, and oscillator strengths. The energy levels of a sensitizer would determine the electron transfer processes which have great influence on the performance of the DSSCs [35]. As shown in Figure 3, **1**, **4**, and **6** provide suitable controls of the energetic and redox properties, in which the energy levels of the HOMO and LUMO match well with the redox potential of I^-/I_3^- and the conduction band of TiO₂. The HOMO-LUMO gap is in sequence of **4** (2.43 eV) < **6** (2.50 eV) < **1** (2.73 eV), that is, the HOMO-LUMO gap decreases by 0.30 and 0.23 eV when going from **1** to **4** and **6**. It means that **4** and **6** have values of HOMO-LUMO gap much closer to that of **N3** with respect to the complex **1**. In addition, as seen from Table 3, the lowest vertical excitation energies are also in the sequence of **4** (766.8 nm) < **6** (724.5 nm) < **1** (633.5 nm), corresponding to the sequence of the HOMO-LUMO gaps. Both facts indicate that the absorption bands are tuned to longer wavelengths when going from **1** to **4** and **6**, thus enhancing its spectral response to the near-infrared light.

TABLE 4: Selected absorption spectral properties of Fe(II)-based complexes (1, 4, and 6) and Ru(II)-based complexes (N3, black dye, and N886) in different organic solvents^{a,b}.

Complexes	λ_{\max} (nm)	f	Solution
Fe(II)-based complexes			
1	571	0.87	CH ₃ CN
4	704	0.36	CH ₃ CN
6	699	0.31	CH ₃ CN
Ru(II)-based complexes			
N3	534	1.42	C ₂ H ₅ OH
Black dye	605	0.75	C ₂ H ₅ OH
	611	0.73	CH ₃ CN
N886	637		C ₂ H ₅ OH

^a Fe(II)-based complexes are obtained from calculations at the B3LYP/6-31G* level, while Ru(II)-based complexes are obtained from experiments.

^b λ_{\max} represents maximum absorption band; f represents calculated oscillator strength (arb. unit) for Fe(II)-based complexes, and f represents experimental molar extinction coefficient ($M^{-1} \text{ cm}^{-1}$) for Ru(II)-based complexes.

On the other hand, the improving trend of Fe(II)-based complexes caused by using the different polypyridyl ancillary ligands can also be shown by comparing with the corresponding Ru(II)-based complexes. The selected absorption spectral properties of Fe(II)- and Ru(II)-based complexes are listed in Table 4. The maximum absorption bands of Fe(II)- and Ru(II)-based complexes show similar trend along with the introduction of different polypyridyl ancillary ligands. As shown in Table 4, the maximum absorption band of **1** centered at 571 nm is redshifted with respect to the corresponding values of **4** (704 nm) and **6** (699 nm), in good agreement with the alterations from **N3** (534 nm) to black dye (605 nm) and **N886** (637 nm). Furthermore, the relative oscillator strength of the maximum absorption band, f_4/f_1 , is calculated to be 2.42 at the B3LYP/6-31G* level. This value is in line with the experimental value of 1.90 obtained by comparing the molar absorption coefficient of **N3** at 534 nm ($1.42 \times 10^4 M^{-1} \text{ cm}^{-1}$) [8] with that of black dye at 605 nm ($0.748 \times 10^4 M^{-1} \text{ cm}^{-1}$) [34]. This means that the Fe(II)- and Ru(II)- based complexes show similar relation between the structural optimizations and the spectral properties. At present, although the efficiencies using Fe(II)-based complexes are not comparable with those using the Ru(II) sensitizers, the greater abundance of Fe can offer considerable opportunities for reduction in cost. Considering that Fe(II)-based complexes exhibit optical properties and trend similar to Ru(II) sensitizers and still do not undergo the barrage of investigations, it can be envisaged that Fe(II)-based complexes would be competent sensitizers for DSSCs.

4. Conclusions

We have performed DFT/TD-DFT calculations to investigate the molecular geometries, electronic structures, and spectral characteristics of Fe(II)-based complexes in both the gas phase and MeCN solution. The good agreement between the calculated results with the experimental observations ensures the reliability of the chosen theoretical methods. Our results show that the first three HOMOs originate from the

combination of Fe 3d orbitals with the 2p orbital and lone pairs of the thiocyanate ligands, while the first four LUMOs are composed of the antibonding combinations of the C and N 2p orbitals. The protonated/deprotonation effect is slight, while the isomerization effect and the solvent effect have great influence on the spectra characteristics of Fe(II)-based complexes. The spectra show ligand-to-ligand charge transfer (LLCT) character at shorter wavelength region, whereas the spectra display multitransition characters of Fe \rightarrow polypyridine metal-to-ligand CT (MLCT) and LLCT transitions at the longer wavelength of the visible region. Structural optimizations by choosing different polypyridyl ancillary ligands lead to alterations of the molecular orbital energies, oscillator strength, and spectral response range. Compared with Ru(II) sensitizers, Fe(II)-based complexes show similar characteristics and improving trend of optical absorption spectra along with the introduction of different polypyridyl ancillary ligands.

Acknowledgments

This work was supported by a Grant from City University of Hong Kong (Project no. 7002657) and Centre for Applied Computing and Interactive Media (ACIM). The authors would also like to thank National Natural Science Foundation of China (10979077, 21003158) and the Fundamental Research Funds for the Central Universities (09CX05002A) for the financial support.

References

- [1] B. O'Regan and M. Grätzel, "A low-cost, high-efficiency solar cell based on dye-sensitized colloidal TiO₂ films," *Nature*, vol. 353, no. 6346, pp. 737–740, 1991.
- [2] M. Grätzel, "Photoelectrochemical cells," *Nature*, vol. 414, no. 6861, pp. 338–344, 2001.
- [3] M. Grätzel, "Solar cells to dye for," *Nature*, vol. 421, no. 6923, pp. 586–587, 2003.
- [4] G. Boschloo and A. Hagfeldt, "Characteristics of the iodide/triiodide redox mediator in dye-sensitized solar cells,"

- Accounts of Chemical Research*, vol. 42, no. 11, pp. 1819–18, 2009.
- [5] M. Grätzel, “Recent advances in sensitized mesoscopic solar cells,” *Accounts of Chemical Research*, vol. 42, no. 11, pp. 1788–1798, 2009.
- [6] A. Hagfeldt, G. Boschloo, L. Sun, L. Kloo, and H. Pettersson, “Dye-sensitized solar cells,” *Chemical Reviews*, vol. 110, no. 11, pp. 6595–6663, 2010.
- [7] P. P. Lainé, S. Campagna, and F. Loiseau, “Conformationally gated photoinduced processes within photosensitizer-acceptor dyads based on ruthenium(II) and osmium(II) polypyridyl complexes with an appended pyridinium group,” *Coordination Chemistry Reviews*, vol. 252, no. 23–24, pp. 2552–2571, 2008.
- [8] M. K. Nazeeruddin, A. Kay, I. Rodicio, R. Humphry-Baker, E. Müller, and P. Liska, “Conversion of light to electricity by cis- X_2 bis(2,2'-bipyridyl-4,4'-dicarboxylate)ruthenium(II) charge-transfer sensitizers ($X = Cl^-$, Br^- , I^- , CN^- , and SCN^-) on nanocrystalline TiO_2 electrodes,” *Journal of the American Chemical Society*, vol. 115, no. 14, pp. 6382–6390, 1993.
- [9] M. K. Nazeeruddin, F. De Angelis, S. Fantacci et al., “Combined experimental and DFT-TDDFT computational study of photoelectrochemical cell ruthenium sensitizers,” *Journal of the American Chemical Society*, vol. 127, no. 48, pp. 16835–16847, 2005.
- [10] Q. J. Yu, Y. H. Wang, Z. Yi et al., “High-efficiency dye-sensitized solar cells: The influence of lithium ions on exciton dissociation, charge recombination, and surface states,” *ACS Nano*, vol. 4, no. 10, pp. 6032–6038, 2010.
- [11] S. Dick and B. A. Gregg, “Crystal structure of tris(2,2'-bipyridine)iron(II) bis(hexafluorophosphate), $(C_{10}H_8N_2)_3Fe(PF_6)_2$,” *New Crystal Structures*, vol. 213, no. 2, p. 356, 1998.
- [12] S. Ferrere and B. A. Gregg, “Photosensitization of TiO_2 by $[Fe^{II}(2,2'-bipyridine-4,4'-dicarboxylic\ acid)_2(CN)_2]$: Band selective electron injection from ultra-short-lived excited states,” *Journal of the American Chemical Society*, vol. 120, no. 4, pp. 843–844, 1998.
- [13] L. M. Lawson Daku, A. Vargas, A. Hauser, A. Fouqueau, and M. E. Casida, “Assessment of density functionals for the high-spin/low-spin energy difference in the low-spin iron(II) tris(2,2'-bipyridine) complex,” *ChemPhysChem*, vol. 6, no. 7, pp. 1393–1410, 2005.
- [14] S. Ferrere, “New photosensitizers based upon $[Fe(L)_2(CN)_2]$ and $[Fe(L)_3]$ ($L =$ substituted 2,2'-bipyridine): Yields for the photosensitization of TiO_2 and effects on the band selectivity,” *Chemistry of Materials*, vol. 12, no. 4, pp. 1083–1089, 2000.
- [15] S. Ferrere, “New photosensitizers based upon $[Fe^{II}(L)_2(CN)_2]$ and $[Fe^{II}L_3]$, where L is substituted 2,2'-bipyridine,” *Inorganica Chimica Acta*, vol. 329, no. 1, pp. 79–92, 2002.
- [16] F. De Angelis, A. Tilocca, and A. Selloni, “Time-dependent DFT study of $[Fe(CN)_6]^{4-}$ sensitization of TiO_2 nanoparticles,” *Journal of the American Chemical Society*, vol. 126, no. 46, pp. 15024–15025, 2004.
- [17] W. Gawelda, A. Cannizzo, V.-T. Pham, F. Van Mourik, C. Bressler, and M. Chergui, “Ultrafast nonadiabatic dynamics of $[Fe^{II}(bpy)_3]^{2+}$ in solution,” *Journal of the American Chemical Society*, vol. 129, no. 26, pp. 8199–8206, 2007.
- [18] A. Govindasamy, C. Lv, H. Tsuboi et al., “Theoretical investigation of the photophysical properties of black dye sensitizer $[(H_3-tctpy)M(NCS)_3]$ ($M = Fe, Ru, Os$) in dye sensitized solar cells,” *Japanese Journal of Applied Physics*, vol. 46, no. 4 B, pp. 2655–2660, 2007.
- [19] B. D. Alexander, T. J. Dines, and R. W. Longhurst, “DFT calculations of the structures and vibrational spectra of the $[Fe(bpy)_3]^{2+}$ and $[Ru(bpy)_3]^{2+}$ complexes,” *Chemical Physics*, vol. 352, no. 1–3, pp. 19–27, 2008.
- [20] P. V. Bernhardt, G. K. Boschloo, F. Bozoglian, A. Hagfeldt, M. Martínez, and B. Sienra, “Tailoring mixed-valence Co^{III}/Fe^{II} complexes for their potential use as sensitizers in dye sensitized solar cells,” *New Journal of Chemistry*, vol. 32, no. 43, pp. 705–711, 2008.
- [21] M. J. Frisch, G. W. Trucks, H. B. Schlegel et al., *Gaussian 09*, Revision A.1, Gaussian, Wallingford, Conn, USA, 2009.
- [22] S. Chiodo, N. Russo, and E. Sicilia, “Newly developed basis sets for density functional calculations,” *Journal of Computational Chemistry*, vol. 26, no. 2, pp. 175–183, 2005.
- [23] D. Andrae, U. Häußermann, M. Dolg, H. Stoll, and H. Preuß, “Energy-adjusted ab initio pseudopotentials for the second and third row transition elements,” *Theoretica Chimica Acta*, vol. 77, no. 2, pp. 123–141, 1990.
- [24] X. Lu, S. Wei, C. -M. Lawrence Wu, W. Guo, and L. Zhao, “Theoretical characterization of ruthenium complexes containing functionalized bithiophene ligands for dye-sensitized solar cells,” *Journal of Organometallic Chemistry*, vol. 696, no. 8, pp. 1632–1639, 2011.
- [25] R. E. Stratmann, G. E. Scuseria, and M. J. Frisch, “An efficient implementation of time-dependent density-functional theory for the calculation of excitation energies of large molecules,” *Journal of Chemical Physics*, vol. 109, no. 19, pp. 8218–8224, 1998.
- [26] G. Scalmani, M. J. Frisch, B. Mennucci, J. Tomasi, R. Cammi, and V. Barone, “Geometries and properties of excited states in the gas phase and in solution: theory and application of a time-dependent density functional theory polarizable continuum model,” *Journal of Chemical Physics*, vol. 124, no. 9, Article ID 094107, pp. 1–15, 2006.
- [27] M. Cossi and V. Barone, “Time-dependent density functional theory for molecules in liquid solutions,” *Journal of Chemical Physics*, vol. 115, no. 10, pp. 4708–4717, 2001.
- [28] S. Miertš, E. Scrocco, and J. Tomasi, “Electrostatic interaction of a solute with a continuum. A direct utilization of AB initio molecular potentials for the prevision of solvent effects,” *Chemical Physics*, vol. 55, no. 1, pp. 117–129, 1981.
- [29] M. Cossi, V. Barone, R. Cammi, and J. Tomasi, “Ab initio study of solvated molecules: a new implementation of the polarizable continuum model,” *Chemical Physics Letters*, vol. 255, no. 4–6, pp. 327–335, 1996.
- [30] V. Barone and M. Cossi, “Quantum calculation of molecular energies and energy gradients in solution by a conductor solvent model,” *Journal of Physical Chemistry A*, vol. 102, no. 11, pp. 1995–2001, 1998.
- [31] V. Barone, M. Cossi, and J. Tomasi, “A new definition of cavities for the computation of solvation free energies by the polarizable continuum model,” *Journal of Chemical Physics*, vol. 107, no. 8, pp. 3210–3221, 1997.
- [32] C. Barolo, M. K. Nazeeruddin, S. Fantacci et al., “Synthesis, characterization, and DFT-TDDFT computational study of a ruthenium complex containing a functionalized tetradentate ligand,” *Inorganic Chemistry*, vol. 44, no. 20, pp. 6852–6864, 2006.
- [33] S. Fantacci, F. De Angelis, and A. Selloni, “Absorption spectrum and solvatochromism of the $[Ru(4,4'-COOH-2,2'-bpy)_2(NCS)_2]$ molecular dye by time dependent density

- functional theory,” *Journal of the American Chemical Society*, vol. 125, no. 14, pp. 4381–4387, 2003.
- [34] M. K. Nazeeruddin, P. Péchy, T. Renouard et al., “Engineering of efficient panchromatic sensitizers for nanocrystalline TiO₂-based solar cells,” *Journal of the American Chemical Society*, vol. 123, no. 8, pp. 1613–1624, 2001.
- [35] R. Argazzi, N. Y. Murakami Iha, H. Zabri, F. Odobel, and C. A. Bignozzi, “Design of molecular dyes for application in photoelectrochemical and electrochromic devices based on nanocrystalline metal oxide semiconductors,” *Coordination Chemistry Reviews*, vol. 248, no. 13-14, pp. 1299–1316, 2004.

Review Article

Progress in Thin Film Solar Cells Based on $\text{Cu}_2\text{ZnSnS}_4$

Hongxia Wang

School of Engineering System, Queensland University of Technology, Brisbane, QLD 4001, Australia

Correspondence should be addressed to Hongxia Wang, hxwang04@yahoo.com.cn

Received 1 June 2011; Accepted 1 July 2011

Academic Editor: Leonardo Palmisano

Copyright © 2011 Hongxia Wang. This is an open access article distributed under the Creative Commons Attribution License, which permits unrestricted use, distribution, and reproduction in any medium, provided the original work is properly cited.

The research in thin film solar cells has been dominated by light absorber materials based on CdTe and Cu(In,Ga)Se₂ (CIGS) in the last several decades. The concerns of environment impact of cadmium and the limited availability of indium in those materials have driven the research towards developing new substitute light absorbers made from earth abundant, environment benign materials. $\text{Cu}_2\text{ZnSnS}_4$ (CZTS) semiconductor material has emerged as one of the most promising candidates for this aim and has attracted considerable interest recently. Significant progress in this relatively new research area has been achieved in the last three years. Over 130 papers on CZTS have been published since 2007, and the majority of them are on the preparation of CZTS thin films by different methods. This paper, will review the wide range of techniques that have been used to deposit CZTS semiconductor thin films. The performance of the thin film solar cells using the CZTS material will also be discussed.

1. Introduction

Thin film solar cells based on polycrystalline cadmium telluride (CdTe), copper indium diselenide (CIS), and copper indium (gallium) diselenide (CIGS) have reached the commercialization stage; however, restrictions on heavy metal usage for Cd and limitations in supply for In and Te have raised concern about limitations on production capacity of the PV devices. To solve this issue, it is necessary to develop alternative light absorber materials that are both nontoxic and easily available. In this context, $\text{Cu}_2\text{ZnSnS}_4$ (CZTS) quaternary semiconductor compound has emerged as one of the promising candidates. All the constitute elements in CZTS are earth abundant and environment benign. Figure 1 illustrates the earth crust content and the current world trading price of the elements used in CZTS and CIS as well as CdTe light absorbers (logarithmic scale is used for clarity). It is found that the abundance of Zn and Sn in earth's crust is 1500 times and 45 times greater than that of In, respectively, and the price of In is almost two orders of magnitude higher than that of Zn and Sn.

2. Basic Information on CZTS Compound and Solar Cells

CZTS is a mineral which has been found in nature [1]. It shares similar structure with the chalcopyrite material CuInS₂ except that half of the In is replaced with Zn and another half with Sn. Crystallographically speaking, CZTS has two principal structures known as stannite-type (space group $I\bar{4}2m$) and kesterite-type (space type $I\bar{4}$). The two structures are similar except the different arrangement of Cu and Zn atoms [2]. However, CZTS material usually appears in kesterite phase because it is more stable thermodynamically compared to the stannite-type [2]. CZTS can be synthesized through solid state chemical reactions between ZnS, Cu₂S, and SnS₂. The investigation on the phase diagram of the system has shown that a single-phase CZTS material can be formed only in a very small region (Figure 2) [3]. Impurities including ternary and quaternary compounds are easier to form than CZTS. Therefore, it is very challenging to make pure CZTS crystals.

Limited reports on the assessment of the photovoltaic performance of CZTS-based thin film solar cells normally

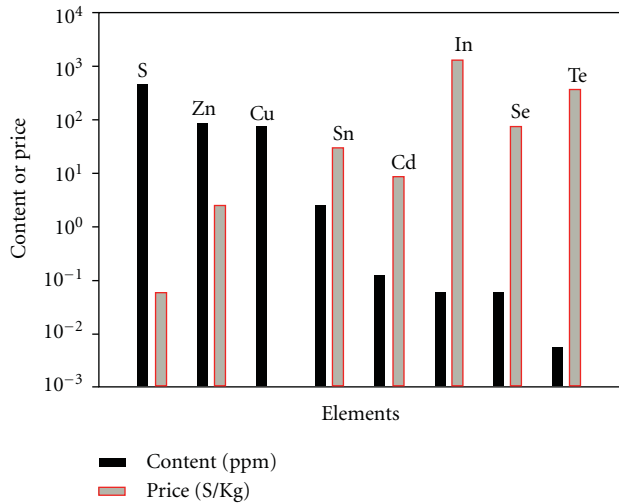


FIGURE 1: Content and the world trading price of the elements used in light absorbers CdTe , $\text{Cu}_2\text{ZnSnS}_4$, CuInSe_2 for thin film solar cells.

adopt the device structure shown in Figure 3. It consists of a molybdenum- (Mo-) coated soda lime glass (SLG) as the electrical contact, a thin CZTS light absorber layer which is in contact with an n-type CdS layer to create a p-n junction, and a thin i-ZnO/Al: ZnO layer on top of the CdS layer playing the role of a window layer and electrical contact.

3. Evolution of the Conversion Efficiency of CZTS-Based Thin Film Solar Cells

The recognition of the photovoltaic effect of CZTS material was reported by Ito and Nakazawa in 1988 [4]. They fabricated a heterodiode that consisted of a transparent cadmium-tin-oxide thin film and a CZTS thin film on a stainless steel substrate. An open-circuit voltage of 165 mV was obtained with the device. In 1997, Friedlmeier et al. fabricated thin film solar cells using a CZTS layer as the light absorber in contact with an n-CdS/ZnO window layer. The best energy conversion efficiency produced by the cells was 2.3% [5]. This record was later broken by Katagiri's group in 1999 who produced a CZTS solar cell with 2.63% power conversion efficiency. In this cell, the CZTS film was deposited on a Mo-coated soda lime glass (SLG) substrate [6]. By optimization of the sulfurization process, the efficiency of the solar cells was increased to 5.45% in 2003 [7], and then to 6.7% in 2008 [8]. Two review papers regarding the efficiency milestones achieved in CZTS-based thin film solar cells were reported by Katagiri in 2005 and in 2009, respectively [9, 10]. The current world record efficiency of CZTS-based thin film solar cells is 9.6%, which was reported by Todorov et al. in 2010. In this cell, the CZTS thin film was partly selenized to have a broader spectral photonresponse [11]. The evolution of the power conversion efficiency of CZTS-based solar cells is summarized in Figure 4.

Since majority of the publications in this area have been devoted to the synthesis and characterizations of CZTS

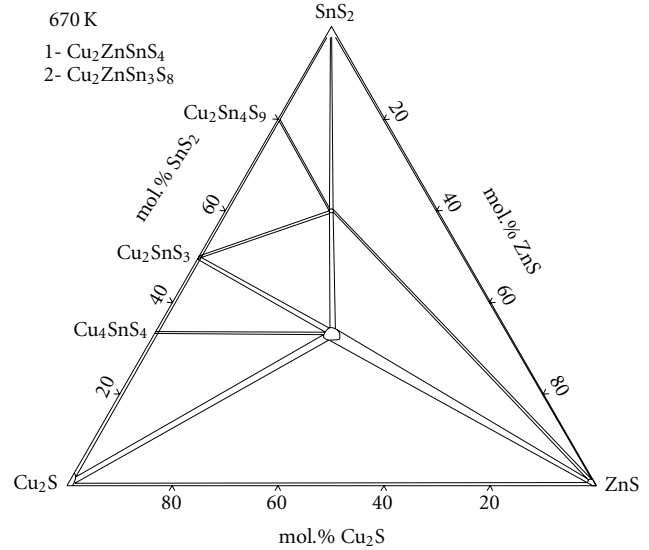


FIGURE 2: Phase diagram of SnS-Cu₂S-ZnS solar cells (taken from [3]).

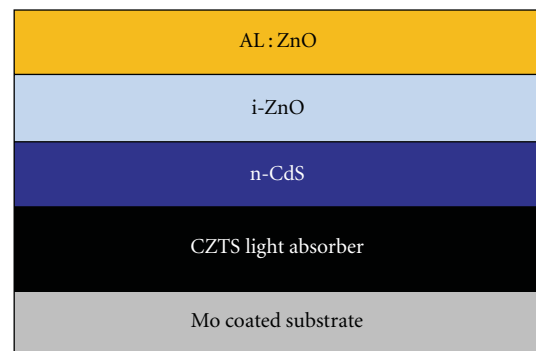


FIGURE 3: Schematics of the structure of CZTS solar cells.

thin films, therefore this paper will review the most recent research activities of employing variable techniques for deposition of CZTS thin films. The main electrical and optical properties of the synthesized materials will be briefly discussed as well.

The techniques for synthesis of CZTS thin films can be classified into two categories: vacuum, and nonvacuum-based method. According to the nature of the approach used for the deposition of the thin films, each category has a few subclassifications, the details of which will be shown in the following.

4. Vacuum-Based Deposition Method

Vacuum-based fabrication techniques normally involve deposition of the constitute atoms of the CZTS compound on a substrate by sputtering or evaporation/coevaporation of the target sources under a certain pressure and temperature. These techniques have the advantage of easily controlling the chemical composition and phase profile in the thin films and normally have good reproducibility.

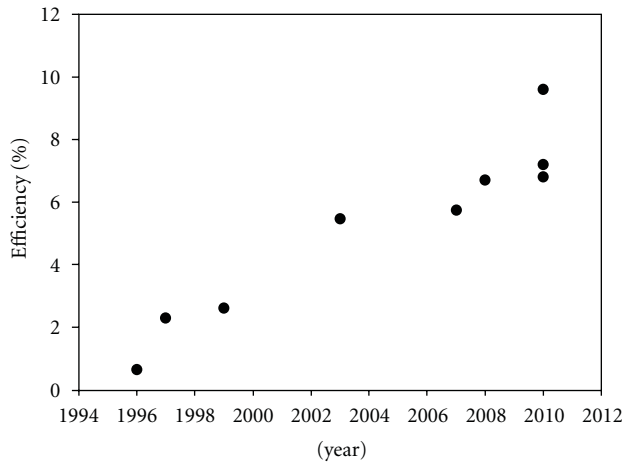


FIGURE 4: Evolution of the conversion efficiency of thin film solar cells using CZTS as light absorber layer.

4.1. Vacuum-Based Sputtering Deposition Technique. An atomic beam sputtering technique was employed by Ito and Nakazawa to deposit CZTS thin films in 1988. The band gap energy of the films was determined to be 1.45 eV [4]. In 2003, Seol et al. used Cu_2S , ZnS , and SnS_2 as target sources to deposit CZTS precursor thin films onto a glass substrate at room temperature by a RF magnetron sputtering technique. The as-deposited films were amorphous. After annealing in $\text{Ar} + \text{S}_2(\text{g})$ atmosphere, a stoichiometric ratio of $\text{Cu}/\text{Zn}/\text{Sn}$ was achieved with the films, but S was deficient. This problem was solved by further annealing the films in a sulphur vapour atmosphere at temperature above 200°C . It was found that the composition of the thin film materials was affected by the RF power in the sputtering [12].

An integrated vacuum apparatus which combined the RF sputtering technique with the sulfurization process was employed to reduce the effect of moisture from ambient air on the property of CZTS films. Target sources were based on ZnS , and SnS and Cu . Both the quality and reproducibility of the CZTS films were significantly improved by this method. A 5.7% conversion efficiency with the CZTS-based thin film solar cells was achieved [13]. By eliminating the metal oxide impurity in the CZTS films using deionized water, the efficiency of the solar cells was further improved to 6.7% [8].

Tanaka et al. used a vacuum-based hybrid sputtering approach to deposit the constitute elements Cu , Zn , Sn on a quartz substrate. Specifically, Sn and Zn metal layers were deposited by DC-sputtering and Cu by RF-sputtering. Stoichiometry CZTS thin films were formed at the substrate temperature above 400°C . However, substantial Zn losses were observed when the temperature was above 450°C [14]. Yoo and Kim studied the influence of Cu content on the structure and morphology of CZTS films. Their results indicated that Cu -rich or a stoichiometric Cu content would lead to the formation of Cu_{2-x}S in the films, whereas a Cu -poor composition favoured the formation of a smooth film surface [15]. Liu et al. reported CZTS films with a high light absorption coefficient ($>10^5 \text{ cm}^{-1}$). The films were synthesized by a DC reactive magnetron sputtering method

using a source target consisting of $\text{Cu}/\text{Zn}/\text{Sn}$ metal mixture with stoichiometric composition ($\text{Cu}:\text{Zn}:\text{Sn} = 2:1:1$, molar ratio). Therefore, the precursor films could be made in one step. The CZTS compound was formed after sulfurization of the precursors. However, besides the desired CZTS materials, secondary phases Cu_{2-x}S and Cu_3SnS_4 were also observed in the materials. And further characterization showed that the carrier concentration of the films was in the order of 10^{18} cm^{-3} [16]. Similar approach was also explored by Momose et al. for the fabrication of CZTS thin films. Cu , Zn , and Sn metals were simultaneously deposited on a SLG substrate by sputtering to form CZTS precursor films. After a rapid sulfurization (7 min) of the precursor at 590°C , the CZTS films were formed. An efficiency of 3.7% was obtained with the best thin film solar cell [17]. Most synthesized CZTS material is kesterite-type due to a better stability thermodynamically compared to the stannite-type. Nevertheless, stannite phase CZTS films which showed a very low sheet resistivity (0.156 Ohm cm) were synthesized by an ion-beam sputtering technique. The band gap energy of the material was determined to be 1.51 eV [18].

4.2. Vacuum-Based Evaporation Deposition. The synthesis of CZTS thin films by a thermal evaporation approach was firstly reported by Friedlmeier et al. in 1997. The elements and binary chalcogenides compounds were deposited onto a substrate in high vacuum. They found that the film composition and grain size were largely dependent on the substrate temperature [5]. Moreover, they observed that the electrical resistivity of the films could be varied between 1 and 100 ohm cm by treating the films with a KCN solution [19]. Katagiri et al. used an electron beam evaporation method to deposit a $\text{Cu}/\text{Sn}/\text{Zn}$ stack layer sequentially on a SLG substrate at 150°C in high vacuum. The precursor film was subsequently annealed in a sulphur-containing atmosphere ($\text{N}_2 + 5\% \text{ H}_2\text{S}$) at 500°C to form the CZTS compound. The characterization of the optical and electrical properties of the film showed that the optical band gap energy was 1.45 eV and the light absorption coefficient was in the order of 10^4 cm^{-1} . The corresponding CZTS thin film solar cells with an architecture of $\text{Al}/\text{ZnO}/\text{CdS}/\text{CZTS}/\text{Mo}/\text{SLG}$ provided an efficiency of 0.66% [20]. The same group later reported that using ZnS to replace Zn as the target source could dramatically enhance the adhesion of CZTS film to the Mo/SLG substrate [21]. An approach based on one-step synthesis of CZTS thin films by coevaporation of precursor sources Cu , Zn , Sn , S simultaneously was reported by Tanaka et al. The CZTS material showed a preferential orientation along [112] plane. The grain size of the film depended on the substrate temperature. Larger grains were obtained at higher substrate temperature [22]. In addition, growth of CZTS crystals on $\text{Si}(100)$ wafers using a high vacuum multi-source evaporation technique was reported by Oishi et al. A temperature-induced orientation growth was observed in the films [23].

From commercial application point of view, it is necessary to develop a process by which high-quality CZTS thin films can be produced rapidly and reproducibly. Such

process has been explored recently. Wang et al. reported the deposition of Cu, Zn, Sn, and S elements on a SLG substrate simultaneously by a rapid thermal evaporation method. The thickness of the light absorber layer was less than $1.0\ \mu\text{m}$ and the annealing time was only a few minutes. Thin film solar cells with 6.8% conversion efficiency were fabricated. The analysis of the electrical property of the PV device indicated that the performance of the cell was limited by the high series resistance and the high charge recombination [24]. A similar method based on rapid deposition (16 min) of CZTS thin films on Mo/SLG substrate was also reported by Schubert et al. ZnS, Sn, Cu, and S target sources were coevaporated simultaneously onto the substrate at 550°C in vacuum. The composition of the precursor films was copper-rich, which resulted in the formation of secondary phases Cu_{2-x}S . Nevertheless, stoichiometry CZTS films were obtained by posttreating the films with KCN aqueous solution. An energy conversion efficiency of 4.1% was achieved with the thin film solar cells [25].

Moriya et al. employed a vacuum-based pulsed laser deposition technique to fabricate CZTS light absorber layer for thin film solar cells and an efficiency of 1.74% was obtained with the devices [26, 27]. The effect of the laser incident energy on the structural, morphological, and optical properties of the CZTS thin films was investigated by Pawar et al. The study revealed that the crystallinity of the films increased with the increase of the laser energy until certain value (e.g., $2.5\ \text{J}/\text{cm}^2$) [28]. Moreover, the pulsed laser deposition technique can also be used to grow CZTS crystals on a GaP substrate. Well-crystallized CZTS crystals were obtained at substrate temperature of 400°C and the crystals showed a preferential orientation along [112], [29].

4.3. Influence of the Stacking Order of the Metallic Layer on the Performance CZTS Solar Cell. Araki et al. studied the effect of the stacking order of Cu, Zn, Sn metal layer on the properties of CZTS thin films and the corresponding solar cell performance. It was found that the films made from the precursor with a stacking order of Mo/Cu/Zn/Sn showed larger grain sizes than that with Mo/Cu/Sn/Zn. The direct contact of Cu and Zn layers should be responsible for the formation of large grains (Figure 5). However, the best cell efficiency (1.79%) was obtained with the precursor where Zn is the bottom layer and Sn is the top layer (stacking order: Mo/Zn/Cu/Sn). This phenomenon was explained by avoiding the formation of voids between Mo and CZTS if Cu layer were in direct contact with the Mo conductive layer [30].

The properties of CZTS films made from precursors with the stacking order of Mo/Zn/Cu/Sn and Mo/Zn/Sn/Cu deposited by a DC magnetron sputtering was also investigated by Fernandes et al. In contrary to Araki et al.'s conclusion, They concluded that the later stacking sequence was in favour of the CZTS crystal growth because Cu layer on top reduced the loss of Zn and Sn in the annealing process, thus leading to a better composition control and crystallinity. However, Cu_xS may be formed on the surface of the film when Cu is the top layer [31]. Obviously, a deep understanding of the

crystal growth mechanism of this quaternary compound is needed to explain these phenomena.

Weber et al. studied the loss of Sn in CZTS during the annealing process. It was found that desorption of SnS from the CZTS at temperature above 350°C led to the losses of Sn in vacuum. The decomposition process of CZTS could be reduced by addition of an inert gas in the chamber where the sintering was carried out [32]. This issue has been addressed by Redinger et al. as well. They suggested to add extra SnS and S material in the precursor to prevent the decomposition of CZTS at high temperature [33].

5. Nonvacuum Deposition Method

The vacuum-based deposition techniques generally suffer from relatively slow throughput, low material utilization, and considerable energy consumption. Therefore, nonvacuum based deposition methods have been developed to reduce the production cost. These methods including spray pyrolysis, electrochemical deposition, and spin coating of precursor solutions, have been widely investigated for preparation of semiconductor thin films such as CIGS and CdTe [34]. They have been attempted to synthesize CZTS thin films as well.

5.1. Spray Pyrolysis Deposition. The synthesis of CZTS thin films by deposition of precursor solutions using spray pyrolysis technique in ambient environment was reported by Nakayama and Ito in 1997. A precursor solution consisting of CuCl, ZnCl_2 , SnCl_4 , and thiourea at suitable concentrations in deionized water/ethanol solvent mixture was sprayed onto a heated SLG substrate. The as-deposited films were stannite-type [35]. Since then, similar approach has been used by other researchers for the fabrication of CZTS thin films using different precursor solutions. Kamoun et al. studied the effect of the substrate temperature and the spray duration on the crystallinity of the CZTS films. The best crystallinity was obtained at the substrate temperature 613 K and a preferential orientation along [112] plane was observed with the films [36]. The effect of the substrate temperature and the pH value as well as the compositions of the precursor solution on the crystallinity and the morphology of the CZTS material were also investigated by Kumar et al. Their results showed that the CZTS material with good crystallinity was obtained at the substrate temperature in the range of 643–683 K with the precursor solution $\text{pH} = 4.5$. But impurities such as ZnS were observed besides the CZTS compound [37, 38]. Prabhakar and Nagaraju used ultrasonic spray pyrolysis technique to deposit CZTS thin films on a SLG substrate. The films with kesterite structure were obtained at 613 K, consistent with the results reported by others [39].

5.2. Spin-Coating of CZTS Precursor Solution. It normally involves three steps to prepare a CZTS thin film by spin-coating technique. (1) Preparation of a precursor solution which contains the ions of interest; (2) Spin-coating the precursor solution on a SLG substrate to make the thin film; (3) annealing the thin film at suitable atmosphere to form CZTS materials.

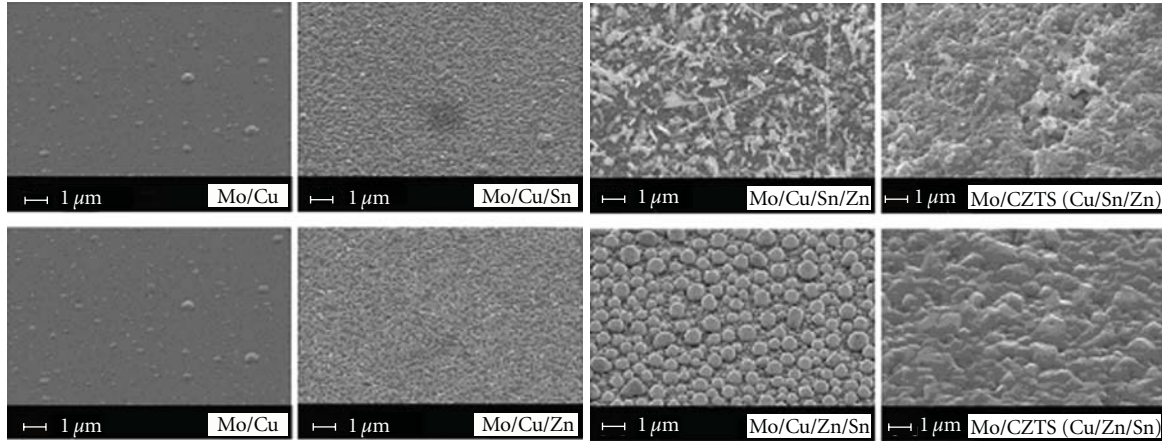


FIGURE 5: SEM pictures of precursor and CZTS films with different stacking order of metal layers (taken from [30]).

Tanaka et al. synthesized CZTS films by spin-coating a sol-gel precursor solution. The precursor solution contained acetate salts of copper (II) and zinc (II) as well as tin (II) chloride in 2-methoxyethanol solvent. Monoethanolamine was added to the solution to prevent the formation of precipitations. CZTS thin films were formed by annealing the precursor films in H_2S containing atmosphere at $500^\circ C$ [40]. They later reported using non-vacuum methods to fabricate all the other components of thin film solar cells besides the CZTS layer. Specifically, the $Zn/ZnO:Al$ window layer was made by a spin-coating method and the CdS buffer layer was made by a chemical bath deposition approach. The CZTS solar cells fabricated by the non-vacuum methods showed an efficiency of 1.01% ($J_{sc} = 7.8 \text{ mA/cm}^2$, $V_{oc} = 390 \text{ mV}$) [41]. The effect of the chemical composition of the precursor solution on the morphology and the optical properties of the CZTS thin films were investigated. Large grains were found in the films made from the precursor solution with copper poor ($Cu/(Zn+Sn) < 0.8$, molar ratio). The band gap energy of the copper-deficient films was larger compared to that of the copper-rich films. The best solar cell showed an efficiency of 2.03% [42].

Pawar et al. studied the effect of the complexing agent trisodium citrate in the precursor solution on the structure, morphology and composition of the CZTS thin films. The results showed that the crystallinity of the films was improved by using the complexing agent. However, the surface of the precursor films were uneven compared to the films deposited from the electrolyte without the complexing agent. Such effect was reduced by postsulfurization treatment of the films [43]. Similarly, Liu et al. employed additive such as ethylxanthate molecule to facilitate the formation of a homogeneous CZTS precursor solution which was used to deposit CZTS films [44].

Fischereder et al. deposited CZTS films by spin coating a precursor solution consisting of metal salts of copper (I), tin (IV), and zinc (II) and thioacetamide in pyridine. They found that the formation of CZTS compound occurred at temperature at low as $105^\circ C$ in vacuum. The band gap energy of the films varied between 1.41 and 1.81 eV by changing the

annealing temperature point [45]. This is probably due to the coexistence of secondary phases in the film under low annealing temperature.

Todorov et al. prepared a CZTS precursor which was based on a hydrazine-based particle-solution slurry consisting of Cu, Zn, Sn, and S elements. The CZTS films or partly selenized CZTS (CZTSSe) thin films were obtained by annealing the precursor films in sulphur or sulfoselenide containing atmosphere at $540^\circ C$. The films showed large grains and uniform composition (Figure 6(a)). The best cell efficiency was 9.66% which was obtained with the CZTSSe-based solar cells. The onset of the photon response in the IPCE spectrum of the thin film solar cells was close to 1200 nm (Figure 6(b)), indicating a lower band gap energy of the materials [11].

5.3. Electrochemical Deposition. Electrochemical deposition is considered to be a promising technique for the low-cost preparation of semiconductor thin films and has been employed by BP and CISEL for the commercial deposition of CdTe and CIGS thin film PV modules [46, 47]. The key for using this method is to find suitable electrochemical potential at which the metal cations can be reduced efficiently while unwanted reactions will not occur. CZTS films made by an electrodeposition method were firstly reported by Scragg et al. A stacking metal layer of Cu/Sn/Zn was deposited sequentially on a Mo/SLG substrate using a three-electrode configuration where Ag/AgCl was used as reference electrode. Cu and Sn was deposited at -1.14 V and -1.21 V , respectively using suitable alkaline solutions, and Zn was deposited at -1.20 V in an acidic environment ($\text{pH} = 3$). CZTS thin films were formed after annealing the precursor in a sulphur atmosphere at $500^\circ C$. The doping density of the films was in the order of 10^{16} cm^{-3} [48]. Further investigation of the photovoltaic performance of the corresponding thin film solar cells indicated that the device performed better under low illumination intensity. At high illumination intensity (equivalent to 1 sun), the recombination in the space charge region was increased, leading to the decrease of the performance [49]. An energy conversion efficiency of 3.2%

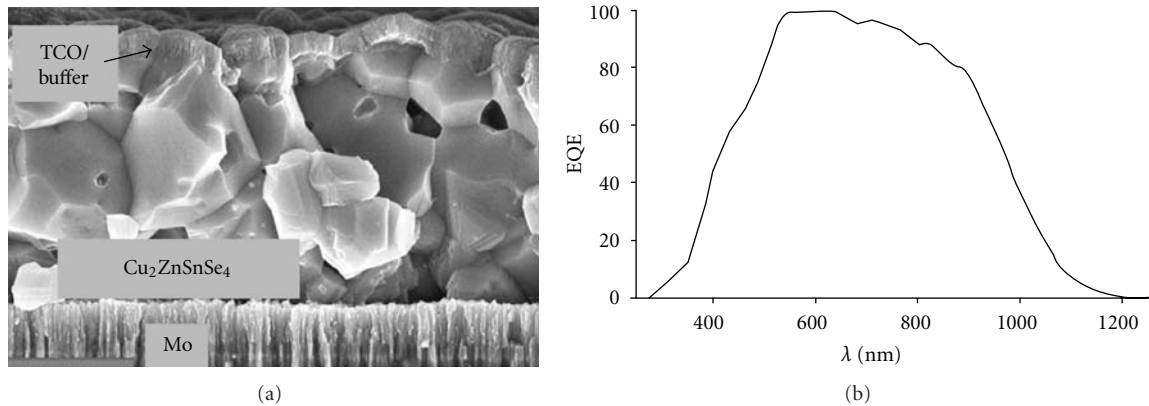


FIGURE 6: SEM of cross section and EQE of thin film solar cells based on CZTSSe light absorber (taken from [11]).

was obtained with a full-structured thin film solar cell. In this cell, the morphology and uniformity of the CZTS thin films were optimized through modification of the stacking order of the electrodeposited metallic layers [50]. Ennaoui et al. electrodeposited Cu-Zn-Sn precursor thin films on a Mo/SLG substrate using an electrolyte containing copper (II), zinc (II), and tin (IV) cations together with complexing agents and additives. The best thin film solar cell showed an efficiency of 3.4% ($J_{sc} = 14.8 \text{ mA/cm}^2$, $V_{oc} = 563 \text{ mV}$, $FF = 41\%$) which was Cu-poor in the CZTS material. Their study also revealed that secondary phases such as ZnS for the Zn-rich material and Cu_2SnS_3 for the Zn-poor film existed at the interface of CZTS/Mo-SLG [51]. Scragg et al. also compared the morphology of the electrodeposited CZTS films which were annealed in different gaseous atmosphere. They found that H_2S containing atmosphere benefited the enhanced crystallinity of the films compared to the sulphur containing environment [52]. Zhang et al. used electrochemical method to grow the atomic layer of Cu, Zn, Sn, and S layer by layer on a Ag substrate. A [112] preferential orientation was observed with the as-deposited CZTS thin film [53].

Besides the conventional electrodeposition approach, a method based on photoelectrochemical deposition was reported by Moriya et al. for the fabrication of CZTS films using an aqueous solution containing the sulphate of Cu^{2+} , Zn^{2+} , and Sn^{2+} as well as sodium thiosulfate. They reported that the pH value of the precursor solution had little influence on the composition of the film [54].

5.4. CZTS Nanocrystal by Hot-Injection Method. Hot injection solution chemical method is an established approach for the synthesis of materials with well-defined size and shape (nanocrystals). It has been widely used in preparation of semiconductor nanocrystals. In 2009, three papers on synthesis of CZTS nanocrystals by hot-injection method appeared in *Journal of the American Chemical Society*. The sizes of the synthesized nanocrystal were less than 20 nm. The band gap energy of the nanocrystals was around 1.5 eV, which is comparable to that of the bulk material [55–57]. Kameyama et al. studied the effect of the reaction temperature in the hot-injection process on the formation of

CZTS nanocrystals. They found that a single-phase CZTS were formed at temperature over 240°C whereas secondary phase such as CuS was formed at low reaction temperature. The valence band and the conduction band of the as-synthesized films was 0.3 eV and -1.2 eV versus Ag/AgCl, respectively [58]. By tuning the composition of the hot chemical solution, the band gap energy of the nanocrystals was adjusted from 3.48 eV (ZnS) to 1.23 eV (CZTS, sphalerite type). The application of the CZTS nanocrystals in dye-sensitized solar cells was investigated, but the efficiency was very low (0.03%) [59]. In contrast, CZTS nanocrystals which was annealed in Se vapour at 500°C for 15 min showed an enhanced grain growth. The thin film solar cells using the CZTSSe light absorber showed an energy conversion efficiency of 7.2%, and the cell did not show significant degradation in a one-month light soaking test [60].

Traditionally, CZTS appears in either kesterite or stannite phase with tetragonal structure. Recently, CZTS nanocrystals with wurtzite phase were synthesized by Lu et al. using hot-injection method. The new structure has a hexagonal structure and showed a band gap energy of 1.4 eV [61].

5.5. Other Nonvacuum Synthesis Methods. Wangperawong et al. reported a novel synthesis method for CZTS precursor films. Firstly, SnS and ZnS materials were coated on a Mo/SLG substrate by chemical bath deposition, and Cu ion was then incorporated into the precursor films via ion exchange mechanism. CZTS films with good crystallinity were formed by annealing the precursor films in a H_2S containing atmosphere at 500°C [62]. Another chemical solution-based non-vacuum method for the synthesis CZTS nanocrystals was based on a dissolution-reprecipitation process which involved the use of KSCN as molten salt to finely tune the supersaturation condition of the precursor solution. The successful preparation of the discrete nanocrystals relied on the precursor properties such as ultrafine size of the aggregates and a high short-range order in the nanocrystals according to the authors [63].

Hydrothermal method has been widely employed for synthesis of nanomaterials. It is thought very difficult to synthesize single-phase CZTS material, however, owing to

TABLE 1: Characteristic parameters of the current best efficiency CZTS-based thin film solar cells with light absorber made by various methods.

Method	Material	η (%)	V_{oc} (V)	J_{sc} (mA/cm ²)	FF	Ref
RF magnetron sputtering	CZTS	6.77	0.61	17.9	0.62	[8]
Thermal evaporation	CZTS	6.8	0.587	17.8	0.65	[24]
Electrodeposition	CZTS	3.4	0.563	14.8	0.41	[51]
Hot injection	CZTSSe	7.2	0.42	30.4	0.527	[60]
Hydrazine	CZTSSe	9.67	0.516	28.6	0.65	[11]

the complexity of the compound and the narrow stable thermodynamic region where the material can exist. Cao and Shen reported the synthesis of CZTS materials at 150°C in an autoclave using a precursor solution containing CuCl_2 , $(\text{C}_2\text{H}_3\text{O}_2)_2\text{Zn}$, SnCl_4 , and S in ethylenediamine. Though CZTS target material was obtained, ZnS impurity was also formed [64].

Zhou et al. reported using a wet ball milling combined with screen-printing technique for the preparation of CZTS thin films. Primary elements copper, zinc, tin, and sulphur were homogeneously mixed under vigorous milling. CZTS powder was formed by sintering the precursor material in an inert gas at 500°C. A screen printable paste made from the CZTS powder was deposited on a Mo-coated polyimide substrate for fabrication of thin film solar cells. The sheet resistance of the thin film was 2.42×10^3 ohm and the carrier density was $3.8 \times 10^{18} \text{ cm}^{-3}$. Hall mobility of the CZTS material was $12.61 \text{ cm}^2 \text{ V}^{-1} \text{ S}^{-1}$. The best conversion efficiency of the thin film solar cells was 0.49% [65].

6. Defect Physics/Chemistry of CZTS

Defect plays an important role in determining the electrical property of semiconductor materials. Chen et al. have studied the defect mechanism of CZTS material. They employed DFT-based first principal calculation to study the thermodynamic stability of the quaternary compound. The results have revealed that the stable chemical potential region for the formation of a stoichiometry CZTS is very narrow, consistent with the previous experimental observations. Theoretical calculation has also predicted that Cu-rich/Zn-poor conditions are necessary for the growth of a single-phase CZTS crystal. The intrinsic defect in CZTS material is p-type Cu_{Zn} antisite (Cu at Zn site) under such growth condition. Nevertheless, the authors have argued that Cu_{Zn} defect is not optimal for solar cell applications due to the relatively deep acceptor levels. Instead, copper vacancy V_{Cu} is preferred for high efficiency solar cells. Moreover, there are self-compensated defect pair complexes such as $[\text{Cu}_{\text{Zn}}^- + \text{Zn}_{\text{Cu}}^+]$ for Cu-rich/Zn-poor growth condition and $[\text{V}_{\text{Cu}}^- + \text{Zn}_{\text{Cu}}^+]$ for Cu-poor/Zn-rich condition in CZTS [66]. These electrically neutral defect complexes can remarkably passivate the deep levels in the band gap, reducing the recombination in the PV devices [67]. Similar results have also been reported by Nagoya et al. and Maeda et al. [68, 69]. These authors have claimed that ZnS should be the main

competing phase under the prevalent Cu-poor and Zn-rich growth condition, and Cu at Zn sites Cu_{Zn} is the most stable defect in the entire stability range of CZTS [67]. Chory et al. have used electron spin resonance (ESR) measurement to investigate the defects of CZTS materials made by a sol-gel method. The study has indicated the existence of Cu(II) in the compound. This phenomenon was explained due to the charge transfer between Sn(IV) and Cu(I), leading to the formation of Sn(II) and Cu(II) [70].

7. Summary

The recent significant progress in $\text{Cu}_2\text{ZnSnS}_4$ has demonstrated the feasibility of developing high efficiency PV devices with low cost and low environment impact materials. A broad range of techniques including vacuum or non-vacuum approaches have been explored to deposit CZTS films. The vacuum-based sputtering method has produced CZTS films for thin film solar cells with an efficiency of 6.77%, which is comparable to the performance of the films synthesized by a rapid thermal evaporation. From application point of view, the rapid vacuum thermal evaporation approach is more promising for large scale production of the thin film materials.

Among the non-vacuum preparation methods, hydrazine-based particle-solution method has demonstrated its capability in fabrication of high quality CZTS materials. This claim is justified by the thin film solar cells with 9.66% energy conversion efficiency using hydrazine method. It seems that hot-injection method is a promising synthesis technique for CZTS material as well. The thin film solar cells with the selenized CZTS nanocrystals have showed 7.2% conversion efficiency. Though electrodeposition has been successfully applied for the deposition of CdTe and CIGS thin films commercially, this method is yet able to compete with other techniques for deposition of high quality CZTS films currently. The best solar cell with the electrodeposited CZTS film has shown 3.4% conversion efficiency. Table 1 summarizes the characteristic parameters of the state-of-the-art thin film solar cells made by different methods. Clearly, the two most high efficiency cells are based on the selenized CZTS light absorber materials (CZTSSe). The short circuit current density of the cells is nearly twofold that of the rest of the cells which are based on CZTS materials. This is attributed to the broader spectral response of the CZTSSe light absorber owing to the lower band gap energy. The open circuit voltage of all the CZTS-based solar cells is around

0.6 eV, which is much lower than the theoretical value of 1.5 eV. A high charge recombination in those devices is probably responsible for the low V_{oc} . A detailed investigation of the electrical properties and kinetics of charge transport in the device is necessary in order to disclose the exact physical reasons for the low V_{oc} .

In order to improve the efficiency of CZTS-based thin film solar cells, a deeper understanding of the fundamental properties of CZTS, particularly the nature of the defects as well as their impact on the properties of CZTS material is important. CZTS material for thin film solar cells which have produced good efficiency normally always shows Cu-poor/Zn-rich in the composition. Therefore, secondary phase(s) should exist in the light absorbers. It is necessary to identify those secondary phases and their effects in order to optimize the fabrication process to make CZTS thin films with desired properties.

Acknowledgment

H. Wang thanks Queensland University of Technology for funding this project via Vice-Chancellor Research Fellowship Scheme.

References

- [1] S. A. Kissin, "A Reinvestigation of the stannite ($\text{Cu}_2\text{FeSnS}_4$)—kesterite ($\text{Cu}_2\text{ZnSnS}_4$) pseudobinary system," *Canadian Mineralogist*, vol. 27, pp. 689–697, 1989.
- [2] S. Schorr, "Structural aspects of adamantine like multinary chalcogenides," *Thin Solid Films*, vol. 515, no. 15, pp. 5985–5991, 2007.
- [3] I. D. Olekseyuk, I. V. Dudchak, and L. V. Piskach, "Phase equilibria in the Cu_2S - ZnS - SnS_2 system," *Journal of Alloys and Compounds*, vol. 368, no. 1-2, pp. 135–143, 2004.
- [4] K. Ito and T. Nakazawa, "Electrical and optical properties of stannite-type quaternary semiconductor thin films," *Japanese Journal of Applied Physics*, vol. 27, no. 11, pp. 2094–2097, 1988.
- [5] T. M. Friedlmeier, N. Wieser, T. Walter, H. Dittrich, and H. W. Schock, "Heterojunctions based on $\text{Cu}_2\text{ZnSnS}_4$ and $\text{Cu}_2\text{ZnSnSe}_4$ thin films," in *Proceedings of the 14th European Conference of Photovoltaic Science and Engineering and Exhibition*, p. 1242, Bedford, UK, 1997.
- [6] H. Katagiri, K. Saitoh, T. Washio, H. Shinohara, T. Kurumadani, and S. Miyajima, "Development of thin film solar cell based on $\text{Cu}_2\text{ZnSnS}_4$ thin films," *Solar Energy Materials and Solar Cells*, vol. 65, no. 1–4, pp. 141–148, 2001.
- [7] H. Katagiri, K. Jimbo, K. Moriya, and K. Tsuchida, "Solar cell without environmental pollution by using CZTS thin film," in *Proceedings of the 3rd World Conference on Photovoltaic Energy Conversion*, pp. 2874–2879, Osaka, Japan, May 2003.
- [8] H. Katagiri, K. Jimbo, S. Yamada et al., "Enhanced conversion efficiencies of $\text{Cu}_2\text{ZnSnS}_4$ -based thin film solar cells by using preferential etching technique," *Applied Physics Express*, vol. 1, no. 4, Article ID 041201, 2 pages, 2008.
- [9] H. Katagiri, " $\text{Cu}_2\text{ZnSnS}_4$ thin film solar cells," *Thin Solid Films*, vol. 480–481, pp. 426–432, 2005.
- [10] H. Katagiri, K. Jimbo, W. S. Maw et al., "Development of CZTS-based thin film solar cells," *Thin Solid Films*, vol. 517, no. 7, pp. 2455–2460, 2009.
- [11] K. Todorov, K. B. Reuter, and D. B. Mitzi, "High-efficiency solar cell with earth-abundant liquid-processed absorber," *Advanced Materials*, vol. 22, no. 20, pp. E156–E159, 2010.
- [12] J. S. Seol, S. Y. Lee, J. C. Lee, H. D. Nam, and K. H. Kim, "Electrical and optical properties of $\text{Cu}_2\text{ZnSnS}_4$ thin films prepared by rf magnetron sputtering process," *Solar Energy Materials and Solar Cells*, vol. 75, no. 1-2, pp. 155–162, 2003.
- [13] K. Jimbo, R. Kimura, T. Kamimura et al., " $\text{Cu}_2\text{ZnSnS}_4$ -type thin film solar cells using abundant materials," *Thin Solid Films*, vol. 515, no. 15, pp. 5997–5999, 2007.
- [14] T. Tanaka, T. Nagatomo, D. Kawasaki et al., "Preparation of $\text{Cu}_2\text{ZnSnS}_4$ thin films by hybrid sputtering," *Journal of Physics and Chemistry of Solids*, vol. 66, no. 11, pp. 1978–1981, 2005.
- [15] H. Yoo and J. Kim, "Growth of $\text{Cu}_2\text{ZnSnS}_4$ thin films using sulfurization of stacked metallic films," *Thin Solid Films*, vol. 518, no. 22, pp. 6567–6572, 2010.
- [16] F. Y. Liu, K. Zhang, Y. Q. Lai, J. Li, Z. A. Zhang, and Y. X. Liu, "Growth and characterization of $\text{Cu}_2\text{ZnSnS}_4$ thin films by dc reactive magnetron sputtering for photovoltaic applications," *Electrochemical and Solid-State Letters*, vol. 13, no. 11, pp. H379–H381, 2010.
- [17] N. Momose, M. T. Htay, T. Yudasaka et al., " $\text{Cu}_2\text{ZnSnS}_4$ thin film solar cells utilizing sulfurization of metallic precursor prepared by simultaneous sputtering of metal targets," *Japanese Journal of Applied Physics*, vol. 50, no. 1, part 3, Article ID 01BG09, 4 pages, 2011.
- [18] J. Zhang, L. X. Shao, Y. J. Fu, and E. Q. Xie, " $\text{Cu}_2\text{ZnSnS}_4$ thin films prepared by sulfurization of ion beam sputtered precursor and their electrical and optical properties," *Rare Metals*, vol. 25, no. 6, pp. 315–319, 2006.
- [19] T. M. Friedlmeier, H. Dittrich, and H. W. Schock, "Growth and characterization of $\text{Cu}_2\text{ZnSnS}_4$ and $\text{Cu}_2\text{ZnSnSe}_4$ thin films for photovoltaic applications," *Ternary and Multinary Compounds*, vol. 152, pp. 345–348, 1998.
- [20] H. Katagiri, M. Nishimura, T. Onozawa et al., "Rare-metal free thin film solar cell," in *Proceedings of the Power Conversion Conference*, pp. 1003–1006, Nagaoka, Japan, August 1997.
- [21] H. Katagiri, N. Ishigaki, T. Ishida, and K. Saito, "Characterization of $\text{Cu}_2\text{ZnSnS}_4$ thin films prepared by vapor phase sulfurization," *Japanese Journal of Applied Physics*, vol. 40, no. 2, pp. 500–504, 2001.
- [22] T. Tanaka, D. Kawasaki, M. Nishio, Q. Guo, and H. Ogawa, "Fabrication of $\text{Cu}_2\text{ZnSnS}_4$ thin films by co-evaporation," *Physica Status Solidi C*, vol. 3, no. 8, pp. 2844–2847, 2006.
- [23] K. Oishi, G. Saito, K. Ebina et al., "Growth of $\text{Cu}_2\text{ZnSnS}_4$ thin films on Si (100) substrates by multisource evaporation," *Thin Solid Films*, vol. 517, no. 4, pp. 1449–1452, 2008.
- [24] K. Wang, O. Gunawan, T. Todorov et al., "Thermally evaporated $\text{Cu}_2\text{ZnSnS}_4$ solar cells," *Applied Physics Letters*, vol. 97, no. 14, Article ID 143508, 2010.
- [25] B. A. Schubert, B. Marsen, S. Cinque et al., " $\text{Cu}_2\text{ZnSnS}_4$ thin film solar cells by fast coevaporation," *Progress in Photovoltaics*, vol. 19, no. 1, pp. 93–96, 2011.
- [26] K. Moriya, K. Tanaka, and H. Uchiki, "Fabrication of $\text{Cu}_2\text{ZnSnS}_4$ thin-film solar cell prepared by pulsed laser deposition," *Japanese Journal of Applied Physics*, vol. 46, no. 9, pp. 5780–5781, 2007.
- [27] K. Moriya, K. Tanaka, and H. Uchiki, " $\text{Cu}_2\text{ZnSnS}_4$ thin films annealed in H_2S atmosphere for solar cell absorber prepared by pulsed laser deposition," *Japanese Journal of Applied Physics*, vol. 47, no. 1, pp. 602–604, 2008.
- [28] S. M. Pawar, A. V. Moholkar, I. K. Kim et al., "Effect of laser incident energy on the structural, morphological and optical properties of $\text{Cu}_2\text{ZnSnS}_4$ (CZTS) thin films," *Current Applied Physics*, vol. 10, no. 2, pp. 565–569, 2010.

- [29] K. Sekiguchi, K. Tanaka, K. Moriya, and H. Uchiki, "Epitaxial growth of $\text{Cu}_2\text{ZnSnS}_4$ thin films by pulsed laser deposition," *Physica Status Solidi*, vol. 3, no. 8, pp. 2618–2621, 2006.
- [30] H. Araki, A. Mikaduki, Y. Kubo et al., "Preparation of $\text{Cu}_2\text{ZnSnS}_4$ thin films by sulfurization of stacked metallic layers," *Thin Solid Films*, vol. 517, no. 4, pp. 1457–1460, 2008.
- [31] P. A. Fernandes, P. M. P. Salomé, and A. F. da Cunha, "Precursors' order effect on the properties of sulfurized $\text{Cu}_2\text{ZnSnS}_4$ thin films," *Semiconductor Science and Technology*, vol. 24, no. 10, Article ID 105013, 2009.
- [32] A. Weber, R. Mainz, and H. W. Schock, "On the Sn loss from thin films of the material system Cu-Zn-Sn-S in high vacuum," *Journal of Applied Physics*, vol. 107, no. 1, Article ID 013516, 2010.
- [33] A. Redinger, D. M. Berg, P. J. Dale, and S. Siebentritt, "The consequences of kesterite equilibria for efficient solar cells," *Journal of the American Chemical Society*, vol. 133, no. 10, pp. 3320–3323, 2011.
- [34] C. J. Hibberd, E. Chassaing, W. Liu, D. B. Mitzi, D. Lincot, and A. N. Tiwari, "Non-vacuum methods for formation of $\text{Cu}(\text{In}, \text{Ga})(\text{Se}, \text{S})_2$ thin film photovoltaic absorbers," *Progress in Photovoltaics*, vol. 18, no. 6, pp. 434–452, 2010.
- [35] N. Nakayama and K. Ito, "Sprayed films of stannite $\text{Cu}_2\text{ZnSnS}_4$," *Applied Surface Science*, vol. 92, pp. 171–175, 1996.
- [36] N. Kamoun, H. Bouzouita, and B. Rezig, "Fabrication and characterization of $\text{Cu}_2\text{ZnSnS}_4$ thin films deposited by spray pyrolysis technique," *Thin Solid Films*, vol. 515, no. 15, pp. 5949–5952, 2007.
- [37] Y. B. K. Kumar, G. S. Babu, P. U. Bhaskar, and V. S. Raja, "Preparation and characterization of spray-deposited $\text{Cu}_2\text{ZnSnS}_4$ thin films," *Solar Energy Materials and Solar Cells*, vol. 93, no. 8, pp. 1230–1237, 2009.
- [38] Y. B. K. Kumar, G. S. Babu, P. U. Bhaskar, and V. S. Raja, "Effect of starting-solution pH on the growth of $\text{Cu}_2\text{ZnSnS}_4$ thin films deposited by spray pyrolysis," *Physica Status Solidi A*, vol. 206, no. 7, pp. 1525–1530, 2009.
- [39] T. Prabhakar and J. Nagaraju, "Ultrasonic spray pyrolysis of CZTS solar cell absorber layers and characterization studies," in *Proceedings of the 35th IEEE Photovoltaic Specialists Conference, (PVSC '10)*, pp. 1964–1969, June 2010.
- [40] K. Tanaka, N. Moritake, and H. Uchiki, "Preparation of $\text{Cu}_2\text{ZnSnS}_4$ thin films by sulfurizing sol-gel deposited precursors," *Solar Energy Materials and Solar Cells*, vol. 91, no. 13, pp. 1199–1201, 2007.
- [41] K. Tanaka, M. Oonuki, N. Moritake, and H. Uchiki, " $\text{Cu}_2\text{ZnSnS}_4$ thin film solar cells prepared by non-vacuum processing," *Solar Energy Materials and Solar Cells*, vol. 93, no. 5, pp. 583–587, 2009.
- [42] K. Tanaka, Y. Fukui, N. Moritake, and H. Uchiki, "Chemical composition dependence of morphological and optical properties of $\text{Cu}_2\text{ZnSnS}_4$ thin films deposited by sol-gel sulfurization and $\text{Cu}_2\text{ZnSnS}_4$ thin film solar cell efficiency," *Solar Energy Materials and Solar Cells*, vol. 95, no. 3, pp. 838–842, 2011.
- [43] B. S. Pawar, S. M. Pawar, S. W. Shin et al., "Effect of complexing agent on the properties of electrochemically deposited $\text{Cu}_2\text{ZnSnS}_4$ (CZTS) thin films," *Applied Surface Science*, vol. 257, no. 5, pp. 1786–1791, 2010.
- [44] Y. F. Liu, M. Y. Ge, Y. Yue et al., "Colloidal $\text{Cu}_2\text{ZnSnS}_4$ nanocrystals generated by a facile route using ethylxanthate molecular precursors," *Physica Status Solidi*, vol. 5, no. 3, pp. 113–115, 2011.
- [45] A. Fischereeder, T. Rath, W. Haas et al., "Investigation of $\text{Cu}_2\text{ZnSnS}_4$ formation from metal salts and thioacetamide," *Chemistry of Materials*, vol. 22, no. 11, pp. 3399–3406, 2010.
- [46] D. R. Johnson, "Microstructure of electrodeposited CdS/CdTe cells," *Thin Solid Films*, vol. 361, pp. 321–326, 2000.
- [47] S. Taunier, J. Six-Kurdi, P. P. Grand et al., " $\text{Cu}(\text{In}, \text{Ga})(\text{S}, \text{Se})_2$ solar cells and modules by electrodeposition," *Thin Solid Films*, vol. 480–481, pp. 526–531, 2005.
- [48] J. J. Scragg, P. J. Dale, and L. M. Peter, "Towards sustainable materials for solar energy conversion: preparation and photoelectrochemical characterization of $\text{Cu}_2\text{ZnSnS}_4$," *Electrochemistry Communications*, vol. 10, no. 4, pp. 639–642, 2008.
- [49] J. J. Scragg, P. J. Dale, and L. M. Peter, "Synthesis and characterization of $\text{Cu}_2\text{ZnSnS}_4$ absorber layers by an electrodeposition-annealing route," *Thin Solid Films*, vol. 517, no. 7, pp. 2481–2484, 2009.
- [50] J. J. Scragg, D. M. Berg, and P. J. Dale, "A 3.2% efficient Kesterite device from electrodeposited stacked elemental layers," *Journal of Electroanalytical Chemistry*, vol. 646, no. 1–2, pp. 52–59, 2010.
- [51] A. Ennaoui, M. Lux-Steiner, A. Weber et al., " $\text{Cu}_2\text{ZnSnS}_4$ thin film solar cells from electroplated precursors: novel low-cost perspective," *Thin Solid Films*, vol. 517, no. 7, pp. 2511–2514, 2009.
- [52] J. J. Scragg, P. J. Dale, L. M. Peter, G. Zoppi, and I. Forbes, "New routes to sustainable photovoltaics: evaluation of $\text{Cu}_2\text{ZnSnS}_4$ as an alternative absorber material," *Physica Status Solidi*, vol. 245, no. 9, pp. 1772–1778, 2008.
- [53] X. Zhang, X. Z. Shi, W. C. Ye, C. L. Ma, and C. M. Wang, "Electrochemical deposition of quaternary $\text{Cu}_2\text{ZnSnS}_4$ thin films as potential solar cell material," *Applied Physics A*, vol. 94, no. 2, pp. 381–386, 2009.
- [54] K. Moriya, K. Tanaka, and H. Uchiki, "Characterization of $\text{Cu}_2\text{ZnSnS}_4$ thin films prepared by photo-chemical deposition," *Japanese Journal of Applied Physics*, vol. 44, no. 1, pp. 715–717, 2005.
- [55] S. C. Riha, B. A. Parkinson, and A. L. Prieto, "Solution-based synthesis and characterization of $\text{Cu}_2\text{ZnSnS}_4$ nanocrystals," *Journal of the American Chemical Society*, vol. 131, no. 34, pp. 12054–12055, 2009.
- [56] Q. J. Guo, H. W. Hillhouse, and R. Agrawal, "Synthesis of $\text{Cu}_2\text{ZnSnS}_4$ nanocrystal ink and its use for solar cells," *Journal of the American Chemical Society*, vol. 131, no. 33, pp. 11672–11673, 2009.
- [57] C. Steinhagen, M. G. Panthani, V. Akhavan, B. Goodfellow, B. Koo, and B. A. Korgel, "Synthesis of $\text{Cu}_2\text{ZnSnS}_4$ nanocrystals for use in low-cost photovoltaics," *Journal of the American Chemical Society*, vol. 131, no. 35, pp. 12554–12555, 2009.
- [58] T. Kameyama, T. Osaki, K. I. Okazaki et al., "Preparation and photoelectrochemical properties of densely immobilized $\text{Cu}_2\text{ZnSnS}_4$ nanoparticle films," *Journal of Materials Chemistry*, vol. 20, no. 25, pp. 5319–5324, 2010.
- [59] P. C. Dai, X. N. Shen, Z. J. Lin, Z. Y. Feng, H. Xu, and J. H. Zhan, "Band-gap tunable $(\text{Cu}_2\text{Sn})_x/3\text{Zn}_{1-x}\text{S}$ nanoparticles for solar cells," *Chemical Communications*, vol. 46, no. 31, pp. 5749–5751, 2010.
- [60] Q. J. Guo, G. M. Ford, W. C. Yang et al., "Fabrication of 7.2% efficient CZTSSe solar cells using CZTS nanocrystals," *Journal of the American Chemical Society*, vol. 132, no. 49, pp. 17384–17386, 2010.
- [61] X. T. Lu, Z. B. Zhuang, Q. Peng, and Y. D. Li, "Wurtzite $\text{Cu}_2\text{ZnSnS}_4$ nanocrystals: a novel quaternary semiconductor," *Chemical Communications*, vol. 47, no. 11, pp. 3141–3143, 2011.

- [62] A. Wangperawong, J. S. King, S. M. Herron, B. P. Tran, K. Pangan-Okimoto, and S. F. Bent, "Aqueous bath process for deposition of $\text{Cu}_2\text{ZnSnS}_4$ photovoltaic absorbers," *Thin Solid Films*, vol. 519, no. 8, pp. 2488–2492, 2011.
- [63] J. Y. Chane-Ching, A. Gillorin, O. Zaberca, A. Balocchi, and X. Marie, "Highly-crystallized quaternary chalcopyrite nanocrystals via a high-temperature dissolution-precipitation route," *Chemical Communications*, vol. 47, no. 18, pp. 5229–5231, 2011.
- [64] M. Cao and Y. Shen, "A mild solvothermal route to kesterite quaternary $\text{Cu}_2\text{ZnSnS}_4$ nanoparticles," *Journal of Crystal Growth*, vol. 318, no. 1, pp. 1117–1120, 2011.
- [65] Z. H. Zhou, Y. Y. Wang, D. Xu, and Y. F. Zhang, "Fabrication of $\text{Cu}_2\text{ZnSnS}_4$ screen printed layers for solar cells," *Solar Energy Materials and Solar Cells*, vol. 94, no. 12, pp. 2042–2045, 2010.
- [66] S. Y. Chen, X. G. Gong, A. Walsh, and S. H. Wei, "Defect physics of the kesterite thin-film solar cell absorber $\text{Cu}_2\text{ZnSnS}_4$," *Applied Physics Letters*, vol. 96, no. 2, Article ID 021902, 2010.
- [67] S. Y. Chen, J. H. Yang, X. G. Gong, A. Walsh, and S. H. Wei, "Intrinsic point defects and complexes in the quaternary kesterite semiconductor $\text{Cu}_2\text{ZnSnS}_4$," *Physical Review B*, vol. 81, no. 24, Article ID 245204, 2010.
- [68] A. Nagoya, R. Asahi, R. Wahl, and G. Kresse, "Defect formation and phase stability of $\text{Cu}_2\text{ZnSnS}_4$ photovoltaic material," *Physical Review B*, vol. 81, no. 11, Article ID 113202, 2010.
- [69] T. Maeda, S. Nakamura, and T. Wada, "First principles calculations of defect formation in in-free photovoltaic semiconductors $\text{Cu}_2\text{ZnSnS}_4$ and $\text{Cu}_2\text{ZnSnSe}_4$," *Japanese Journal of Applied Physics*, vol. 50, no. 4, part 2, Article ID 04DP07, 2011.
- [70] C. Chory, F. Zutz, F. Witt, H. Borchert, and J. Parisi, "Synthesis and characterization of $\text{Cu}_2\text{ZnSnS}_4$," *Physica Status Solidi*, vol. 7, no. 6, pp. 1486–1488, 2010.

Research Article

Influence of Parameters of Cold Isostatic Pressing on TiO₂ Films for Flexible Dye-Sensitized Solar Cells

Yong Peng,¹ Jefferson Zhe Liu,² Kun Wang,¹ and Yi-Bing Cheng¹

¹Department of Materials Engineering, Monash University, Clayton, Melbourne, VIC 3800, Australia

²Department of Mechanical and Aerospace Engineering, Monash University, Clayton, Melbourne, VIC 3800, Australia

Correspondence should be addressed to Yi-Bing Cheng, yibing.cheng@monash.edu

Received 22 February 2011; Accepted 9 May 2011

Academic Editor: Leonardo Palmisano

Copyright © 2011 Yong Peng et al. This is an open access article distributed under the Creative Commons Attribution License, which permits unrestricted use, distribution, and reproduction in any medium, provided the original work is properly cited.

Cold Isostatic Pressing (CIP) is used to make TiO₂ working electrodes for flexible dye-sensitized solar cells (DSCs). Different CIP processes, varying pressures from 50 MPa to 200 MPa and holding time 1 s up to 600 s, are performed to study the effect of CIP on the resistivity of TiO₂ electrode thin films and the power conversion efficiency (PCE) of DSCs. The results show that the CIP process has significantly improved the PCE of DSC devices. Electrochemical impedance spectroscopy (EIS) analysis indicates a clear correlation between the PCE enhancement and the resistivity reduction in TiO₂ thin films after various CIP processes. Porosity reduction and localized joints formed between some TiO₂ nanoparticles due to the friction heat in the CIP process are believed to be responsible for the resistivity reduction of the TiO₂ working electrode thin films.

1. Introduction

Since dye-sensitized solar cell (DSC) was reported in 1991, it has been seen as a viable potential alternative to existing solar cell technologies [1, 2]. Due to its characteristics of being portable, of low costs, and high power conversion efficiency (PCE), flexible dye-sensitized solar cells have attracted interests of scientists and manufacturing industries in the last decade. However, the PCE of flexible DSCs has been relatively low because the plastic substrate cannot be sintered at high-temperature. The high temperature sintering, usually at ~500°C, benefits inter-TiO₂ particle connections and reduces internal resistance of TiO₂ working electrodes. Hence, in past years, many low-temperature processing methods were utilized to improve contacts between TiO₂ particles. Mechanical rolling and uniaxial pressing were such low-temperature techniques used to produce flexible working electrodes for DSCs [3, 4]. These techniques can improve the contacts between TiO₂ particles but would have some difficulty to achieve uniformity for large size devices.

Cold isostatic pressing (CIP) has been widely used as an effective pretreatment technique for compaction of ceramic and metal powders [5]. Compared with uniaxial pressing, samples compressed with CIP have higher relative density,

better mechanical properties, and more even microstructures [6]. In some reports [7, 8], ceramic powders could be compressed to a maximum relative density of 70% after the CIP process. After being applied with high CIP pressure, nanoparticles can be sintered to a relative density of 99% or higher. Recent work by Weerasinghe et al. [9] has demonstrated CIP as an effective way to improve TiO₂ film quality for plastic-based DSCs. Systematic study of the CIP process on the properties of TiO₂ thin film and underlying mechanism, however, is still missing. Such knowledge is highly desired to optimize the CIP process for future DSC developments.

In this paper, we report a study on the compaction of TiO₂ nanoparticles in thin films subject to different CIP pressures and holding times. The photovoltaic and electrochemical impedance measurements show that the CIP process is an effective way for the improvement of the conversion efficiency of flexible DSCs due to the significant reduction of the electrical resistivity of the TiO₂ thin films. The possible reasons of resistivity reduction are also discussed in terms of porosity reduction of TiO₂ thin films and joints formed among TiO₂ nanoparticles caused by the friction heat in the CIP process.

2. Experimental

2.1. Cell Preparation. Working electrodes of DSCs are made of TiO_2 (P25, Degussa, Australia). First, TiO_2 nanoparticles were mixed with ethanol absolute to make a slurry with a TiO_2 content of about 30 wt% in a planetary ball mill [10] (Pulverisette 6, Fritsch). Then, the milled slurry was used to make films on ITO/PEN plastic substrates ($13 \Omega/\square$, Pecell Technologies, Inc., Japan) via doctor blading. After being dried at 150°C for 30 min in air, films were compressed in a CIP machine (ABB Autoclave Systems, INC., USA). The applied pressure was 200 MPa, 100 MPa, and 50 MPa, and the holding time 1 s, 300 s, and 600 s, respectively. After being compressed, the films were used as working electrodes.

N719 dye, (Cis-bis(isothiocyanato) bis(2,2'-bipyridyl-4,4'-dicarboxylato)-ruthenium(II)bis-terabutyl-ammonium (Solaronix SA, Switzerland)), was used to sensitize working electrodes. Working electrodes were immersed into a dye solution with a content of 0.5 mM N719 dye in 1:1 ethanol and acetonitrile solution overnight. Sensitized working electrodes were then attached with a Pt|ITO|PEN counter electrode. After being filled with an electrolyte (0.04 M I_2 , 0.4 M 4-tert-butylpyridine, 0.4 M LiI, 0.3 M N-methylbenzimidazole in 1:1 acetonitrile and 3-methoxypropionitrile solution), cells were prepared for tests.

2.2. Measurements. I-V characters of the cells were taken in an Oriol Solar Simulator system with monochromatic light by attaching a Pt|ITO|PEN to the dye-sensitized working electrodes under one sun for opening tests. The electrochemical impedance spectroscopy (EIS) of cells was taken in an electrochemistry station (Bio-Logic SAS). EIS spectra were recorded over a frequency range of $0.05\text{--}10^5$ Hz under a lamp with a light density of 1 sun and adding a negative 0.6 V voltage to working electrodes. Resistance of cells was calculated via EC-Lab software (Bio-Logic SAS). The microstructures of the TiO_2 films were analyzed by using SEM (JEOL JSM 7001F) and TEM (Philips CM20). Film thickness measurements were taken via a Dektak 150 stylus profiler (Veeco Instruments Inc.).

3. Results and Discussion

Figure 1 shows a high-quality TiO_2 film compressed with a CIP pressure of 200 MPa and holding time of 300 s. Figure 2 summarizes the PCE of the DSC devices after various CIP processes. In comparison to the PCE of the cells without CIP (0.8%), the improvement by the CIP process is significant. The highest PCE is obtained in the device compressed under a pressure of 200 MPa and holding time of 300 s. In most cases, the PCE of cells improves with the increase of both holding time and CIP pressure. The only exception is that under a pressure of 200 MPa, a holding time longer than 300 s leads to a slight decrease of PCE.

In our experiments, the only variable in the tested cells is the TiO_2 working electrode film. Hence, the enhancement of the PCE of the DSC cells can be attributed to the characteristic change of working electrodes under different CIP processes. Figure 3 shows SEM images of several TiO_2

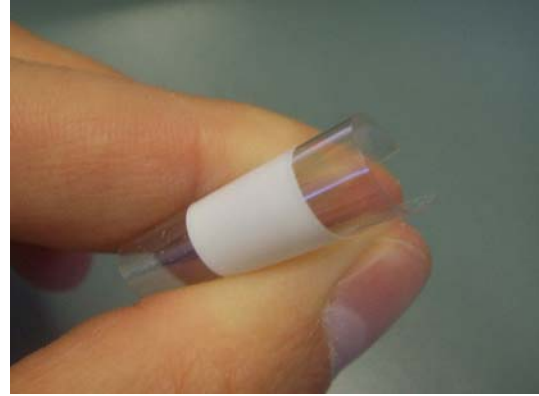


FIGURE 1: A Photo of a high-quality TiO_2 film produced by the CIP technique for flexible DSCs.

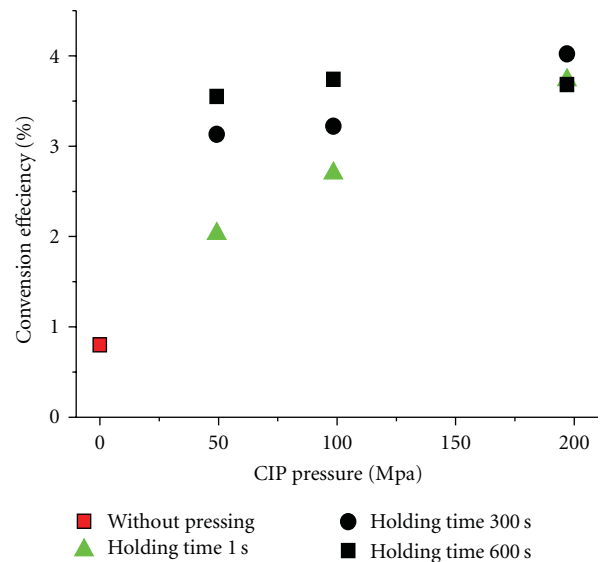


FIGURE 2: PCE of DSCs after the CIP process with pressure of 200 MPa, 100 MPa and 50 MPa and holding time of 1 s, 300 s, and 600 s, respectively. The PCE of the sample without CIP was 0.8%.

films. Without CIP (Figure 3(a)), cracks can be observed in the TiO_2 film. Figures 3(b)–3(d) show that CIP compactions under pressure of 50 MPa, 100 MPa, and 200 MPa, respectively, have produced high-quality films without obvious cracks. Pressed at 100 MPa and 200 MPa, microstructures of crack sealing appear in the TiO_2 films. Figure 4 shows TEM images of the samples before and after the CIP process. Soft aggregation can be observed in the film before CIP (Figure 4(a)), and some interparticle joints can be found after the CIP compaction (Figures 4(b) and 4(c)).

Figure 5 shows the EIS analysis of the DSC cells. A schematic equal circuit of flexible DSCs is shown in Figure 6. The resistance R_h consists of the resistance of substrate, resistance between substrate and electrolyte, and resistance between substrate and TiO_2 film [11, 12], which are represented by R_s , R_{ITO} , and R_{CO} in Figure 6. R_1 is the resistance of the interface of electrolyte and counter

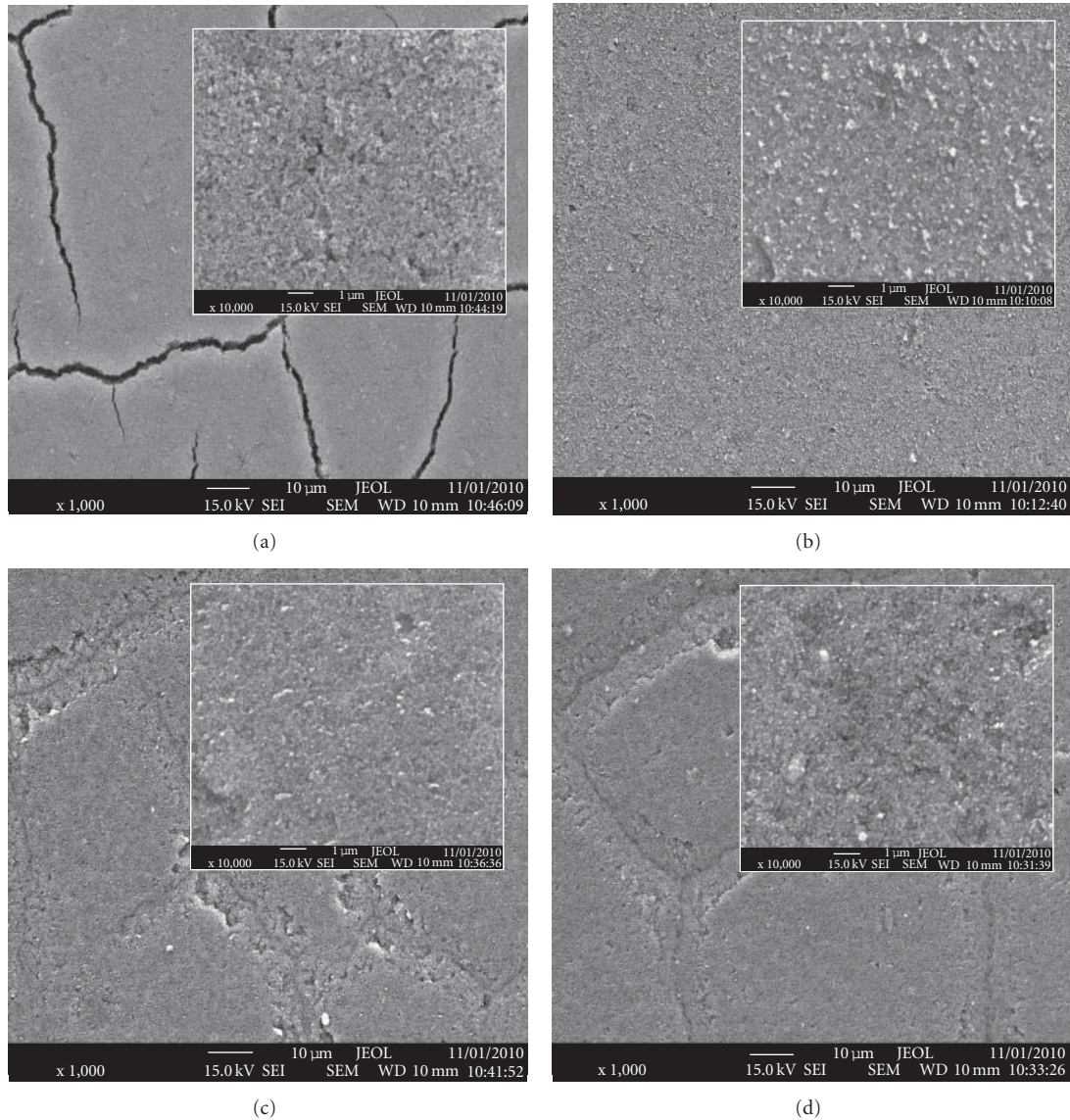


FIGURE 3: SEM pictures of films after various CIP processes. (a) film without CIP; (b) film with a CIP pressure of 50 MPa and holding time 1 s; (c) film with a CIP pressure of 100 MPa and holding time 600 s; (d) film with a CIP pressure of 200 MPa and holding time 600 s. The small inset shows the higher magnifications of each sample. The mark bar for the inset is 1 μm .

electrode represented by the semicircle in the EIS at the high-frequency band. Resistance R_2 represents transport resistance of electrons in TiO_2 films and the charge-transfer resistance of the charge recombination process between electrons in the TiO_2 film, dye and dye, I^-/I_3^- in the electrolyte, which are R_t and R_{ct} , respectively, in Figure 6. From Figure 5(b), it is very clear that R_h of the samples is significantly reduced by the CIP compaction, which can be attributed to the reduction of resistance between substrate and TiO_2 film. The overall internal resistance of a DSC device comprised of R_1 , R_2 , and R_h . According to Figure 5(d), the internal resistance decreased with the increase of CIP pressure up to 100 MPa and holding time up to 600 s, indicating that the electron transportation in these samples increased. However, an increase in the internal resistance of the device was found when the TiO_2 films had been compressed at 200 MPa

for 600 s. Under this condition, there could be mechanical damage to the ITO coating on the PEN film. A lower internal resistance was recorded if the sample was pressed at 200 MPa but a shorter holding time.

It is well known that the CIP pressing leads to high relative density, good mechanical property, and uniform microstructures in ceramic films. Figure 7 depicts the thickness of TiO_2 electrode films after the CIP compaction. The original film thickness before the CIP pressing was around 8.2 μm . In our experiments, there was little change of the films in the lateral direction before and after the CIP pressing, thus the reduction of the film thickness is proportional to the increase of the packing density of nanoparticles. It is seen from Figure 7 that with increase of CIP pressure and holding time, the film thickness decreases gradually. At 200 MPa and a holding time of 600 s, the relative

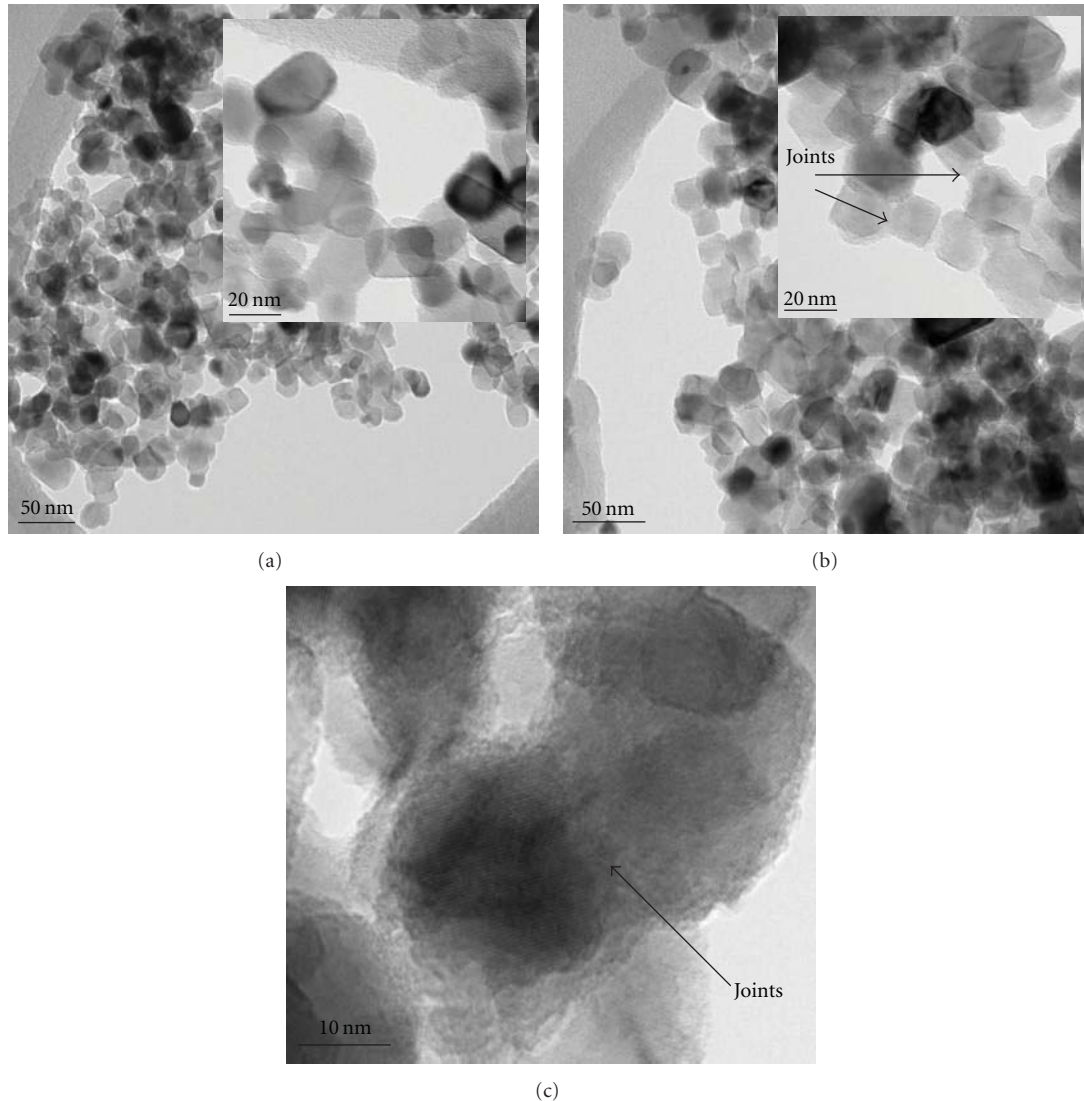


FIGURE 4: TEM images of TiO_2 films (a) without CIP and (b, c) with a CIP pressure of 200 MPa and holding time of 600 s. The small inset shows the higher magnification image of each sample.

packing density is increased to about 50%. Such an increase in packing density leads to the improved physical contacts between the nanoparticles and consequently the reduction of the resistivity, which can explain the observed reduction in resistivity (Figure 5) and improvement in the power conversion efficiency of the cells (Figure 2).

The improvement of the relative packing density of the TiO_2 film by the CIP compaction, however, cannot explain all the observed resistivity reduction and conversion efficiency improvement. In Figure 7, the samples pressed at 50 MPa, 100 MPa, and 200 MPa for one second, respectively, show a relatively small reduction in the film thickness compared to the one without CIP, but the reduction in resistivity (Figure 5) and the improvement in PCE (Figure 2) are quite significant. Moreover, the TiO_2 film prepared by CIP under 200 MPa for 1 s has lower resistivity and higher PCE than those pressed at 50 MPa for 300 s and 600 s (Figure 5), despite its packing density that is lower than the latter samples. It is

assumed that the formation of the strong joints among TiO_2 particles may help explain these observations. Subjected to a high CIP pressure, the friction between TiO_2 nanoparticles would take place and thus convert the mechanical energy to thermal energy. The increased temperature would promote the atom diffusion among the nanoparticles, leading to the formation of interparticle chemical bonds. It is difficult to directly observe the formation of such chemical bonds in our experiments, thus a simple theoretical analysis is proposed. TiO_2 nanoparticles after the CIP process preserved its structural integrity (Figure 4). If the holding time is short, for example, several seconds, the heat flux out of the thin film can be assumed negligible. It suggests that the majority of the mechanical work is converted to thermal energy. The work done by the CIP is about $W = PA\Delta h$, where P is the CIP pressure being applied to films, A is the surface area of the thin film, and Δh is the reduction of the film thickness. The increase of the thermo-energy is $U = \rho Ah_0 C\Delta T$, where ρ is

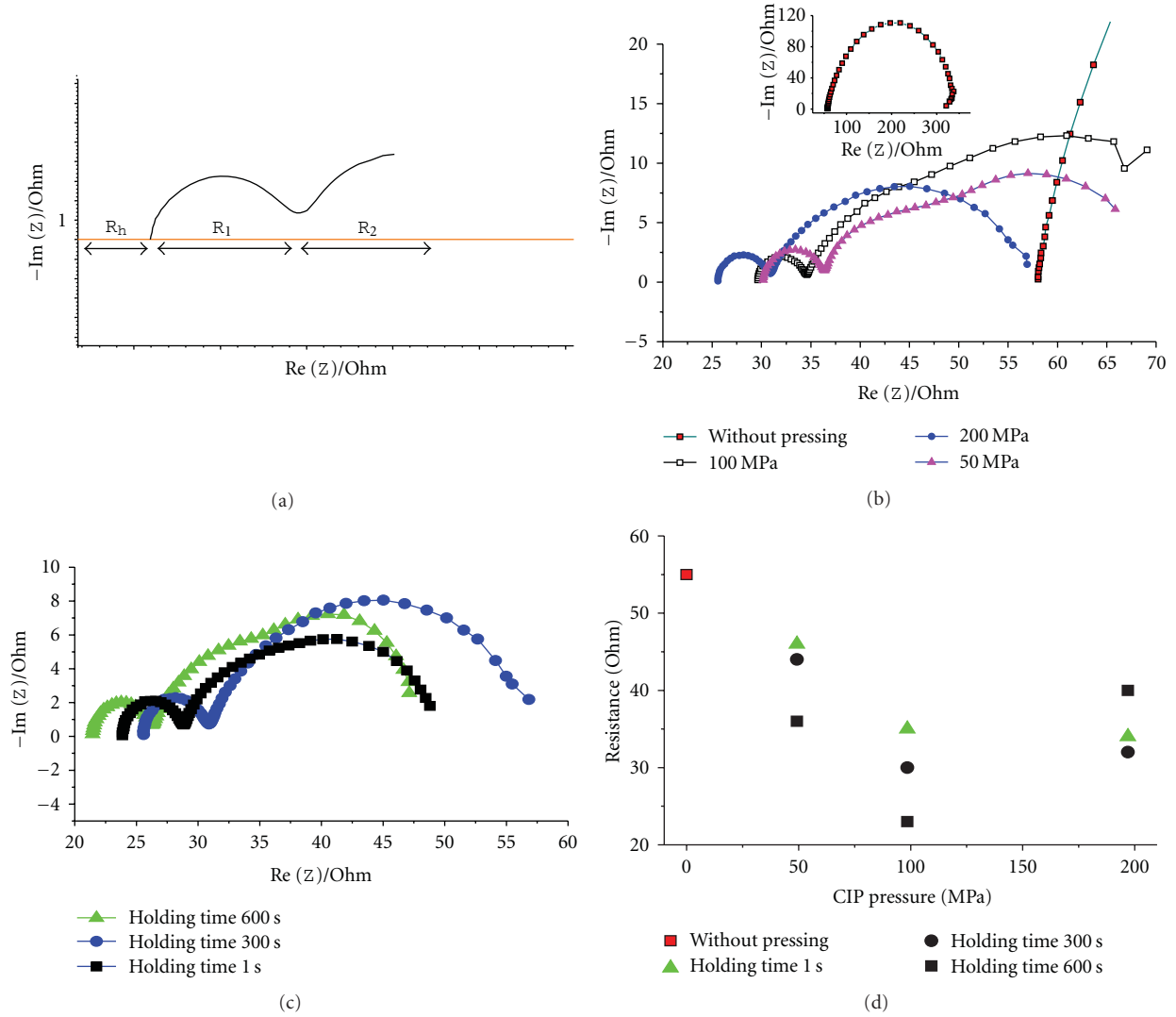


FIGURE 5: Nyquist impedance results of DSCs after various CIP processes. (a) Schematic diagram of the $-\text{Im}(Z)$ versus $\text{Re}(Z)$ curve; (b) Nyquist impedance results of samples without CIP and with CIP at different pressures for 300 s; (c) Nyquist impedance results of samples with the same CIP pressure of 200 MPa but different holding time; (d) calculated overall internal resistance of TiO_2 films after various CIP pressing. The overall internal resistance of the sample without pressing is 55 ohm.

the density of the TiO_2 nanoparticle film (average measured value is around 0.726 g/cm^3), h_0 is the thickness of the film before CIP, C is the heat capacity of TiO_2 film [13] (around $57 \text{ J/mol}\cdot\text{K}$), and ΔT is the average temperature increase of the whole thin film. Thus, we have $\Delta T = P\Delta h/\rho h_0 C$. For a thin film pressed at CIP pressure 200 MPa and holding time 1 s, the estimated average temperature increase ΔT throughout the thin film is about 20 K. If we consider that the friction occurs at the contact points of the nanoparticles, the temperature increase at the contact points could be much higher than the ΔT of the film. For example, if we assume the TiO_2 nanoparticles of a diameter 20 nm (Figure 4) as a group of hexagonal close-packed balls subject to a 200 MPa pressure, according to Hertz contact model [14] between two elastic balls, the contact area is about 5% of the total surface. If all heat was produced as a result of

interparticle friction, then the local temperature increase at the contact area could be one order of magnitude higher. In addition, it is well known that diffusion activation energy of atoms is lower at the nanoparticles interface/surface than in the bulk material. The high surface (interface)/volume ratio of the nanostructured materials thus leads to a higher diffusion coefficient than the corresponding bulk material [15–17]. Indeed, the formation of strong joints among gold nanoparticles has been observed when subjected to a sufficiently high pressure [18]. It is, therefore, possible that some chemical bonds would be formed due to the interparticle diffusion among the TiO_2 nanoparticles under the CIP pressing. The ΔT estimated for CIP pressures of 50 MPa and 100 MPa at a holding time 1 s are only about 1 K and 7 K, respectively. We can thus assume that there would mainly be physical contacts between the nanoparticles in these two

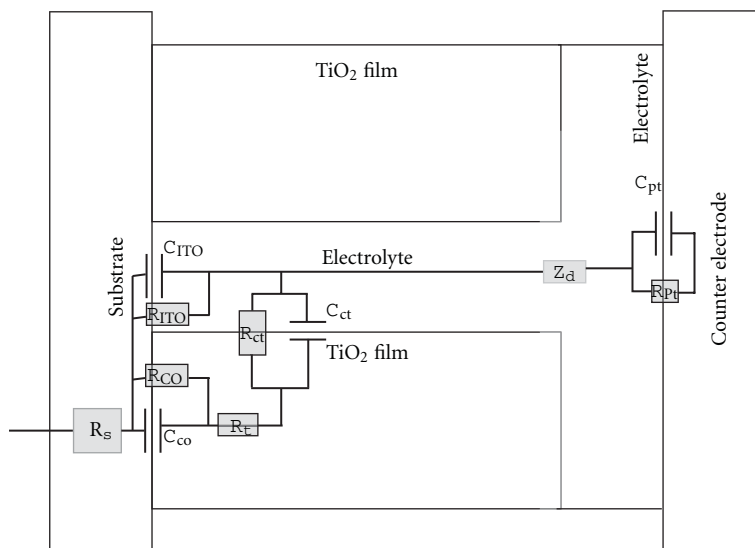


FIGURE 6: Equal circuit of DSC. R_{ct} is the charge-transfer resistance of the charge recombination process between electrons in the TiO_2 film and I_3^- in the electrolyte; R_t is the transport resistance of electrons in TiO_2 films; R_{ITO} is the charge-transfer resistance at exposed ITO/electrolyte interface; R_{co} is the contact resistance of ITO/ TiO_2 interface; R_{pt} is the charge-transfer resistance of exposed Pt/electrolyte interface; C_{ct} , C_{ITO} , C_{co} , and C_{pt} are the chemical capacitance of the TiO_2 film, corresponding double-layer capacitance at the exposed ITO/electrolyte interface, capacitance at ITO/ TiO_2 interface, and capacitor of Pt/electrolyte interface, respectively. R_s consists of the substrate resistance and series resistance between substrate and wires [11, 12].

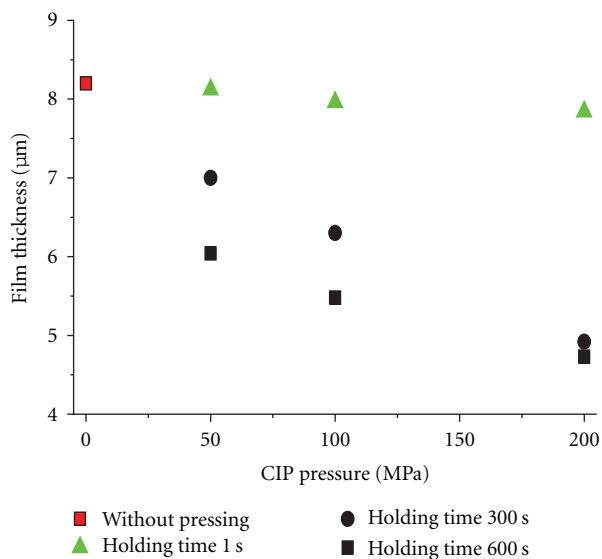


FIGURE 7: TiO_2 film thicknesses after CIP compressing at different conditions; the film thickness before CIP pressing was $8.2 \mu\text{m}$.

cases. At CIP pressure 50 MPa and holding times 300 s and 600 s, the film thickness further reduced and the estimated average temperature increases ΔT would be about 14 K and 25 K, respectively. They are close to the estimated value for CIP pressure 200 MPa and holding time 1 s. Since the holding time in these two cases is much longer, the heat flux out of the electrode thin film could significantly lower the estimated temperature. This explains the relatively lower PCE in these two samples.

4. Conclusions

In this paper, the effects of the CIP technique on the improvement of conversion efficiency of DSCs have been studied with the CIP pressure varying from 50 MPa to 200 MPa and holding time from 1 s to 600 s. Our results show a general trend that with the increase of the pressure and holding time, the resistivity of the TiO_2 thin film electrode decreases and the PCE improves. At pressure 200 MPa, holding time longer than 300 s does not lead to a significant efficiency improvement, which may be attributed to the mechanical damage to the ITO coating on the PEN film. The effects of the CIP pressure on the efficiency of DSCs on plastic substrates could be related to the improvement of the packing density of TiO_2 films and the possible formation of chemical bonds among the nanoparticles.

Acknowledgment

Support from the Victorian Organic Solar Cell Consortium (VICOSC) is greatly appreciated by the authors.

References

- [1] M. Gratzel, "Recent advances in sensitized mesoscopic solar cells," *Accounts of Chemical Research*, vol. 42, no. 11, pp. 1788–1798, 2009.
- [2] L. M. Gonçalves, V. de Zea Bermudez, H. A. Ribeiro, and A. M. Mendes, "Dye-sensitized solar cells: a safe bet for the future," *Energy & Environmental Science*, vol. 1, no. 6, pp. 655–667, 2008.

- [3] H. Lindstrom, A. Holmberg, E. Magnusson, S.-E. Lindquist, L. Malmqvist, and A. Hagfeldt, "A new method for manufacturing nanostructured electrodes on plastic substrates," *Nano Letters*, vol. 1, no. 2, pp. 97–100, 2001.
- [4] T. Yamaguchi, N. Tobe, D. Matsumoto, and H. Arakawa, "Highly efficient plastic substrate dye-sensitized solar cells using a compression method for preparation of TiO₂ photoelectrodes," *Chemical Communications*, no. 45, pp. 4767–4769, 2007.
- [5] I. M. Robertson and G. B. Schaffer, "Review of densification of titanium based powder systems in press and sinter processing," *Powder Metallurgy*, vol. 53, no. 2, pp. 146–162, 2010.
- [6] M. Trunec and K. Maca, "Compaction and pressureless sintering of zirconia nanoparticles," *Journal of the American Ceramic Society*, vol. 90, no. 9, pp. 2735–2740, 2007.
- [7] I.-W. Chen and X.-H. Wang, "Sintering dense nanocrystalline ceramics without final-stage grain growth," *Nature*, vol. 404, no. 6774, pp. 168–171, 2000.
- [8] K. T. Kim, S. C. Lee, and H. S. Ryu, "Densification behavior of aluminum alloy powder mixed with zirconia powder inclusion under cold compaction," *Materials Science & Engineering A*, vol. 340, no. 1-2, pp. 41–48, 2003.
- [9] H. C. Weerasinghe, P. M. Sirimanne, G. P. Simon, and Y.-B. Cheng, "Cold isostatic pressing technique for producing highly efficient flexible dye sensitized solar cells on plastic substrates," *Journal of Progress in Photovoltaics*. In press.
- [10] H. C. Weerasinghe, P. M. Sirimanne, G. P. Simon, and Y.-B. Cheng, "Fabrication of efficient solar cells on plastic substrates using binder-free ball milled titania slurries," *Journal of Photochemistry & Photobiology A*, vol. 206, no. 1, pp. 64–70, 2009.
- [11] Q. Wang, S. Ito, M. Gratzel et al., "Characteristics of high efficiency dye-sensitized solar cells," *Journal of Physical Chemistry B*, vol. 110, no. 50, pp. 25210–25221, 2006.
- [12] L. Y. Han, N. Koide, Y. Chiba, A. Islam, and T. Mitate, "Modeling of an equivalent circuit for dye-sensitized solar cells: improvement of efficiency of dye-sensitized solar cells by reducing internal resistance," *Comptes Rendus Chimie*, vol. 9, no. 5-6, pp. 645–651, 2006.
- [13] D. de Ligny, P. Richet, E. F. Westrum Jr., and J. Roux, "Heat capacity and entropy of rutile (TiO₂) and nepheline (NaAlSiO₄)," *Physics and Chemistry of Minerals*, vol. 29, no. 4, pp. 267–272, 2002.
- [14] S. P. Timonshenko and J. N. Goodier, *Theory of Elasticity*, McGraw-Hill, New York, NY, USA, 1970.
- [15] M. R. Ranade, A. Navrotsky, H. Z. Zhang et al., "Energetics of nanocrystalline TiO₂," *Proceedings of the National Academy of Sciences of the United States of America*, vol. 99, no. 2, pp. 6476–6481, 2002.
- [16] A. A. Levchenko, G. Li, J. Boerio-Goates, B. F. Woodfield, and A. Navrotsky, "TiO₂ stability landscape: polymorphism, surface energy, and bound water energetics," *Chemistry of Materials*, vol. 18, no. 26, pp. 6324–6332, 2006.
- [17] S.-M. Lee, D. G. Cahill, and T. H. Allen, "Thermal conductivity of sputtered oxide films," *Physical Review B*, vol. 52, no. 1, pp. 253–257, 1995.
- [18] Q. Jiang, S. H. Zhang, and J. C. Li, "Grain size-dependent diffusion activation energy in nanomaterials," *Solid State Communications*, vol. 130, no. 9, pp. 581–584, 2004.